A Study of the Axial Crush Response of Hydroformed Aluminum Alloy Tubes

by

Bruce W. Williams

A thesis

presented to the University of Waterloo

in fulfilment of the

thesis requirement for the degree of

Doctor of Philosophy

in

Mechanical Engineering

Waterloo, Ontario, Canada, 2007

I hereby declare that I am the sole author of this thesis. This is a true copy of the thesis, including any required final revisions, as accepted by my examiners.

I understand that my thesis may be made electronically available to the public.

Abstract

There exists considerable motivation to reduce vehicle weight through the adoption of lightweight materials, such as aluminum alloys, while maintaining energy absorption and component integrity under crash conditions. To this end, it is of particular interest to study the crash behaviour of lightweight tubular hydroformed structures to determine how the forming behaviour affects the axial crush response. Thus, the current research has studied the dynamic crush response of both non-hydroformed and hydroformed EN-AW 5018 and AA5754 aluminum alloy tubes using both experimental and numerical methods.

Experiments were performed in which hydroforming process parameters were varied in a parametric fashion after which the crash response was measured. Experimental parameters included the tube thickness and the hydroformed corner radii of the tubes.

Explicit dynamic finite element simulations of the hydroforming and crash events were carried out with particular attention to the transfer of forming history from the hydroforming simulations to the crash models. The results showed that increases in the strength of the material due to work hardening during hydroforming were beneficial in increasing energy absorption during crash. However, it was shown that thinning in the corners of the tube during hydroforming decreased the energy absorption capabilities during axial crush. Residual stresses resulting from hydroforming had little effect on the energy absorption characteristics during axial crush.

The current research has shown that, in addition to capturing the forming history in the crash models, it is also important to account for effects of material non-linearity such as kinematic hardening, anisotropy, and strain-rate effects in the finite element models. A model combining a non-linear kinematic hardening model, the Johnson-Cook rate sensitive model, and the Yld2000-2d anisotropic model was developed and implemented in the finite element simulations. This combined model did not account for the effect of rotational hardening (plastic spin) due to plastic deformation. It is recommended that a combined constitutive model, such as the one described in this research, be utilized for the finite element study of materials that show sensitivity to the Bauschinger effect, strain-rate effects, and anisotropy.

Acknowledgements

I would like to express my sincere gratitude to my supervisor Professor Michael Worswick for his support, guidance, and assistance. I would like to thank him for making my Ph.D. a fulfilling journey.

I also wish to acknowledge the friendship and help of the forming group at the University of Waterloo: Nader Abedrabbo, Alexander Bardelcik, Rassin Grantab, Blake Hodgins, Jose Imbert, Dino Oliveira, Oleg Orlov, Christopher Salisbury, Hari Simha, Mikhail Sorine, Alan Thompson, and Sooky Winkler.

I would also like to thank Andy Barber, Howard Barker, and Eckhard Budziarek. Their knowledge and experience was much appreciated in the development of the experimental apparatus.

I thank Guillaume D'Amours, Ahmed Rahem, and Hamid Shakeri from the Aluminum Technology Centre and Robert Mayer from the General Motors Technology Centre for their assistance and expertise throughout the project.

Finally, I would like to thank my wife Joanna for her understanding throughout my ten or so years at university, and to our little girl Allison who was an inspiration to complete this research.

Table of Contents

List of Figures

xiv

List of Tables

Chapter 1 – Introduction

Mild steels have been the primary material used for structural components in automobiles that could be subjected to dynamic crash events. Recently, researchers have studied alternative lightweight materials that could be employed, mainly due to environmental concerns. Reducing weight can lead to reduced fuel consumption and lower emissions, both of which are of great concern to the automotive industry. Aluminum and magnesium alloys, advanced high-strength steels, and composites are all proposed candidates for replacing mild steel in automotive structures. Aluminum is attractive due to its low-weight, good corrosion resistance, and the fact that it can be recycled with much less energy than that required to produce primary aluminum. One disadvantage to using aluminum is its lower ductility compared to steel. For this reason, there has been considerable attention in past years to understand and improve the formability of aluminum alloys. However, further effort is required to study the energy absorption characteristics of aluminum alloys in the as-formed condition during crash events.

In recent years, tube hydroforming has become a popular method to produce complex three-dimensional structural shapes. In tube hydroforming, a fluid pressure is applied to the inside of the tube causing it to deform and conform to the shape of a die. There are several advantages to hydroforming over conventional processes to produce closed structural sections, such as stamping and welding, that include a reduction in the number of parts and the overall assembly weight. In addition, hydroformed tubes offer increased strength and stiffness, and more precise component dimensions, all of which lead to lower manufacturing cost. In view of these advantages, hydroforming is already being used to fabricate structural

components on several current vehicles using mild steel tubes and some aluminum applications exist in luxury automobiles.

The purpose of this research is to study the interaction between the hydroforming process and crash response of aluminum alloy tubes. The research focuses on axial crush structures that are designed to absorb crash energy by progressive axial folding. Experimental parameters that are varied within the low and high pressure hydroforming processes include the tube thickness and the corner radius of the tubes. Numerical studies are carried out using explicit dynamic finite element models incorporating advanced constitutive material models to capture the entire forming and crash history. This research considers wrought Al-Mg-Mn aluminum alloys that are candidates for automotive structural applications.

The balance of this chapter provides a review of previous work relevant to this research. The differences between various hydroforming processes such as the low and high pressure operations will be discussed. Details will also be provided regarding numerous impact studies that have been performed with various materials. A brief review of theoretical equations to predict the axial crush response will be given, with a more in-depth discussion provided in Chapter 3. Several advanced constitutive models, which can be implemented in finite element analysis, will be outlined in this chapter with a more in-depth discussion provided in Chapter 4. Finally, a summary is given to discuss how the current research will address some of the relevant issues in the fields of forming and crash.

1.1 Tube Hydroforming

Tube hydroforming is a manufacturing process in which a tube is formed within a closed die by applying fluid pressure, usually by hydraulic fluid or water, on the inside of the tube. Tube hydroforming has become popular in recent years because it can be applied in high-volume production with low unit cost and can lead to improvements in the quality of the product. Figure 1.1 shows examples of how hydroformed components are currently used in automotive structures [1]. In a typical hydroforming process, the tube, which is often pre-formed to allow insertion within the die, is sealed at the tube ends and a pressure intensifier applies fluid pressure to the inside of the tube.
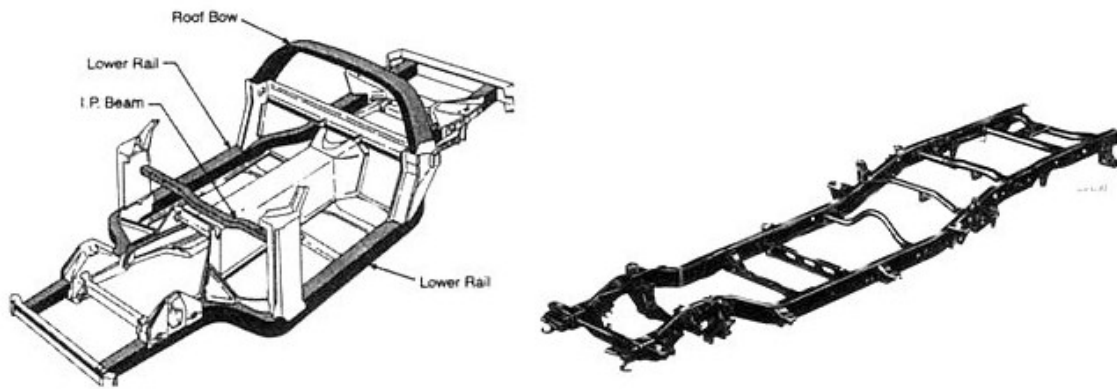
Figure 1.1: Hydroformed structural components within automobiles [1]

Prior to the late 1980s, hydroforming was mostly used for smaller components such as musical instruments and plumbing fittings until Standard Tube Canada (now a unit of Copperweld) began producing larger frame members by a process known as "Vari-form" [1]. This is a low pressure process, as depicted in Figure 1.2, in which the tube is pressurized during the die closing stage such that pinching and wrinkling of the tube can be reduced. In low pressure hydroforming, the perimeter of the die is approximately equal to the circumference of the tube, thus circumferential stretching of the tube is avoided using this process. Once the die is closed, a higher fluid pressure, known as the calibration pressure, is applied to form the tube into the die cavity.
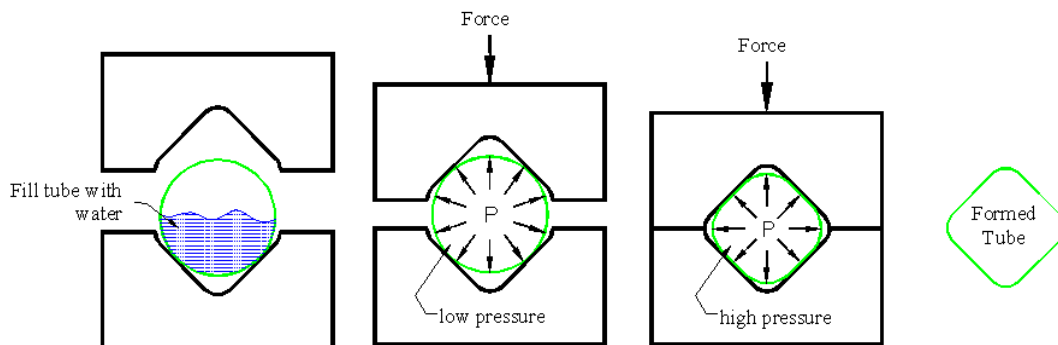
Figure 1.2: Low pressure hydroforming process

The first North American automobile in high volume production that incorporated a hydroformed component was the Chrysler minivan in 1990, in which the instrument-panel

beam was produced by the Vari-form process. Since this time, the use of hydroformed components has increased significantly on automobiles. General Motors uses hydroformed chassis rails for the Chevrolet Corvette and hydroformed frame rails for the GMC Sierra and Chevrolet Silverado [1].

If the calibration pressure required for forming is in excess of about 83 MPa, then the process is generally referred to as high pressure hydroforming [1]. In this process, the perimeter of the die cavity is generally larger than the circumference of the tube such that the tube must expand to conform to the die shape. As a result, the tube will thin and be subjected to higher circumferential strains compared to the low pressure process. The high pressure process allows tubes with a more complex geometry to be produced compared to the low pressure process, but the equipment for this process must be larger and capable of withstanding higher pressures.

An estimate for the calibration pressure, P, required to produce a tube with a given corner radius [1] is given by,

$$P = \frac{t}{R}\sigma_{UTS} \tag{1.1}$$

where, σ_{UTS} is the ultimate tensile strength, t is the tube thickness, and R is the corner radius.

In bulge forming, a type of hydroforming process, an internal pressure is applied to a tube allowing the tube to expand into an unsupported region. Several researchers [2,3,4] have shown that ductile damage criteria used with finite element models can accurately predict failure of the tube. Bulge forming is often used in assessing the formability of a material, but is not practical for structural components.

End-feeding is often used during hydroforming to push the tube ends into the die, producing compressive axial strains that will act to reduce thinning during tube expansion and thereby improve formability. However, if there is excessive end-feeding then the tube could buckle and wrinkle [2,5]. If the axial force is too low then friction will prevent deformation and material will not be pushed into the die such that there will not be a significant benefit on the formability of the tube. Figure 1.3 is a schematic plot of the end-feeding axial force versus the internal pressure showing regions of buckling and wrinkling, tube yielding, necking and bursting, and safe regions [6]. Several researchers have

4

developed optimization strategies for the pressure versus axial force profile during hydroforming [1,7,8].
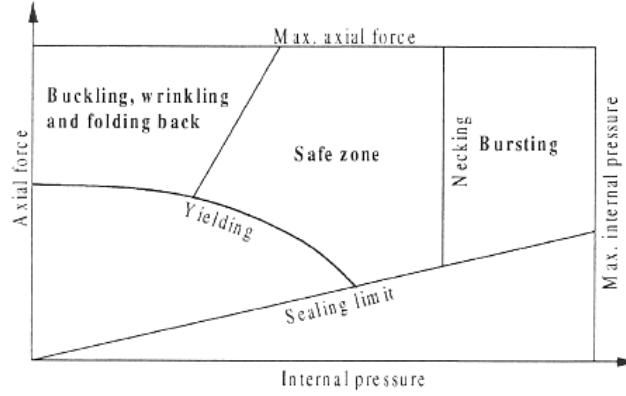
Figure 1.3: Diagram of working regions for end-feed process [6]

The following equations have been discussed by Marciniak et al. [9] to describe hydroforming of a circular tube into a square die, without end-feeding. A non-sticking model was proposed in which the tube is formed within a frictionless die. Also, a sticking model was studied in which any part of the tube that contacts the die wall, no longer changes in thickness during forming. These two cases are depicted in Figure 1.4. In the case of non-sticking friction, for a given corner radius, R, the thickness can be determined using [9],

$$t = \frac{t_0}{\left[\frac{4}{\pi} - \frac{R}{R_0} \left(\frac{4}{\pi} - 1 \right) \right]} \tag{1.2}$$

where, t_0 and R_0 are the initial thickness and radius, respectively. For the case of sticking friction [9],

$$t = t_0 \left(\frac{R}{R_0} \right)^{\frac{4}{\pi} - 1} \tag{1.3}$$

If there is no end-feeding and the assumption of plain strain is applied, then the longitudinal strain would be zero such that,

$$\varepsilon_\theta = -\varepsilon_t = \ln\left(\frac{t_0}{t}\right) \qquad (1.4)$$

from which an effective strain can be calculated. If the effective strain is known, then an effective stress, $\bar{\sigma}$, can be calculated which in turn can be used to solve for the circumferential stress, σ_θ, in the tube using [9],

$$\sigma_\theta = \frac{2}{\sqrt{3}}\bar{\sigma} \qquad (1.5)$$

from which the pressure, P, to cause yielding can be determined by,

$$P = \frac{\sigma_\theta t}{R} \qquad (1.6)$$
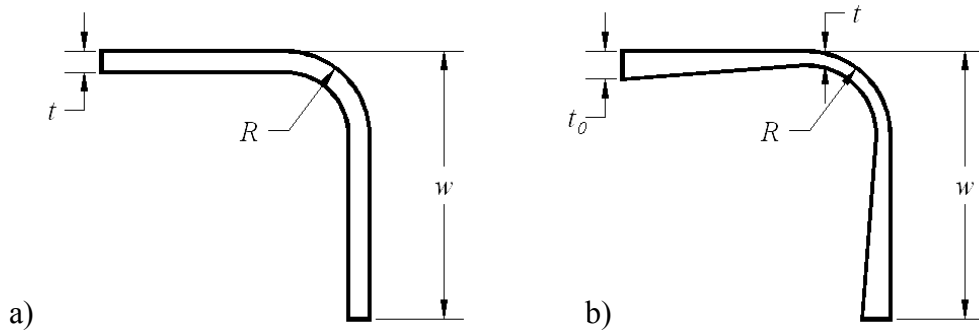
Figure 1.4: Cross-sectional profile for a) non-sticking friction and b) sticking friction assumptions

When end-feeding of the tube is used, the change in shape of the tube can depend not only on the pressure in the tube but also the end-feed level. Johnson et al. [10] outlines a procedure to describe the strains induced in a circular tube hydroforming process with end-feeding. However, forming within a square cross-section can complicate the equations. The details for describing hydroforming of a circular tube into a die with a square cross-section, with end-feeding are detailed in Chapter 3.

1.2 Axial Crush Testing

Drop tower facilities have been extensively used in the automotive industry to provide an inexpensive means of testing components to study dynamic behaviour, failure mode, energy absorption, materials, and geometry. The drop tower shown in Figure 1.5 [11], includes a drop platform which is raised to a specified height and released such that there is free-flight motion with acceleration due to gravity. The platform is guided by rails or cables that do not interfere with the vertical motion but act as a safety precaution.
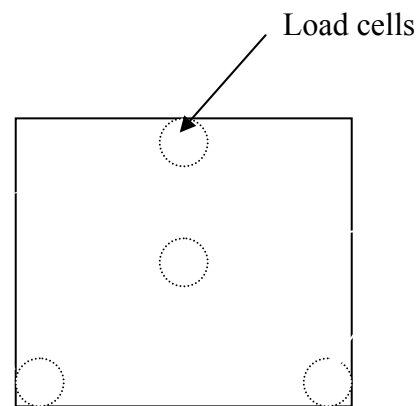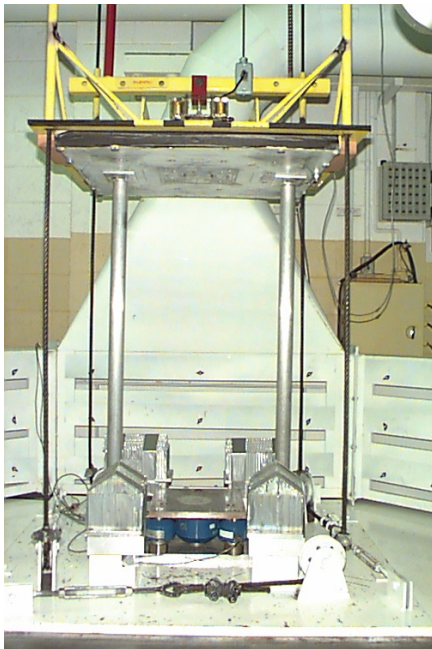
Load cells

Figure 1.5: Drop tower and load cell configuration used for axial crush testing [11]

The tube is attached to a fixture at the bottom of the drop tower with three load cells arranged in a triangular pattern [12]. As the tube deforms during impact, several lobes are formed, as seen in Figure 1.6 which shows the crushed shape of a square aluminum tube [13]. During each lobe formation there is a maximum and minimum force such that an oscillating response is obtained from the load versus crush distance response, examples of which can be seen in Figure 1.7. A peak in the force versus crush distance plot represents the formation of a new lobe. The energy absorbed is taken as the area under the crush force versus distance curve. The figure shows that there is a large peak load before the first lobe

forms, resulting in a large deceleration which is detrimental to occupant protection in actual crash events. As a result, fold initiators are usually introduced into structures designed for energy absorption [13]. Fold initiators are typically geometric defects placed within the tube walls that will trigger lobe formation at lower loads.

Figure 1.6: Deformation of 6061-T4 aluminum tube [13]
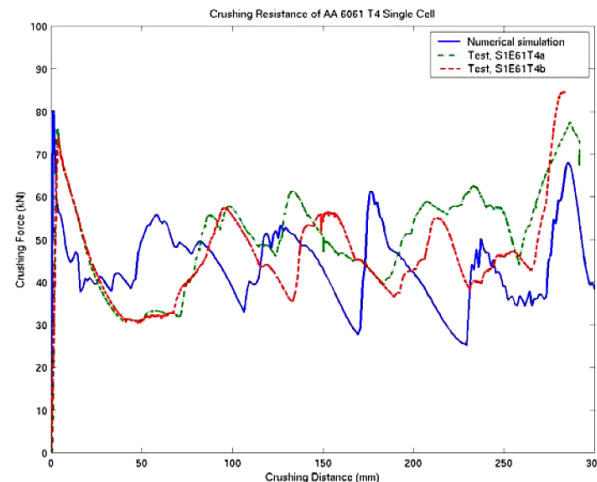
Figure 1.7: Crush force versus distance of 6061-T4 tubes [13]

1.3 Theoretical Equations for Axial Crush

During axial crush, a circular tube will deform in an axisymmetric (concertina) or non-axisymmetric (diamond) pattern as shown in Figure 1.8 [14]. In some cases the tube can switch from an axisymmetric to diamond behaviour during the impact test. Figure 1.9a

shows a symmetric crush mode for a tube with a square cross-section, while Figure 1.9b shows an asymmetric crush mode, both of which may form during crush of a square tube.

a)   b)
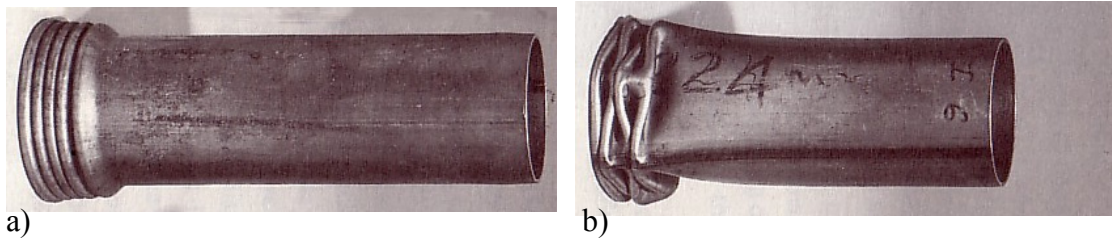
Figure 1.8: a) Axisymmetric and b) diamond pattern in deformation of round tube [14]

a)   b)
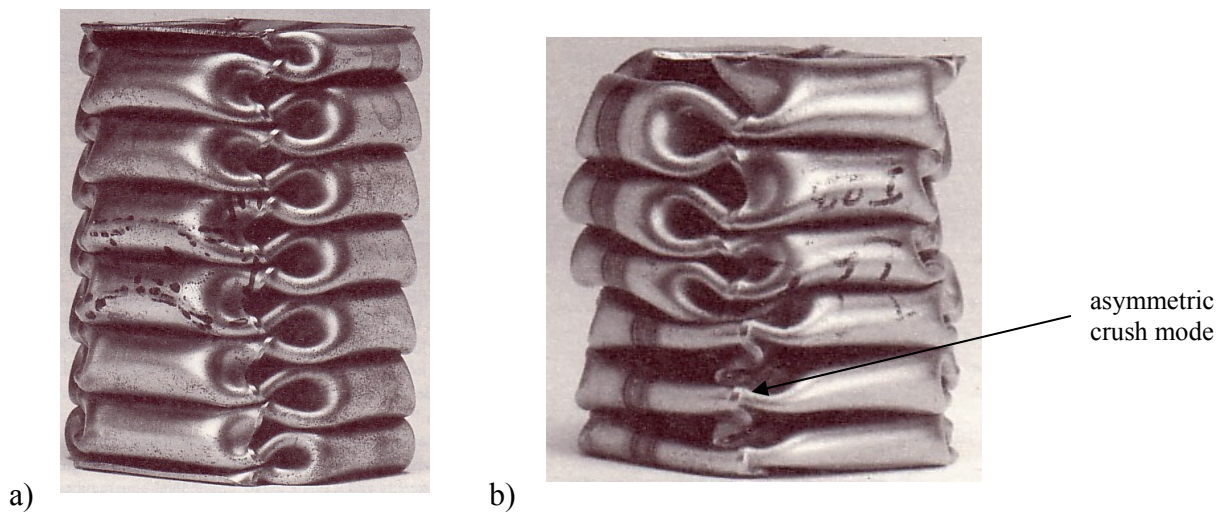
Figure 1.9: a) Symmetric and b) asymmetric deformation of square tubes [14]

In order to predict the axial crush response, several researchers have proposed theoretical equations to describe the mean load required for buckling of the tube. Due to the oscillating nature of the crush response, a mean load is often used to describe the crush load which can be considered an average of the force causing the progressive buckling. An equation developed by Alexander [15] to describe the mean crush load, P_m, required for collapse of a circular tube undergoing an axisymmetric crush mode, as shown in Figure 1.10, is given by,

$$P_m = 6.08\sigma_{YS}t^{1.5}\sqrt{D} \tag{1.7}$$

where, σ_{YS} is the yield strength of the material, t is the tube thickness, and D is the mean diameter of the tube. This equation was determined by equating the work of the mean crush force to the work of the bending moment and work resulting from circumferential stretching of the cylinder.
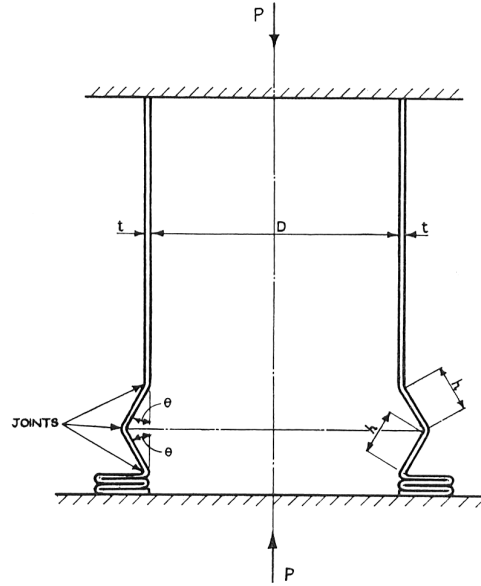
Figure 1.10: Axisymmetric crush mode of cylindrical shell [15]

The following equations were also developed to describe the mean crush load for tubes that deform with an axisymmetric pattern [16,17],

{ Alexander, [15] }
$$P_m = \sigma_0 t^2 \left[8.462 \left(\frac{R}{t} \right)^{1/2} + 1.814 \right] \qquad (1.8)$$

{ Singace et al., [18] }
$$P_m = \sigma_0 t^2 \left[7.874 \left(\frac{R}{t} \right)^{1/2} + 1.408 \right] \qquad (1.9)$$

{ Wierzbicki et al., [19] }
$$P_m = 11.22 \sigma_0 t^2 \left(\frac{R}{t} \right)^{1/2} \qquad (1.10)$$

{ Jones and Abramowicz, [17] }
$$P_m = \left[20.79 \left(\frac{2R}{t} \right)^{1/2} + 11.90 \right] \left(\frac{2\sigma_0}{\sqrt{3}} \right) \left(\frac{t^2}{4} \right) \quad (1.11)$$

where, R is the initial radius of the tube, t is the tube thickness, and σ_0 is known as the energy equivalent flow stress. The energy equivalent flow stress is a representation of the stress acting in the folds of the structure during deformation and several methods have been proposed to define this value, as will be discussed in Chapter 3.

The equations below predict the mean crush load (P_m) for tubes that deform with a diamond crush pattern [17],

$$\{ \text{Jones and Abramowicz, [17]} \} \qquad P_m = 86.14 \left(\frac{2R}{t} \right)^{1/3} \left(\frac{2\sigma_0}{\sqrt{3}} \right) \left(\frac{t^2}{4} \right) \tag{1.12}$$

$$\{ \text{Wierzbicki, [20]} \} \qquad P_m = \left(2\sigma_0 \pi R t \right) \left[3.64 \left(\frac{t}{R} \right)^{2/3} \right] \tag{1.13}$$

$$\{ \text{Pugsley and Macaulay, [21]} \} \qquad P_m = \left(2\sigma_0 \pi R t \right) \left[10 \left(\frac{t}{R} \right) + 0.03 \right] \tag{1.14}$$

Abramowicz and Jones [22] developed the following equation to describe the mean crush load for a square tube undergoing symmetric crush,

$$P_m = 9.53 \sigma_0 w^{1/3} t^{5/3} \tag{1.15}$$

where, w is the cross-sectional width of the tube. More recently, the following theoretical equation for the mean crush load for a square tube has been developed to better capture the observed symmetric crush pattern during axial crush [13],

$$P_m = 4\pi \sigma_0 w^{1/3} t^{5/3} \tag{1.16}$$

The above relationships were developed for quasi-static crushing in which the impact velocities are not higher than tens of meters per second [14]. At higher impact velocities, the crush deformation can be considered to be dynamic and strain-rate effects must be accounted for if the material is strain-rate sensitive. The following equation relates the dynamic mean load, $P_m{}^d$, to the static mean load, $P_m{}^s$ [14],

$$\frac{P_m{}^d}{P_m{}^s} = 1 + \left(\frac{V_0}{hD_{SR}} \right)^{1/q_{SR}} \tag{1.17}$$

where, V_0 is the impact velocity, h is equal to $2D$ for round tubes and equal to $w/0.33$ for square tubes, and D_{SR} and q_{SR} are material constants for a strain-rate sensitive material. This model was based on a Cowper-Symonds constitutive equation of the form [14],

$$\frac{\sigma_0{}'}{\sigma_0} = 1 + \left(\frac{\dot{\varepsilon}}{D_{SR}}\right)^{1/q_{SR}} \tag{1.18}$$

where, $\sigma_0{}'$ is the dynamic flow stress and $\dot{\varepsilon}$ is the strain rate.

Several investigations have been carried out to compare experimental axial crush data to theoretical predictions involving circular and square tubes. Abramowicz and Jones [17,22] and Gupta [23] studied the axial crush response of circular mild steel tubes and showed good agreement between theory and experiment. Langseth and Hopperstad [24] showed that theoretical equations can also capture the experimental response for extruded, square AA6060 aluminum alloy tubes. Composite materials can also be considered for structural components and Shin et al. [25] and Mamalis et al. [26] have obtained experimental axial crush data for fibre reinforced composite structures.

Although theoretical predictions have provided agreement with experimental data, more recent studies have compared experimental results to predictions from finite element simulations. Bardi et al. [16] compared results from finite element simulations to experimental and theoretical predictions, showing good agreement for circular AA6061 aluminum alloy and mild steel tubes. Langseth et al. [27,28] have also shown good agreement between simulation and experiment for square AA6060 aluminum alloy tubes. Otubushin [29] validated simulations incorporating the Cowper-Symonds constitutive equation for strain-rate effects against experimental mild steel axial crush data. Tarigopula et al. [30] have recently studied the axial crush behaviour of thin-walled square tubes and spot-welded top-hat sections of DP800 steel showing agreement between simulation and experiment. Finite element simulations have also been performed by Krauss and Laananen [31] to study the effect of crush initiator geometry on the axial crush response of square tubes.

1.4 Relationship Between Forming and Crashworthiness

The axial crush investigations discussed above were performed with tubes for which there was no prior forming history or for which the forming history did not need to be considered. To date, only limited work has been carried out on the interaction between forming and crashworthiness.

Bending and hydroforming operations result in thickness changes, work hardening, and residual stresses which can be important factors affecting the energy absorption of the structure during a crash event. The degree to which these factors affect the crash response must be studied both experimentally and through simulations. Kellicut et al. [32] performed simulations of an S-shaped tube that was bent and hydroformed before a crash event. The thickness changes, work hardening, and residual stresses were carried forward from the bending simulation to the hydroforming simulation and then to the impact simulation. In some simulations, only the thickness changes were carried forward while in other simulations, only the work hardening was considered. Kellicut et al. [32] found that including the thickness changes and residual stresses did not have a significant affect on the crash response compared to when they were not included. However, it was found that when work hardening was included, there was a significant influence, indicating that the crash response of the S-shaped member shows a strong sensitivity to the effects of work hardening during forming. There were no data available to compare the simulation results to experimental results. Therefore, it is relevant to compare experimental and simulation data to determine whether or not the simulations can accurately predict the axial crush response.

1.5 Advanced Constitutive Models to Describe Material Nonlinearity

A generalized isotropic yield surface, as described by Hosford [33], can be expressed by the following equation,

$$\phi = (S_1 - S_2)^{2k} + (S_2 - S_3)^{2k} + (S_3 - S_1)^{2k} = 2\overline{\sigma}^{2k} \qquad (1.19)$$

where, $S_i = S_i(\sigma_{ij})$ are principle values of the deviatoric stress tensor, σ_{ij}, and $\overline{\sigma}$ is the isotropic effective flow stress. If $k=1$ then Equation 1.19 generates the von Mises yield surface. Whereas, if k approaches ∞ then the Tresca yield surface is obtained. This

equation was depicted by Karafillis and Boyce [34], as shown in Figure 1.11 for various *k*-values.
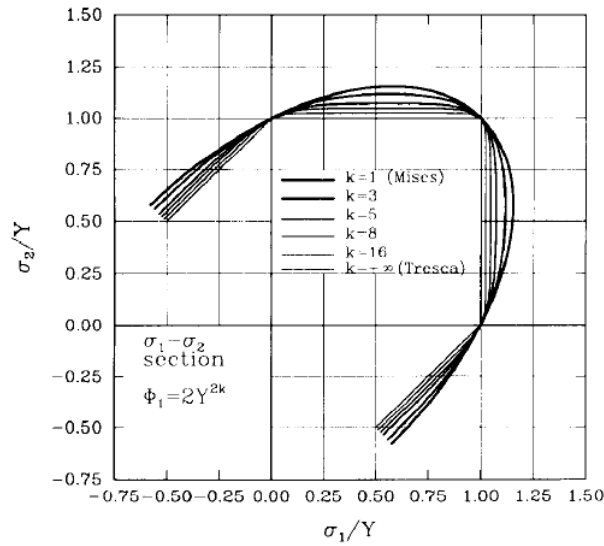
Figure 1.11: Isotropic yield surfaces bounded by the von Mises and Tresca yield surfaces [34]

The von Mises yield criterion is widely used to describe the yielding behaviour of materials during plastic deformation. However, many materials do not exactly behave according to this criterion under all loading conditions, such that it is important to study advanced constitutive models and their effect on the prediction of the hydroforming and impact response of aluminum alloy tubes. Anisotropy, kinematic hardening, and strain-rate effects could all be significant in metal forming. Each of these constitutive behaviours is outlined below, with more detailed description given in Chapter 4.

1.5.1 Anisotropy

Since the AA5754 material in the current study is cold-rolled prior to tube formation, a texture would have developed in the material, such that anisotropy could be significant. Two common anisotropic yield criteria have been developed by Hill [35] and Barlat and Lian [36] to describe yielding behaviour. The following yield function was proposed by Hill [35] to account for variations in strength measured along different material axes,

14

$$\phi = F(\sigma_{xx} - \sigma_{yy})^2 + G(\sigma_{zz} - \sigma_{xx})^2 + H(\sigma_{xx} - \sigma_{yy})^2$$
$$+ 2L\sigma_{yz^2} + 2M\sigma_{zx}^2 + 2N\sigma_{xy}^2 - 1 = 0 \tag{1.20}$$

where, *F, G, H, L, M,* and *N* are material constants. This equation is still widely used to describe the anisotropic behaviour of mild steel. The following yield function was developed by Barlat and Lian [36] to describe planar anisotropy, under plane stress conditions,

$$\phi = a|K_1 + K_2|^M + a|K_1 - K_2|^M + c|2K_2|^M - 2\bar{\sigma}^M = 0 \tag{1.21}$$

with,

$$K_1 = \frac{\sigma_{xx} + h\sigma_{yy}}{2} \tag{1.22}$$

and,

$$K_2 \sqrt{\left(\frac{\sigma_{xx} - h\sigma_{yy}}{2}\right) + \rho^2\sigma_{xy}^2} \tag{1.23}$$

where, *a, c, h,* and *ρ* are constants that describe the degree of anisotropy. With an *M*-value of 2, the Barlat and Lian [36] yield function corresponds to Hill's 1948 yield function, which is shown in Figure 1.12a for plane stress conditions. The shape of the yield surface for an *M*-value of 14 is shown in Figure 1.12b. *M*-values of 6 and 8 have been recommended to describe the anisotropic behaviour of BCC and FCC materials, respectively [36].
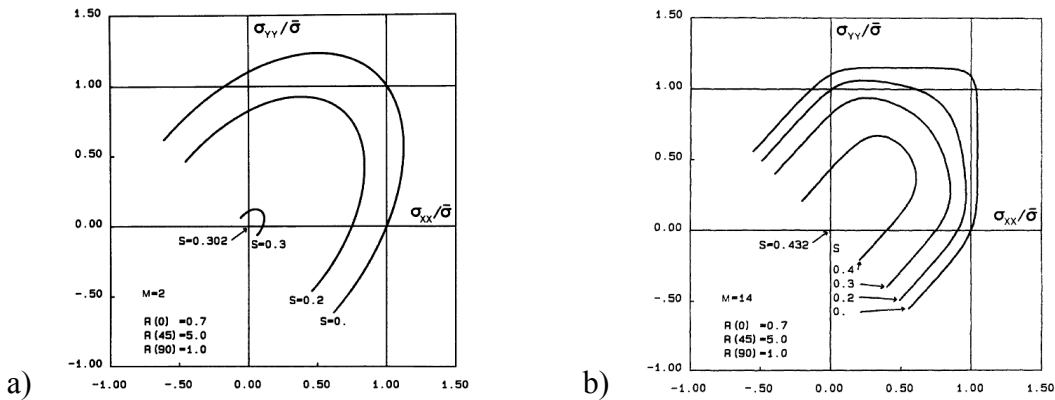
Figure 1.12: Shape of yield surface with an M-value of a) 2 and b) 14

Improvements to the Barlat and Lian's [36] anisotropic yield functions have been achieved by Barlat et al. [37,38] to more accurately capture biaxial stress conditions and *r*-values for aluminum alloy sheets. The anisotropic model recently developed by Barlat et. al [39,40], referred to as Yld2000-2d, has been shown to better describe the anisotropic behaviour of aluminum alloys under plane stress conditions. The yield function for this model is described by,

$$\phi = \left| X_1' - X_2' \right|^a + \left| 2X_2'' + X_1'' \right|^a + \left| 2X_1'' + X_2'' \right|^a - 2\overline{\sigma}^a = 0 \tag{1.24}$$

where, *a* has the same definition as *M* in Equation 1.21. The *X's* are principal values of the tensors X_{ij}' and X_{ij}'' defined by,

$$X_{ij}' = L_{ijkl}'\sigma_{kl} \qquad X_{ij}'' = L_{ijkl}''\sigma_{kl} \tag{1.25}$$

which are used to transform the stress state. This transformation procedure is described by Karafillis and Boyce [34] and can be referred to as the 'isotropy plasticity equivalent (IPE) stress transformation'. Equation 1.25 represents the transformation of the stress state of the anisotropic material to the corresponding stress state in two isotropic materials. The yielding behaviour in each of the isotropic stress states can then be described by an isotropic yield function of the type of Equation 1.19. The concept is depicted in Figure 1.13 for just a single transformation, where the tensor $\widetilde{S}_{ij}$ is used in place of X_{ij}. The tensor operators, L_{ijkl}', L_{ijkl}'' for the Yld2000-2d model are described in detail in Chapter 4.

The Yld2000-2d prediction is compared to an isotropic prediction and experimental data in Figure 1.14 for an Al-2.5 wt.% Mg. sheet alloy showing the shape of the yield surface in the normalized (by the uniaxial yield stress in the rolling direction) σ_x and σ_y directions. The Yld2000-2d prediction better captures the measured yielding response of the material compared to the isotropic prediction. The Yld2000-2d model requires the calibration of eight parameters, as discussed in Chapter 5, that are based on tensile testing of specimens taken from 0°, 45°, and 90° relative to the rolling direction, as well as the r-values in these three directions. The balanced biaxial yield stress, σ_b is also required which can be measured using a hydraulic bulge test [41]. The model has since been extended by Barlat et al. [42] for three-dimensional stress states.
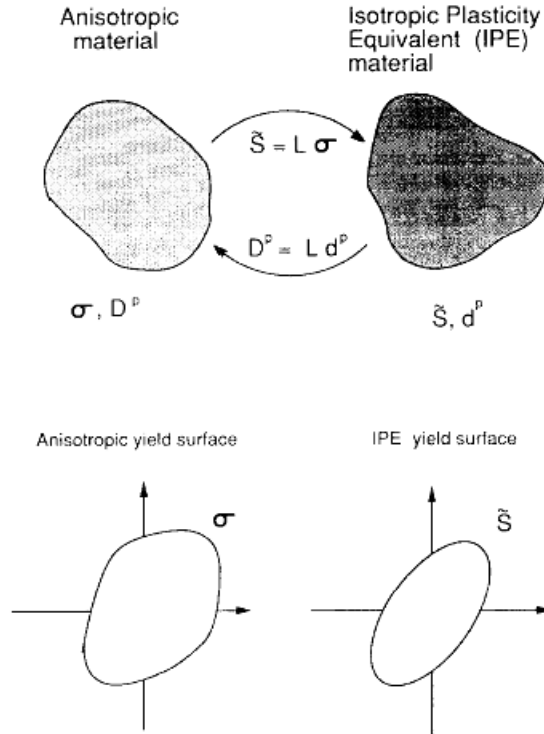
Figure 1.13: Transformation of anisotropic yield surface in stress space, σ_{ij} to isotropic yield surface in $\widetilde{S}_{ij}$ space [34]
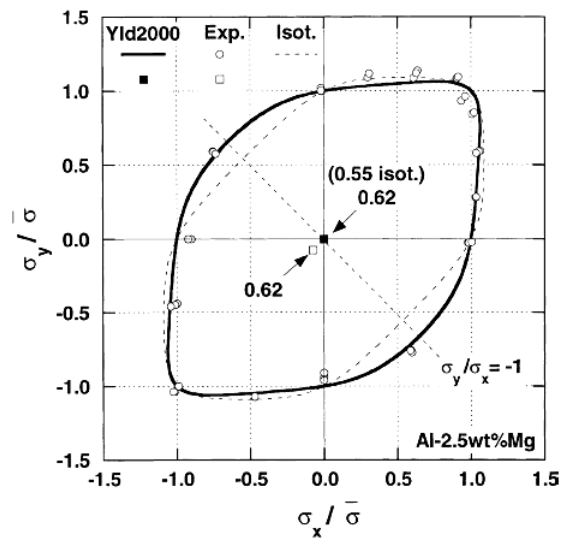
Figure 1.14: Normalized yield surface for an Al-2.5 wt.% Mg sheet [39]

1.5.2 Kinematic Hardening

Many materials that have undergone plastic deformation show a different stress-strain response during reverse loading compared to the initial loading behaviour, which is known as the Bauschinger effect. On reverse loading, the material will yield sooner than what is predicted using isotropic material behaviour such that kinematic hardening models must be used to describe this effect. Figure 1.15 shows the stress-strain behaviour from tension-compression and compression-tension tests performed by Lee et al. [41] using pre-strained specimens from an AA5754 aluminum sheet alloy. The results show that the materials yield sooner on reverse loading. Data collected by Lee et al. [41] was used to predict the springback response of the aluminum alloy.

During a hydroforming operation with end-feeding, the tube is compressed where upon impact, the compressed sections will undergo bending in a fold. A kinematic model would predict a different folding response, specifically on the tensile side of the bend, compared to an isotropic model. The significance of the Bauschinger effect on the energy absorption during crush was therefore studied in this research using a non-linear isotropic-kinematic hardening model [43].
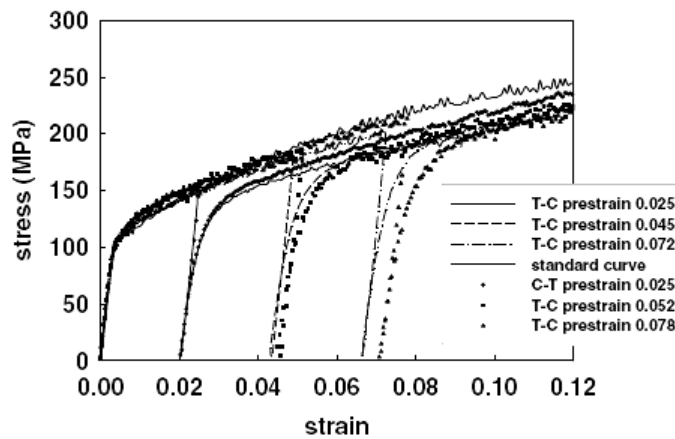
Figure 1.15: Reverse loading behaviour of pre-strained AA5754 sheet alloy [41]

Models often account for the Bauschinger effect by translating the location of the origin of the yield surface in stress space [43,44,45]. The term, α_{ij} is used to represent the

location of the yield surface origin, also know as the back stress, and is depicted in Figure 1.16 for plane stress conditions. In the case of purely kinematic hardening, the size of the yield surface always remains constant and just translates in space. The yield function to describe kinematic hardening is given by [43],

$$\phi = f\left(\sigma_{ij} - \alpha_{ij}\right) - \sigma_0 = 0 \tag{1.26}$$

where, $f\left(\sigma_{ij} - \alpha_{ij}\right)$ is the yielding criterion, σ_{ij} is the current state of stress, and σ_0 is the initial yield stress of the material. However, most materials are better described by a model which can account for both translation and expansion of the yield surface. The combined isotropic-kinematic hardening yield surface is also depicted in Figure 1.16.
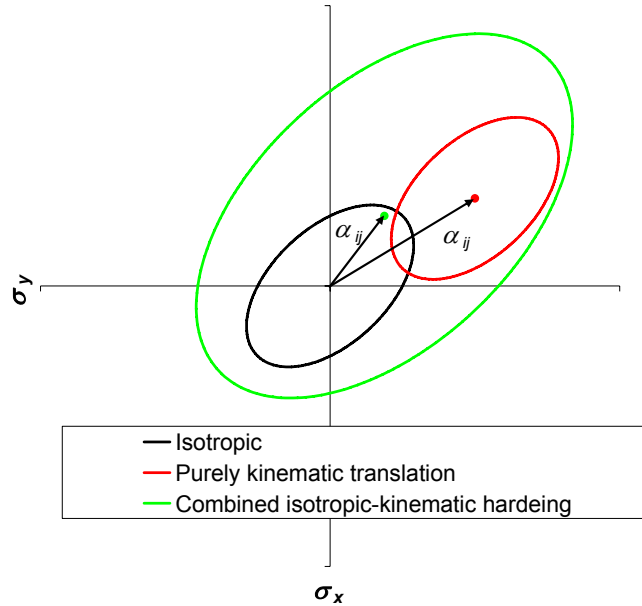
Figure 1.16: Depicted translation of yield surfaces with kinematic hardening

The combined isotropic-kinematic hardening yield function is expressed by [43],

$$\phi = f\left(\sigma_{ij} - \alpha_{ij}\right) - \sigma^0 = 0 \tag{1.27}$$

where for the von Mises yield criterion,

$$f\left(\sigma_{ij} - \alpha_{ij}\right) = \sqrt{\frac{3}{2}\left(\sigma'_{ij} - \alpha'_{ij}\right)\left(\sigma'_{ij} - \alpha'_{ij}\right)} \tag{1.28}$$

19

with σ'_{ij} as the deviatoric stress of σ_{ij} and α'_{ij} as the deviatoric of the back stress, α_{ij}. The radius of the yield surface is given by,

$$\sigma^0 = \overline{\sigma}_{iso} - \overline{\alpha} \tag{1.29}$$

where, $\overline{\sigma}_{iso}$ is the isotropic yielding behaviour and $\overline{\alpha}$ represents the effective size of the shift of the yield surface, as depicted in Figure 1.17.
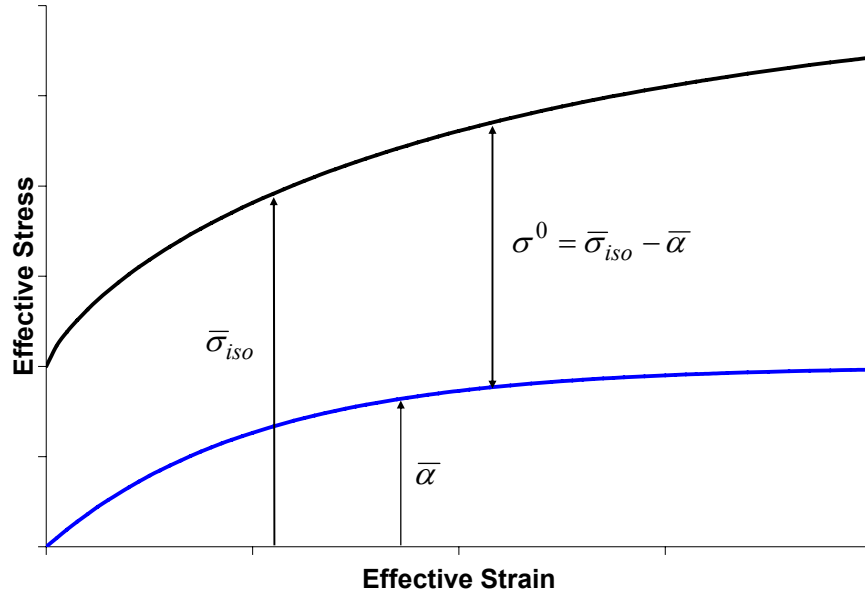
Figure 1.17: Hardening behaviour of material considering the effect of kinematic hardening

Several models have been used to capture the increment in α_{ij} due to deformation. The following equation was suggested by Prager [44] for the case of linear kinematic hardening,

$$d\alpha_{ij} = C_{kin} d\varepsilon_{ij}^{P} \tag{1.30}$$

where, C_{kin} is a constant. In order to capture the non-linear behaviour in which the loading tends back to the isotropic curve, the increment in the center of the yield surface can be described by the following equation developed by Fredrick and Armstrong [45],

$$d\alpha_{ij} = C_{kin} d\varepsilon_{ij}^{P} - \gamma \alpha_{ij} d\overline{\varepsilon}^{P} \tag{1.31}$$

20

where, γ is a constant. The following equation has also been used to describe the increment in the location of the yield surface [45,46],

$$d\alpha_{ij} = \frac{C_{kin}}{\sigma^0}\left(\sigma_{ij} - \alpha_{ij}\right)d\bar{\varepsilon}^P - \gamma\alpha_{ij}d\bar{\varepsilon}^P \tag{1.32}$$

Integrating either Equation 1.31 or 1.32, under uniaxial loading conditions results in the following equation for $\bar{\alpha}$ [46],

$$\bar{\alpha} = \frac{C_{kin}}{\gamma}\left[1 - \exp\left(-\gamma\bar{\varepsilon}^P\right)\right] \tag{1.33}$$

which is required to determine the size of the yield surface (Equation 1.29).

Chaboche [43,47] has suggested that, to more accurately capture the transient behaviour on reverse loading, α_{ij} can be described by the superposition of several terms, described by,

$$\alpha_{ij} = \sum_a \alpha_{ij_a} \tag{1.34}$$

in which,

$$d\alpha_{ij_a} = C_{kin_a}d\varepsilon_{ij}^P - \gamma_a\alpha_{ij_a}d\bar{\varepsilon}^P \tag{1.35}$$

with the parameters $C_{kin\,a}$ and γ_a being material constants.

1.5.3 Strain-rate Effects

Although strain-rate effects are important for materials such as steel, aluminum alloys do not generally show as significant an effect in the ranges of $10^{-4} - 10^3$ s^{-1}. Research in this range has shown that the effect of strain-rate on the yield strength for a 5454-O aluminum alloy, which is similar to the AA5754 alloys used in the current research, at room temperature is in the order of 10% [48]. Tensile testing by Langseth and Hopperstad [27], on AA6060 aluminum alloy has shown the strain-rate sensitivity of the yield strength also to be small, in the order of 5-10% in the strain-rate range of $10^{-4} - 10^3$ s^{-1}. Strain-rate effects for AA5754 and AA5182 aluminum alloys have been studied at the University of Waterloo by Smerd et al. [49] using a tensile split-Hopkinson bar apparatus at strain-rate ranges up to

1500 s^{-1}. Results of this testing have shown that the strength increase at high rates is less than 5%.

The strain-rate response for the AA5754 tube alloy used in the current research will be studied to determine whether or not strain-rate effects can be neglected in the crash models. Concurrent research was performed using tensile split-Hopkinson bar apparatus at strain-rates of 500 s^{-1} to 1500 s^{-1} [50] to determine the coefficients necessary for strain-rate sensitive material models, such as the Johnson-Cook [51] and Zerilli-Armstrong [52] constitutive models, which were then used to study the axial crush behaviour in the current research.

The Cowper-Symonds equation, given above as Equation 1.18, can be used to describe how the strength of the material is affected by strain-rate. Alternatively, the Johnson-Cook and Zerilli-Armstrong equations account for both strain-rate and temperature effects due to adiabatic heating at high rates of strain. A general form of the Johnson-Cook equation is given by [53],

$$\bar{\sigma} = \left[A + B\bar{\varepsilon}^{p^n} \right] \left[1 + C_{JC} \ln \frac{\dot{\bar{\varepsilon}}^p}{\dot{\varepsilon}_0} \right] \left[1 - \left(\frac{T - T_{room}}{T_{melt} - T_{room}} \right)^m \right] \tag{1.36}$$

where A, B, n, C_{JC} and m are material constants, T is the temperature of the material, T_{room} is room temperature, and T_{melt} is the melting temperature of the material. The parameter, $\dot{\bar{\varepsilon}}^p$ represents the effective plastic strain-rate and $\dot{\varepsilon}_0$ represents the reference strain-rate at which the hardening law parameters were calculated. In Equation 1.36, the terms in the first bracket represent a power law hardening behaviour.

The Zerilli-Armstrong equation [50,52] for an FCC material is expressed as,

$$\bar{\sigma} = \Delta\sigma'_G + C_2 \bar{\varepsilon}^{p^{1/2}} \exp(-C_3 + C_4 \dot{\bar{\varepsilon}}^p) T + kl^{-1/2} \tag{1.37}$$

where, $\Delta\sigma'_G$ is a term that considers the effect of dislocation density on the yielding behaviour, T is the material temperature, and C_2, C_3, C_4 are material parameters requiring calibration. The final term in the equation, is the Hall-Petch equation and accounts for the effect of grain size, l, on the strength of the material, with k as a material constant.

As an alternative to the split-Hopkinson bar apparatus tests, quasi-static axial crush tests were performed in the current research to compare with results from dynamic impact tests. This was carried out in order to determine the coefficients based on data from the actual strain-rate range experienced during dynamic crush.

1.6 Failure

1.6.1 Modes of Failure

Common failure modes for aluminum alloy sheet and tube include ductile fracture and shear localization [54]. Since the strains during axial crush of a tube can be very large it is important to understand these potential failure mechanisms.

Ductile fracture has been studied extensively in regard to the failure of aluminum alloys [55,56,57,58] and it has been shown that there are three common modes of failure in ductile materials that occur during deformation including: plastic failure, ductile fracture, and shear fracture. These three modes of failure are depicted in Figure 1.18.

a) Plastic Failure   b) Ductile fracture   c) Shear fracture or Void Sheeting
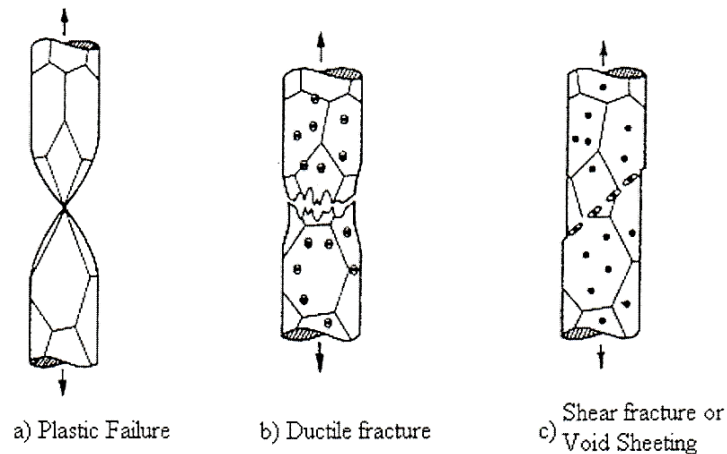
Figure 1.18: Modes of failure in a ductile material [57]

In a pure material that contains few inclusions or second phase particles, fracture can occur by plastic failure in which the strain localizes, causing a reduction in the cross-section. This type of failure mechanism is less common since most materials contain second phase particles and inclusions that act as sites for void nucleation and growth.

During necking, strain localization occurs and voids begin to nucleate and grow around second phase particles due to large tensile hydrostatic stresses, and eventually coalesce. The coalescence of voids usually occurs at the center of the material and forms an internal crack that can propagate until the remaining material can no longer support the applied load. Deformation bands at 45° appear at the edge of the material during the final fracture which leads to the cup and cone shape associated with ductile failure. A dimpled surface can be observed under magnification which is due to void coalescence in both the center and edges of the specimen, but the void size and spacing is smaller towards the edge of the specimen than it is at the center. Unlike plastic failure, there is a volume change within the material due to the growth of the voids.

Shear fracture occurs when shear bands form within a volume of material that changes shape by shearing within an isolated slip band [54]. Plastic flow becomes concentrated within the shear band, which leads to shear localization. Shear bands can span the entire cross-section of the material and will lead to failure when separation occurs within the slip bands.

1.6.2 Failure Modelling

The Forming Limit Diagram was developed [59,60] to give a measure of when a sheet material will fail by necking during forming and is the most commonly adopted approach in the forming industry. In the late 1970s, it was reported that the forming limit behaviour of pre-strained steel was different from as-received steel giving rise to questions on the generality of the FLD [61]. Figure 1.19 shows the forming limit curves generated for a 2008 T4 aluminum alloy [62,63], in which the material was pre-strained both parallel (P1 and P2) and perpendicular to the forming direction (P3 and P4). The figure shows that the strain-path dependence is significant in cases where the pre-strain is along the minor axis. Even though research such as this has shown that the FLDs should not be used in cases where there are strain-path changes, FLDs are still widely used today. Applications of finite element methods (FEM) for predicting metal forming in cases of complicated strain path changes, such as hydroforming and flanging operations, have resulted in research into alternative models for predicting material failure.

Graf and Hosford [62] discovered that there is a forming limit criterion based on the state of stress that appears to be independent of strain path. Stoughton [64] has shown that a transformation can be made between strains and stresses such that a stress-based FLD can be obtained, as shown in Figure 1.20 for a 2008 T4 aluminum alloy [63]. The forming curves in Figure 1.20 were determined by converting the strains in Figure 1.19 to stresses. The stress-based FLD does not show a strain-path dependence illustrating that this method can be used in cases of non-proportional loading.

One drawback of using the stress-based FLD is that the forming stresses can rarely be measured experimentally. In complicated forming operations, strains must be measured and then converted to stresses using elastic-plastic constitutive equations after which the stresses can be compared to stress-based forming limits. Another concern arises in applying stress-based forming limits to dynamic events, as in crashworthiness studies, associated with the strong oscillations in stress due to stress wave propagation and variation of the yielding behaviour with increased strain-rate.
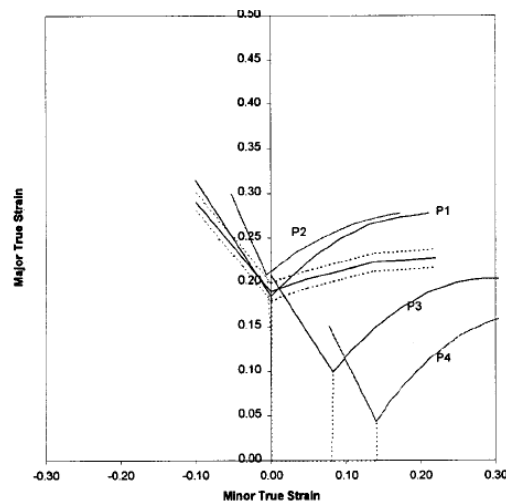
Figure 1.19: Strain-path dependence of 2008 T4 Al [63] (P1 and P2 pre-strained parallel to forming direction and P3 and P4 pre-strained perpendicular to forming direction)
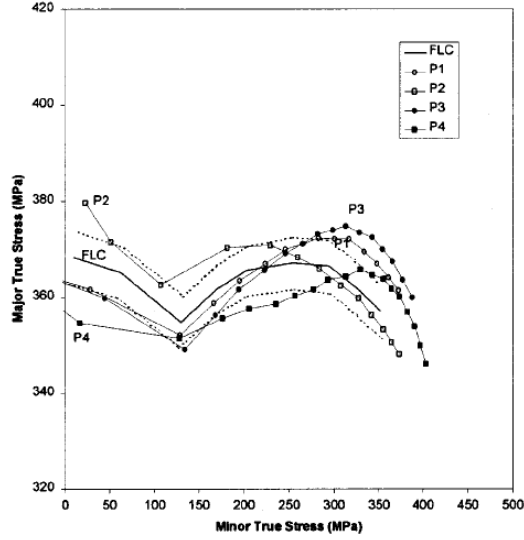
Figure 1.20: Stressed-based FLD of 2008 T4 Al [63] (P1 and P2 pre-strained parallel to forming direction and P3 and P4 pre-strained perpendicular to forming direction)

1.6.3 Gurson-Tvergaard-Needleman Damage Model

Damage-based constitutive models have also been used to study failure. In the 1970s, Gurson [65] developed a continuum theory of ductile rupture by void nucleation and growth which has been widely adopted in metal forming predictions. This model was developed based on the remote state of stress required to initiate yielding of an incompressible rigid-plastic sphere containing a central spherical void. Modifications to the model have been made by Tvergaard and Needleman to capture void nucleation and coalescence [66,67,68]. Gholipour et al. [69,70] have shown that this approach is useful in predicting formability of Al-Mg alloys under combined tube bending and hydroforming operations. However, it needs to be determined whether this model is effective for predicting failure during axial crush of hydroformed aluminum alloy tubes.

The yield function, ϕ, of the Gurson damage model is given by Equation 1.38,

$$\phi = \left(\frac{\sigma_{eq}}{\overline{\sigma}}\right)^2 + 2f\cosh\left(\frac{3\sigma_{hyd}}{2\overline{\sigma}}\right) - 1 - f^2 = 0 \tag{1.38}$$

26

where, $\bar{\sigma}$ is the flow stress, f is the void volume fraction, σ_{eq} is the remote equivalent stress given by,

$$\sigma_{eq} = \left[\frac{3}{2}\sigma_{ij}{}'\sigma_{ij}{}'\right]^{\frac{1}{2}} \tag{1.39}$$

and σ_{hyd} is the hydrostatic component of remote stress σ_{ij}, given by,

$$\sigma_{hyd} = \frac{1}{3}\sigma_{kk} \tag{1.40}$$

where, $\sigma_{ij}{}'$ are the deviatoric components of σ_{ij}. For the case of zero porosity, $f = 0$, Equation 1.38 reduces to the von Mises yield criterion. Tvergaard and Needleman introduced the following yield criterion [66,67,68], which is a modification of the Gurson model, referred to as the Gurson-Tvergaard-Needleman (GTN) constitutive model,

$$\phi = \left(\frac{\sigma_{eq}}{\bar{\sigma}}\right)^2 + 2f^*q_1 \cosh\left(q_2\frac{3\sigma_{hyd}}{2\bar{\sigma}}\right) - 1 - q_3 f^{*2} = 0 \tag{1.41}$$

where, q_1, q_2, and q_3 are calibration coefficients first introduced by Tvergaard to give more accurate predictions compared to numerical results. In Tvergaard's work $q_1=1.5$, $q_2=1$, and $q_3=q_1$, but more recently, values of $q_1=1.25$, $q_2=0.95$, and $q_3=q_1{}^2$ have been recommended by Worswick and Pick [71]. Tvergaard and Needleman then proposed that an effective porosity, f^*, be used to replace the porosity, f, in order to account for the onset of rapid void coalescence near failure.

$$f^* = \begin{cases} f & \text{if} & f < f_c \\ f_c + \dfrac{f_u{}^* - f_c}{f_f - f_c}(f - f_c) & \text{if} & f \geq f_c \end{cases} \tag{1.42}$$

In this equation, f_c is the porosity value at the initiation of void coalescence and f_f is the porosity level at final fracture, with $f_u{}^* = 1/q_1$. Figure 1.21 gives the relationship between effective stress, hydrostatic stress, and porosity, showing that as porosity and hydrostatic stress increase, the load carrying capacity of the material decreases, as represented by the effective stress [68].
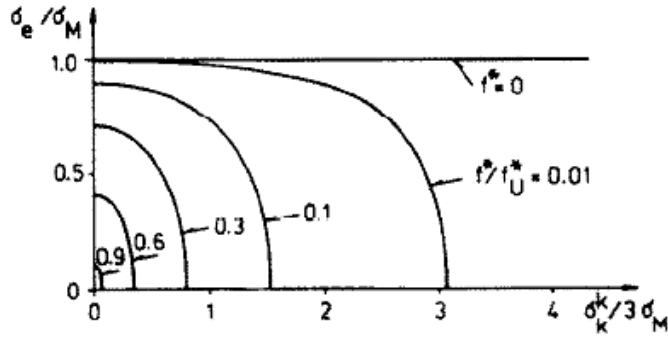
Figure 1.21: GTN yield surface showing dependence on value of porosity [68]

The change in void volume fraction during an increment in deformation is determined by the rate at which voids grow $(\dot{f})_{growth}$ and the nucleation of new voids $(\dot{f})_{nucleation}$ which can be expressed as,

$$\dot{f} = (\dot{f})_{growth} + (\dot{f})_{nucleation} \tag{1.43}$$

where, the rate of void growth is given by,

$$(\dot{f})_{growth} = (1-f)\dot{\varepsilon}_{ij}{}^{p}\delta_{ij} \tag{1.44}$$

and the rate of void nucleation, which is assumed to occur at second phase particles, is given by,

$$(\dot{f})_{nucleation} = A_{GTN}h\dot{\bar{\varepsilon}}^{p} + \frac{1}{3}B_{GTN}\dot{\bar{\sigma}} \tag{1.45}$$

in which, $\dot{\varepsilon}_{ij}{}^{p}$ is the macroscopic plastic strain rate, $\dot{\bar{\varepsilon}}^{p}$ is the effective plastic strain rate, h is the slope of the material flow stress versus effective plastic strain, and $\dot{\bar{\sigma}}$ is the rate of effective stress. A_{GTN} and B_{GTN} are chosen such that the nucleation follows a statistical normal distribution, as described by Chu and Needleman [72]. If a strain-controlled nucleation mechanism is adopted then A_{GTN} and B_{GTN} are set to,

$$A_{GTN} = \frac{1}{h}\frac{f_{N}}{S_{N}\sqrt{2\pi}}\exp\left[-\frac{1}{2}\left(\frac{\bar{\varepsilon}^{p} - \varepsilon_{N}}{S_{N}}\right)^{2}\right] \quad , \quad B_{GTN} = 0 \tag{1.46}$$

However, if stress-controlled nucleation is used then,

$$A_{GTN} = B_{GTN} = \frac{f_N}{S_N \sqrt{2\pi}} \exp\left[-\frac{1}{2}\left(\frac{(\bar{\sigma} + \sigma_{hyd}) - \sigma_N}{S_N}\right)^2\right]$$ (1.47)

In these equations, f_N is the void volume fraction of nucleating particles, ε_N and σ_N are the average strain and stress at which particles nucleate voids, S_N is the standard deviation of ε_N or σ_N, and $\bar{\varepsilon}^p$ is the effective plastic strain. These parameters are calibrated through finite element simulations and optical micrographs.

An investigation was performed by Gholipour et al. [69,70] involving EN-AW 5018 aluminum alloy tubes. Damage parameters were calibrated from the results of bending and hydroforming experiments and finite element simulations. It was found that the initial porosity and initial fraction of second phase particles for the EN-AW 5018 material were 0.002 and 0.020, respectively. Finite element simulations were performed with values of either 0.35 or 0.15 for the average strain at which particles nucleate voids, ε_N. Agreement was found between simulation and experiment when using a value of 0.35 for ε_N, with a failure porosity of 0.01 to predict burst in a bent, hydroformed tube.

1.7 Summary

The deformation behaviour of a tube during hydroforming has been well researched for mild steels that exhibit high elongations, but the parameters controlling formability, including end-feeding, require further research for low elongation materials, such as aluminum alloys for which only a limited amount of work has been performed.

The axial crush response of tubes that have had no previous forming operations is relatively well understood, but the effect of forming on crash behaviour has received only limited attention. Thus, a requirement exists to understand the influence of forming history on the crash response of lightweight materials, such as the Al-Mg-Mn alloys to be considered in the current research. Furthermore, there is a need to validate finite element crash models that incorporate forming history so that the reliability of large-scale vehicle crash safety models can be ensured.

There also exits a requirement to assess the need to incorporate advanced constitutive models in the finite element simulation of metal forming and crash. The constitutive models explored in this research include the Gurson-Tvergaard-Needleman damage model, a non-linear isotropic-kinematic hardening model, the Yld2000-2d anisotropic model, and the Johnson-Cook strain-rate model. Several researchers have used these models to describe the material behaviour for a range of forming operations. However, the axial crush structure considered herein represents an opportunity to apply these models when high levels of deformation occur, such as those associated with bending in the folds of the crushed specimen. Thus, the validity of the models under high levels of deformation and complex loading histories will be examined.

The balance of this report is organized as follows: Chapter 2 discusses the experimental method for the hydroforming and impact operations and provides the results from these experiments; Chapter 3 compares theoretical predictions to experimental data; Chapter 4 provides details on the finite element models including a description of how the constitutive models were implemented within the finite element code; Chapter 5 provides details of the material characterization studies performed that were necessary to determine parameters required in the finite element simulations; Chapter 6 provides results and discussion of the finite element simulations; and Chapter 7 gives conclusions and recommendations stemming from this research.

Chapter 2 – Hydroforming and Impact Experiments

Hydroforming and axial crush experiments were performed with aluminum alloy tubes of designation EN-AW 5018 and AA5754, which are candidates for lightweight structural components in the automotive industry. In all, 16 different testing conditions were considered for each alloy. The main parameters that varied between these configurations included: thickness of the tube, corner radius of the tube, and the nature of the hydroforming process used to form the tube; that is, low versus high pressure hydroforming.

2.1 Stress versus Strain Response

This section provides the measured stress versus strain behaviour for both aluminum alloys, which was mainly required to describe their hardening behaviour in the finite element simulations. A more in-depth material characterization of the AA5754 alloy is provided in Chapter 5, regarding material parameters developed to describe damage, kinematic hardening, anisotropy, and strain-rate effects.

2.1.1 AA5754 Aluminum Alloy Tube

The primary material considered for this research was taken from a 2000 m supply of an AA5754 aluminum alloy tube with a wall thickness of about 3 mm and 76.2 mm outer diameter, supplied by VAW, a German corporation currently owned by Hydro Aluminium. The chemical composition was 0.2% Si, 0.34% Fe, 0.022% Cu, 0.27% Mn, 2.76% Mg,

0.018% Cr, 0.012% Zn, 0.012% Ti [73], with the balance being Al. The magnesium and manganese substantially strengthen the alloy and introduce good work hardening characteristics [74]. These tubes were created from sheet using a roll forming process, induction seam welded, and then annealed to the O-temper. No investigation was performed on the weld seam itself, such that any variations in strength within the tube were not taken into consideration in the finite element models. A non-destructive ultrasonic measurement device was used to measure the thickness at various points around the circumference of the tube, as shown in Figure 2.1 [75], with the average thickness being 3.07 mm.
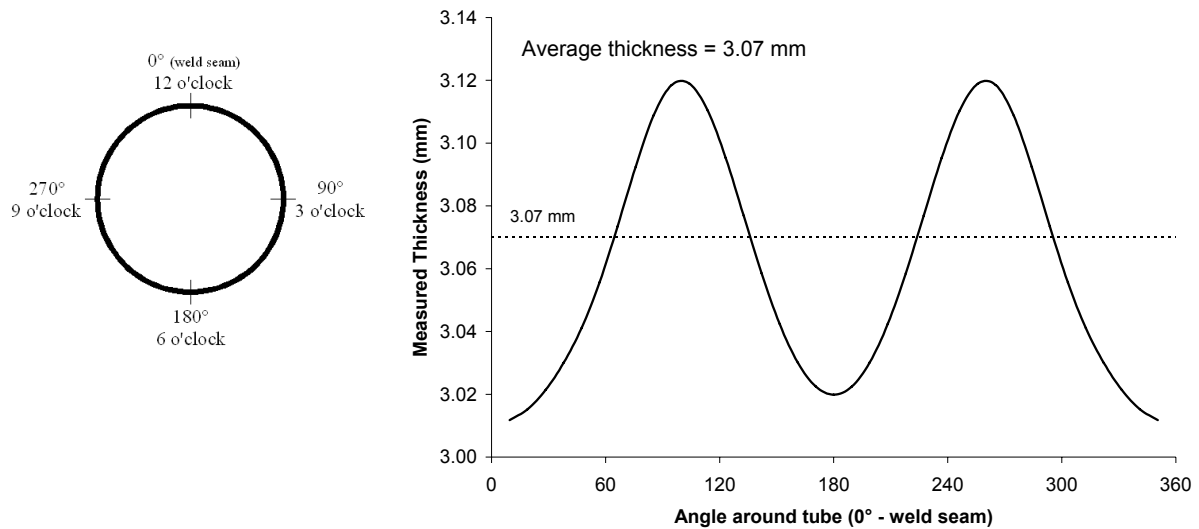
Figure 2.1: Thickness variation of AA5754 aluminum alloy tube

Several tensile tests were performed on specimens taken from the 3, 6, and 9 o'clock positions around the tube, with the weld seam corresponding to the 12 o'clock position. The engineering stress versus strain curves, given in Figure 2.2, show that curves obtained from the 3 and 9 o'clock positions were similar, but at the 6 o'clock position the stress was slightly greater. The differences in thickness and the stress-strain behaviour resulted from the roll forming operation that was used to produce the tube. The yield strength was approximately 100 MPa and the tensile strength ranged from 215 to 225 MPa.

The finite element simulations require the input of the effective stress versus effective plastic strain curve which is used to describe the hardening behaviour of the alloy, which is

32

the same as the true stress versus plastic strain response of the material from a uniaxial tensile test. The true stress versus plastic strain response of the material is given in Figure 2.3, along with two curve fits to the measured data.
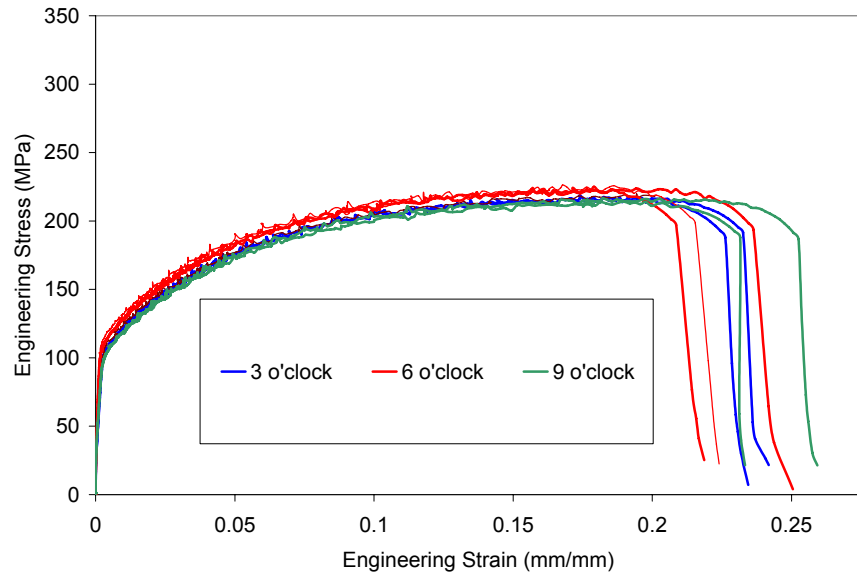
Figure 2.2: Engineering stress vs. strain curve for as-tubed AA5754 alloy
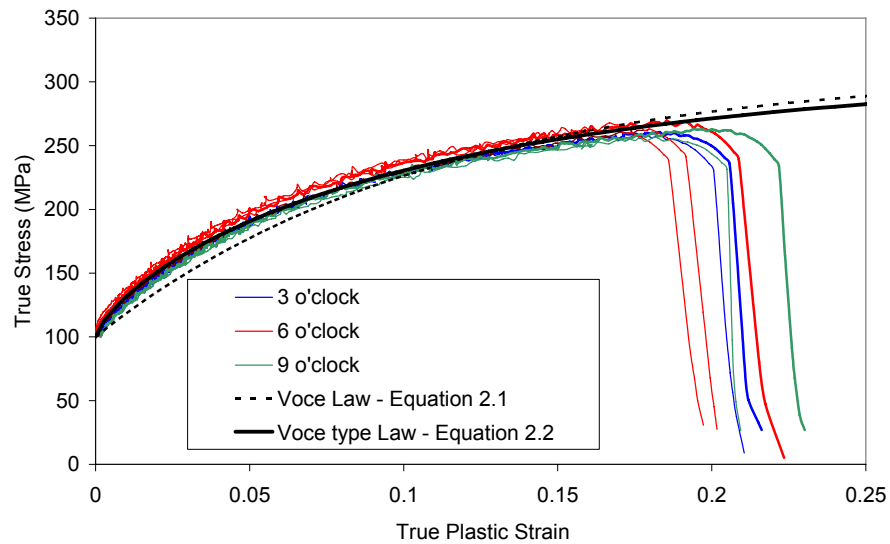
Figure 2.3: True stress vs. plastic strain curve for as-tubed AA5754 alloy

It has been shown that aluminum alloys appear to follow a Voce-type hardening response for large strains [41], given by [76],

$$\bar{\sigma} = A + (B - A)[1 - \exp(-C\bar{\varepsilon}^P)] \tag{2.1}$$

for which the parameters were determined to be $A = 100$ MPa, $B = 310$ MPa, and $C = 9.2$. A second curve fit, based on a four parameter Voce-type law [77], gave a slightly better prediction of the measured data,

$$\bar{\sigma} = a - (a - \sigma_y)\exp(-b\bar{\varepsilon}^{P^c}) \tag{2.2}$$

where $a = 315$ MPa, $b = 5.5$, $c = 0.77$, and $\sigma_y = 100$ MPa.

Necking and failure initiated in the tensile specimens at plastic strains of about 0.2. However, under different loading conditions, such as in axial crush, much larger strains can be attained without failure, such that it was necessary for the data to be extrapolated beyond a plastic strain of 0.2 to values of about unity, as shown in Figure 2.4. Higher effective strains without necking can be obtained from hydraulic bulge testing [41], tube bulging [78], or shear testing [79]. However, these tests were not performed for either the EN-AW 5018 or AA5754 alloys in the current research mainly because the necessary test apparatus was not available. This testing should be considered in future research.
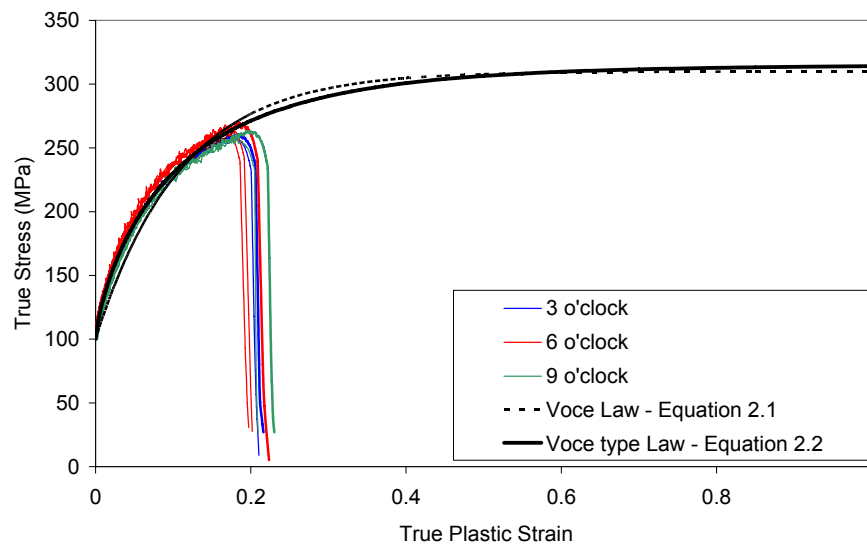
Figure 2.4: True stress-strain curve extrapolated to plastic strain of unity

2.1.2 EN-AW 5018 Aluminum Alloy Tube

Experiments were also performed using EN-AW 5018 aluminum alloy with 76.2 mm diameter tubes with 2.0 and 3.5 mm thicknesses, which was also supplied by Hydro Aluminium. The chemical composition of this alloy was 0.113% Si, 0.271% Fe, 0.023% Cu, 0.476% Mn, 3.435% Mg, 0.164% Cr, 0.014% Zn, 0.0042% Ti, with the balance being Al. The tube was created from sheet using a tube rolling process and induction seam welding. The tubes were cold drawn from a larger diameter tube to a diameter of 76.2 mm and then annealed. Since the tubes were annealed, no significant strength differences were found at various positions around the circumference of the tube, nor were there significant thickness variations.

Several as-tubed tensile tests were performed [80] to determine the behaviour of the material which was extrapolated in the form of the true stress versus plastic strain response, as shown in Figure 2.5. The curves for both thicknesses, which are almost identical, are shown in the figure [80]. A curve fit, such as the power law or Voce law, was not utilized for this material. Instead, the curves were discretized into about 100 points which were then used as input to describe the effective stress versus effective plastic strain response, in the finite element simulations. The yield strength was about 120 MPa and the tensile strength was approximately 300 MPa for both thicknesses.
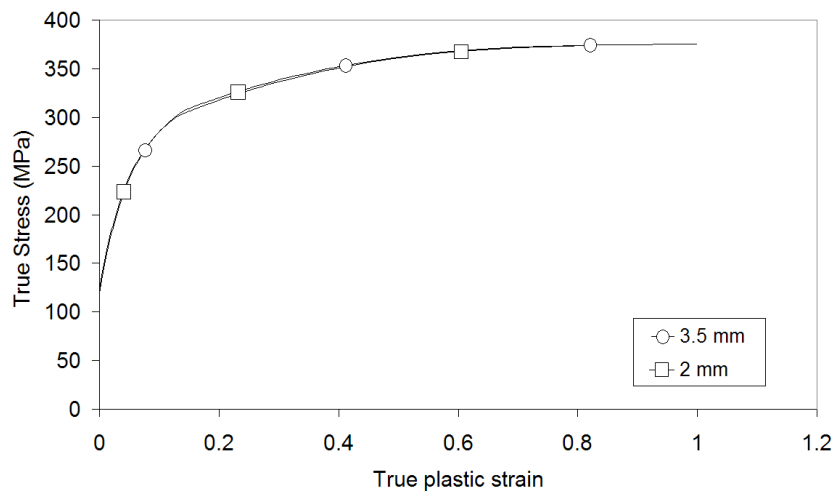
Figure 2.5: True stress vs. plastic strain curves for EN-AW 5018 aluminum alloy tubes [80]

2.2 Hydroforming – Experimental Procedure

2.2.1 Low Pressure Hydroforming – Procedure

During a low pressure hydroforming process, as depicted in Figure 1.2, the tube is slightly pressurized during the die closing stage such that pinching and wrinkling of the tube can be avoided. In the current research, for the low pressure hydroforming operation, the perimeter of the die was approximately equal to the circumference of the tube, thus avoiding circumferential stretching of the tube. The pressure in the tube during the die closure was held at about 3 MPa followed by applying a higher pressure once the die was closed in order to fully form the tube. A schematic of the hydroforming die is shown in Figure 2.6. All low pressure hydroforming was conducted at the Aluminum Technology Centre using a 1,000 tonne Interlaken hydroforming press, shown in Figure 2.7 [75].
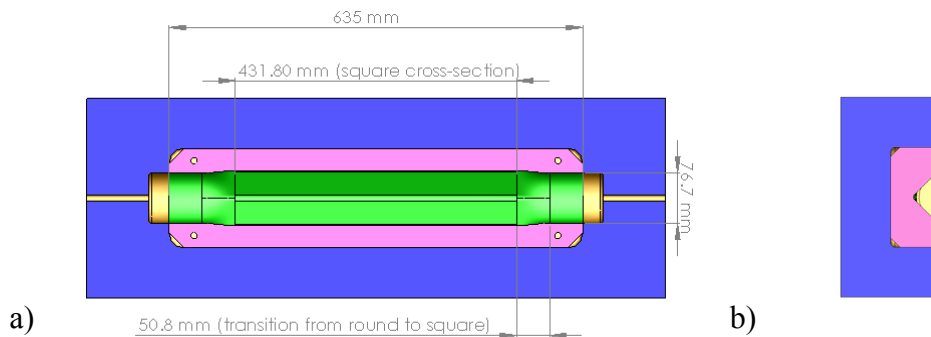
Figure 2.6: a) Schematic of hydroforming die half and b) cross-sectional view of die
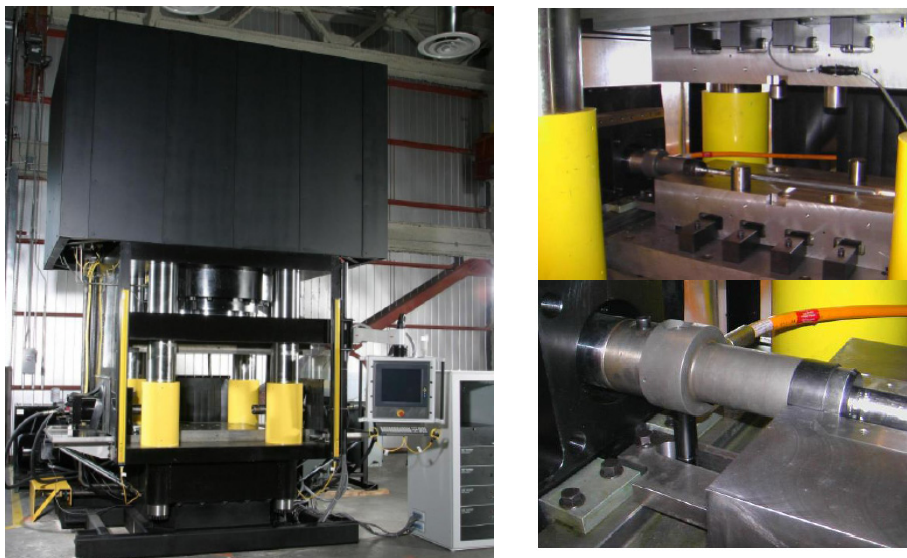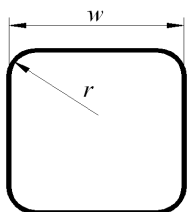
Figure 2.7: 1,000 tonne hydroforming press at the Aluminum Technology Centre [75]

In the current research, three low pressure hydroforming inserts were fabricated with three different corner radii: 6, 12, and 18 mm. The cross-sectional dimensions of the dies are given in Table 2.1. In all cases, there was a clearance of about 0.5 mm between the tube and die walls, such that the per cent change in perimeter of the low pressure dies relative to the circumference of the tube was actually about 0.8 per cent. For each radius, several tubes were hydroformed and then prepared for impact testing using both the EN-AW 5018 and AA5754 alloys, as discussed below. Internal water pressures of 113, 56, or 38 MPa were applied to the 3 mm AA5754 alloy to form the tubes to 6, 12, or 18 mm corner radii, respectively. Pressures of 100, 50, 33 MPa and 175, 88, and 58 MPa were applied to the 2.0 and 3.5 mm thickness EN-AW 5018 alloy tubes for corner radii of 6, 12, or 18 mm, respectively. These pressures were determined based on Equation 1.1.

Table 2.1: Dimensions of Hydroforming Inserts

Hydroforming Process	w (mm)	r (mm)	% change in perimeter (relative to non-hydroformed tube)	
low pressure	62.9	6	0.8	
low pressure	65.5	12	0.8	
low pressure	68.1	18	0.8	
high pressure	76.7	6	23.9	
high pressure	76.7	12	19.6	
high pressure	76.7	18	15.3	

In order to seal the tube during hydroforming without end-feeding, so-called "floating" end-plugs were used which incorporate a polymeric high pressure seal, as shown in Figure 2.8. The axial force acting on the end-plugs due to the internal pressure was counteracted by the back of the hydroforming die wall.

Figure 2.8: End-plugs used to seal tubes during hydroforming without end-feeding

2.2.2 High Pressure Hydroforming – Procedure

During the high pressure hydroforming operation used in this research, the initially circular tube of 76.2 mm was formed within a die that had a square cross-section of about 76.2 mm with a corner radius of either 6, 12, or 18 mm. This required circumferential expansion and caused thickness reduction of the tube during hydroforming. The dimensions of the three inserts used in the testing are given in Table 2.1.

All high pressure hydroforming of the 3.0 mm, AA5754 tubes was conducted using end-feeding. For each of the three inserts (6, 12, and 18 mm corner radii), tubes were formed using two different levels of end-feed: one utilized 60 mm of end-feed at each end of the tube and the other profile was selected such that there was 40 mm of end-feed at each end. Several tubes were hydroformed for each radius and end-feed profile and then prepared for impact, as discussed below.

High pressure hydroforming of the EN-AW 5018 tubes with 2.0 and 3.5 mm thicknesses was conducted using only the insert with the 6 mm corner radius. These experiments were performed prior to the AA5754 tests and, at that time, the hydroforming press did not incorporate actuators for end-feeding. Since end-feeding could not be used, there was little expansion of the tube before bursting. For both the 2.0 mm and 3.5 mm tubes, bursting would occur at a corner radius of approximately 22 mm. Based on these burst tests, it was decided to form the tubes to corner radii of 24, 27, 30, and 33 mm for an initial study of the effect of hydroforming on the crush response.

2.2.3 Hydroforming Test Matrix

Table 2.2 summarizes the hydroforming test conditions for the EN-AW 5018 and AA5754 tubes. The number of tubes hydroformed corresponds to the number of tubes impacted, which is provided in the impact test matrix given below in Section 2.3. The EN-AW 5018 high pressure tubes were formed at the University of Waterloo. All other tubes were hydroformed at the Aluminum Technology Centre, and then sent to the University of Waterloo to be prepared for impact. The general naming convention throughout the report is to list 'HP' or 'LP' to describe either the high or low pressure process, followed by the tube thickness, corner radius, and whether it was the 1st or 2nd tube measured. An example of this naming convention is HP 3.5mm R24mm #2, which corresponds to a high pressure EN-AW 5018 alloy tube with 3.5 mm thickness that was hydroformed to a corner radius of 24 mm.

Table 2.2: Hydroforming Test Matrix

EN-AW 5018 aluminum alloy				AA5754 aluminum alloy			
Hydroforming Process	Corner Radius (mm)	Thickness (mm)	End-feeding	Hydroforming Process	Corner Radius (mm)	Thickness (mm)	End-feeding
high pressure	33	2.0	---	high pressure	6	3.0	40 mm
high pressure	30	2.0	---	high pressure	12	3.0	40 mm
high pressure	27	2.0	---	high pressure	18	3.0	40 mm
high pressure	24	2.0	---	high pressure	6	3.0	60 mm
low pressure	6	2.0	---	high pressure	12	3.0	60 mm
low pressure	12	2.0	---	high pressure	18	3.0	60 mm
low pressure	18	2.0	---	low pressure	6	3.0	---
high pressure	33	3.5	---	low pressure	12	3.0	---
high pressure	30	3.5	---	low pressure	18	3.0	---
high pressure	27	3.5	---				
high pressure	24	3.5	---				
low pressure	6	3.5	---				
low pressure	12	3.5	---				
low pressure	18	3.5	---				

2.3 Axial Crush Test Procedure

2.3.1 Drop Tower Testing

Impact testing of the EN-AW 5018 alloy tubes formed using the high pressure hydroforming process and non-hydroformed, circular tubes was performed using a drop tower apparatus (Figure 1.5) available at the General Motors Technical Center. One repeat test was performed for each case in Table 2.2, with both wall thicknesses of 2.0 and 3.5 mm for a total of 20 experiments.

The hydroformed tubes were trimmed such that the length of the square section of the tube prior to impact was 400 mm. The length of the non-hydroformed circular tubes was also 400 mm. Crush initiators were not used in these experiments. In order to mount a tube in the drop tower, each end of the tube was welded to a 200 x 200 x 19.1 mm, AA6061-T4 plate to help maintain alignment during impact. A bottom plate was required to attach the tube to the drop tower and the top plate was used to limit sliding between the tube and drop platform. A 5 mm thick rubber pad was placed on top of the aluminum plate to prevent metal to metal contact between the plate and the drop platform which reduces the degree of high frequency oscillation obtained in the data. The drop height was about 7.6 m and was selected such that the impact velocity was 12 m/s. The mass of the platform was 216 kg for the 2.0 mm tubes and 414 kg for the 3.5 mm tubes. Load cells were arranged in a "triangular plus one" pattern (Figure 1.5), such that the pressure distribution during impact was centred about the load cells [11,12].

For tubes impacted using the drop tower, it was found that there was a large tilt of the drop tower platform resulting in off-axis loading occurring at the later stages of the impact, as shown in Figure 2.9. As a result, all subsequent axial crush testing was performed on a sled-track.
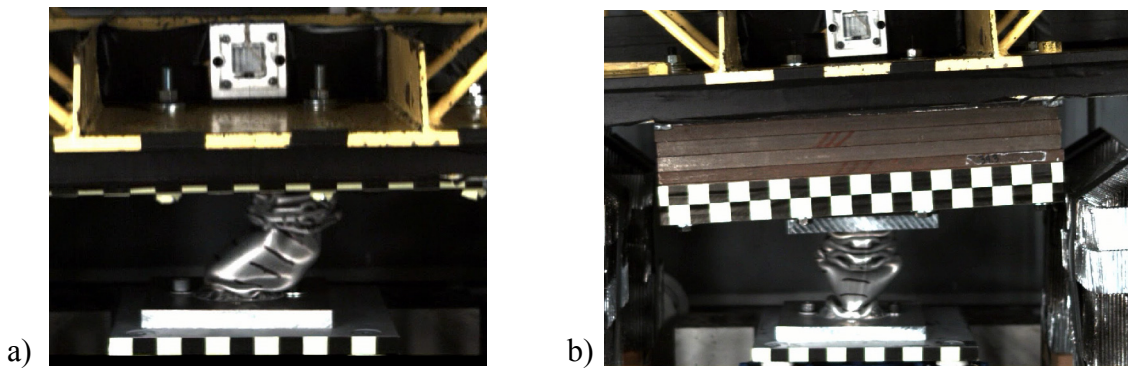
Figure 2.9: Impact of tube on drop tower showing a) off-axis loading and b) tilt of drop tower platform after impact

2.3.2 Sled-Track Testing

The EN-AW 5018 tubes formed using the low pressure hydroforming process and all of the AA5754 alloy tubes were impacted, two at a time, on a sled-track at the General Motors Technical Center, as depicted in Figure 2.10. The stability of the sled-track prevented off-axis loading from occurring during impact. The low pressure EN-AW 5018 aluminum tubes were welded to the aluminum mounting plates and no crush initiators were used. Sled-track tests were performed for tubes with 6, 12, and 18 mm corner radii with 2.0 and 3.5 mm tube thicknesses. There were two tubes impacted per test, as shown in Figure 2.11, at an initial impact velocity of 6.3 m/s.

All AA5754 tubes impacted were clamped to aluminum plates, rather than welded, as can be seen in Figure 2.11. The AA5754 tubes formed using the low pressure process, as well as the AA5754 annealed high pressure tubes, were impacted at 6.3 m/s. AA5754 alloy tubes formed using the high pressure process (non-annealed) were impacted at 7.0 m/s and the non-hydroformed, circular tubes were impacted at 7.5 m/s. The mass of the sled-track was 1120 kg.

41
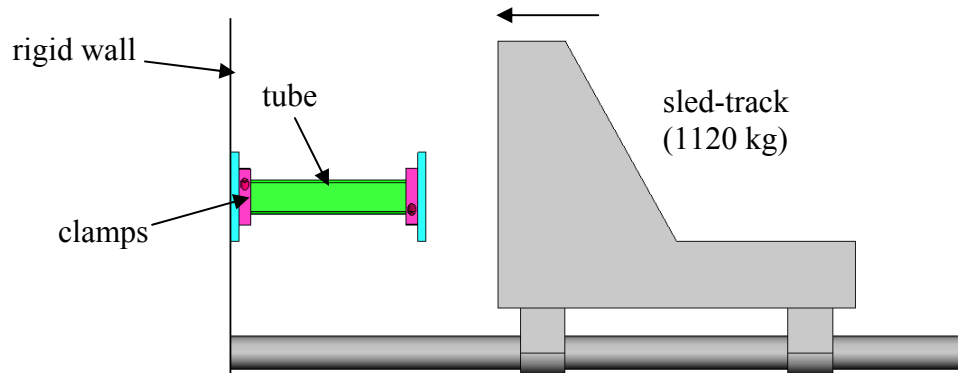
Figure 2.10: Schematic of sled-track testing apparatus

Figure 2.11: Two axial crush specimens mounted on sled-track

2.3.3 Crush Initiators

One issue that arose when testing the EN-AW 5018 alloy tubes, which were welded to support plates, was that the weld connection might have acted as a trigger for fold initiation. This type of connection would be difficult to model in the finite element simulations such that the initial peak loading behaviour might not be entirely captured in the predictions. As a result, most of the AA5754 tubes incorporated crush initiators and instead of welding the tubes to aluminum plates for support, the tubes were clamped to support plates using bosses. Clamping the tubes to support plates enforced the folding to initiate at the location of the crush initiators. Thus, the simulations should better capture the initial loading

response during impact. Prior to impact, the tubes were trimmed to a 400 mm length. Each clamp was 25 mm thick, giving a 350 mm length available for crush.

Each fold initiator was formed into the tubes using the apparatus illustrated in Figure 2.12. The depth of each initiator was approximately 5 mm from the surface of the tube and the width was 38.1 mm. In all cases, the location of the initiators was 50 mm from the top of the tube, or when clamped prior to testing, 25 mm from the upper clamp.
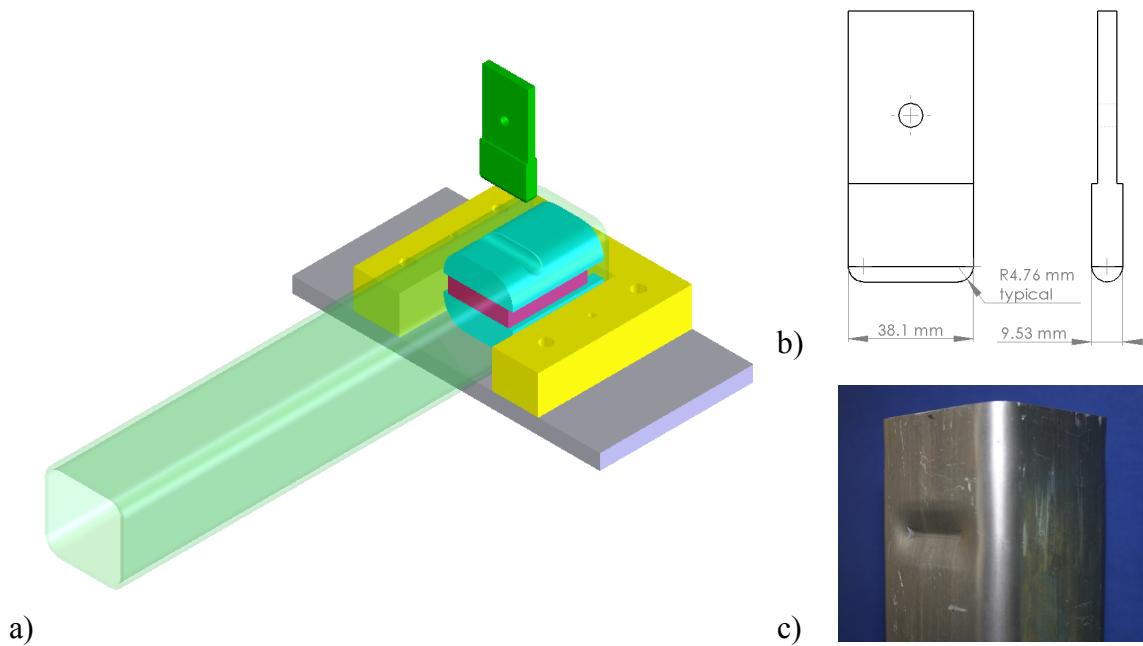
Figure 2.12: a) Model of components required to create fold initiators, b) tube indenter, and c) photo of the formed crush initiator

2.3.4 Axial Crush Test Matrix – Dynamic

A total of 32 EN-AW 5018 tubes and 58 AA5754 tubes were impacted, as summarized in Tables 2.3 and 2.4. In addition to the hydroformed tubes, impact tests were also performed on non-hydroformed, circular tubes. The non-hydroformed, circular tubes did not contain fold initiators.

Table 2.3: Axial Crush Test Matrix – EN-AW 5018 Aluminum Alloy Tube

Hydroforming Process	Radius (mm)	Thickness (mm)	End-feeding	Annealed (yes/no)	Support	Crush Initiator	Test Apparatus	Number of Tubes Impacted
--	round	2.0	none	no	welded	none	drop tower	2
high pressure	33	2.0	none	no	welded	none	drop tower	2
high pressure	30	2.0	none	no	welded	none	drop tower	2
high pressure	27	2.0	none	no	welded	none	drop tower	2
high pressure	24	2.0	none	no	welded	none	drop tower	2
low pressure	18	2.0	none	no	welded	none	sled-track	2
low pressure	12	2.0	none	no	welded	none	sled-track	2
low pressure	6	2.0	none	no	welded	none	sled-track	2
--	round	3.5	none	no	welded	none	drop tower	2
high pressure	33	3.5	none	no	welded	none	drop tower	2
high pressure	30	3.5	none	no	welded	none	drop tower	2
high pressure	27	3.5	none	no	welded	none	drop tower	2
high pressure	24	3.5	none	no	welded	none	drop tower	2
low pressure	18	3.5	none	no	welded	none	sled-track	2
low pressure	12	3.5	none	no	welded	none	sled-track	2
low pressure	6	3.5	none	no	welded	none	sled-track	2

Table 2.4: Axial Crush Test Matrix – AA5754 Aluminum Alloy Tube

Hydroforming Process	Radius (mm)	Thickness (mm)	End-feeding	Annealed (yes/no)	Support	Crush Initiator	Test Apparatus	Number of Tubes Impacted
--	round	3.0	none	no	clamped	none	sled-track	4
high pressure	6	3.0	40 mm	no	clamped	flat	sled-track	4
high pressure	12	3.0	40 mm	no	clamped	flat	sled-track	4
high pressure	18	3.0	40 mm	no	clamped	flat	sled-track	4
high pressure	6	3.0	60 mm	no	clamped	flat	sled-track	4
high pressure	12	3.0	60 mm	no	clamped	flat	sled-track	4
high pressure	18	3.0	60 mm	no	clamped	flat	sled-track	4
high pressure	6	3.0	60 mm	yes	clamped	flat	sled-track	4
high pressure	12	3.0	60 mm	yes	clamped	flat	sled-track	4
high pressure	18	3.0	60 mm	yes	clamped	flat	sled-track	4
low pressure	6	3.0	none	no	clamped	none	sled-track	2
low pressure	12	3.0	none	no	clamped	none	sled-track	2
low pressure	18	3.0	none	no	clamped	none	sled-track	2
low pressure	6	3.0	none	no	clamped	flat	sled-track	4
low pressure	12	3.0	none	no	clamped	flat	sled-track	4
low pressure	18	3.0	none	no	clamped	flat	sled-track	4

2.3.5 Quasi-Static Axial Crush Testing

Quasi-static axial crush tests were performed in order to compare the crush response of the hydroformed tubes between dynamic and quasi-static cases. The quasi-static tests were performed using a hydraulic press with a constant velocity of 0.167 mm/s applied to the specimen. For reference, the dynamic tests were performed with a sled-track velocity of about 7.0 m/s. The crush force was measured by a load cell attached to the hydraulic cylinder and a linear displacement transducer measured the crush distance. The AA5754 alloy tubes were clamped to steel plates in order to hold the tube in position during the test, as shown in Figure 2.13, and the initial length of the tube was 350 mm. Experiments were performed using tubes formed using the high pressure hydroforming process with 60 mm of end-feed for corner radii of 6, 12, and 18 mm. Two tests were performed for each corner radius for a total of six tests.

Figure 2.13: Experimental set-up for quasi-static axial crush testing

2.4 Hydroforming Experiments – Results and Discussion

2.4.1 AA5754 Low Pressure Hydroforming

The corners of a tube formed using the low pressure hydroforming process undergo bending with the outer surface experiencing tension and the inner surface experiencing

compression. The experimental engineering strains were measured by comparing the change in shape of circular grids that were etched onto the tube prior to the tube forming operation. All strain (and thickness) measurements were taken at the half-length position of the tube.

Figure 2.14 shows the measured engineering strain for the outer surface of an AA5754 alloy tube formed using the low pressure process with a corner radius of 6 mm. Strain measurements were performed at every circle grid around the perimeter of the tube. The results show that the maximum strain in the corner was about 0.22 with a compressive strain of about 0.08 in the flat regions of the tube. Results for corner radii of 12 and 18 mm are presented in Appendix A.
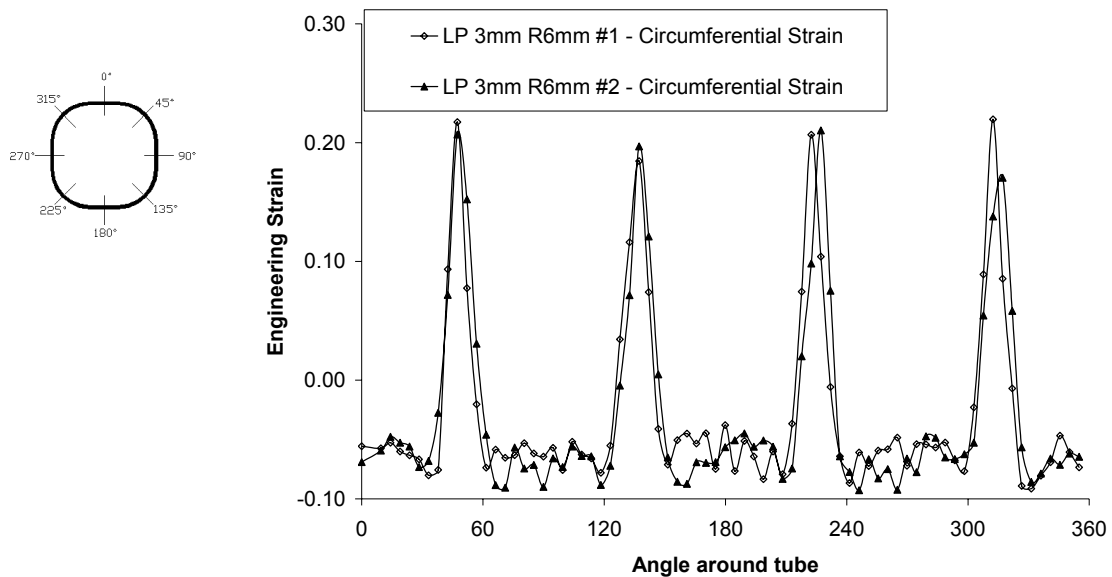
Figure 2.14: Predicted and measured strains for AA5754 tube formed using low pressure hydroforming process

A non-destructive, ultrasonic measurement device can be used to measure the thickness change within the tubes after the hydroforming operation. However, the as-hydroformed thicknesses were not measured for tubes formed using the low pressure process because the thickness change was very small and difficult to resolve.

46

2.4.2 AA5754 High Pressure Hydroforming

End-feeding was used for high pressure forming of the AA5754 alloy tubes to achieve smaller corner radii than that obtained with the EN-AW 5018 alloy tubes for which end-feeding was not available. The tube was sealed through metal-to-metal contact with the tube and end-feed actuator, which required an initial end-feed displacement of about 4 mm [75]. Two nominal levels of end-feeding were used, namely 60 and 40 mm. For each level, tubes with 6, 12, and 18 mm corner radii were produced. For the 6 mm radius, the value of 60 mm of end-feed was prescribed at each end of the tube. The internal tube pressure and end-feed displacement versus time profile used to form these tubes is given in Figure 2.15 [75]. The same profile was used to produce tubes with 12 and 18 mm corner radii except that the loading was terminated once the tube was formed to a 12 or 18 mm corner radius. The actual level of end-feed specified for the 12 and 18 mm corner radius tubes was 59.9 and 57.8 mm, respectively.
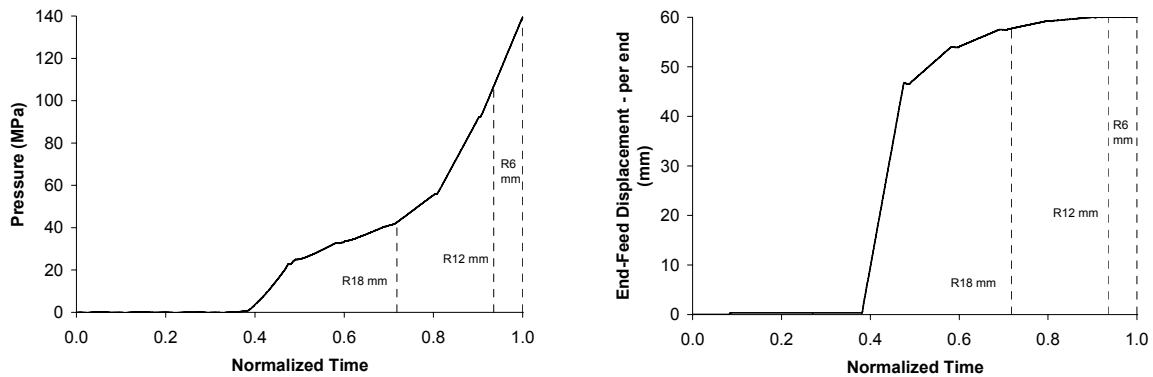
Figure 2.15: Internal tube pressure and end-feed displacement versus time for the 60 mm end-feed case

The second level utilized 40 mm of end-feed at each end of the tube. The pressure and end-feed displacement for the 6 mm corner radius tubes is shown in Figure 2.16 [75]. This same profile was used to produce tubes with 12 and 18 mm corner radii, but requiring 39.7 and 38.6 mm of end-feed, respectively. Again, the process was terminated once the required corner radius was achieved.
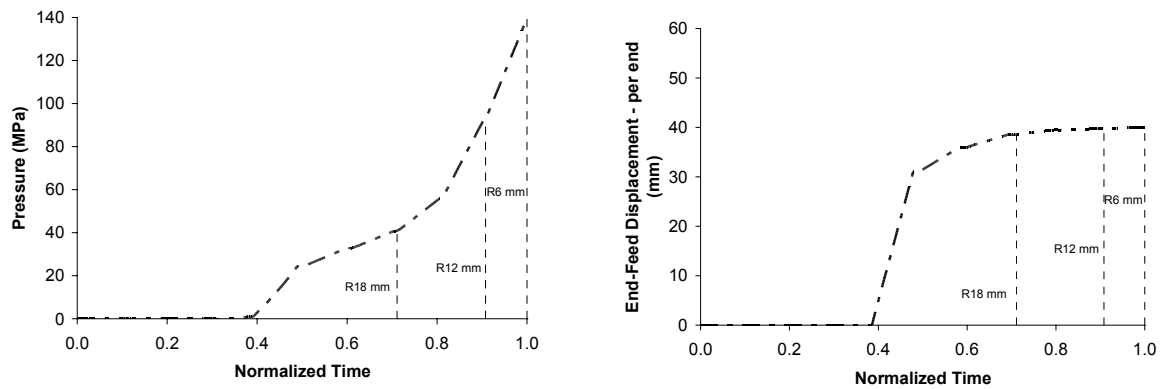
Figure 2.16: Internal tube pressure and end-feed displacement versus time for the 40 mm end-feed case

Figure 2.17 shows the measured engineering strains for AA5754 tubes formed using the high pressure process, with the end-feed level of 60 mm. The circumferential strains were about 0.50 in the corners and about 0.10 in the flat sections. The longitudinal strains were about –0.18, showing that end-feeding caused a large axial compression of the tube. The results for all three corner radii cases with both the 60 and 40 mm end-feed levels are given in Appendix A.
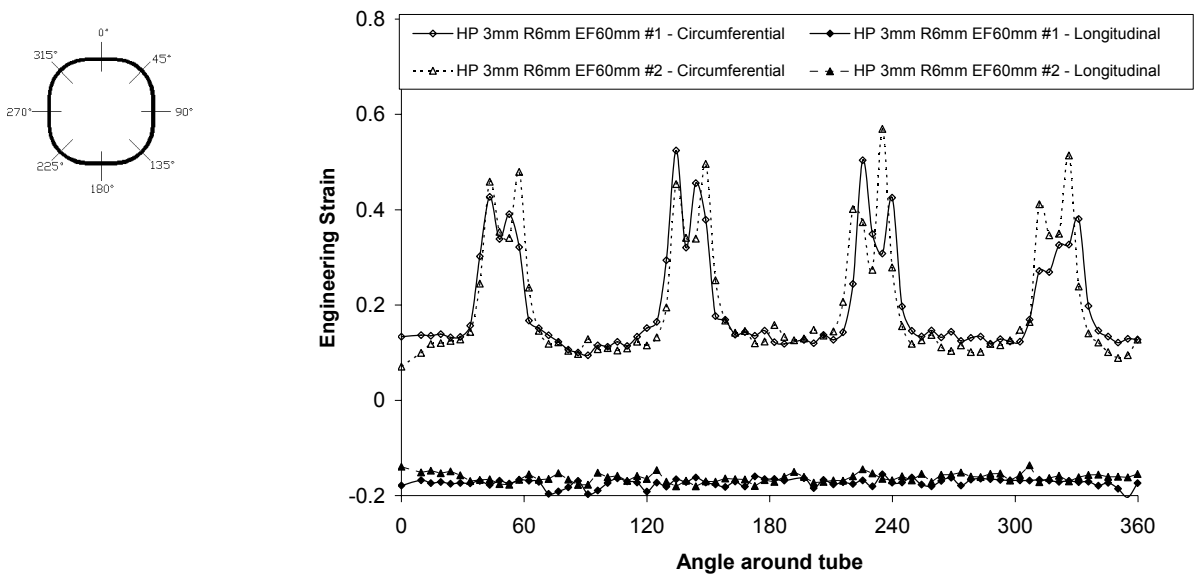
Figure 2.17: Measured strains for AA5754 tubes formed using high pressure hydroforming process with 60 mm of end-feed and a 6 mm corner radius

48

An ultrasonic measurement device was used to measure the as-hydroformed thicknesses of the tubes formed using the high pressure process [75]. Figure 2.18 shows the measured per cent change in thickness for tubes formed to a 6 mm corner radius with 60 mm of end-feed. The results show that the largest thickness reductions, of about 18%, occurred just on either side of a corner of the tube. In this region, frictional forces due to contact with the die prevented material from forming into the corner, resulting in thinning. However, Figure 2.17 shows that these regions corresponded to the highest regions of strain hardening (work hardening) which could result in a counter-acting effect between thinning and work hardening on the energy absorption during axial crush.

Figure 2.19 shows a cross-section of a hydroformed tube with 60 mm of end-feed formed to a 6 mm corner radius that shows the thinning in the corners of the tube. The thickness measurements for the AA5754 tubes with both the 60 and 40 mm levels of end-feed with the 6, 12, and 18 mm corner radii are presented in Appendix A.
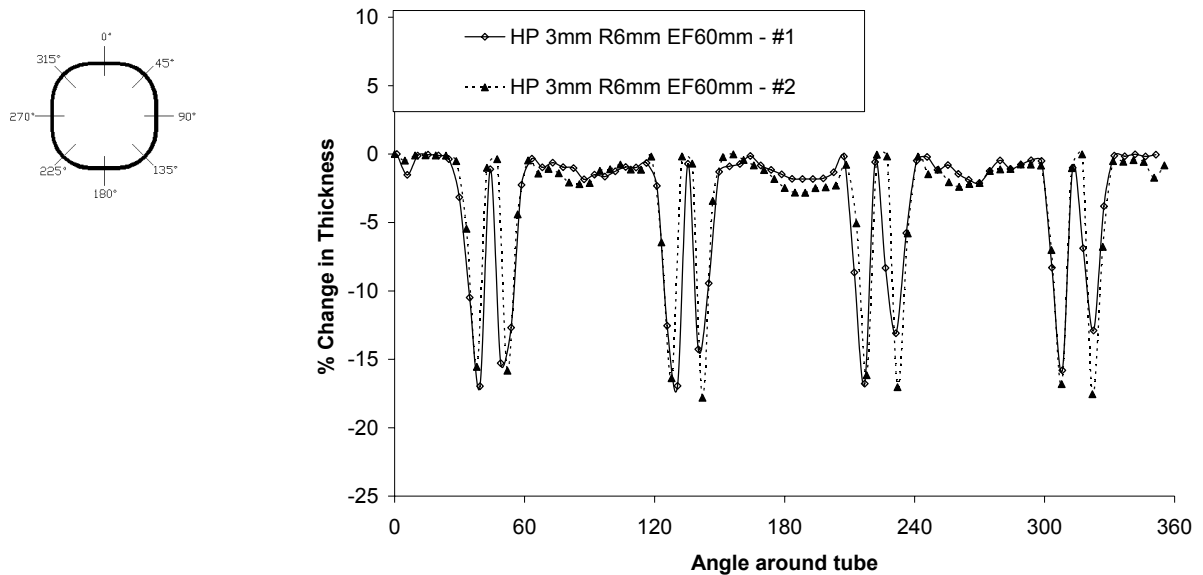
Figure 2.18: Per cent change in thickness for AA5754 tubes formed using high pressure hydroforming process with 60 mm of end-feed and a 6 mm corner radius

49
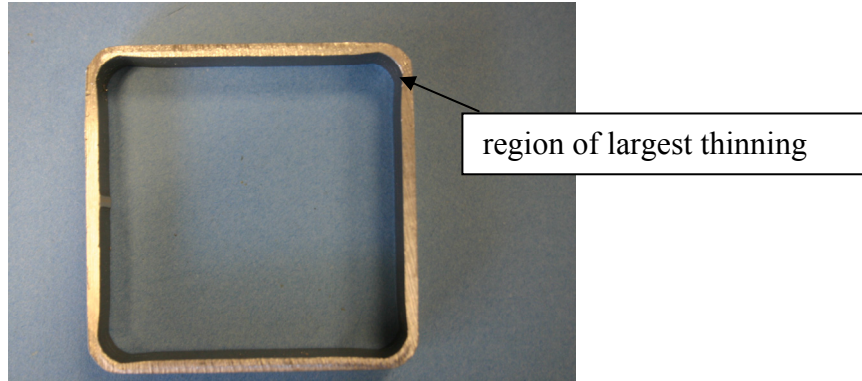
Figure 2.19: Cross-section of tube formed using high pressure process with a 6 mm corner radius and 60 mm of end-feed

An LVDT displacement transducer was used to measure the corner expansion in one of the corners of the tube during forming. The corner radius, R, was then determined using the following equation,

$$R = \frac{(\sqrt{2}-1)R_0 - s}{\sqrt{2}-1}$$ (2.3)

where, s is the corner expansion. The measured corner radius versus the end-feed displacement is presented in Figure 2.20 for the six configurations used in the high pressure process for the AA5754 aluminum alloy tubes. Figure 2.21 shows the corner radius versus the internal tube pressure for each of the six conditions. These experimental results are compared to theoretical predictions in Chapter 3.
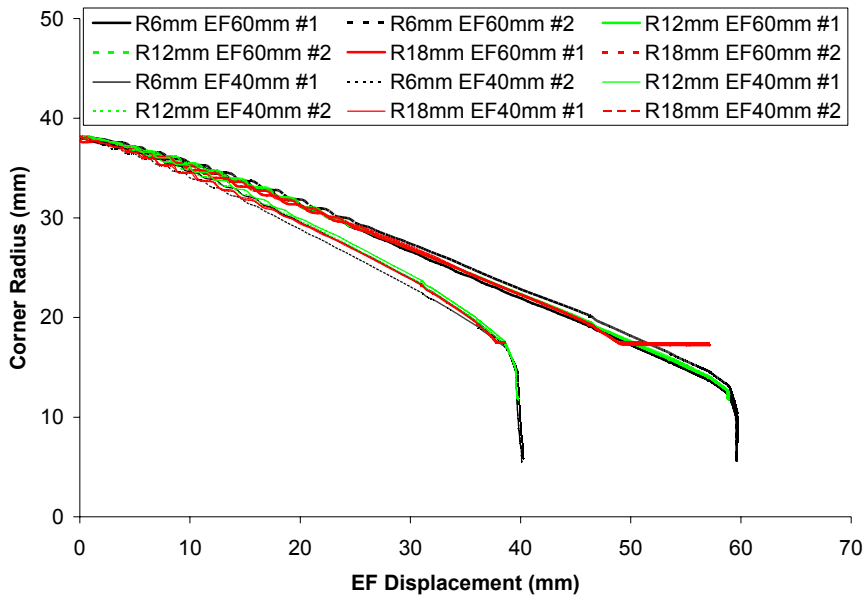
Figure 2.20: Measured corner radius vs. end-feed displacement during high pressure hydroforming of AA5754 alloy tubes
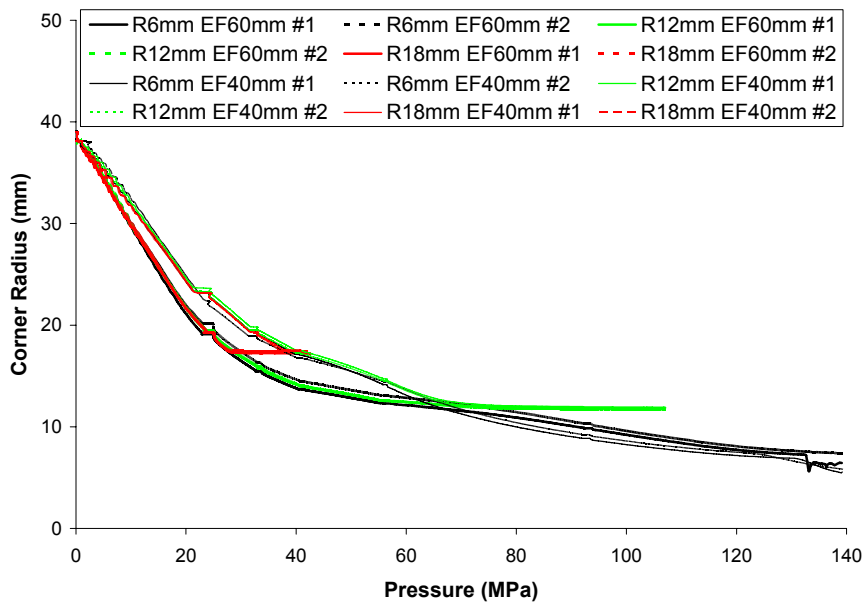
Figure 2.21: Measured corner radius vs. internal tube pressure during high pressure hydroforming of AA5754 alloy tubes

2.4.3 EN-AW 5018 Low Pressure Hydroforming

The strain measurements for the EN-AW 5018 alloy formed using the low pressure process were similar to the strains measured for the AA5754 alloy formed using the low pressure process. However, the etched circle grids were not as clear as for the AA5754 tubes, resulting in some inaccuracy in the strain measurements. The strain measurement results for an EN-AW 5018 tube formed using the low pressure process with a corner radius of 6 mm are shown in Figure 2.22. The strains are plotted versus the angle around the tube with the weld seam at 0°. Experimental measurements were made for every other circle grid around the perimeter of the tube. However, if the image of the deformed grid was not clear then a measurement was not taken. The plot shows that the tensile bending strains in the corners varied between 0.10 and 0.20, whereas in the flat sections of the tube it was found that there was a small compressive strain of approximately 0.03 on the outer surface of the tube. The results for all EN-AW 5018 alloy tubes formed using the low pressure process are presented in Appendix A. The strains in the corners of the tubes were reduced with the larger corner radius. As with the AA5754 low pressure tubes, thicknesses were not measured because there was little change resulting from the low pressure hydroforming process.
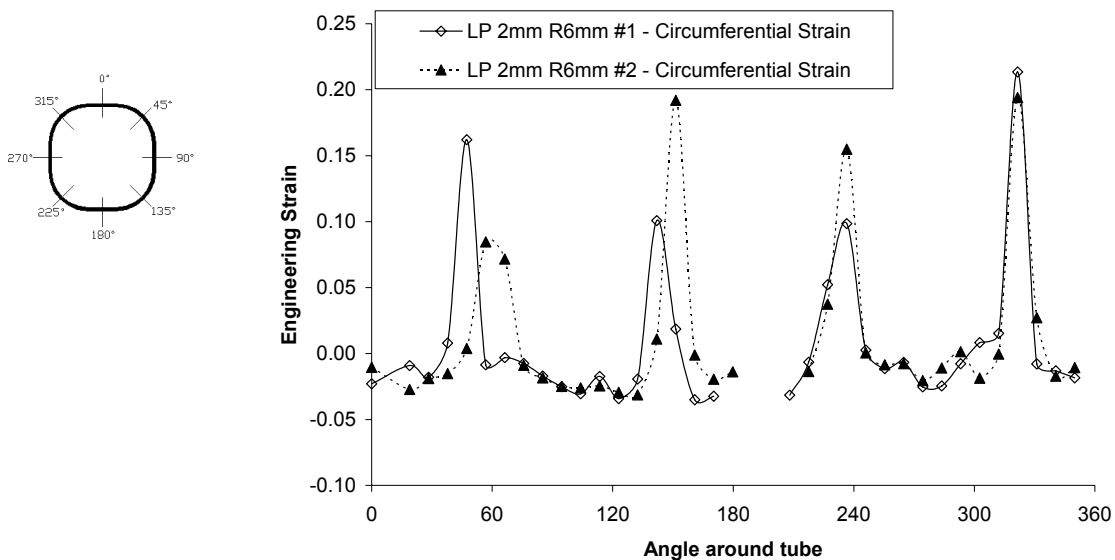
Figure 2.22: Measured strains for EN-AW 5018 tube formed using low pressure hydroforming process

2.4.4 EN-AW 5018 High Pressure Hydroforming

Figure 2.23 shows the measured engineering strains for the outer surface of a 3.5 mm thickness tube formed to a corner radius of 27 mm. Although no end-feeding force was applied, the tubes would naturally draw into the die about 5 mm at each end, resulting in a small longitudinal strain that can be seen in Figure 2.23. The circumferential strains vary from about 0.05 to 0.11. Although the figure does not show a clear trend, it does suggest that lower strains occurred near the center of the flat regions while higher strains existed within the material being formed into the corner regions. The results for the 33, 30, 27, and 24 mm corner radii cases for both the 2.0 and 3.5 mm tubes are presented in Appendix A. Thickness measurements were not performed on these tubes.
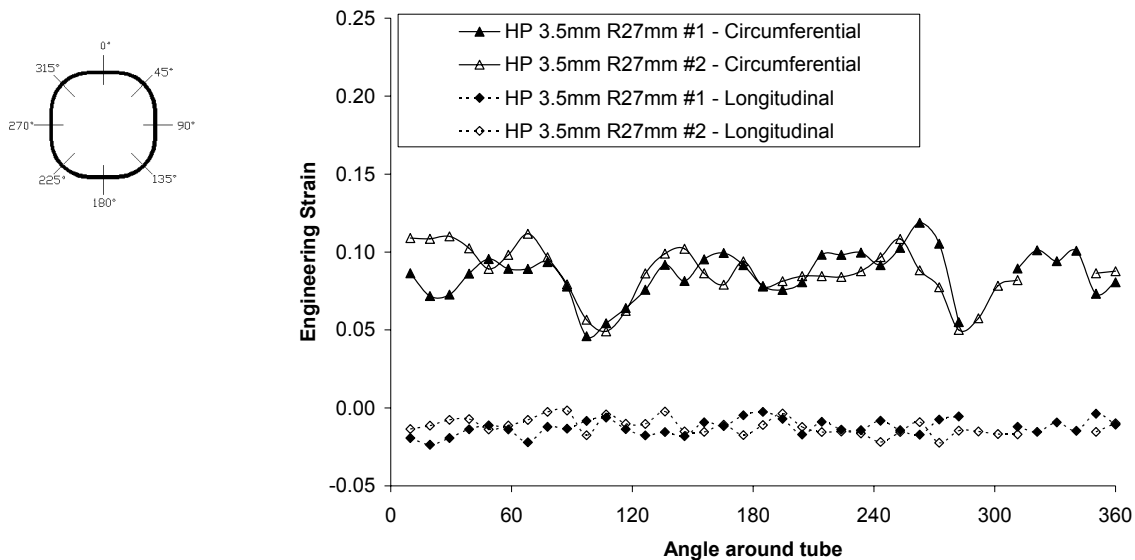
Figure 2.23: Measured strains for 3.5 mm thickness, EN-AW 5018 tube formed using high pressure hydroforming process

2.5 Axial Crush Experiments – Results and Discussion

The general folding behaviour obtained for square tubes was symmetric and the folding behaviour for the round tubes was a non-axisymmetric (diamond) mode, as shown in Figure 2.24.

53
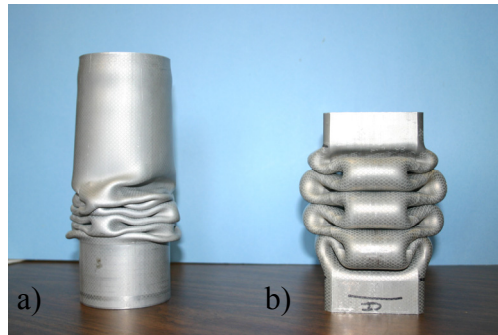
Figure 2.24: Folding behaviour for AA5754 alloy tubes: a) round tube – diamond mode and b) square high pressure hydroformed tube – symmetric mode

Figure 2.25 shows a typical plot of the measured crush load versus crush distance, which in this case is for AA5754 tubes formed using the low pressure hydroforming process with a 6 mm corner radius, with crush initiators.
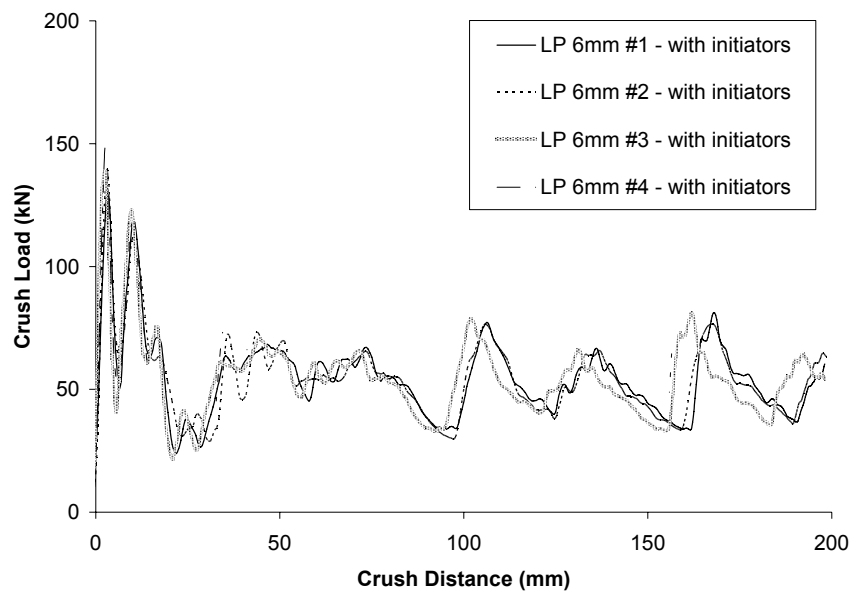
Figure 2.25: Crush response of AA5754 tubes formed using low pressure hydroforming process with 6 mm corner radius

The energy absorbed and mean crush load, P_m, can be determined from the crush data, based on the following equations,

$$E = \int_{x_1}^{x_2} F(x)dx \qquad\qquad (2.4)$$

$$P_m = E \big/ (x_2 - x_1) \qquad\qquad (2.5)$$

where, E is the energy absorbed between crush distance x_1 and x_2. The energy absorption and mean loads were calculated up to 200 mm crush distance for almost all crush responses obtained. In some cases, the tubes would deform less than 200 mm such that the energy absorption would be taken up to the maximum deformation. The crush response, energy absorption, mean load, and distance at which these values were calculated, are given in tables in Appendix B.

2.5.1 AA5754 Experimental Crash Results – Dynamic Testing

The measured mean crush loads for the AA5754 tubes formed using the low and high pressure processes are presented in Figure 2.26 and Figure 2.27, respectively. The mean crush loads are presented as a function of the radius ratio of the tube. The radius ratio is the ratio of the corner radius of the hydroformed tube to the initial radius of the tube. A measured crush load at a radius ratio of unity represents the non-hydroformed, round tubes. The mean loads for the circular tubes were just above 80 kN, whereas the mean loads for the tubes formed using the low pressure process were around 50 kN. The difference between these mean loads shows that there is a significant difference in the energy absorption capabilities of circular and square tubes, which will be addressed in Chapters 3 and 6. It should be noted, that because end-feeding was not used in the low pressure process, the mass of the low pressure hydroformed tubes was the same as the circular tubes, which was about 750 grams.

The results in Figure 2.26 show that the mean load was about 15% greater for the tubes without fold initiators compared to tubes with initiators. Figure 2.28 shows the crush response for a tube with and without the fold initiators formed to a corner radius of 6 mm

55

using the low pressure process, illustrating that the fold initiators reduced, but did not eliminate the initial peak load.
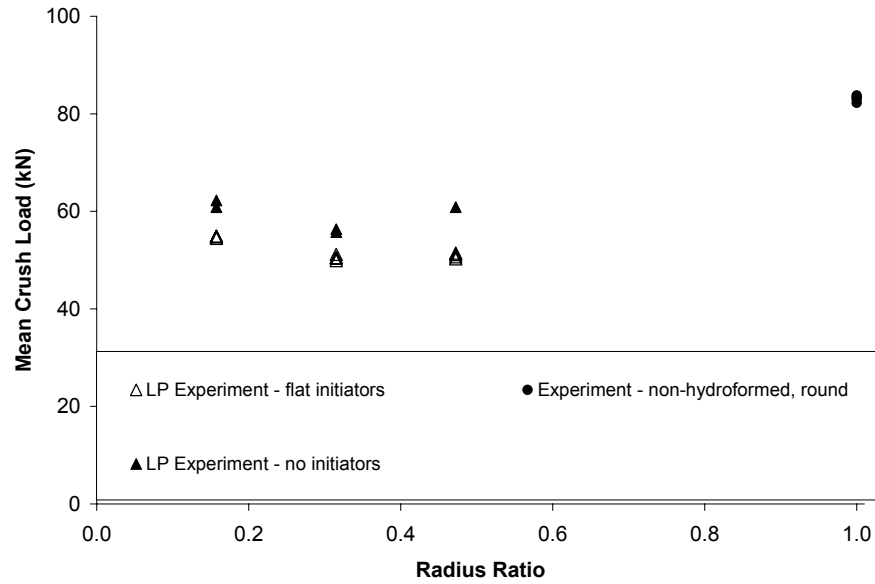
Figure 2.26: Mean crush loads for AA5754 axial crush structures formed using low pressure hydroforming process
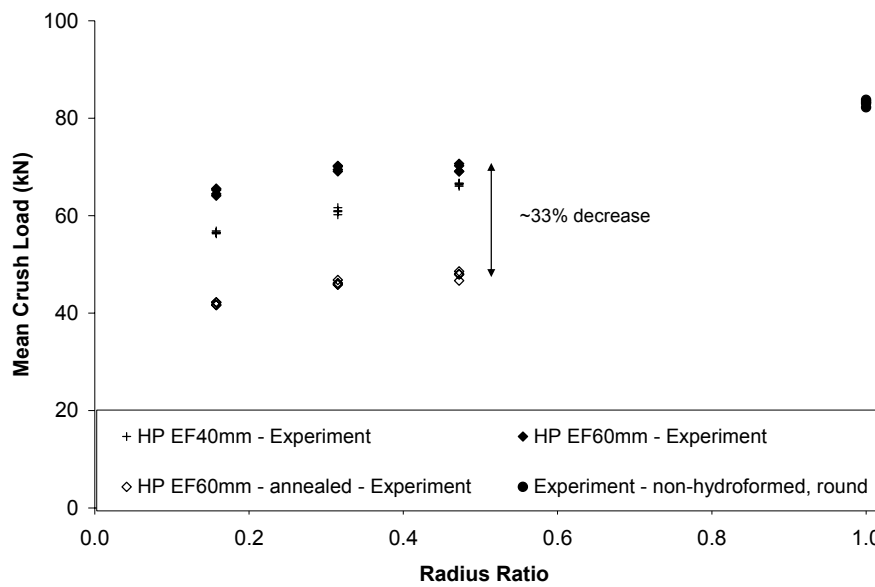
Figure 2.27: Mean crush loads for AA5754 axial crush structures formed using high pressure hydroforming process
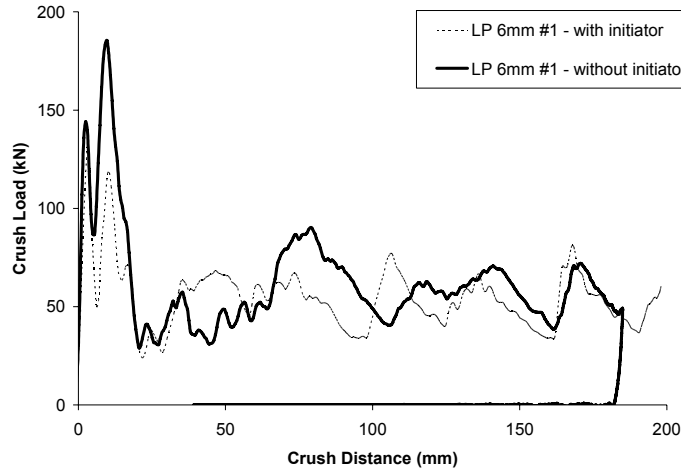
Figure 2.28: Crush response of tube with and without fold initiators

Figure 2.27 shows that work hardening can have a significant effect on the energy absorption characteristics. The mean load for the annealed tubes decreased by approximately 33% compared to the 60 mm end-feed tubes that were not annealed. It can also be seen that the mean load decreased slightly with decreasing radius ratio. This comparison shows that increased thinning due to circumferential expansion of the tube during hydroforming can reduce the energy absorption characteristics.

Differences in the mean crush loads between the 60 mm and 40 mm end-feed levels can also be observed in Figure 2.27, with a decrease in average load of about 11% between the 60 and 40 mm end-feed cases. However, it is important to note that during end-feeding, material was pushed into the die, thereby increasing the mass of the tube. Therefore, the tubes that had 60 mm of end-feed have a larger mass per unit length than tubes with 40 mm of end-feed. The masses of the AA5754 tubes with a 400 mm length are given in Table 2.5.

Table 2.5: Mass of hydroformed and trimmed AA5754 tubes (400 mm length)

Corner Radius	LP Tubes	HP Tubes 40 mm End-Feed	HP Tubes 60 mm End-Feed
6 mm	~ 751 g	~ 875 g	~ 916 g
12 mm	~ 753 g	~ 878 g	~ 921 g
18 mm	~ 751 g	~ 867 g	~ 887 g

57

Since the mass of the tubes increased with end-feeding, it could be expected that the mean load would increase because there was a greater cross-sectional area to absorb energy during crash. Therefore, the specific energy absorption (energy absorbed / mass) was considered to compare the 60 and 40 mm end-feed levels. The specific energy can be used to determine if the increase in mean crush loads of the tubes with 60 mm of end-feed resulted entirely from the increases in mass of the tubes, compared to the tubes with 40 mm of end-feed. In the calculation of the specific energy, the value used for the mass of the tube was based on the mass of a tube of length equal to the crush distance at which the energy absorption was calculated.

The specific energy absorption for tubes formed using the high pressure hydroforming process with 60 and 40 mm levels of end-feed is given in Figure 2.29. Even when considering the specific energies, the tubes with 60 mm of end-feed had a greater value than tubes formed with 40 mm of end-feed. This suggests that the higher mean crush loads measured for tubes with 60 mm of end-feed was due to more than just the greater mass of the tubes, relative to the tubes with 40 mm of end-feed.
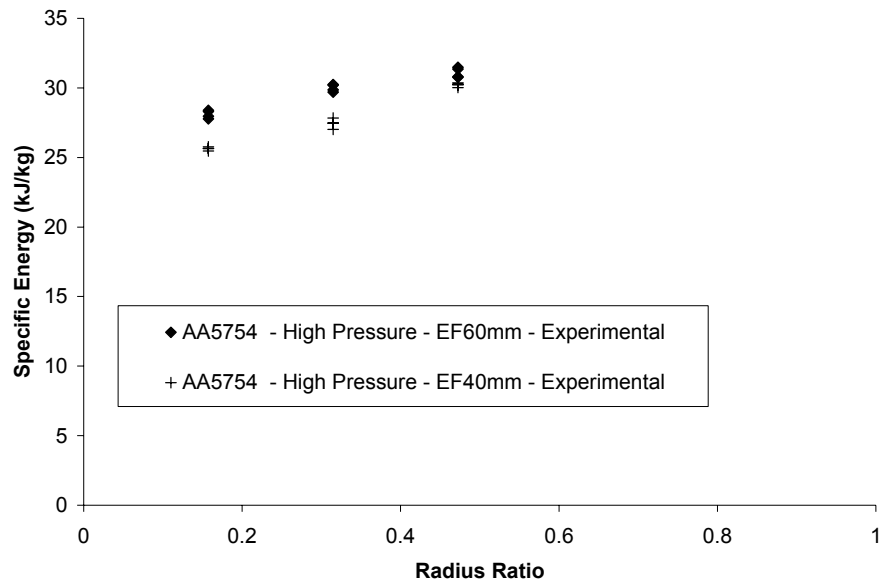
Figure 2.29: Comparison of specific energy absorption from crush between tubes formed with two levels of end-feed

Equation 1.15, $P_m = 9.53\sigma_0 w^{1/3} t^{5/3}$, which was developed to describe the mean crush load for a square tube undergoing symmetric crush, can be used to help explain these results. Since the mean load, or energy absorption, is proportional to the thickness to the power of 5/3, the specific energy would increase with increasing thickness (unless the mass was also proportional to the tube thickness by a factor of 5/3). The tubes with 60 mm of end-feed had slightly larger thicknesses than the tubes with 40 mm of end-feed, hence they had a higher specific energy absorption.

From Figure 2.26 and Figure 2.27, it can be seen that tubes formed using the high pressure process (~ 920 grams) have higher mean loads than tubes formed using the low pressure process (~ 750 grams). In order to compare the energy absorption characteristics between tubes formed using the high and low pressure processes, it might be attractive to compare the specific energy absorption. Instead, it would be best to compare the energy absorption characteristics for tubes of the same mass. This would require additional tubes of different diameter and thickness, but the same mass, and fabrication of new hydroforming tooling. Therefore, an analysis of the energy absorption characteristics of tubes with the same mass, formed using either the high or low pressure hydroforming processes, was performed using finite element simulations. The results of these simulations are presented and discussed in Chapter 6.

2.5.2 AA5754 Experimental Crash Results – Quasi-static Testing

The measured quasi-static and dynamic crush responses are shown in Figure 2.30 for tubes with a 12 mm corner radius formed using the high pressure hydroforming process. The results for tubes with 6 and 18 mm corner radii can be found in Appendix B. The figures show that the dynamic crush load was slightly greater than the quasi-static response, particularly during the initial fold.

Figure 2.31 presents the measured mean loads showing that there was an average increase of 6% between the quasi-static and dynamic results. Figure 2.30b shows that the peak loads from the dynamic tests were greater than from the quasi-static tests, indicating that the 6% increase might be due to the crush behaviour on the initial fold. However, it was

found that there was still an average increase in the mean loads of about 4% between quasi-static and dynamic cases, when considering only the crush force data between 100 to 200 mm of crush distance. This shows that peak load was not responsible for the entire measured difference of 6% between quasi-static and dynamics cases.
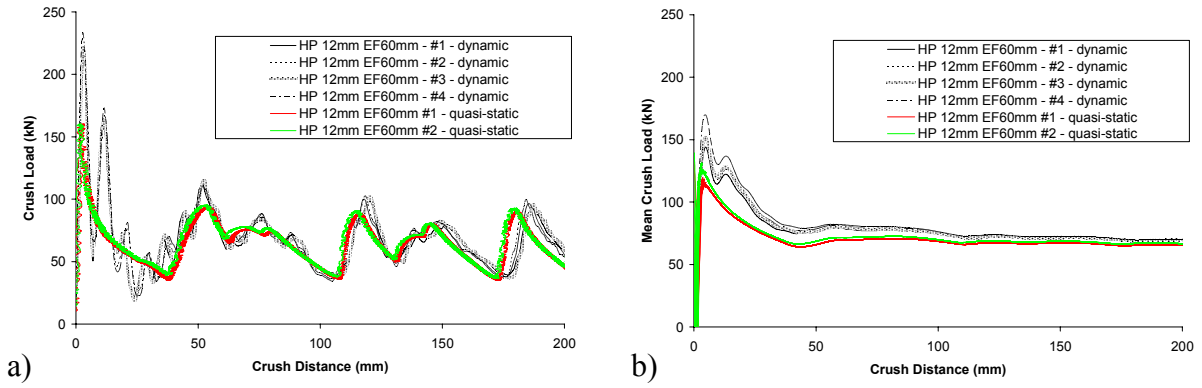
Figure 2.30: Comparison of quasi-static and dynamic crush response of AA5754 alloy tube a) crush load vs. displacement and b) mean crush load vs. displacement
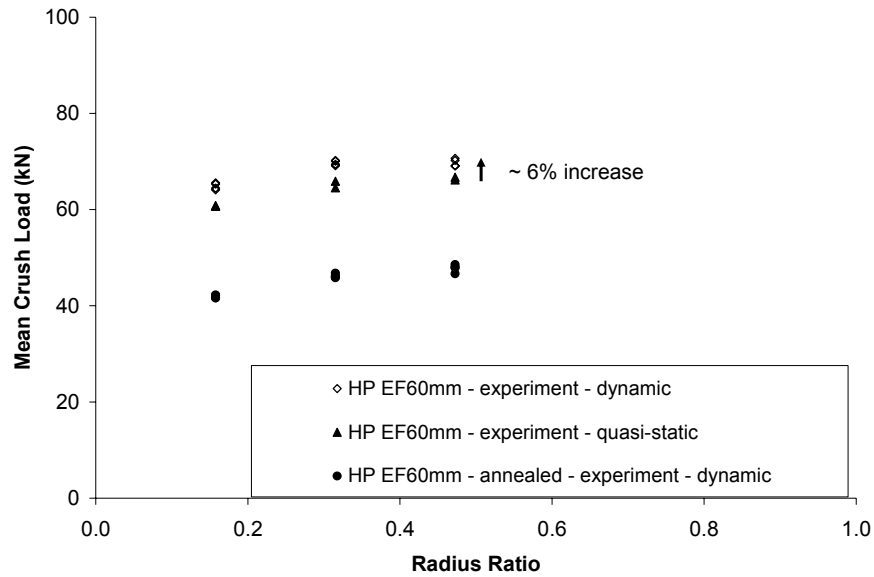
Figure 2.31: Comparison of quasi-static and dynamic mean loads for AA5754 alloy tube formed using the high pressure hydroforming process

2.5.3 EN-AW 5018 Experimental Crash Results

The results of the high pressure EN-AW 5018 testing has been summarized by Williams et al. [81,82] and will only be discussed briefly in this thesis. The measured mean crush loads at 200 mm crush displacement for the EN-AW 5018 tubes formed using both the low and high pressure hydroforming processes are shown in Figure 2.32. Tubes formed using the high pressure hydroforming process showed a significant decrease in energy absorption with decreasing radius ratio. This reduction was attributed to thinning due to circumferential expansion during hydroforming, which had a significant influence on the energy absorption characteristics during crash (recall, that the EN-AW 5018 tubes did not utilize end-feeding). However, the figure also shows that the corner radius of tubes formed using the low pressure process did not significantly affect the mean load measured during impact.
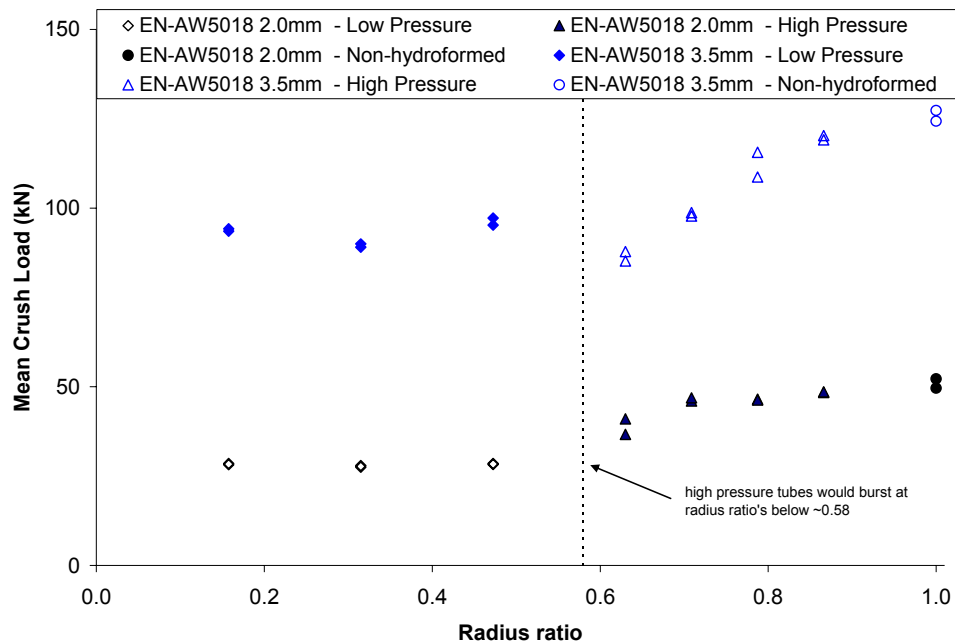
Figure 2.32: Mean crush loads for EN-AW 5018 axial crush structures

Chapter 3 – Theoretical Predictions

This chapter outlines the theoretical formulation adopted in this work to predict the forming behaviour of the tubes during hydroforming and the mean crush response during crash. The hydroforming predictions focus mainly on the high pressure process with end-feeding. As will be discussed below, a major assumption that limits the accuracy of the hydroforming prediction is that of sticking friction. In fact, it is suggested that the best way to predict the hydroforming response is by using finite element simulations, as opposed to any theoretical equations. However, it will be shown that the theoretical impact equations can provide a reasonable expectation of the mean load experienced during crash, if values such as tube thickness and work hardening after hydroforming can be adequately predicted. The theoretical models did not account for effects such as anisotropy, kinematic hardening, and strain-rate.

3.1 Hydroforming – Theoretical Analysis

3.1.1 High Pressure Hydroforming – Methodology

Several researchers have developed procedures to predict the behaviour of tubes during hydroforming [10,83,84,85,86,87], but analytical formulations could not be found that account for the effect of end-feeding during hydroforming within a die incorporating a square cross-section. Expanding on the concepts provided in the literature, the following methodology was developed in the current research for cases where there was end-feeding. For cases in which there was no end-feed the reader is referred to the article by Mayer [88].

During a forming operation in which the material is assumed to be incompressible, the volume of the material remains constant, which leads to the following equation,

$$\varepsilon_t + \varepsilon_l + \varepsilon_\theta = 0 \tag{3.1}$$

where, ε_t, ε_l, and ε_θ are the true thickness, longitudinal, and circumferential strains, respectively. As shown in Figure 3.1, an increment of end-feed, Δl, will result in a new cross-sectional area, A_{new}, of the tube over the length, $l_0 - \Delta l$, equal to,

$$A_{new} = A_{old} + \frac{\Delta l/A_0}{(l_0 - \Delta l)} \tag{3.2}$$

where, A_0 is the initial cross-sectional area of the tube, l_0 is the initial tube length, and A_{old} is the previous cross-sectional area of the tube. This equation is based on the assumption that the increase in area is uniform along the entire length of the tube.
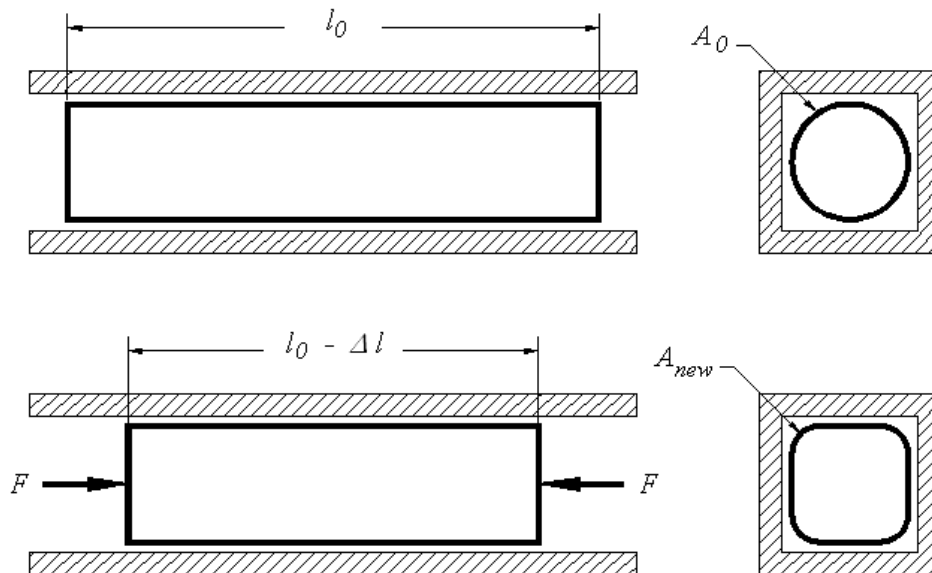
Figure 3.1: End-feeding of tube during hydroforming

An assumption of sticking friction [9] in the circumferential direction was used in the calculations, meaning that once the material contacts the die wall its thickness will no longer change. As depicted in Figure 3.2 for a one-quarter cross-section of the tube, the thickness at

63

the midpoint of the width is equal to the initial thickness, t_0, but decreases to a thickness, t, when the tube has formed to a corner radius, R.
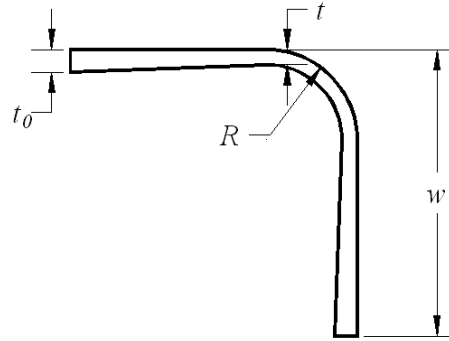
Figure 3.2: Cross-section profile of tube under assumption of sticking friction

The area of this assumed profile can be set equal to the area calculated from Equation 3.2. If the radius is known, then the thickness, t, can be determined. Further details are provided in Appendix C. The thickness, longitudinal, and circumferential strains are calculated using,

$$\varepsilon_t = \ln\left(\frac{t}{t_0}\right) \qquad \varepsilon_l = \ln\left(\frac{l_o - \Delta l}{l_0}\right) \qquad \varepsilon_\theta = -(\varepsilon_t + \varepsilon_l) \qquad (3.3)$$

which are then used to determine the effective strain, $\bar{\varepsilon}$,

$$\bar{\varepsilon} = \frac{\sqrt{2}}{3}\left[(\varepsilon_t - \varepsilon_l)^2 + (\varepsilon_l - \varepsilon_\theta)^2 + (\varepsilon_\theta - \varepsilon_t)^2\right]^{1/2} \qquad (3.4)$$

which is used to calculate the effective stress using Equation 2.1. However, the tube radius, R, which is required to calculate the area is an unknown value. As a result, another equation was required in the analysis. The corner radius of the tube depends on friction, internal pressure, and the end-feed displacement. It should be noted that it was assumed the longitudinal strain was uniform along the length of the tube.

In forming operations, the following expression is often used to describe the stress ratio, α, during loading [10],

$$\alpha = \frac{\sigma_{11}}{\sigma_{22}} = \frac{\sigma_l}{\sigma_\theta} \qquad (3.5)$$

where in hydroforming, σ_l is the longitudinal stress and σ_θ is the circumferential stress. Under plane stress conditions $(\sigma_{33} = \sigma_t = 0)$, the effective stress can be described by [10],

$$\bar{\sigma} = \left[\sigma_1{}^2 + \sigma_2{}^2 - 2\sigma_1\sigma_2\right]^{1/2} = \left[\alpha^2 - \alpha + 1\right]^{1/2}\sigma_{22} \qquad (3.6)$$

where, for a tube subject to an internal pressure, P,

$$\sigma_{22} = \sigma_\theta = \frac{PR}{t} \qquad (3.7)$$

In plasticity theory, the stress ratio, α, can be related to a strain ratio, $\beta = d\varepsilon_{11}/d\varepsilon_{22}$ using the following equation [10],

$$\alpha = \frac{1 + 2\beta}{2 + \beta} \qquad (3.8)$$

The procedure used to solve for R, is to estimate a value for the corner radius and then calculate the effective stress using Equations 3.1-3.8. An iterative process was then carried out to determine the actual corner radius, R, for which,

$$\{A + (B - A)[1 - \exp(-C\bar{\varepsilon})]\} - \left[\alpha^2 - \alpha + 1\right]^{1/2}\sigma_{22} = 0 \qquad (3.9)$$

within a specified tolerance. The process is then repeated for increments in end-feed, Δl, from which the strain and thickness profiles can be predicted. The predicted data can then be plotted as a function of the angle around the tube and compared to experimental data. The pressure versus end-feed profiles, given in Figure 2.15 and Figure 2.16, were used as input to the procedure, corresponding to the 60 mm and 40 mm end-feed cases.

3.1.2 Comparison of Theory versus Experiments – Hydroforming

The transient deformation behaviour predicted using the theoretical model described above is shown in Figure 3.3 and Figure 3.4. Shown, are the theoretical corner radii as a function of the internal tube pressure and end-feed displacement. The results show that the theoretical predictions capture the experimental behaviour relatively well. In Figure 3.4, it can be seen that for the case with 60 mm of end-feed there is some discrepancy between the

predicted and measured corner radius beyond a pressure of about 40 MPa. It should be noted, that based on Equation 3.7, for an initial radius of 38.1 mm with a thickness of 3.07 mm and tensile strength of 225 MPa, the pressure required to cause expansion is about 18 MPa. As seen in Figure 3.4 at 18 MPa, the corner radius was between 25 to 30 mm, showing that during the early stages of hydroforming, end-feeding was primarily responsible for changing the shape of the tube. However, at later stages in the hydroforming process, the internal pressure was mainly responsible for expansion of the tube. At higher internal pressures, it became more difficult to end-feed the tube due to frictional forces acting between the tube and die wall.
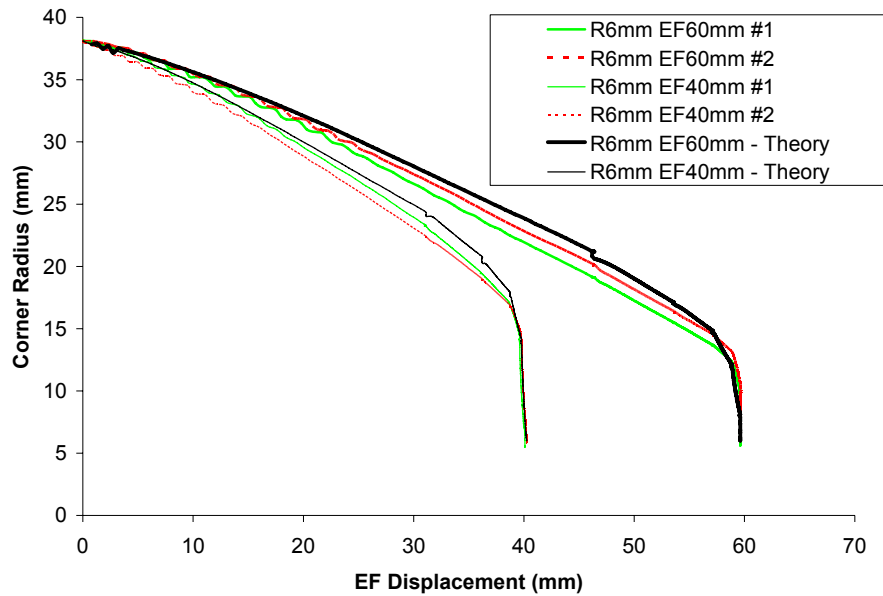
Figure 3.3: Theoretical and experimental results for corner expansion vs. end-feed displacement during high pressure hydroforming
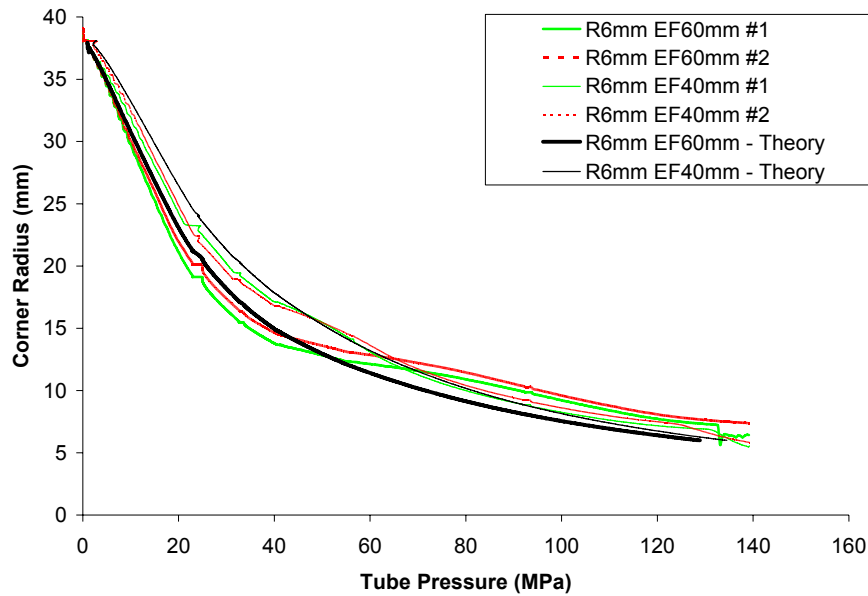
Figure 3.4: Theoretical and experimental corner expansion vs. internal tube pressure during high pressure hydroforming

Figure 3.5 compares the analytical predictions with measured strain data for the high pressure process in which the tube was formed to a radius of 6 mm with 60 mm of end-feed. Figure 3.6 shows the per cent thickness reduction from the predictions and experiments. The results show that the analytical predictions provided reasonable predictions of the strains after hydroforming. However, the analytical models do not entirely capture the measured thickness behaviour in the corners of the tube. There was almost no change of the thickness in the actual corner, whereas in the predictions, the thickness is equal throughout the corner radius, which is attributed to the assumption of sticking friction. The results for all cases are presented in Appendix C.

Once the strain and thickness profiles were determined, a nominal value for the thickness and effective strain can be determined by taking the average throughout the cross-section, for each of the six cases studied as given in Table 3.1. The predictions show that the thickness decreases, but the effective strain increases with decreasing corner radius. These values were used to predict the mean load during axial crush, as discussed below in Section 3.3.

67
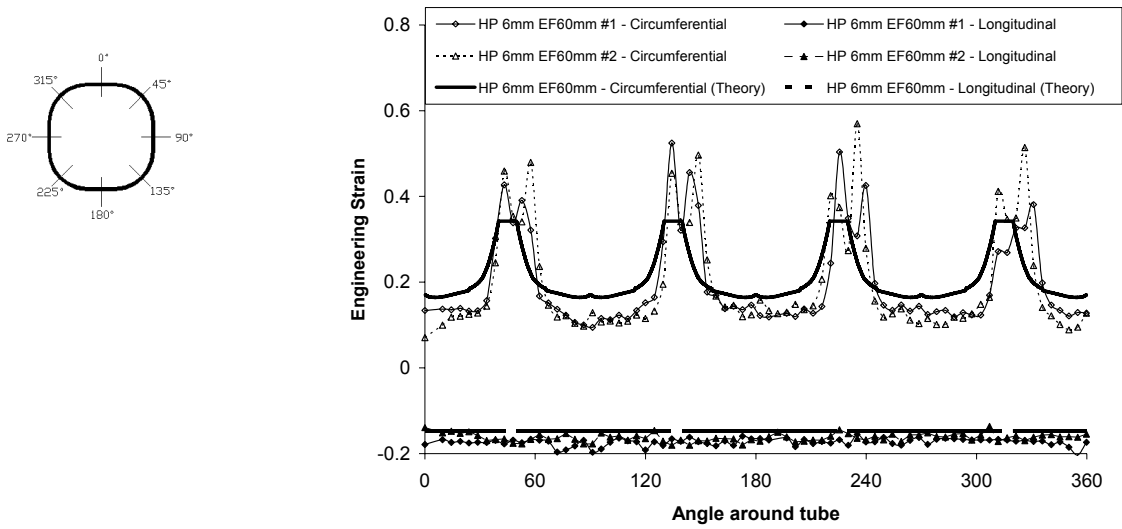
Figure 3.5: Comparison of analytical predictions with experimental strain data for tube formed to 6 mm radius with 60 mm of end-feed
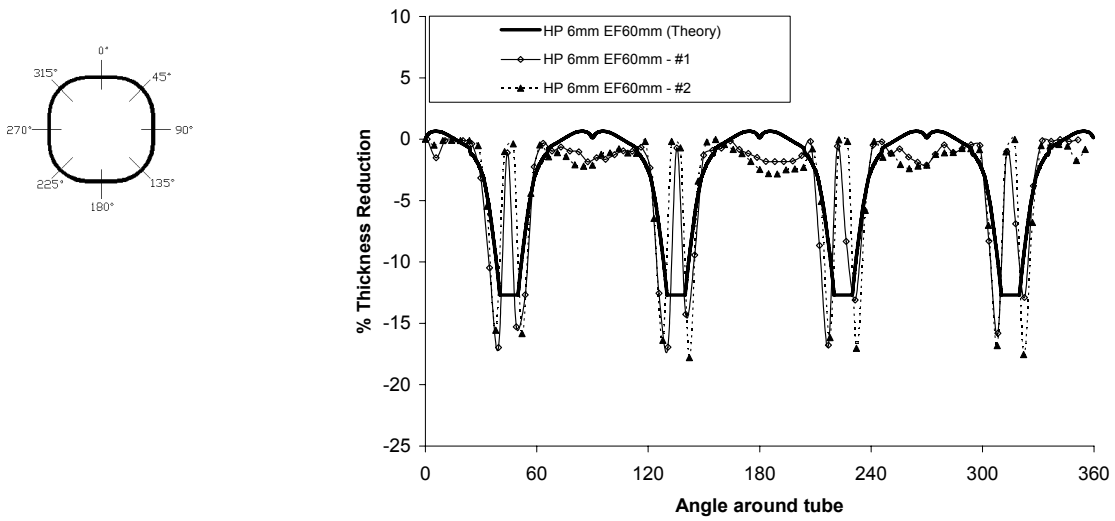
Figure 3.6: Comparison of analytical predictions with experimental thickness data for tube formed to 6 mm radius with 60 mm of end-feed

68

Table 3.1: Predicted thickness and effective strain from high pressure hydroforming, assuming sticking friction

Description	Average Thickness	Average Effective Strain
HP R6mm EF60mm	2.98 mm	0.208
HP R12mm EF60mm	3.01 mm	0.194
HP R18mm EF60mm	3.05 mm	0.163
HP R6mm EF40mm	2.86 mm	0.188
HP R12mm EF40mm	2.90 mm	0.170
HP R18mm EF40mm	2.96 mm	0.145

3.1.3 High Pressure Hydroforming – Simplified Approximation

Due to the assumptions in the calculations above, the results should only be taken as an approximation of the behaviour of the tube during hydroforming. An alternative estimate of the thickness can also be obtained based on volume conservation with the assumption of a uniform thickness of the hydroformed tube, as shown in Figure 3.7. This assumption is often referred to as non-sticking friction, in which it was assumed that the increase in volume of the tube due to end-feeding was distributed evenly throughout the tube. The calculated nominal thickness was then used to estimate the effective strain in the hydroformed tube using Equations 3.3 and 3.4. The estimated thickness and strain values are given in Table 3.2 and further details of the calculations can be found in Appendix C. In general, the thicknesses are slightly less than those predicted using the sticking friction assumption (Table 3.1) by an average of about 0.08 mm, but the effective strain is greater by approximately 0.02. These values are used in Section 3.3 to predict the mean load during impact.
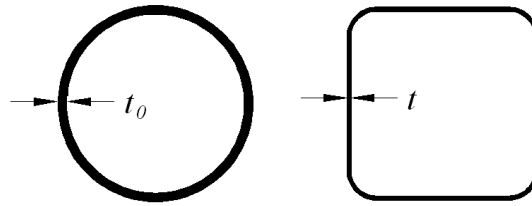
Figure 3.7: Cross-section profile of non-hydroformed and hydroformed tube with uniform thickness assumption

Table 3.2: Approximated thickness and effective strain values from high pressure hydroforming, assuming a uniform thickness

Description	Average Thickness	Average Effective Strain
HP R6mm EF60mm	2.83 mm	0.244
HP R12mm EF60mm	2.94 mm	0.213
HP R18mm EF60mm	3.05 mm	0.181
HP R6mm EF40mm	2.71 mm	0.229
HP R12mm EF40mm	2.81 mm	0.191
HP R18mm EF40mm	2.92 mm	0.154

3.1.4 Low Pressure Hydroforming

Analytical predictions were also developed for the low pressure hydroforming experiments. In the experiments, the low pressure die geometry was designed such that the perimeter of the cross-section was equal to the original circumference of the tube, suggesting that the total circumferential strain would be zero. Since end-feeding was not used with the low pressure process the longitudinal strain was zero, meaning that the thickness strain was zero, such that there were no changes in the thickness of the tube. This might suggest, from Equation 3.4, that the effective strain in the cross-section was zero, but this was not the case.

In the low pressure process, the tube was subjected to bending strain in the corners such that changes in the circumferential and thickness strain would occur locally, as depicted

in Figure 3.8. In this figure, sections on the compressive side of the bend would thicken and sections on the tensile side would thin, resulting in local work hardening.
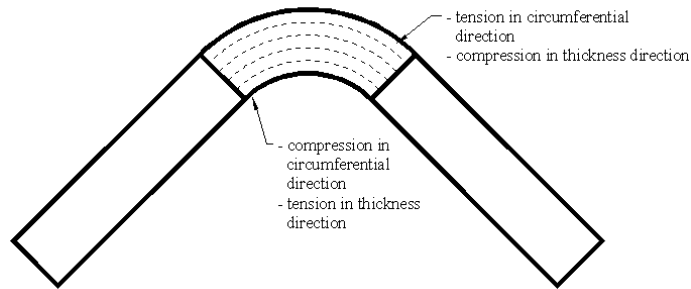
Figure 3.8: Bending in low pressure hydroforming

In order to analyse the low pressure process, the cross-section would have to be divided into several sections through the thickness of the material, as well as sections around the perimeter to account for effects such as friction. On this basis, it is recommended that finite element models be used to describe the behaviour of the tube during deformation, as opposed to analytical models which would become complicated. However, in order to evaluate an approximate value for the work hardening in the tube resulting from the low pressure process, the following method is suggested.

The tensile bending strain, ε_b, for a material that is originally flat can be predicted using the following equation [9],

$$\varepsilon_b = \frac{t_0/2}{R - t_0/2} \tag{3.10}$$

For a tube material subject to bending, the tensile and compressive bending strains can be approximated by the following equations,

$$\varepsilon_{tensile} = \ln \left[\frac{1 + \dfrac{t_0/2}{R - t_0/2}}{1 + \dfrac{t_0/2}{R_0 - t_0/2}} \right] \qquad (3.11)$$

$$\varepsilon_{compressive} = \ln \left[\frac{1 - \dfrac{t_0/2}{R - t_0/2}}{1 - \dfrac{t_0/2}{R_0 - t_0/2}} \right] \qquad (3.12)$$

where, R_0 is the original radius of the tube. Details for the development of these equations can be found in Appendix C. These equations were used to approximate the strains in the corners of the low pressure tubes, which were then taken as the circumferential strain. The effective strain was calculated using Equation 3.4 for the tensile and compressive sides of the bend. The strains in the sides of the tube were caused by flattening of the tube wall during the low pressure hydroforming process. If the outer surface of the bends were in tension, then the outer surface of the flat regions of the tube were in compression. Similarly, the flat regions on the inside of the tube were in tension.

In order to obtain a very approximate value of the work hardening during the low pressure operation, it was assumed that the maximum strain in the bend was at the corner, decreasing to a strain of zero at the end of the bend where it meets the flat regions of the tube. The strain in the flat regions was then taken to be constant and determined such that the circumference and volume of the tube remained constant, as described in detail in Appendix C. Figure 3.9 compares the measured circumferential strains with this simple approximation, for the outer surface of an AA5754 tube formed to a corner radius of 6 mm using the low pressure process. The 12 and 18 mm cases are presented in Appendix C. The results show that the compressive circumferential strains in the flat regions are actually greater than what is predicted using the above method. Consequently, the predicted effective strain acting in the cross-section using this method would not be entirely accurate, but should provide a reasonable approximation that can be applied to the axial crush predictions.
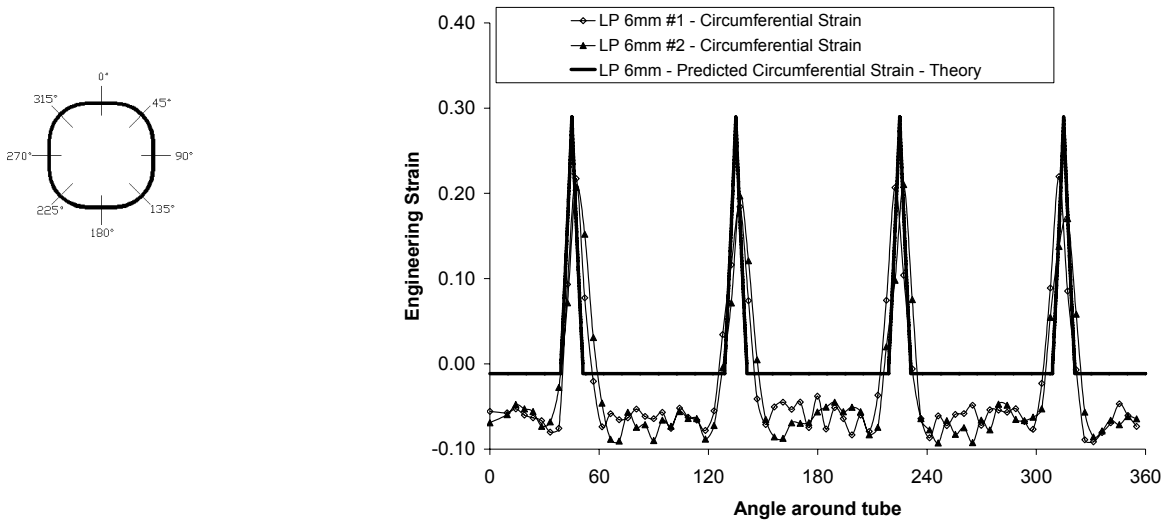
Figure 3.9: Circumferential strain profile: measured vs. simple approximation

Table 3.3 presents the predicted nominal effective strain acting in the tube cross-section for the 6, 12, and 18 mm corner radii tubes formed using the low pressure process. Further details of how these values were obtained can be found in Appendix C. The values in this table were used to predict the mean load during axial crush in the next section.

Table 3.3: Thickness and approximated effective strain values from low pressure hydroforming

Description	Thickness	Average Effective Strain
LP R6mm	3.07 mm	0.054
LP R12mm	3.07 mm	0.023
LP R18mm	3.07 mm	0.014

3.2 Energy Equivalent Flow Stress

Several theoretical equations to describe the mean crushing load during axial crush were presented in Chapter 1. All of these equations require definition of the energy

equivalent flow stress, σ_0, which gives a representative value of the stress acting in the folds of the axial crush structure. Equation 1.11 can be written as,

$$\frac{P_m}{M_0} = \left[20.79 \left(\frac{2R}{t} \right)^{1/2} + 11.90 \right] \tag{3.13}$$

where, $M_0 = \frac{2\sigma_0}{\sqrt{3}} \frac{t^2}{4}$ is a measure of the bending moment acting in the folds of an axial crush structure. The bending moment is illustrated in Figure 3.10 which depicts a representative stress distribution in a bend, showing σ_0 gives a measure of the nominal stress acting in the bend. It is taken to be an engineering stress as opposed to a true stress and there are several methods discussed in literature that have been used to determine the energy equivalent flow stress in a fold of an axial crush structure.
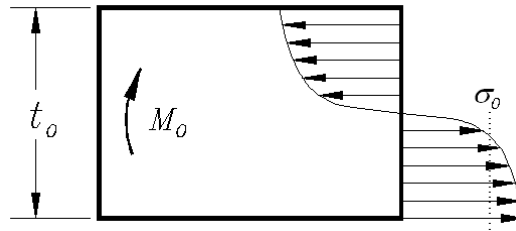
Figure 3.10: Stress distribution in material subject to bending

3.2.1 Energy Equivalent Flow Stress – Method 1

Wierzbicki and Abramowicz [89,90] proposed a model that accounted for three regions of bending in an axial crush fold of a rectangular column, as depicted in the 'Basic Folding Element' shown in Figure 3.11. The three regions are as follows: horizontal plastic hinge zones denoted by 1 in the figure; inclined plastic hinge zones denoted by 2; and regions of extensional deformation denoted by 3 and 4.

74

a)   b)
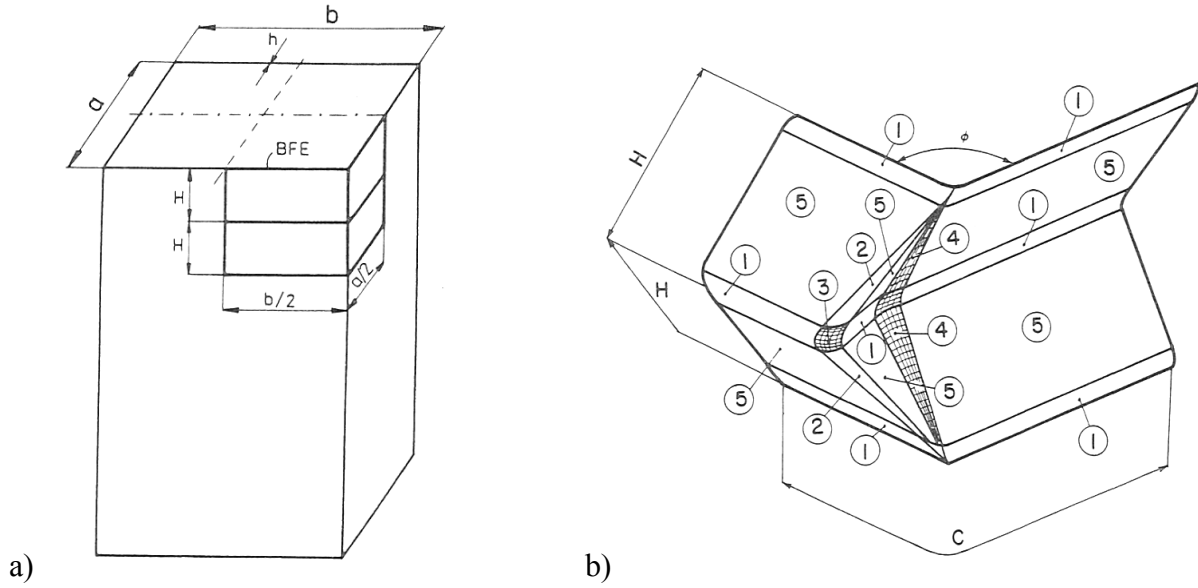
Figure 3.11: a) Rectangular column and b) Basic Folding Element depicting regions of deformation in an axial crush structure [89]

The following expressions were developed to determine the strains acting in each of the three bending regions,

$$\varepsilon_0^1 = 0.93\left(\frac{t}{b}\right)^{2/3} \qquad \varepsilon_0^2 = 0.69\left(\frac{t}{b}\right)^{1/3} \qquad \varepsilon_0^3 = 1.3\left(\frac{t}{b}\right)^{1/3} \qquad (3.14)$$

where regions $i = 1$ to 3 represent the horizontal hinge, inclined hinge, and extensional zones, respectively. A representative stress in each of the three regions is then calculated using the following weighted stress function,

$$\sigma_0^i = \frac{2}{\varepsilon_0^{i2}} \int_0^{\varepsilon_0^i} \bar{\sigma}(\varepsilon)\varepsilon d\varepsilon \qquad i = 1,2,3 \qquad (3.15)$$

Finally, the energy equivalent flow stress is defined as,

$$\sigma_0 = \left(\sigma_0^1 \sigma_0^2 \sigma_0^3\right)^{1/3} \qquad (3.16)$$

In this model, the weighted stress was integrated with respect to an initial strain of zero. It was found that if the initial strain was not equal to zero, then Equation 3.15 provided

unrealistic values of the stress in the fold. In order to include the pre-strain from hydroforming, an alternative model is suggested in the current research to describe an average stress in the three regions of bending, given by,

$$\sigma_0^i = \frac{1}{e_2 - e_1} \int_{e_1}^{e_2} \bar{\sigma}_{eng}(e)de \qquad i = 1,2,3 \qquad (3.17)$$

where, an engineering stress is calculated. In this expression, e_1 is the value of mean effective strain calculated from the hydroforming operation (as given in Tables 3.1 to 3.3) but converted to an engineering strain. The bending strain, e_2, in each of the three regions is then,

$$e_2 = e_1 + e_0^i \qquad (3.18)$$

where, e_0^i are the engineering strains converted from true strains calculated using Equation 3.14. The energy equivalent flow stress is then determined using Equation 3.16. All predictions using this method will be referred to as Method 1.

3.2.2 Energy Equivalent Flow Stress – Method 2

Bardi et al. [16] suggest that the energy equivalent flow stress can be calculated by using the mean level of stress under the uniaxial stress-strain curve up to the point of failure. The AA5754 specimens would fail at engineering strains of about 0.22, as seen above in Figure 2.2, such that σ_0 for Method 2 was determined using Equation 3.17 with e_2 equal to 0.22 and e_1 equal to the values given in Tables 3.1 to 3.3, but converted to engineering strains.

3.2.3 Energy Equivalent Flow Stress – Method 3

Langseth and Hopperstad [90] found good agreement between theoretical and predicted results when using,

$$\sigma_0 = \frac{\sigma_{YS} + \sigma_{UTS}}{2} \qquad (3.19)$$

where, σ_{YS} is the yield stress of the material. In the current research, the following equation was used as Method 3 for evaluating the energy equivalent flow stress,

$$\sigma_0 = \frac{\overline{\sigma}_{eng} + \sigma_{UTS}}{2} \qquad (3.20)$$

where, $\overline{\sigma}_{eng}$ was calculated based on the effective strains given in Tables 3.1 to 3.3, after converting the true strains to engineering strains. A tensile strength of 225 MPa for the AA5754 alloy was used in all calculations.

3.2.4 Energy Equivalent Flow Stress – Method 4

Method 4 involved the following relationship, which has previously been used to describe the energy equivalent flow stress in axial crush predictions [89,91,92],

$$\sigma_0 = \sqrt{\frac{\overline{\sigma}_{eng}\sigma_{UTS}}{n+1}} \qquad (3.21)$$

where, n is the strain hardening exponent which was determined to be 0.17 for the AA5754 as-tubed alloy based on the engineering stress-strain curve, shown in Figure 2.2.

3.3 Axial Crush Predictions – Hydroformed Tubes

All predictions were calculated using Equation 1.16, $P_m = 4\pi\sigma_0 w^{1/3}t^{5/3}$, to describe the mean crush load of the hydroformed tubes. Figure 3.12 compares the predicted and measured results for a tube formed using the high pressure process with 60 mm of end-feed. The experimental data was previously presented above in Figure 2.27. The predictions were based on the nominal thicknesses and effective strains presented in Table 3.1. Predictions were made for each of the four methods discussed to calculate the energy equivalent flow stress. The results show that Method 4 provided the best agreement with the experimental data. The predictions based on Methods 2 and 3 over predicted the measured data by about 11% while those using Method 1 gave an over prediction of about 7.5%.
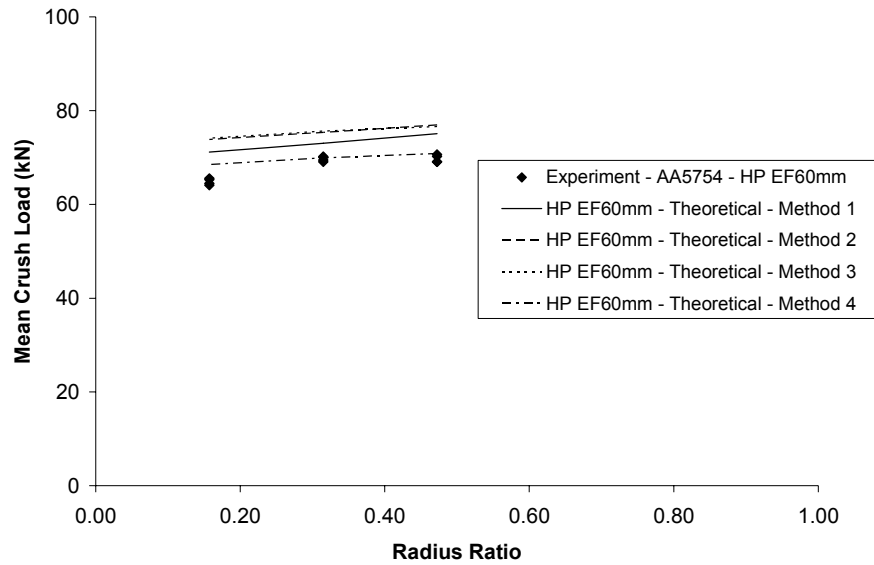
Figure 3.12: Theoretical versus experimental axial crush predictions for AA5754 tubes formed using high pressure hydroforming process, assuming sticking friction

Figure 3.13 shows the theoretical and measured mean loads for tubes formed with 60 mm of end-feed that were annealed prior to impact, such that the initial yield stress of 100 MPa, was used in the calculations (effective strain was equal to zero). The figure again shows that the best prediction of the experimental results is realized using Method 4 to determine σ_0, while Methods 1, 2, and 3 gave large over predictions.

Figure 3.14 compares the predictions based on thickness and effective strain values determined based on the assumption of sticking friction (Table 3.1) or non-sticking friction (Table 3.2), using Method 4 to determine the energy equivalent flow stress. There was a small difference between the two methods, indicating that the simple assumption of a constant thickness for the non-sticking case during hydroforming can yield values that can be used to give a good indication of the mean load obtained from axial crush.
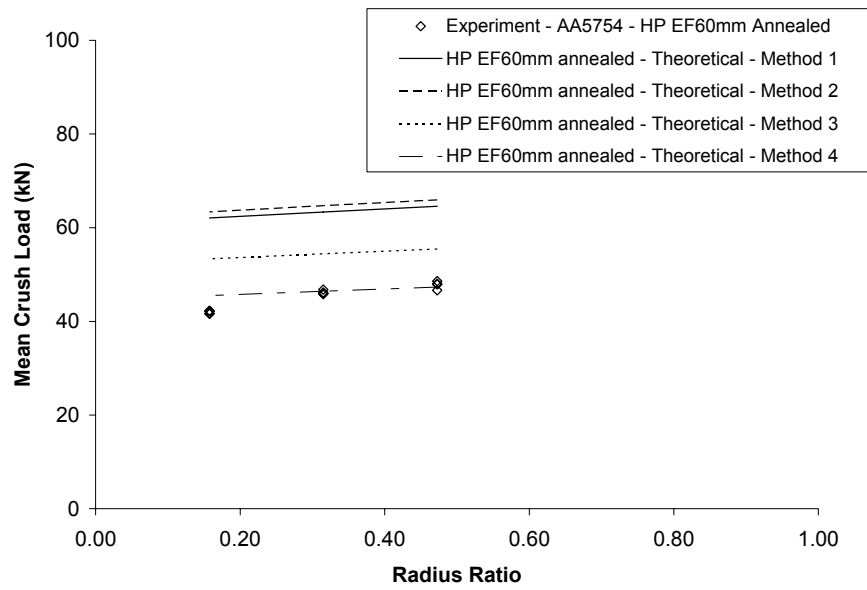
Figure 3.13: Theoretical versus experimental axial crush predictions for annealed AA5754 tubes formed using high pressure hydroforming process
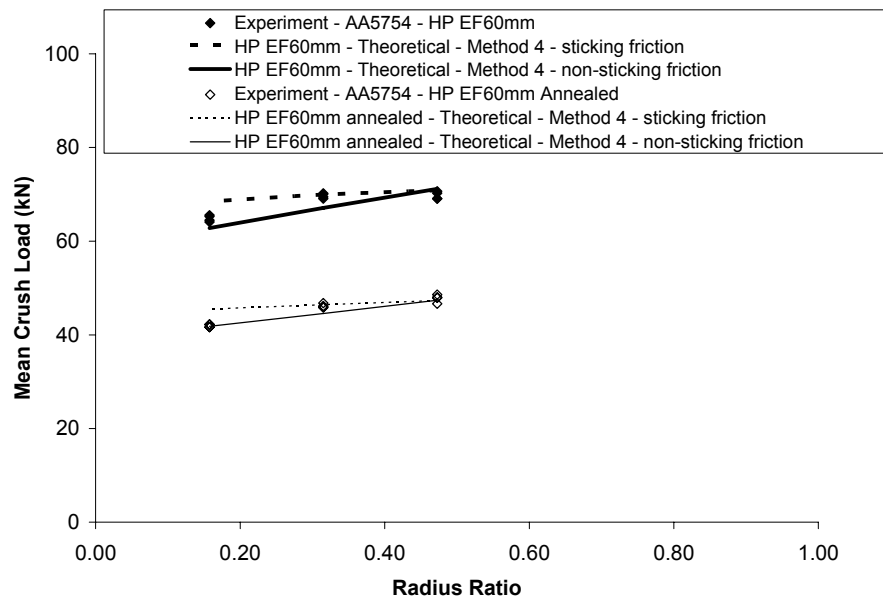
Figure 3.14: Theoretical versus experimental axial crush predictions for AA5754 tubes formed using high pressure hydroforming process, assuming constant thickness

Figure 3.15 shows the results for the low pressure tubes for which the theoretical values were determined based on the data given in Table 3.3. The theoretical calculations based on Method 4 provided reasonable predictions of the experimental data.
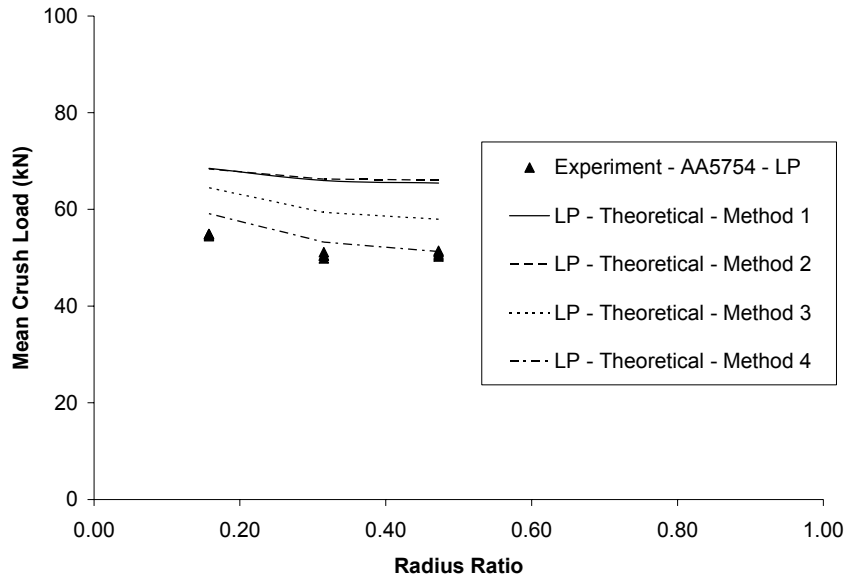
Figure 3.15: Theoretical versus experimental axial crush predictions for AA5754 tubes formed using low pressure hydroforming process

The results show that a reasonable prediction of the mean load during axial crush can be obtained even when using simplified methods to determine the nominal thickness and work hardening in a cross-section of the hydroformed tube. It should be noted that for different materials, alternative methods for calculating the energy equivalent flow stress might better capture measured data. The actual predicted mean load values can be found in Appendix C.

3.4 Axial Crush Predictions – Axisymmetric versus Non-axisymmetric Crush

Analytical predictions are given in Figure 3.16, considering both the axisymmetric and non-axisymmetric (diamond) modes of folding for a round tube of diameter 38.1 mm, based on the material properties for AA5754 and the above equations. The theoretical predictions were calculated using Equations 1.8 – 1.14 and the mean load values are given in

Appendix C. The energy equivalent flow stress was calculated using Method 4. Also, shown in the figure are the measured mean loads for the non-hydroformed tubes. The predictions show that tubes which deform in the diamond mode have a significantly higher mean load than tubes that deform in an axisymmetric manner. Most of the non-hydroformed tubes deformed with a non-axisymmetric crush mode (Figure 2.24) such that it was expected that the diamond mode predictions best captured the experimental results.
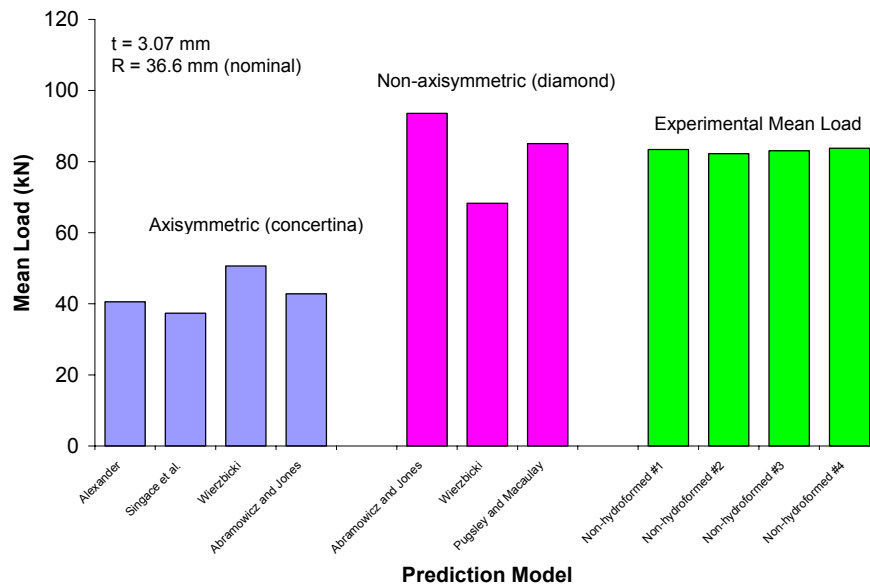
Figure 3.16: Measured crush response and theoretical predictions for a round tube

The theoretical equations presented above for circular tubes can then be used with Equation 1.16 to determine the expected change in energy absorption for crush of a tube formed using the low pressure hydroforming process relative to the energy absorption of the original round tube. The theoretical predictions for per cent change in mean load between a hydroformed and non-hydroformed, circular tube are given in Figure 3.17. The prediction for the hydroformed tube was based on an AA5754 alloy tube with a 65.5 mm cross-section formed using the low pressure process to a corner radius of 12 mm. The results show that when using the diamond mode equations to predict the behaviour of the round tube, reductions in the mean load can be expected in the range of 22% to 43% for the square tubes, relative to the round tubes. This corresponds to the measured drop in mean load in the experiments, which was about 40%. Hence, the drop in mean load between the low pressure

81

and high pressure experiments was realistic. However, if the axisymmetric equations are used, then most of the equations actually predict a large increase in the energy absorption during crash, which was not realistic.
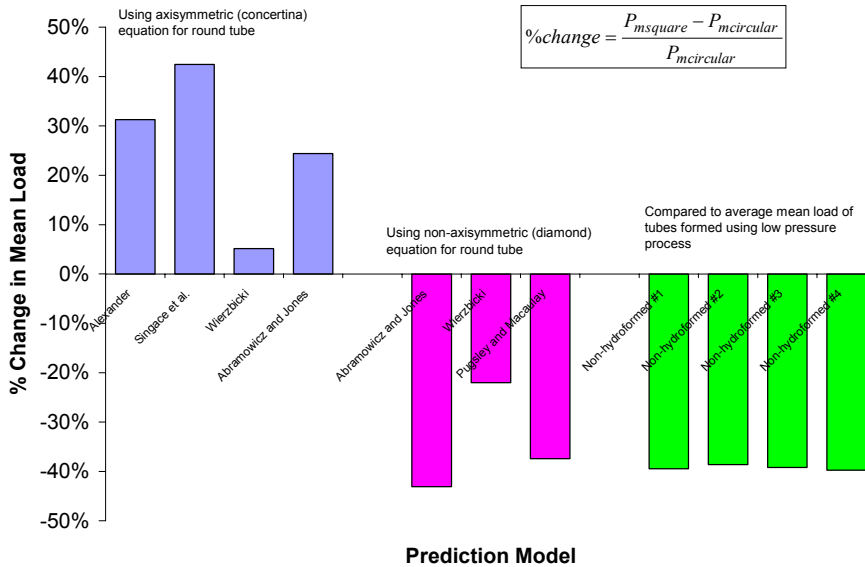
Figure 3.17: Comparison of per cent change in mean load between non-hydroformed, circular tubes and tubes formed using the low pressure hydroforming process

Figure 3.18 shows the predicted and measured per cent change in mean load between non-hydroformed circular tubes and tubes formed to a corner radius of 12 mm using high pressure hydroforming with 60 mm of end-feed. The results also show that the measured response is better predicted when using the diamond mode equations compared to the axisymmetric equations. In this case, the reduction in mean load was about 16%.
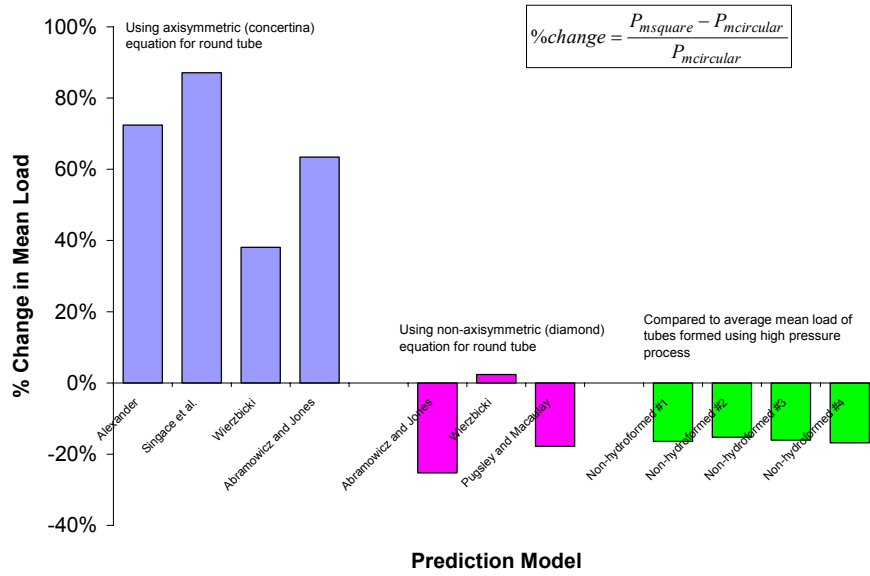
Figure 3.18: Comparison of per cent change in mean load between non-hydroformed, circular tubes and tubes formed using the high pressure hydroforming process

Chapter 4 – Finite Element Models

This chapter presents details regarding the development of the finite element models, including the implementation of the constitutive models required to describe the deformation behaviour of the material. These constitutive models include the von Mises yield criterion, a non-linear isotropic-kinematic hardening model, the Johnson-Cook strain sensitive model, the Yld2000-2d anisotropic model, and the Gurson-Tvergaard-Needleman constitutive model. Also, details are provided regarding the implementation of a model combining the effects of kinematic hardening, anisotropy, and strain-rate effects. Each of the models were implemented for use in the explicit dynamic finite element code, LS-DYNA. Details are then provided concerning the development of the finite element models required to describe the hydroforming and impact operations.

4.1 Implementation of Constitutive Material Models

The von Mises yield criterion is widely used to study the deformation behaviour of metal alloys. However, most alloys rarely conform exactly to the behaviour predicted by this criterion, such that it is important to study alternative constitutive models that capture the material's non-linear deformation behaviour.

Since the tubes were impacted at initial velocities of about 7 m/s, the effects of strain-rate should be considered. In this research, the Johnson-Cook constitutive model was utilized in the finite element models to describe the strain-rate effects.

Kinematic hardening models are often adopted when a material experiences reverse loading. In the current research, end-feeding was used during the high pressure hydroforming process which resulted in compressive strains along the longitudinal direction of the tube. During impact, these compressed sections would undergo bending, during which the outer surface of the fold experiences tension. Hence, the material was subjected to reverse loading from compression to tension. In this research, a non-linear isotropic-kinematic hardening model was used to study the influence of kinematic hardening on the predicted energy absorption during crash.

Since aluminum sheet alloys generally have *r*-values less than unity, anisotropy may have an effect on the predicted energy absorption during crash. The Yld2000-2d anisotropic constitutive model was used in this study to compare the predicted axial crush response to the measured data.

A model combining the effects of strain-rate, kinematic hardening, and anisotropy was also developed and implemented in the finite element simulations. This model was used to study the influence of each of the three effects separately, followed by a study of the combined effects.

The Gurson-Tvergaard-Needleman damage model can predict the development of damage and failure based on void growth, nucleation, and coalescence. This model was considered in the current research to determine if voids (porosity) had a significant influence on the predicted energy absorption characteristics during crash.

4.1.1 Isotropic Material Behaviour

The von Mises yield criterion can be expressed by,

$$\phi = \sqrt{\frac{3}{2}\sigma'_{ij}\sigma'_{ij}} - \overline{\sigma} = 0 \tag{4.1}$$

where, σ'_{ij} is the deviatoric stress tensor and $\overline{\sigma}$ is the isotropic flow stress. At the beginning of the stress update procedure in LS-DYNA the increment in total strain, $d\varepsilon_{ij}$, is used to calculate the trial stresses, $\sigma_{ij}{}^{T}$ according to,

$$\sigma_{ij}^{T} = \sigma_{ij}^{n} + C_{ijkl}^{e} d\varepsilon_{kl} \tag{4.2}$$

where σ_{ij}^{n} is the stress state at the beginning of the time step, n, and C_{ijkl}^{e} is the elastic stiffness tensor. If,

$$\sqrt{\frac{3}{2}\sigma_{ij}'^{T}\sigma_{ij}'^{T}} \leq \overline{\sigma} \tag{4.3}$$

is true, then the stresses are within the elastic region such that the effective plastic strain for the time step is zero and the stresses for the next time step are given by,

$$\sigma_{ij}^{n+1} = \sigma_{ij}^{T} \tag{4.4}$$

However, if false, then the stresses must be returned to the yield surface. For the von Mises yield surface, a radial return method can be utilized, as depicted in deviatoric stress space in Figure 4.1. The stresses must be returned along the normal to the yield surface, n_{ij} which is given by [93],

$$n_{ij} = \frac{3\sigma_{ij}'}{2\overline{\sigma}} \tag{4.5}$$

The stress state lying on the yield surface which is used for the start of the next time increment is then given by [94],

$$\sigma_{ij}^{n+1} = \frac{\overline{\sigma}}{\sqrt{\frac{3}{2}\sigma_{ij}'^{T}\sigma_{ij}'^{T}}}\sigma_{ij}'^{T} + \frac{\sigma_{kk}^{n}}{3} \tag{4.6}$$

The equations used to calculate the increment of effective plastic strain are given below in Section 4.1.6. In the current research, the piecewise linear isotropic plasticity model in LS-DYNA [94] was used to perform all simulations involving von Mises yielding. The isotropic hardening behaviour of the AA5754 aluminum alloy tube was described using Equation 2.2 and the data in Figure 2.5 was used to describe the behaviour of the EN-AW 5018 tube alloy.
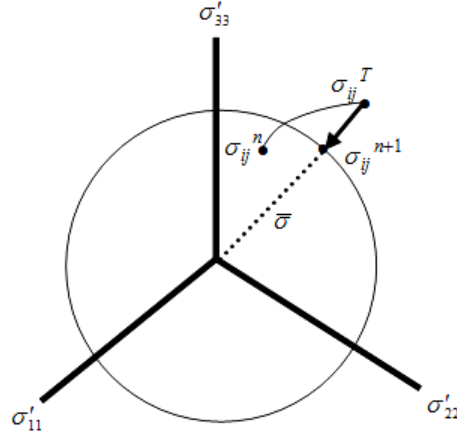
Figure 4.1: Radial return method for von Mises yielding

4.1.2 Johnson-Cook Strain-Rate Model

A Johnson-Cook material model is available in LS-DYNA based on the power law type hardening given in Equation 1.36. However, the four parameter Voce-type hardening law given by Equation 2.2 was used in the current research to describe the behaviour of the AA5754 alloy tube. As a result, a modified version of the Johnson-Cook equation was considered, given by,

$$\overline{\sigma} = \left[a - \left(a - \sigma_y\right)\exp\left(-b\overline{\varepsilon}^{p^c}\right)\right]\left[1 + C_{JC}\ln\frac{\dot{\overline{\varepsilon}}^p}{\dot{\varepsilon}_0}\right]\left[1 - \left(\frac{T - T_{room}}{T_{melt} - T_{room}}\right)^m\right] \quad (4.7)$$

where a reference strain-rate of 0.0033 s^{-1} (quasi-static) was used to determine the parameters a, b, c, and σ_y. Consequently, a user-defined material model (UMAT) for the stress update developed by Simha [95] was used for the axial crush simulations.

The same equations described in Section 4.1.1 were used with this user-subroutine. However, Equation 4.7 was used in place of Equation 2.2 to describe the hardening behaviour of the material. The effective plastic strain-rate, $\dot{\overline{\varepsilon}}^p$, from the previous time step was used in Equation 4.7, which is a reasonable assumption for an explicit implementation.

The rise in temperature (ΔT) due to plastic deformation at high rates was described by [49],

$$\Delta T = \beta \frac{1}{\rho C_P} \int \sigma_{ij} d\varepsilon_{ij}{}^P \tag{4.8}$$

where β is the fraction of plastic work that is converted into heat, C_p is the specific heat capacity, ρ is the density, $\varepsilon_{ij}{}^P$ is the plastic strain, and σ_{ij} is the stress state. Although, it has been shown by Rosakis et al. [96] that β depends strongly on both strain and strain rate, the current work assumed a value of unity. In reality, β should be less than unity since the material undergoes work hardening.

4.1.3 Non-Linear Isotropic-Kinematic Hardening Model

The yield function for the non-linear isotropic-kinematic hardening model, outlined in Chapter 1, is expressed by [43],

$$\phi = \sqrt{\frac{3}{2}(\sigma'_{ij} - \alpha'_{ij})(\sigma'_{ij} - \alpha'_{ij})} - \sigma^0 = 0 \tag{4.9}$$

with σ'_{ij} as the deviatoric stress of σ_{ij} and α'_{ij} as the deviatoric component of the back stress, α_{ij}. The normal to the yield surface is given by,

$$n_{ij} = \frac{3(\sigma'_{ij} - \alpha'_{ij})}{2\sigma^0} \tag{4.10}$$

The radius of the yield surface, σ^0 is given by,

$$\sigma^0 = \overline{\sigma}_{iso} - \overline{\alpha} \tag{4.11}$$

where, $\overline{\sigma}_{iso}$ is the isotropic yielding behaviour (Equation 2.2) and,

$$\overline{\alpha} = \frac{C_{kin}}{\gamma}\left[1 - \exp\left(-\gamma \overline{\varepsilon}^P\right)\right] \tag{4.12}$$

where C_{kin} and γ are material constants requiring calibration. The increment of the back stress, $d\alpha_{ij}$, was described using [45,46],

$$da_{ij} = \frac{C_{kin}}{\sigma^0}\left(\sigma_{ij} - \alpha_{ij}\right)d\bar{\varepsilon}^P - \gamma\alpha_{ij}d\bar{\varepsilon}^P \qquad (4.13)$$

where, $d\bar{\varepsilon}^P$ is the increment in effective plastic strain. The method used to implement this constitutive model as a user-defined subroutine in the current research was similar to the method of implementation for the von Mises yield criterion described above.

In order to return the stress state to the yield surface, both the location of the yield surface and the size of the yield surface will change. However, in this research the stress update was calculated based only on the location of the yield surface at the beginning of the time step, $\alpha_{ij}{}^n$. That is, the location of the yield surface was held constant during the stress return [97], as depicted in Figure 4.2. This was deemed a reasonable assumption for an explicit solution and will be further addressed in Chapter 5. With this assumption, the radial return method can then be implemented to return the stress to the yield surface according to,

$$\sigma_{ij}{}^{n+1} = \frac{\sigma^0}{\sqrt{\frac{3}{2}(\sigma_{ij}'^{T} - \alpha_{ij}'^{n})(\sigma_{ij}'^{T} - \alpha_{ij}'^{n})}}(\sigma_{ij}'^{T} - \alpha_{ij}'^{n}) + \alpha_{ij}'^{n} + \frac{\sigma_{kk}{}^{n}}{3} \qquad (4.14)$$
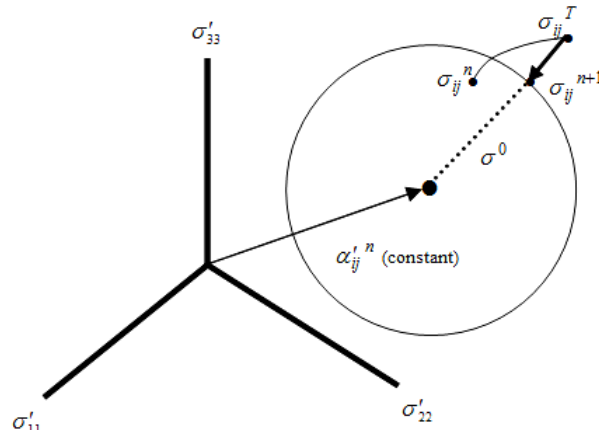
Figure 4.2: Return method for kinematic hardening model assuming that the location of the yield surface is constant during the stress return

The location of the yield surface was then updated at the end of the time step using Equation 4.13 to calculate the increment in the location of the yield surface such that,

$$\alpha_{ij}{}^{n+1} = \alpha_{ij}{}^{n} + d\alpha_{ij}{}^{n+1} \tag{4.15}$$

The UMAT should only be used for explicit solutions since α_{ij} is held constant during the stress return scheme [97] which is a valid assumption assuming small strain increments. Further validation of this assumption is discussed in Chapter 5 after the calibration parameters for the model have been presented. Also, the UMAT provided the location of the yield surface, α_{ij}, at the end of a simulation (hydroforming) which could then be used as input to the next simulation (impact).

4.1.4 Yld2000-2d Anisotropic Model

The plane stress yield criterion developed by Barlat et al. [39,40], referred to as Yld2000-2d, was used to describe the anisotropic behaviour of the AA5754 alloy. The yield function in the model can be expressed by,

$$\phi = \left(\frac{\phi' + \phi''}{2}\right)^{1/a} - \overline{\sigma} = 0 \tag{4.16}$$

where,

$$\phi' = \left| X_1' - X_2' \right|^{a} \qquad \phi'' = \left| 2X_2'' + X_1'' \right|^{a} + \left| 2X_1'' + X_2'' \right|^{a} \tag{4.17}$$

with recommended values of $a=8$ for FCC materials and $a=6$ for BCC materials. The X's are principal values of X_{ij}' and X_{ij}'' defined by,

$$X_{ij}' = L_{ijkl}' \sigma_{kl} \qquad X_{ij}'' = L_{ijkl}'' \sigma_{kl} \tag{4.18}$$

where for plane stress, the terms in transformation tensor, L_{ijkl} are given by,

$$\begin{bmatrix} L_{1111}' \\ L_{1122}' \\ L_{2211}' \\ L_{2222}' \\ L_{1212}' \end{bmatrix} = \begin{bmatrix} 2/3 & 0 & 0 \\ -1/3 & 0 & 0 \\ 0 & -1/3 & 0 \\ 0 & 2/3 & 0 \\ 0 & 0 & 1 \end{bmatrix} \begin{bmatrix} \alpha_1 \\ \alpha_2 \\ \alpha_7 \end{bmatrix} \tag{4.19}$$

$$
\begin{bmatrix} L''_{1111} \\ L''_{1122} \\ L''_{2211} \\ L''_{2222} \\ L''_{1212} \end{bmatrix} = \frac{1}{9} \begin{bmatrix} -2 & 2 & 8 & -2 & 0 \\ 1 & -4 & -4 & 4 & 0 \\ 4 & -4 & -4 & 1 & 0 \\ -2 & 8 & 2 & -2 & 0 \\ 0 & 0 & 0 & 0 & 1 \end{bmatrix} \begin{bmatrix} \alpha_3 \\ \alpha_4 \\ \alpha_5 \\ \alpha_6 \\ \alpha_8 \end{bmatrix}
$$

such that there are eight α coefficients to be determined from tensile testing of the sheet material at 0°, 45°, and 90° relative to the rolling direction and the biaxial yield stress.

The principle values of X' and X'' are calculated using,

$$
X_1 = \frac{1}{2}\left(X_{11} + X_{22} + \sqrt{(X_{11} - X_{22})^2 + 4X_{12}{}^2} \right)
$$

$$
X_2 = \frac{1}{2}\left(X_{11} + X_{22} - \sqrt{(X_{11} - X_{22})^2 + 4X_{12}{}^2} \right) \tag{4.20}
$$

under plane stress conditions.

In order to return the stresses to the yield surface during the stress update in the finite element code, the following equations are required [40, 98]. The stress state can be described by,

$$
\sigma_{ij}{}^{n+1} = C^e_{ijkl}(d\varepsilon_{ij} - d\varepsilon_{ij}{}^P) \tag{4.21}
$$

where, $d\varepsilon_{ij}$ is the total strain increment and $d\varepsilon_{ij}{}^P$ is the plastic strain increment which can be described using the associated flow rule,

$$
d\varepsilon_{ij}{}^P = d\lambda \frac{d\phi}{d\sigma_{ij}} \tag{4.22}
$$

where $d\lambda$ is the plastic multiplier and $d\phi/d\sigma_{ij}$ is the normal to the yield surface. It has been shown by Yoon et al. [40] that since $\bar{\sigma}(\sigma_{ij})$ is a first order homogeneous function, the plastic multiplier is equivalent to the increment in plastic strain, $d\bar{\varepsilon}^P$ according to,

$$
d\bar{\varepsilon}^P = \frac{\sigma_{ij} d\varepsilon_{ij}{}^P}{\bar{\sigma}} = \frac{\sigma_{ij} d\lambda \, d\bar{\sigma}/d\sigma_{ij}}{\bar{\sigma}} = \frac{d\lambda \bar{\sigma}}{\bar{\sigma}} = d\lambda \tag{4.23}
$$

where, $\bar{\sigma}(\sigma_{ij}) = \sigma_{ij}\, d\bar{\sigma}(\sigma_{ij})/d\sigma_{ij}$ is a property of the homogeneous function. Equation 4.21 then becomes,

$$\sigma_{ij}^{\ n+1} = C_{ijkl}^e d\varepsilon_{kl} - d\bar{\varepsilon}^P C_{ijkl}^e \frac{d\bar{\sigma}}{d\sigma_{ij}} \tag{4.24}$$

where the normal to the yield surface, $d\bar{\sigma}/d\sigma_{ij}$, has been presented by Yoon et al. [40] and is not presented in this thesis due to brevity. The increment in effective plastic strain is calculated based on the equations given below in Section 4.1.6.

This research utilized the user-defined subroutine for the stress update developed by Abedrabbo et al. [99] for all simulations incorporating the Yld2000-2d anisotropic model. In this subroutine, the stress is returned to the yield surface in a number of increments, s, during each time step, n, as depicted in Figure 4.3. The state of stress for each increment is calculated according to,

$$\sigma_{ij}^{\ s+1} = \sigma_{ij}^{\ s} - d\lambda^s C_{ijkl}^e \frac{d\bar{\sigma}}{d\sigma_{ij}^{\ s}} \tag{4.25}$$

which is then used to check whether or not,

$$\left| f(\sigma_{ij}^{\ s+1}) - \bar{\sigma}(\bar{\varepsilon}^{p\,s+1}) \right| \leq tolerance \tag{4.26}$$

with,

$$\bar{\varepsilon}^{p\,s+1} = \bar{\varepsilon}^{p\,s} + d\lambda^s \tag{4.27}$$

Once the required tolerance has been achieved, the increment in effective plastic strain and stress state for the next time step, are given by $\bar{\varepsilon}^{p\,n+1} = \bar{\varepsilon}^{p\,s+1}$ and $\sigma_{ij}^{\ n+1} = \sigma_{ij}^{\ s+1}$. It should be noted that the normal to the yield surface is recalculated for each increment. This return method has often been referred to as the cutting-plane algorithm [99].

Since the Yld2000-2d anisotropic model was developed for plane stress conditions, the total strain increment in the thickness direction, $d\varepsilon_{zz}$, given by [99],

92

$$d\varepsilon_{zz} = \frac{(d\varepsilon_{xx}{}^{p} + d\varepsilon_{yy}{}^{p}) + \nu(d\varepsilon_{xx} + d\varepsilon_{yy}) - 2\nu(d\varepsilon_{xx}{}^{p} + d\varepsilon_{yy}{}^{p})}{\nu - 1} \tag{4.28}$$

must be provided to the finite element code at the end of the time step, where ν is Poisson's ratio. The plastic strain increments, $d\varepsilon_{xx}{}^{p}$ and $d\varepsilon_{yy}{}^{p}$ are determined by Equation 4.22.
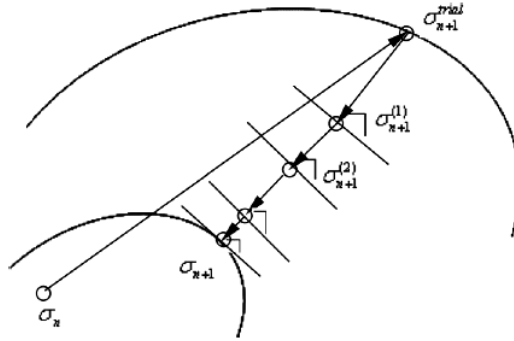
Figure 4.3: Depicted stress return method for Yld2000-2d anisotropic model [99]

4.1.5 Implementation of Combined Constitutive Model

As part of the current research, the user-defined subroutines developed by Simha [95] and Abedrabbo et al. [99] for the Johnson-Cook and Yld2000-2d constitutive models were then combined with the subroutine for the kinematic hardening model developed in the current research in order to study the combined effects of strain-rate, anisotropy, and kinematic hardening. In addition to studying the combined effects, the model allowed each individual effect to be isolated and compared relative to an isotropic prediction. There are several issues that arise when combining strain-rate effects, anisotropy, and kinematic hardening which are discussed below in Chapter 6 after the simulation results have been presented.

The yield function used to described the yielding behaviour for the combined model was given by,

$$\phi = \left(\frac{\phi' + \phi''}{2} \right)^{1/a} - \sigma^0 = 0 \tag{4.29}$$

where,

$$\sigma^0 = \bar{\sigma}_{JC} - \bar{\alpha} \tag{4.30}$$

with Equation 4.7 used to describe the hardening behaviour of the material. It should be noted that strain-rate effects were not considered for the kinematic term, $\bar{\alpha}$. Equation 4.18 becomes,

$$X'_{ij} = L'_{ijkl}(\sigma_{kl} - \alpha_{kl}) \qquad X''_{ijkl} = L''_{ij}(\sigma_{kl} - \alpha_{kl}) \tag{4.31}$$

for the combined model.

The cutting-plane algorithm described in the above section was again implemented to return the stresses to the yield surface, taking into account the modifications to the above equations for the combined model. The normal to yield surface required in Equation 4.25 for the combined model was calculated using the same derivatives developed by Barlat et al. [39] and Yoon et al. [40] for the Yld2000-2d model when Equation 4.31 is implemented in place of Equation 4.18. A similar form of Equation 4.23 can be used for the combined model to show that the increment in effective plastic strain is equivalent to the plastic multiplier according to,

$$d\bar{\varepsilon}^P = \frac{S_{ij}d\varepsilon_{ij}^P}{\sigma^0} = \frac{S_{ij}d\lambda \, d\sigma^0 \big/ d\sigma_{ij}}{\sigma^0} = \frac{d\lambda \sigma^0}{\sigma^0} = d\lambda \tag{4.32}$$

with, $S_{ij} = \sigma_{ij} - \alpha_{ij}$.

As was the case for the user-defined material model described in Section 4.1.3, the combined model assumed that the location of the yield surface, α_{ij}, was constant during the stress return procedure. The location of the yield surface was then updated at the end of the time step, according to Equation 4.15. This assumption was considered reasonable for the explicit implementation and will be further discussed in Chapter 5.

4.1.6 Increment in Effective Plastic Strain

The sections above describe the procedure to return the state of stress to the yield surface. However, as the stresses are returned to the yield surface the increment in effective plastic strain must be calculated. In the combined model, the yield function is a function of the stress state, σ_{ij}, the back stress, α_{ij}, and the effective plastic strain, $\bar{\varepsilon}^p$. The yield function can be linearized with respect to these variables using a Taylor's expansion, giving the expression [97,99,100],

$$0 = \phi^s(\sigma_{ij}, \alpha_{ij}, \bar{\varepsilon}^p) + \frac{\partial \phi^s}{\partial \sigma_{ij}}(\sigma_{ij}^{s+1} - \sigma_{ij}^s) + \frac{\partial \phi^s}{\partial \alpha_{ij}}(\alpha_{ij}^{s+1} - \alpha_{ij}^s) + \frac{\partial \phi^s}{\partial \bar{\varepsilon}^p}(\bar{\varepsilon}^{p\,s+1} - \bar{\varepsilon}^{p\,s}) \quad (4.33)$$

which can then be used to determine the increment in effective plastic strain during an increment, s. As mentioned in the sections above, it was assumed that the location of the yield surface remains constant during the stress return, such that $\alpha_{ij}^{s+1} - \alpha_{ij}^s = 0$. From Equation 4.25,

$$\sigma_{ij}{}^{s+1} - \sigma_{ij}{}^s = -d\lambda C_{ijkl}^e n_{kl} = -d\bar{\varepsilon}^p C_{ijkl}^e n_{kl} \quad (4.34)$$

where, $n_{ij} = d\bar{\sigma}/d\sigma_{ij}$. Also, $\bar{\varepsilon}^{p\,s+1} - \bar{\varepsilon}^{p\,s} = d\bar{\varepsilon}^p = d\lambda$. Substitution of these values in Equation 4.33 yields the following equation to describe the increment in effective plastic strain [99,100],

$$d\bar{\varepsilon}^p = \frac{\phi^s}{\dfrac{\partial \bar{\sigma}^s}{\partial \sigma_{ij}} C_{ijkl}^e \dfrac{\partial \bar{\sigma}^s}{\partial \sigma_{kl}} - \dfrac{\partial \phi^s}{\partial \bar{\varepsilon}^p}} \quad (4.35)$$

where, for the von Mises yield criterion or the kinematic hardening yield function,

$$\frac{\partial \bar{\sigma}}{\partial \sigma_{ij}} C_{ijkl}^e \frac{\partial \bar{\sigma}}{\partial \sigma_{kl}} = 3\mu \quad (4.36)$$

with μ as the shear modulus.

There are five constitutive models presented in the above sections. The following equations were used to determine the increment in effective plastic strain for each of the five models:

Von Mises [94]:
$$d\bar{\varepsilon}^p = \frac{\phi^s}{3\mu + \dfrac{d\bar{\sigma}}{d\bar{\varepsilon}^p}}$$
(4.37)

Johnson-Cook:
$$d\bar{\varepsilon}^p = \frac{\phi^s}{3\mu + \dfrac{d\bar{\sigma}_{JC}}{d\bar{\varepsilon}^p}}$$
(4.38)

Kinematic Hardening [97]:
$$d\bar{\varepsilon}^p = \frac{\phi}{3\mu + \dfrac{d\sigma^0}{d\bar{\varepsilon}^p}}$$
(4.39)

Yld2000-2d [99]:
$$d\bar{\varepsilon}^p = \frac{\phi}{\dfrac{\partial\bar{\sigma}}{\partial\sigma_{ij}} C^e_{ijkl} \dfrac{\partial\bar{\sigma}}{\partial\sigma_{kl}} + \dfrac{d\bar{\sigma}}{d\bar{\varepsilon}^p}}$$
(4.40)

Combined Model:
$$d\bar{\varepsilon}^p = \frac{\phi}{\dfrac{\partial\bar{\sigma}}{\partial\sigma_{ij}} C^e_{ijkl} \dfrac{\partial\bar{\sigma}}{\partial\sigma_{kl}} + \dfrac{d\sigma^0}{d\bar{\varepsilon}^p}}$$
(4.41)

where all values are calculated at the current increment, *s,* in the stress update procedure.

4.1.7 Gurson-Tvergaard-Needleman Damage Model

The yield function for the Gurson-Tvergaard-Needleman damage model which was described in detail in Chapter 1 is given by,

$$\phi = \left(\frac{\sigma_{eq}}{\bar{\sigma}}\right)^2 + 2f^* q_1 \cosh\left(q_2 \frac{3\sigma_{hyd}}{2\bar{\sigma}}\right) - 1 - q_3 f^{*2} = 0$$
(4.42)

The GTN constitutive model was implemented as a user-defined subroutine in LS-DYNA. This computer code was originally developed by Worswick and Pelletier [101] for brick elements. As part of this research, the algorithm was updated to support shell elements [95].

The implementation of the GTN constitutive model is described in detail by Worswick and Pelletier [101]. It should be noted that due to the non-linearity of this yield function, the plastic multiplier, $d\lambda$, cannot be determined explicitly. Worswick and Pelletier [101] solve for the plastic multiplier using a Newton-Raphson scheme.

4.2 Hydroforming Models

All simulations performed in this research were carried out using shell elements for which there is the assumption of plane stress. Mesh sensitivity studies were performed to determine the effect of element type and mesh size. Simulations were performed using a mesh size for the tube of either 2 or 4 mm. The results of these mesh sensitivity studies are presented in Chapter 6. In all cases, there were seven integration points through the thickness of the tubes. In all simulations, the hardening behaviour of the EN-AW 5018 alloy was described using the stress-strain curve provided in Figure 2.5 while the behaviour of the AA5754 alloy was described using Equation 2.2.

4.2.1 Simulation of Low Pressure Hydroforming

There were three components modelled in the low pressure hydroforming simulations: the lower die, the upper die, and the tube itself. Both die halves were meshed using rigid shell elements of approximately 1 x 1 mm size, with the properties of steel being specified for the material, as required by the penalty stiffness based contact algorithms used to control contact between the die halves and the tube. All nodes for the bottom die were constrained and the top die was only allowed to move in the vertical direction. The finite element mesh is shown in Figure 4.4 with a 4 mm mesh size for the tube. The floating end-plugs, shown in Figure 2.8, were not modelled in the simulations since there was no end-feeding during the low pressure process and the end-plugs would not have contributed to the deformation of the tube.

A control-volume approach was used in LS-DYNA to apply the hydroforming pressure using material properties of water for the fluid. During the die closure, the internal tube pressure was specified at 3 MPa. Once the die was closed, the pressure was increased to

the calibration pressure, as discussed in Chapter 2, over a period of about 10 ms. Simulations were performed for the 6, 12, and 18 mm corner radii cases, for the 2 and 3.5 mm EN-AW 5018 alloy tubes and the 3 mm AA5754 alloy tubes, giving a total of nine hydroforming simulations.

upper die (~1x1 mm mesh)

lower die (~1x1 mm mesh)

tube (~4x4 mm mesh)
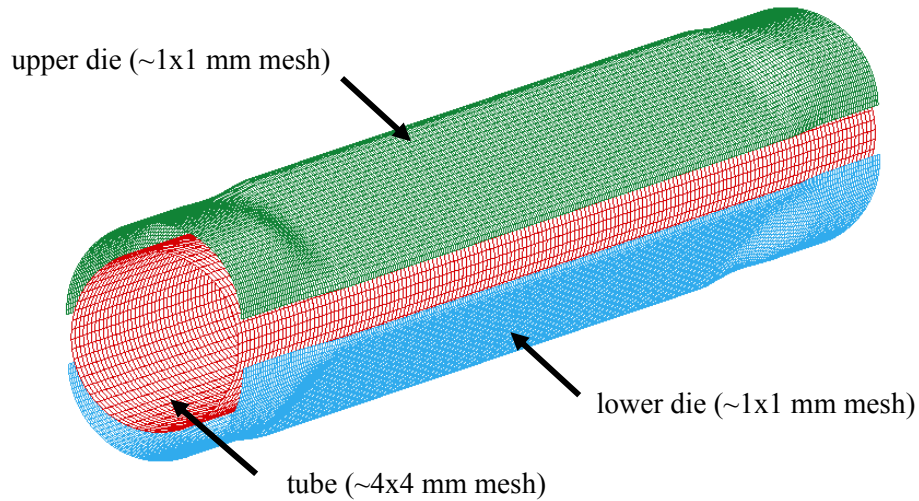
Figure 4.4: Components required for low pressure LS-DYNA simulations

A contour plot of the predicted thickness distribution for an AA5754 alloy tube formed using the low pressure process with a die corner radius of 6 mm is shown in Figure 4.5. All low pressure hydroforming simulations were performed using the von Mises yield criterion with isotropic hardening. The blue contours show that the thickness was reduced from 3.07 mm to 2.99 mm while in the corners of the tube the red contours show that the thickness increased to 3.2 mm. Overall, the thickness throughout the section remains relatively unchanged from 3.07 mm, which was the case for all of the tubes formed using the low pressure process.
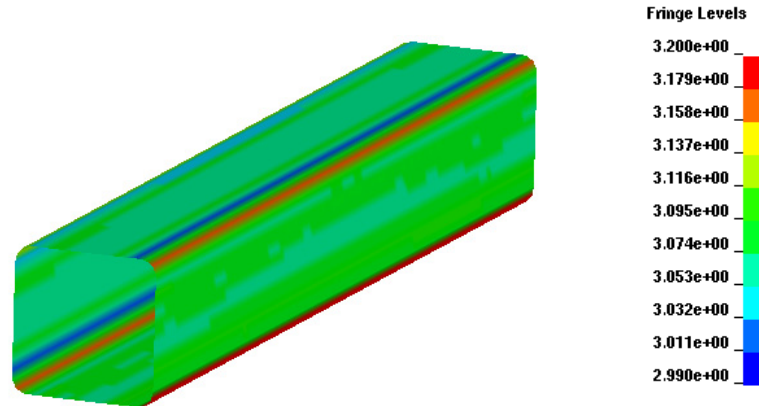
Figure 4.5: Contour plot of thickness change for AA5754 alloy tube formed using low pressure hydroforming process

4.2.2 Simulation of High Pressure Hydroforming

The high pressure simulations were similar to the low pressure simulations, except that instead of two die halves, the high pressure dies were modelled as a single mesh, as shown in Figure 4.6a. For the finite element models of the high pressure process which utilized end-feeding, the actuators were modelled in order to prevent unrealistic thickness changes at the ends of the tube during the simulation [75]. The mesh shown in Figure 4.6b was used to represent the end-feed actuators which were treated as rigid. During the simulations of the high pressure process for the AA5754 alloy tubes, the end-feed displacement and internal tube pressure were applied versus time and matched the experimental profiles, described in Chapter 2. Simulations involving the EN-AW 5018 aluminum alloy tubes did not include the floating end-plugs in the models, since there was no end-feeding.

Figure 4.7 shows contour plots of the effective plastic strain and thickness changes for an AA5754 alloy tube with a 6 mm corner radius formed using the high pressure process with 60 mm of end-feed. The simulation shown was performed using the von Mises yield criterion with isotropic hardening. The results show that the strains and thicknesses remain reasonably uniform along the length of the tube. The largest effective strain value was about 0.68 while the thinnest point of the cross-section was predicted to be 2.63 mm.

a)   b)
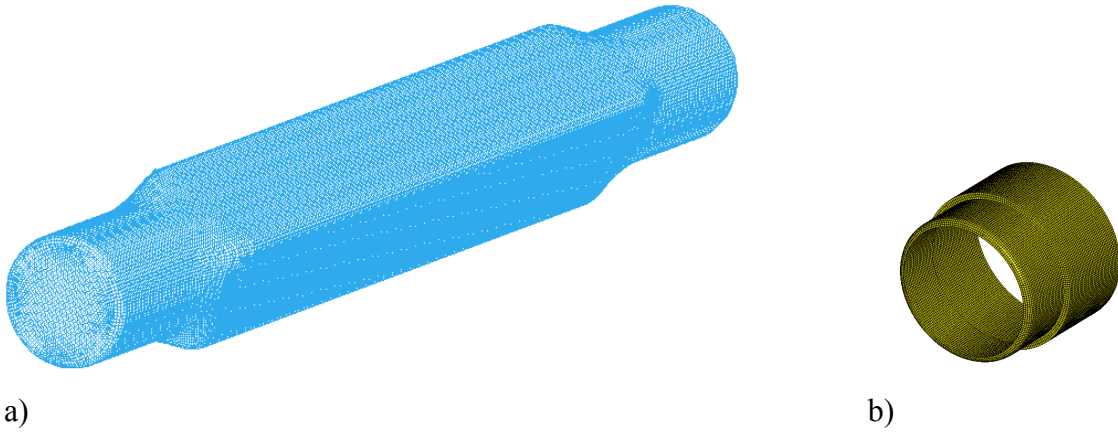
Figure 4.6: Mesh geometry for a) high pressure die with a 6 mm corner-fill radius and b) end-feed actuator

a)   b)
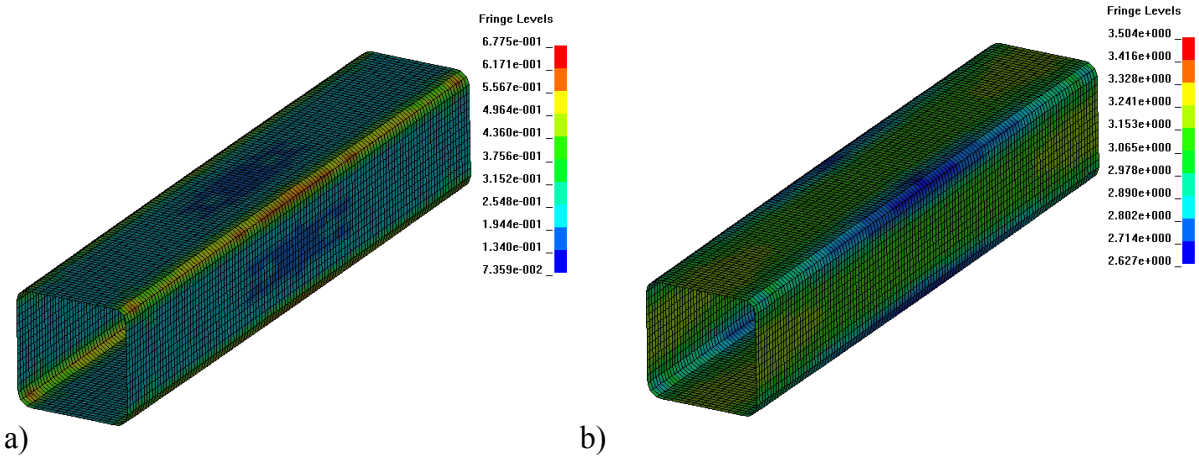
Figure 4.7: Contour plot of predicted a) circumferential strain and b) thickness for a tube formed to a 6 mm corner radius with 60 mm of end-feed

4.3 Fold Initiator Model

The changes in thickness, work hardening, and residual stresses from the hydroforming simulation were transferred forward to an implicit springback simulation. After springback, a simulation was then performed to model forming of the crush initiators. The simulations developed to form the fold initiators in the tube were based on the

components shown in Figure 2.12. The meshes used to model the indenter, die, and deformed tube are shown in Figure 4.8. Each fold initiator was created by forcing the indenter against the tube, creating an indent with a depth of approximately 5 mm. After a second springback simulation, the forming history was then transferred forward to the impact simulation.
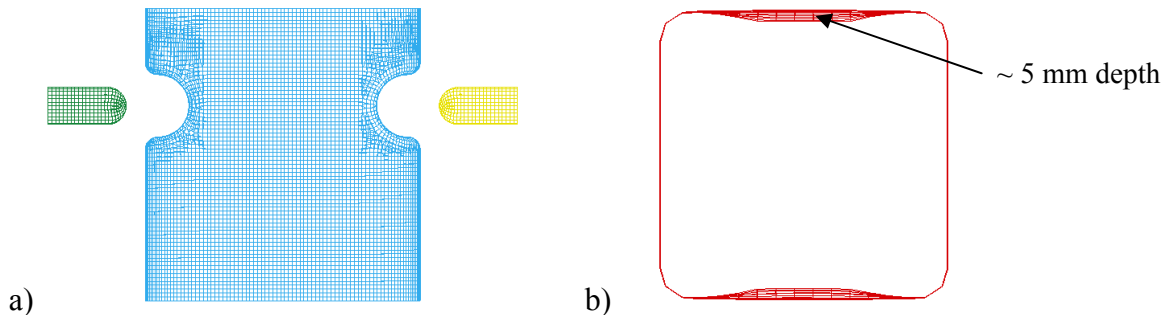
Figure 4.8: a) Mesh geometry of components used to model the fold initiators and b) meshed tube with fold initiators

4.4 Axial Crush Impact Model

A rigid wall was used to simulate the face of either the drop platform or sled-track impact mass in the impact models. The mass and impact velocity specified for the rigid wall corresponded to the experimental values for each test simulated. A second rigid wall was used at the bottom of the tube to prevent the tube from deforming past the bottom plane during the simulation. All nodes along the bottom edge of the tube were fully constrained and all nodes along the top edge were only allowed to move in the vertical direction. The geometry and masses of the aluminum plates welded to the tubes, the support clamps, and rubber pad used in the experiments were not taken into account in the simulations, but these issues will be addressed below in Section 4.5.

Figure 4.9 shows the predicted crush pattern of AA5754 alloy tubes formed using the low pressure and high pressure hydroforming operation with a 6 mm corner radius. The high pressure tube was formed using 60 mm of end-feed. The figure shows that the crush response was similar to the observed folding behaviour (also shown). The predicted crush

force and displacement versus time for the 6 mm tube formed using the high pressure process is presented in Figure 4.10, showing that the impact duration was less than 70 ms. The crush force versus displacement response is shown in Figure 4.11. The mean crush force versus displacement response was determined by taking the energy absorbed (area under the curve) at a given crush distance and then dividing this value by the corresponding crush distance. Most of the results presented in Chapter 6 are based on the mean load taken at a crush distance of 200 mm. In some cases, the maximum crush distance was slightly less than 200 mm such that the mean load was taken at the maximum crush distance.
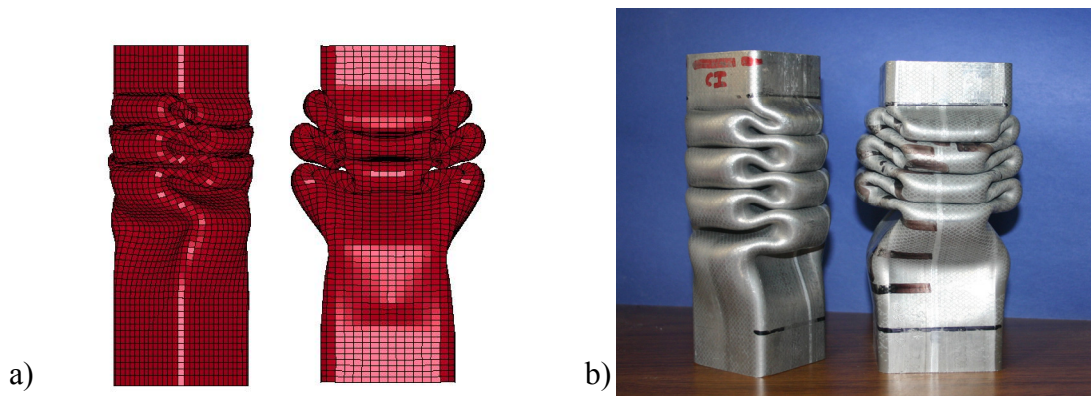
Figure 4.9: a) Predicted and b) Experimental folding behaviour for tubes formed using the low (left) and high (right) pressure hydroforming operation
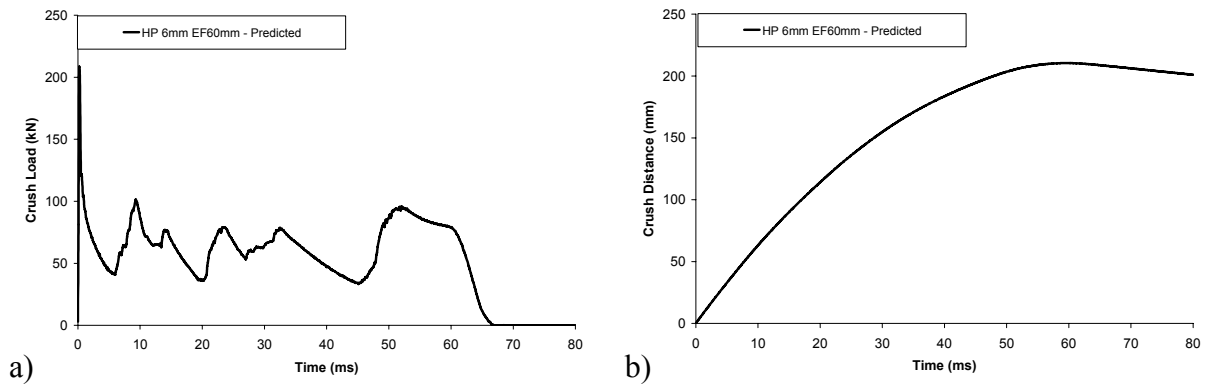
Figure 4.10: a) Predicted crush load versus time and b) predicted crush distance versus time for a tube with a 6 mm corner radius formed using the high pressure process
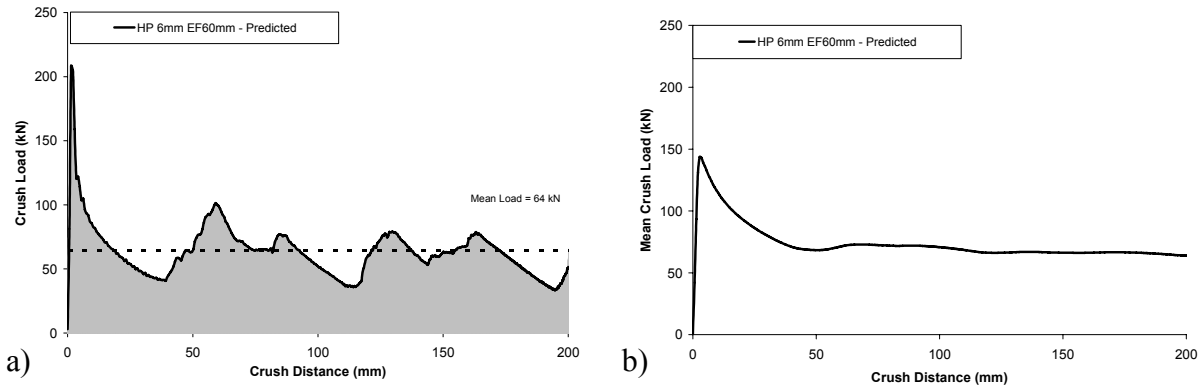
Figure 4.11: a) Predicted crush load versus distance and b) mean crush load versus distance for a tube with a 6 mm corner radius formed using the high pressure process

4.5 Axial Crush Apparatus – Structural Vibrations

Figure 4.12 shows the predicted and measured crush response of tubes formed using the low pressure hydroforming process with a corner radius of 6 mm, plotted to a crush distance of 100 mm. The figure shows that there were several oscillations in the measured data that were not predicted in the finite element simulations. These oscillations were seen in all of the measured axial crush data. Consequently, it was deemed necessary to determine the cause of the oscillations.

In the experiments, the crush force was measured using load cells beneath the tube arranged in a triangular pattern (Figure 1.5), whereas in the simulations the load was based on the reaction forces generated by the moving rigid wall impacting the specimen. In order to try and capture the load cell response, a simulation was performed incorporating a simplified version of the load cell arrangement, as shown in Figure 4.13. The clamps, plates, and rubber pad used in the experiments were all modelled. The simulations were based on the impact of a tube with a 6 mm corner radius formed using the low pressure hydroforming process.
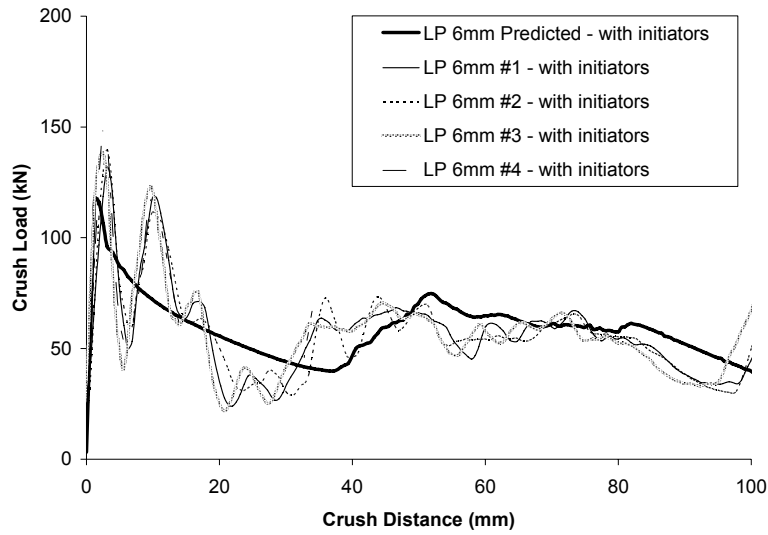
Figure 4.12: Crush response of AA5754 tubes formed to 6 mm radius using low pressure hydroforming process
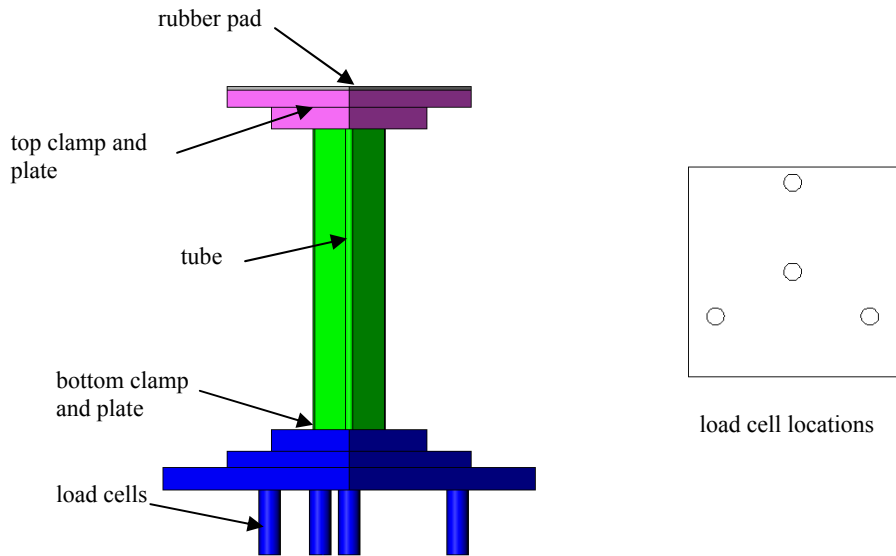
Figure 4.13: Model of impact simulation incorporating simplified geometry used to represent load cells

The bottom clamp, bottom plate, and load cells were all modelled as a single component to eliminate contact issues. That is, as a single contiguous finite element mesh with the same material properties assigned to each component. The load cells were taken to

be rods of 25.4 mm diameter and 76.2 mm length. The top clamp and plate were also modelled as a single component. A solid mesh and an elastic material model were used to describe these components in the simulations using the properties of steel. In the experiments, the plates were aluminum, but were modelled as steel in the simulations to create a single component to avoid contact issues. The 5 mm thick rubber pad which was used in the experiments was modelled using brick elements in the simulation with a linear elastic modulus of 2800 MPa and density of 1100 kg/m^3. Contact definitions were created between the tube and the clamps to prevent unrealistic movement of the tube during the simulations. The nodes along the bottom edge of the 76.2 mm length rods were fully constrained. In order to capture the response of the load cells, the forces acting on the nodes along the bottom edge of these rods were analysed in the simulations.

Figure 4.14 shows the predicted crush forces from the nodal loads along the bottom edges of the rods, the reaction force at the rigid wall that simulated the impact platform, and the corresponding results measured from the experiments, all plotted versus time. The figure shows that there are several large oscillations in the force acting on the rods (load cells) with a period similar to that of the oscillations measured in the experiments. Whereas the oscillations in the experiment dissipated over time, the magnitude of the oscillations in the simulations do not decrease over time indicating that the simulations were under-damped. One cause of this might be that the rubber pad was modelled as linear. The figure also shows an enlarged view of the nodal force curve, showing several high frequency oscillations, of smaller magnitude, with a period of about 0.05 ms. The natural frequency of a spring-mass system can be calculated using,

$$\omega = \sqrt{\frac{AE/l}{m}} \tag{4.43}$$

where, A is the area of the rods, E is the elastic modulus of the rods, l is the length of the rods, and m is the mass of the rods. The period corresponding to the natural frequency was calculated to be 0.093 ms, which is slightly greater than the period of the high frequency oscillations shown in Figure 4.14.

The mass of the impact platform on the sled-track would have affected the frequency and magnitude of oscillations in the data. Therefore, it is suggested that the oscillations

105

measured with the load cells were due to structural vibrations in the system. The actual experimental setup would act as a damper such that the oscillations would decrease over time as seen in Figure 4.12. This damping effect would not have been captured in the simulations because the impact platform and all of the connections in the setup were not modelled.
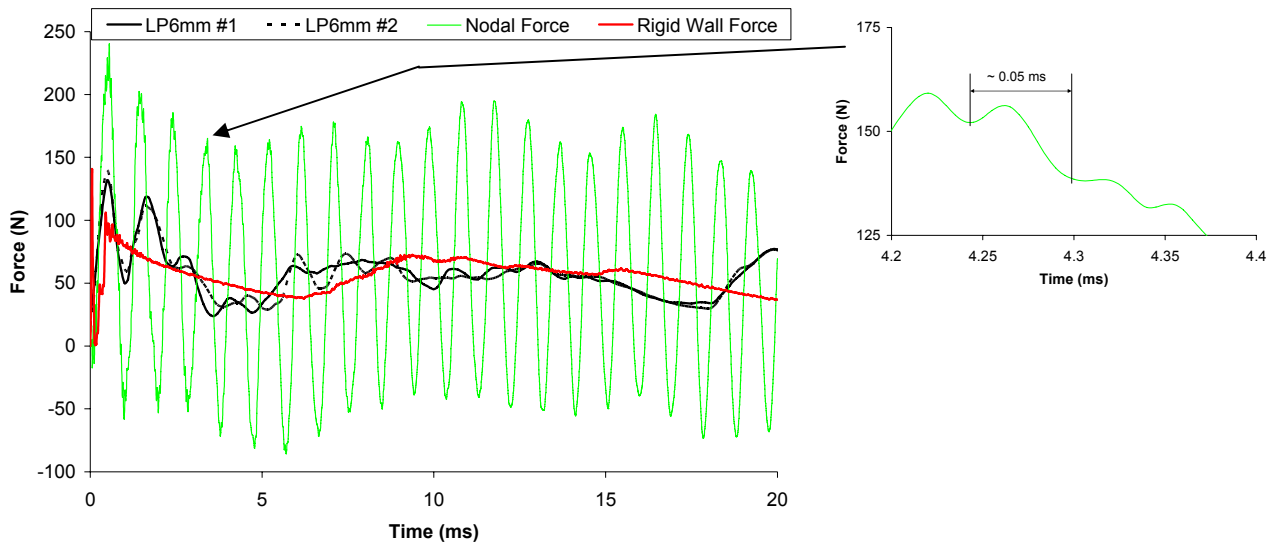
Figure 4.14: Axial crush simulation showing structural vibration

It appears that the oscillations in the measured data were confined primarily to the load cells and that the oscillations are not expected to affect the overall energy absorption calculated for the tube, since the oscillating nature of the results still allow an accurate mean load to be determined. Future research should consider filtering the impact data to remove the oscillations.

The balance of the finite element models presented in this thesis are from shell element meshes utilizing rigid walls to represent the impact mass and load cells. It is recognized that the high frequency oscillations present in the measured response will not be captured in such models. However, the predicted mean crush forces are representative of the measured mean crush forces.

Chapter 5 – Material Characterization

This chapter discusses the calibration of the material coefficients required as input parameters for the finite element simulations. The calibration was accomplished using both experimental and numerical results. All parameters were calibrated for the AA5754 alloy except for the coefficient of friction that was required in the hydroforming simulations, which was based on data from the EN-AW 5018 alloy.

5.1 Coefficient of Friction

HydroDraw 625, a solid-film lubricant, was used in all of the hydroforming experiments. The lubricant was sprayed onto the tube and allowed to dry prior to testing. Twist-compression tests [102,103] were performed in which a tooling steel sample was revolved at four rotations per minute on a sample of EN-AW 5018 sheet alloy at a pressure of 48.2 MPa. The circular P20 steel sample had an outside diameter of 25.4 mm and an inside diameter of 19.1 mm, leading to an effective sliding distance of 4.65 mm/s. The results of three twist compression tests are presented in Figure 5.1. As shown in Figure 2.15, the maximum end-feed level during the hydroforming operation was about 60 mm. However, for the majority of the sliding distance, the internal tube pressure was less than 48.2 MPa. The average coefficient of friction for the three tests, up to a 60 mm sliding distance, was about 0.05. This value was utilized in the hydroforming simulations for both the EN-AW 5018 and AA5754 alloys. A more thorough investigation could be performed in future research that would study the behaviour of the lubricant for a range of pressures. A

coefficient of friction should be determined as a function of both pressure and sliding distance which could then be incorporated in the finite element simulations.
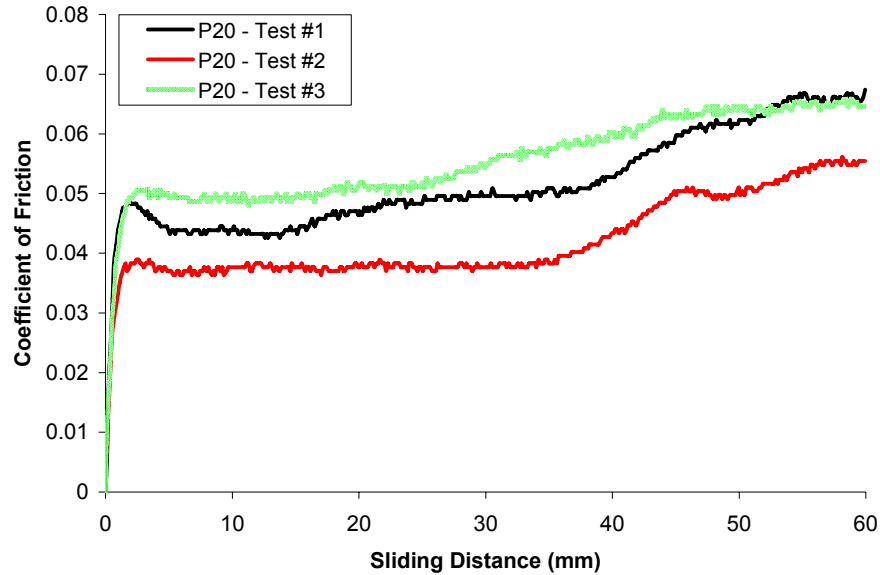
Figure 5.1: Coefficient of friction from twist-compression tests of HydroDraw 625 lubricant with EN-AW 5018 aluminum alloy sheet and P20 steel

5.2 Calibration of Parameters for the GTN Damage Model

The key parameters required for the GTN model that were determined based on optical metallography were the initial void volume fraction and the initial second phase particle fraction of the as-received tube material. The fraction of voids was also measured from optical micrographs of samples taken from impacted tubes. The porosity values measured from these samples were then used, along with simulations to determine the parameter, σ_N, which is the mean stress at which particles nucleate voids.

Samples for microscopic evaluation were mounted in an epoxy resin, ground using silicon carbide paper, and then polished using colloidal silica [104]. The damage evolution within the prepared samples was measured using a BX61 Olympus optical microscope with a computer-controlled motorized stage. Optical micrographs were taken using a digital camera with ImagePro software. Figure 5.2 shows a micrograph of the undeformed AA5754 tube material [104]. The micrograph is composed of 48 images taken at a magnification of 40x with a resolution of about 0.17 μm/pixel. The grey-scale tones in this image were then used

to distinguish between second-phase particles and voids. An example of this can be seen in Figure 5.3b, where, based on the grey-scale shade selected, the darker parts of the image were taken to be voids. The initial area fraction of voids was determined to be 0.0024. The area fraction of second-phase particles was then determined by selecting a different level of grey-scale so that both particles and voids were selected (Figure 5.3c), and then subtracting the area fraction of both particles and voids determined from this image from the area fraction of voids. The initial area fraction of second-phase particles was determined to be 0.014.
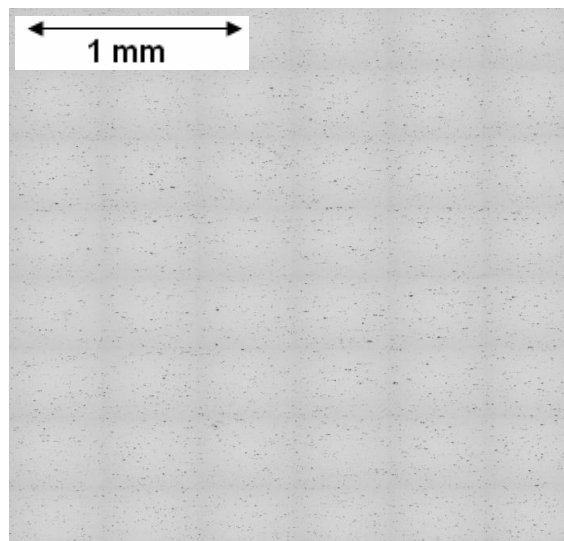
Figure 5.2: Micrograph of undeformed AA5754 alloy tube [104]

After impact, analysis was performed on sections that were taken from the corner of the tube where the folded material had the tightest radius, as shown in Figure 5.4. Samples were taken from a low pressure hydroformed tube with a 12 mm corner radius and a high pressure tube with a 12 mm corner radius and 60 mm of end-feed [73]. Several images in the bend regions were combined to form a single larger image, as shown in Figure 5.5. The area fraction of voids was then measured at seven locations through the thickness of the bend and compared with predictions from the seven integration points through the thickness of the shell elements used in the simulations.
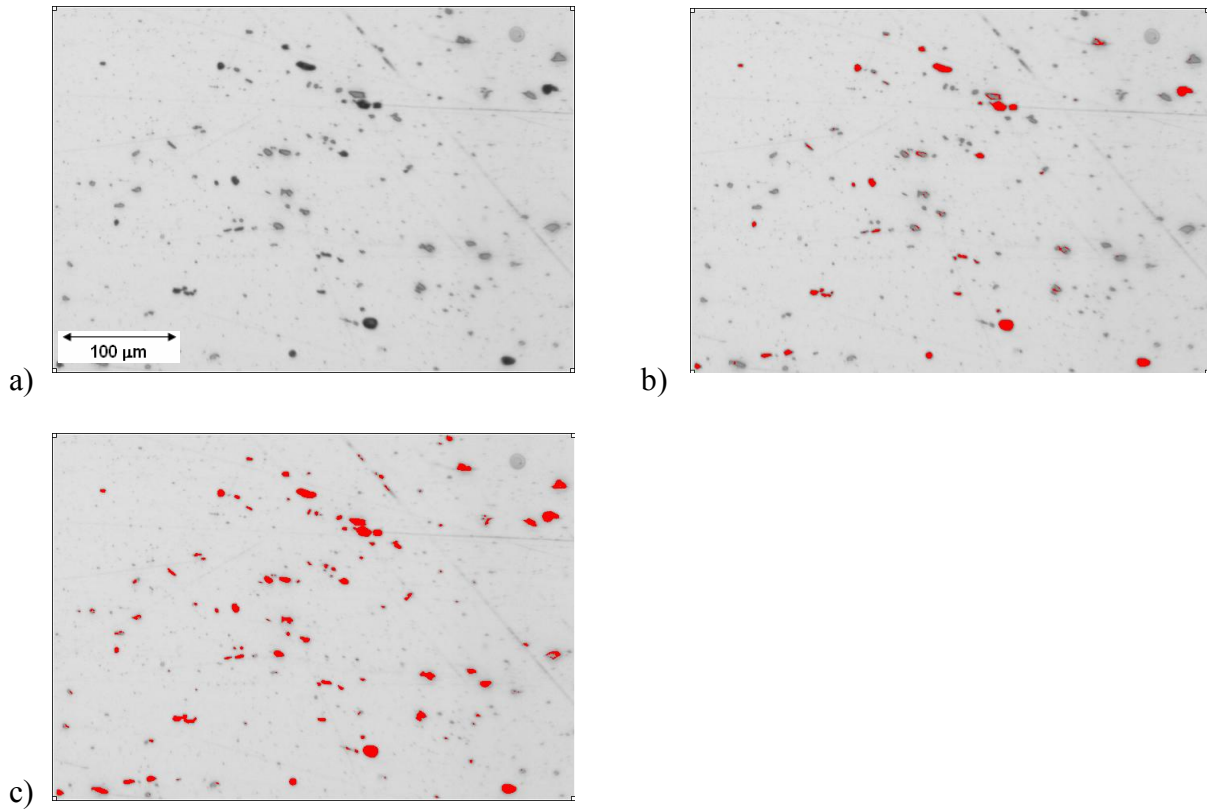
Figure 5.3: Micrograph of AA5754 alloy tube showing a) undeformed sample b) initial voids (highlighted in red) and c) initial voids and second phase particles (highlighted in red)
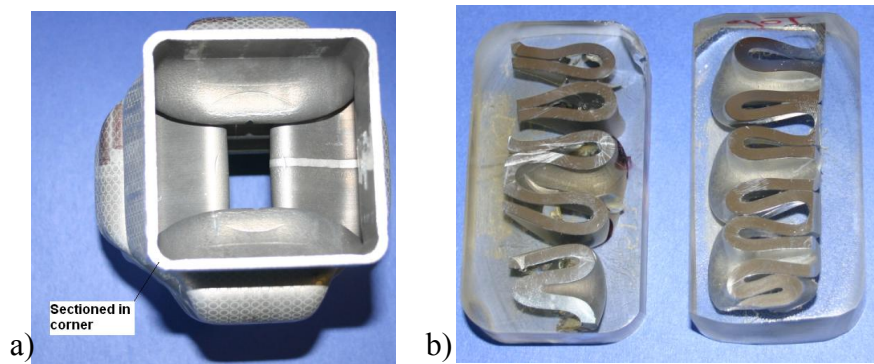
Figure 5.4: a) View of hydroformed and impacted tube sample b) Section from corner of tube formed using the low pressure (left) and high pressure process (right)
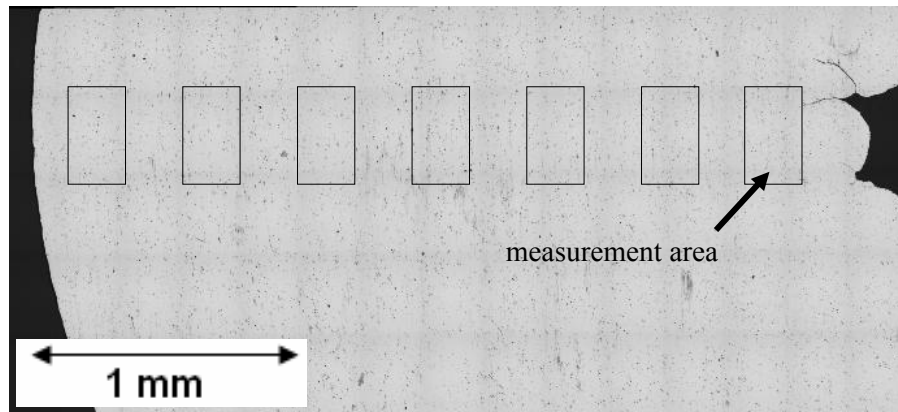
Figure 5.5: Image of a tight bend in an axial crush structure showing approximate locations at which porosity was measured

Impact simulations were performed using two nucleation levels for the nucleation stresses, σ_N = 500 and 550 MPa, considering the high pressure hydroformed tube with 60 mm of end-feed and a 12 mm corner radius. In each case the standard deviation, S_N, was taken to be 50 MPa. The simulations were performed using the user-defined material model discussed in Chapter 4. The predicted porosity for each case was then averaged between several elements selected from an impact simulation at locations corresponding to those at which damage measurements were taken in the experiments. The predicted and measured results are presented in Figure 5.6, where the error bars represent one standard deviation of the average measured and predicted porosity.

In all cases, the porosity on the compressive side of the bend was less than the initial porosity of 0.0024, but then increased through to the tensile side of the bend. All values of measured void fractions were less than 0.006. The simulation performed using a nucleation stress of 550 MPa reasonably captured the experimental result, whereas, there was an over-prediction of the damage level for the case with 500 MPa. As a result, a value of 550 MPa was adopted in subsequent simulations based on tubes formed to corner radii of 6, 12, and 18 mm using the high pressure process with 60 mm of end-feed. The results of all impact simulations performed using the GTN damage model are presented in Chapter 6.
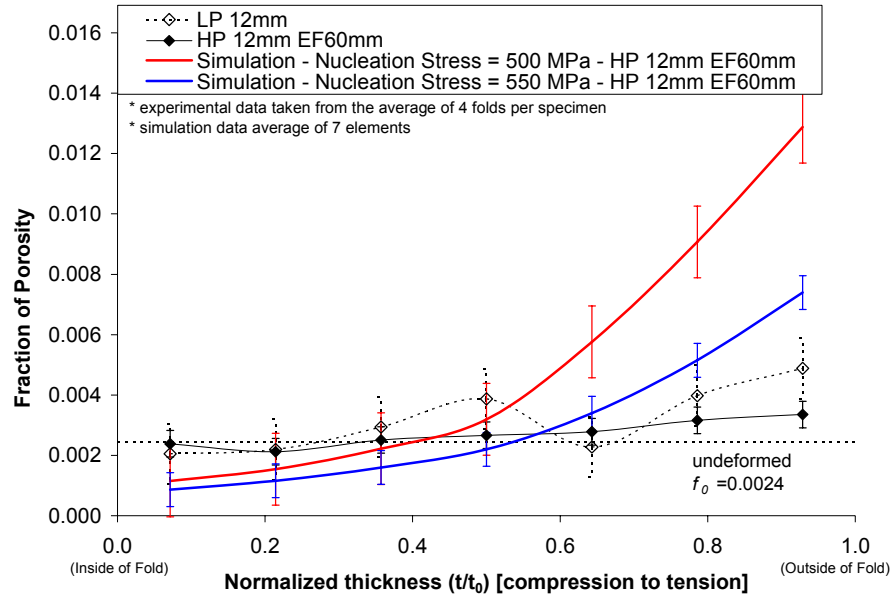
Figure 5.6: Predicted and measured porosity in axial crush folds from the corner of impacted tubes

5.3 Calibration of Parameters for the Johnson-Cook Strain-Rate Model

Values determined from split-Hopkinson bar apparatus testing in the strain-rate range of 500 to 1500 s^{-1} by Smerd et al. [49] for a 1.6 mm thickness AA5754 alloy sheet gave C_{JC} values in the ranges of about 0.002 to 0.004 and m values in the range of 2.38 to 2.66, when using Equation 1.36. Experiments by Salisbury et al. [50] with the AA5754 tube alloy used in the current research, also in the strain-rate range of 500 to 1500 s^{-1}, gave C_{JC} values in the range of 0.009 to 0.012 and m values between 2.31 to 2.50. In the current research, an m value of 2.4 was used to describe the thermal softening behaviour of the material. However, the C_{JC} value was determined based on the results of the dynamic and quasi-static axial crush testing.

In Chapter 2, it was shown that there was an average decrease of about 6% in the mean loads of axially crushed tubes when comparing quasi-static tests to dynamic tests. Several simulations were performed by adjusting the parameter C_{JC}, until the measured difference between the predicted mean loads from dynamic and quasi-static models was

about 6%. The simulations were performed using the user-defined material model discussed in Chapter 4.

Since an explicit dynamic solver was used in the finite element simulations, it was not realistic to perform the quasi-static simulations using the experimental crush rate of 0.167 mm/s due to computational cost. Although implicit simulations could be performed, it would be difficult to separate out differences between the solutions of the implicit and explicit solvers of LS-DYNA in the results. Instead, the results from simulations at an impact velocity of 7.0 m/s with isotropic hardening and von Mises yielding were used to represent the crush loads of the quasi-static tests, such that inertial effects were ignored. Some simulations were performed at lower impact velocities of 2.0 m/s, but only small differences were obtained in the crush response compared to the 7.0 m/s simulation results, such that it was considered reasonable to neglect inertial effects in the current results.

The predicted mean crush loads taken at a crush distance of 200 mm are presented in Figure 5.7 for tubes formed using the high pressure process to a corner radius of 12 mm with 60 mm of end-feed. Simulations were performed with C_{JC} values of 0.003, 0.006, and 0.010, all with an m-value of 2.4. The increases in mean load relative to the isotropic prediction, which was performed with a C_{JC} and m value of zero, were 3.3%, 6.3%, and 10.2%, respectively for the three C_{JC} values. The simulation performed with a C_{JC} of 0.006, with an increase of 6.3% was the closest to the experimentally measured average increase of 6%.
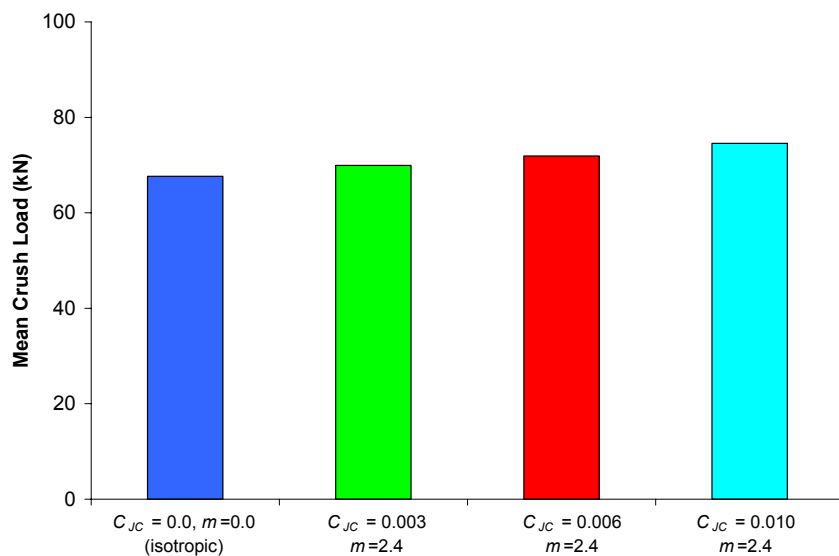
Figure 5.7: Comparison of mean crush load between isotropic and Johnson-Cook simulations

Including the results from the simulations performed for tubes formed using the high pressure process with 6 and 18 mm corner radii, which are presented in Appendix E, the average increase in predicted mean load was determined to be 6.1% when using a C_{JC} value of 0.006. This value was considered reasonable since it was between the values previously reported [49,50] for an AA5754 alloy that were determined from tensile split-Hopkinson bar testing and was adopted for all subsequent simulations. The axial crush predictions using this model are presented in further detail and compared to measured data in Chapter 6.

Data from the impact simulations was used to determine localized strain-rates experienced during dynamically tested axial crush structures. The tightest folding during axial crush occurred in the corners of the tube, as opposed to the flat regions. The effective plastic strain-rates are shown in Figure 5.8 for three typical elements selected along the corner regions and three typical elements from the flat regions of the tube. The impact velocity in the simulation was 7.0 m/s. The results show that the strain-rates in the flat regions were less than 50 s^{-1} (less than the magnitude of the oscillations) and ranged from 100 to 450 s^{-1} in the corner regions. Future research should consider performing uniaxial tensile tests in strain-rate ranges less than 500 s^{-1} to further verify the accuracy of the C_{JC} value determined in the current research.
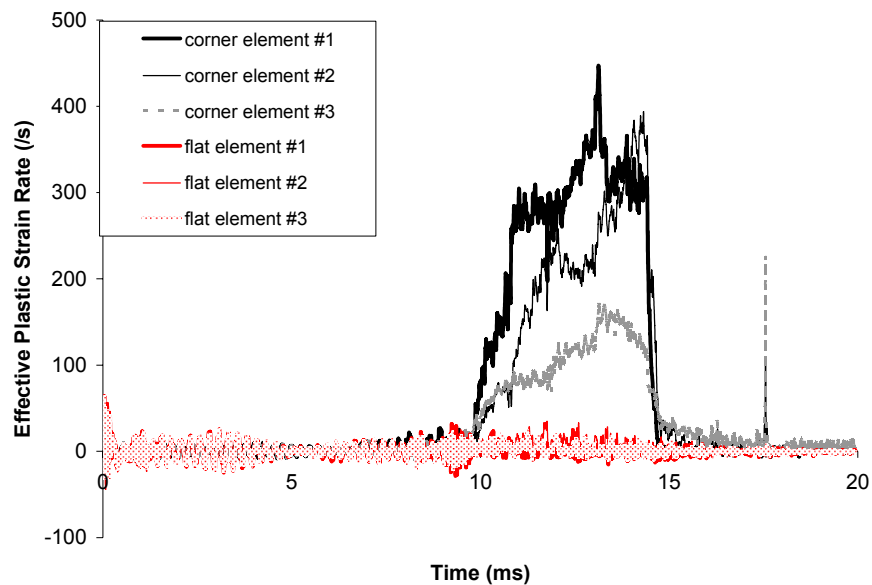
Figure 5.8: Predicted strain-rates in folds of axial crush structure

114

5.4 Kinematic Hardening Experiments

5.4.1 Measurement of the Kinematic Hardening Response

It is difficult to obtain the compressive stress-strain behaviour of a sheet material because large compressive loads will buckle the specimen. Apparatus used to test sheet material in compression often involves placing a large compressive stress on the sides of a specimen to prevent buckling during testing [41,105]. In the current research, pre-strained specimens were taken from the middle of tubes that were hydroformed with end-feeding, as shown in Figure 5.9. End-feeding was used to longitudinally compress the tube, while the hydroforming die and internal water pressure prevented buckling of the specimen. The pre-strained specimens were then placed in a standard tensile testing machine and tested to failure at 10 mm/min. Tension-compression tests were not performed in this research. It should be noted, that in an actual tensile or compression test the only principle stress would be in the longitudinal direction, whereas, in hydroforming there are also stresses in the circumferential and radial directions. However, it will be shown near the end of this section that the specimens taken from the hydroformed tubes were somewhat representative of a compressed uniaxial specimen.

Specimens were taken from tubes hydroformed to three different end-feed displacements of 20, 30, and 60 mm (at each end of the tube), using the end-feed and pressure profiles that were given in Figure 2.15. Corresponding levels of effective plastic pre-strain of 0.05, 0.11, and 0.19 on the uniaxial specimen were calculated from simulation results. A more accurate method to determine the level of pre-strain would have been to use an extensometer to measure the strains during compression, but this was not feasible when hydroforming the tubes. Specimens were taken from the 3 and 9 o'clock positions on the tube for each of the three configurations for a total of six tensile tests. Tensile testing results are shown in Figure 5.10, along with the curve describing the behaviour of the material under monotonic loading (Equation 2.2).
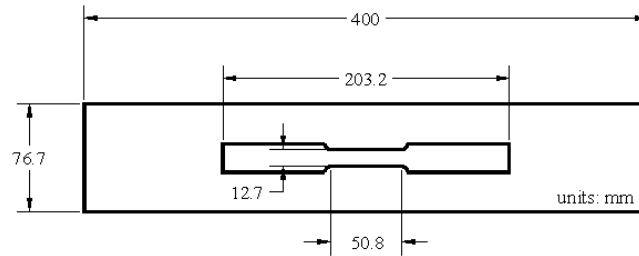
Figure 5.9: Tensile specimen sectioned from hydroformed tube
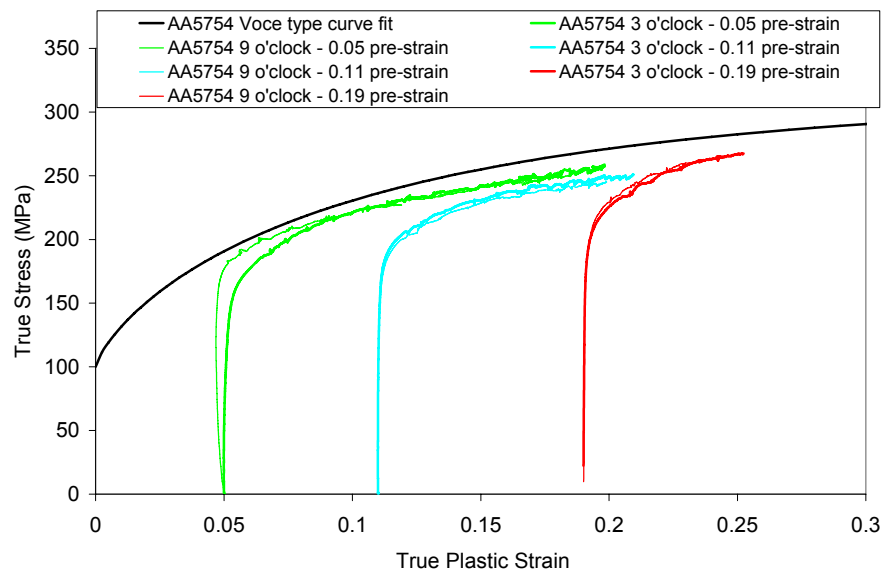
Figure 5.10: Compression-tension test showing different stress-strain responses upon reverse loading

The results show that on reverse loading the specimens yielded sooner than was predicted in the monotonic case. The yield stresses on reverse loading for pre-strains of 0.05, 0.11, and 0.19 were about 165, 185, and 210 MPa, respectively. It is difficult to determine whether or not there is a permanent softening of the material or if the curves tend back to the isotropic curve at higher strains. Ideally, any kinematic hardening model used should capture this transient behaviour after yielding.

5.4.2 Calibration of Kinematic Hardening Parameters

In order to account for linear isotropic-kinematic hardening in the Gurson-Tvergaard-Needleman constitutive model, Tvergaard [106] introduced a fictitious yield surface, σ_F, developed by Mear and Hutchinson [107],

$$\sigma_F = \frac{\sigma_m + \sigma_{reverse}}{2} = b_{GTN}\sigma_m + \left(1 - b_{GTN}\right)\sigma_y \tag{5.1}$$

where, σ_y is the initial yield stress, $\sigma_{reverse}$ is the yield stress on reverse loading, and σ_m is the initial matrix flow stress. The parameter, b_{GTN} is in the range of zero to unity where a value of unity represents the fully isotropic case and a value of zero represents the fully kinematic case. Using Equations 5.1 and 2.2 and a yield stress on reverse loading of 210 MPa, a b_{GTN} value of about 0.83 can be calculated for a pre-strain of 0.19. Figure 5.11 shows the measured kinematic response at an effective pre-strain of 0.19, the isotropic stress-strain response, and the calculated kinematic response using a b_{GTN} value of 0.83. The results show that the predicted curve does not tend back to the isotropic curve after yielding, such that a large under-prediction in the energy absorption would be predicted from axial crush simulations if a linear isotropic-kinematic model were used in the models. Some simulations were performed in this research using a user defined GTN model [108] incorporating linear kinematic hardening, but the results are not presented because they are not realistic due to the large under-prediction in stress upon reverse loading. The model was developed based on the parameter b_{GTN} being constant. The data given in Figure 5.10 could be used to show that the parameter b_{GTN} is not constant for the AA5754 alloy tube. However, the equations developed by Tvergaard [106] would need to be re-developed based on a b_{GTN} that can vary with plastic strain. Instead, the non-linear combined isotropic-kinematic hardening model described in Chapters 1 and 4 was implemented in the finite element simulations. This model required the calibrations of two coefficients, C_{kin} and γ.
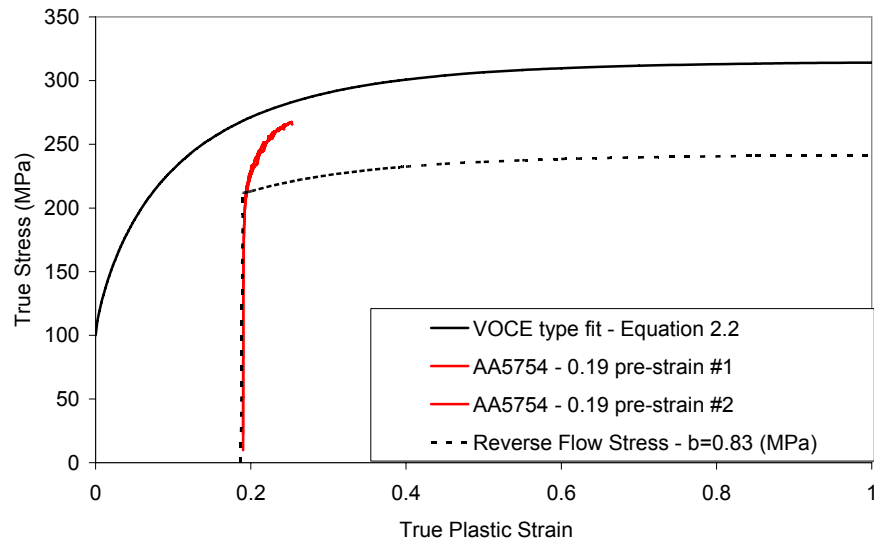
Figure 5.11: Predicted and measured stress-strain response using a linear combined isotropic-kinematic hardening model

Using a regression curve-fit model based on the equations presented in Section 4.1.3, values of C_{kin} and γ were determined for each of the six compression-tension tests conducted. The values given in Table 5.1 were calculated over the intervals of plastic strain shown in Figure 5.12. Although the parameters are similar for the same level of effective pre-strain, there are large differences between the 0.05, 0.11, and 0.19 cases.

Table 5.1: Kinematic hardening parameters (for stress units of MPa)

Experiment	C_{kin}	γ
0.05 pre-strain #1	381.7	30.9
0.05 pre-strain #2	180.7	30.1
0.11 pre-strain #1	304.6	11.4
0.11 pre-strain #2	293.4	9.7
0.19 pre-strain #1	768.4	26.4
0.19 pre-strain #2	825.1	29.6
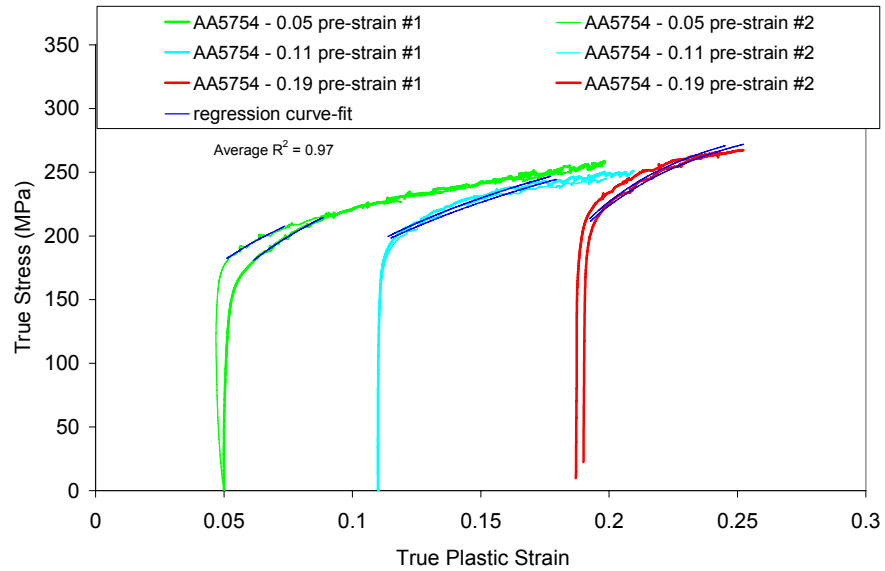
Figure 5.12: Plot of stress-strain curves showing strain range over which kinematic parameters were calculated

Single element simulations with 1 mm shell elements were performed using these values, in which compressive strains of 0.05, 0.11, or 0.19 were placed on the specimen followed by a stress reversal to tension. All simulations were performed using the user-defined material model discussed in Section 4.1.3. An average of the values for the 0.19 pre-strain case, C_{kin}=796.8 MPa and γ=28.0, was used to model the kinematic behaviour of the AA5754 material. The results are presented in Figure 5.13 showing that when using these values, the kinematic hardening model does not entirely capture the transient behaviour after yielding for the 0.05 and 0.11 pre-strain cases (the initial compressive pre-strain curve is not shown). However, the kinematic hardening response for the 0.19 pre-strain is well captured.

Although the modified non-linear isotropic-kinematic hardening model does not exactly capture the experimental behaviour using just the one set of parameters, it is a reasonable approximation and does allow parametric investigation of kinematic hardening effects. In order to better capture the reverse loading behaviour a more complicated model is required that might require defining multiple yield surfaces [109,110]. Models of this nature were not explored, but could be considered in future research. Values of C_{kin}=796.8 MPa and γ=28.0 were employed for all subsequent simulations.
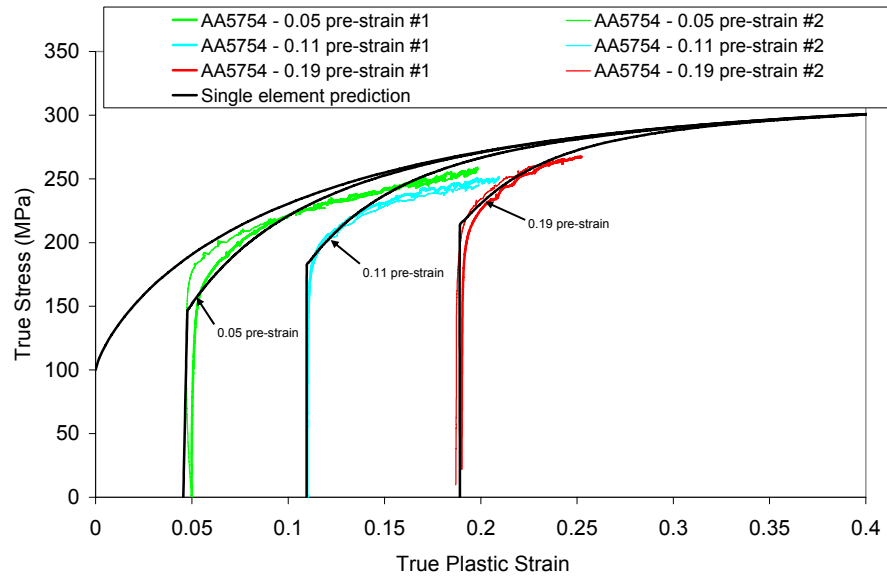
Figure 5.13: Results from single element simulation of compression-tension

It should be noted, that in an actual uniaxial test, the only stress would be in the longitudinal direction, whereas in hydroforming there were also applied stresses in the circumferential and radial directions. Since these stresses existed, there would also be a shift of the yield surface away from uniaxial compression. However, the shift in the yield surface is relatively small compared to the size of the yield surface. The maximum pressure experienced in the tube during hydroforming was about 140 MPa (Figure 2.15) which is representative of the radial stress that acted on the specimens taken from the middle of the tube. The yield stress of the AA5754 alloy is about 100 MPa, such that there would only be a small shift of the yield surface in the radial direction of less than 10 MPa (using Equation 4.12). The isotropic and kinematic yield surfaces for plane stress are depicted in Figure 5.14 for an effective plastic strain of 0.19, which was calculated using C_{kin}=796.8 MPa and γ=28.0. The shift of the yield surface in the x-direction (longitudinal) due to uniaxial compression can be calculated to be -27.4 MPa (using Equation 4.12). As determined from the hydroforming simulations, in the middle of the tube at an effective plastic strain of 0.19 the shift was predicted to be 18.9 MPa in the y-direction (circumferential) and -12.9 MPa in the x-direction (longitudinal). The yield surface for the specimen from the hydroformed tube is also depicted in Figure 5.14. It can be seen that upon reverse loading, both yield surfaces

120

show that the specimens would yield at about the same value in tension. Since the normal to the yield surface is slightly different between the two cases, the evolution of the transient response during reverse loading might also be slightly different. However, the figure shows that specimens taken from the hydroformed tube were somewhat representative of a uniaxial specimen.
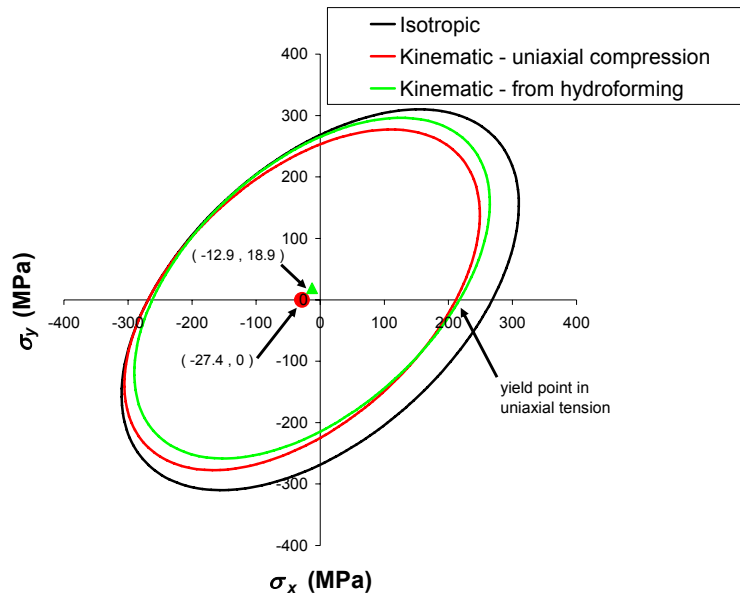
Figure 5.14: Isotropic and kinematic plane stress yield surfaces for an AA5754 alloy at an effective plastic pre-strain of 0.19 ($\sigma_{xy} = 0$)

In Chapter 4, details were presented regarding implementation of the kinematic hardening model in the finite element models. Recall that the term, $\alpha_{ij}^{s+1} - \alpha_{ij}^{s}$ in Equation 4.33 (s is the current increment in the procedure) was neglected in the calculation of the increment of effective plastic strain. This was considered a reasonable assumption for an explicit implementation of the stress update. This can be demonstrated by examining Figure 5.15. In this figure, the effective shift in the location of the yield surface (Equation 4.12) for the AA5754 alloy is plotted based on values of C_{kin}=796.8 MPa and γ=28.0. The effective stress, according to Equation 2.2 is also presented. At an effective plastic strain of about 0.14, $\overline{\alpha}$ is at about 98% of its saturation value of 28.5 MPa. In the folds of an axial crush structure, most of the deformation strains are much higher than 0.14 such that it was a

reasonable assumption to assume $\alpha_{ij}^{s+1} - \alpha_{ij}^{s} \approx 0$ in the calculations. However, for cases in which the effective plastic strains were less than 0.14, some slight inaccuracies in the predicted kinematic behaviour would occur. Future implementation of the kinematic hardening model should account for the shift of the location of the yield surface during the stress update, rather than assuming the location is constant during the update and then updating the location at the end of the time-step.
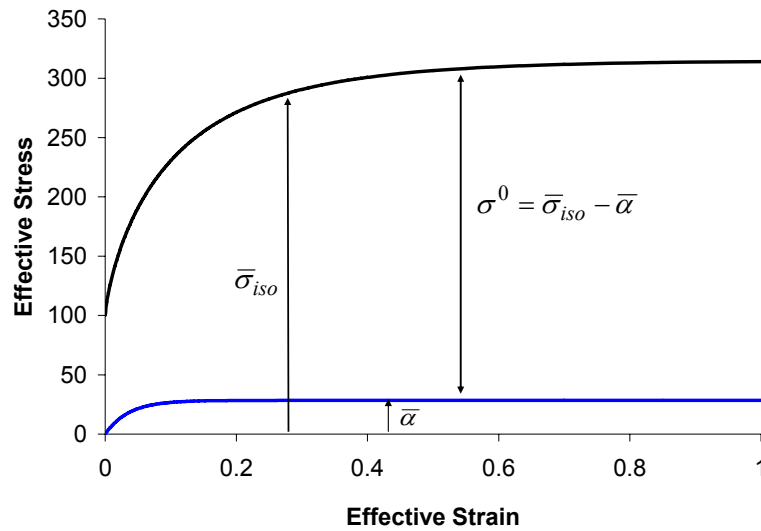
Figure 5.15: Comparison of the effective shift of the yield surface and the effective stress based on the parameters calibrated for the AA5754 alloy

5.5 Calibration of Parameters for the Yld2000-2d Anisotropic Model

The Yld2000-2d anisotropic constitutive model required the calibration of eight coefficients. Lee et al. [41] performed a study on AA5754 alloy sheet material and determined the coefficients for the Yld2000-2d constitutive model given in Table 5.2. The r-values for the 0°, 45°, and 90° directions were 0.76, 0.71, and 0.79, respectively. The AA5754 sheet used in the current study was not exactly the same composition as the AA5754 alloy used in the study by Lee et al. [41], such that a new set of values was obtained for the current material. Tensile specimens were taken from the AA5754 sheet material used to form the tubes in the current study. Figure 5.16 shows the stress-strain response obtained

from tensile specimens taken at 0°, 45°, and 90° relative to the rolling direction [111]. After the tensile specimens failed at strains of about 0.2, the widths and thicknesses were measured near the fracture location to determine the r-values of the sheet for each of the three directions. The r-values were measured to be 0.67, 0.76, and 0.6 for the 0°, 45°, and 90° directions, respectively. These data were used to determine the eight coefficients required for the Yld2000-2d model [112], which are also given in Table 5.2.

Table 5.2: Parameters for the Yld2000-2d Anisotropic Constitutive Model

Material	α_1	α_2	α_3	α_4	α_5	α_6	α_7	α_8
AA5754 sheet (Lee et al., 2005)	0.879	1.136	0.952	1.048	1.009	0.952	1.034	1.237
AA5754 sheet (current research)	0.924	1.061	1.014	1.067	1.032	1.052	1.03	1.108
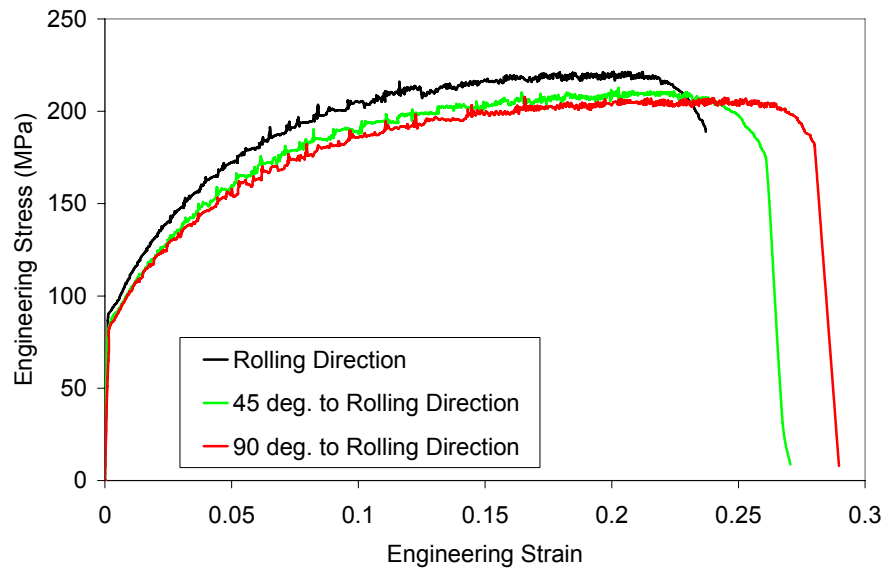
Figure 5.16: Stress-strain response of samples from AA5754 sheet alloy at 0°, 45°, and 90°

Figure 5.17 shows the yield surfaces based on both sets of anisotropic parameters given in the table, as well as the isotropic yield surface, at an effective plastic strain of 0.19. The results show that there is reasonable agreement between the two sets of anisotropy coefficients. The predicted yield surface at an effective stress of 0.19 is shown in Figure 5.18 showing the product of combining kinematic hardening and anisotropy. This yield surface

123

was determined based on C_{kin}=796.8 MPa and γ=28.0 with the current set of anisotropic parameters. This shift in the x-direction was -27.4 MPa.
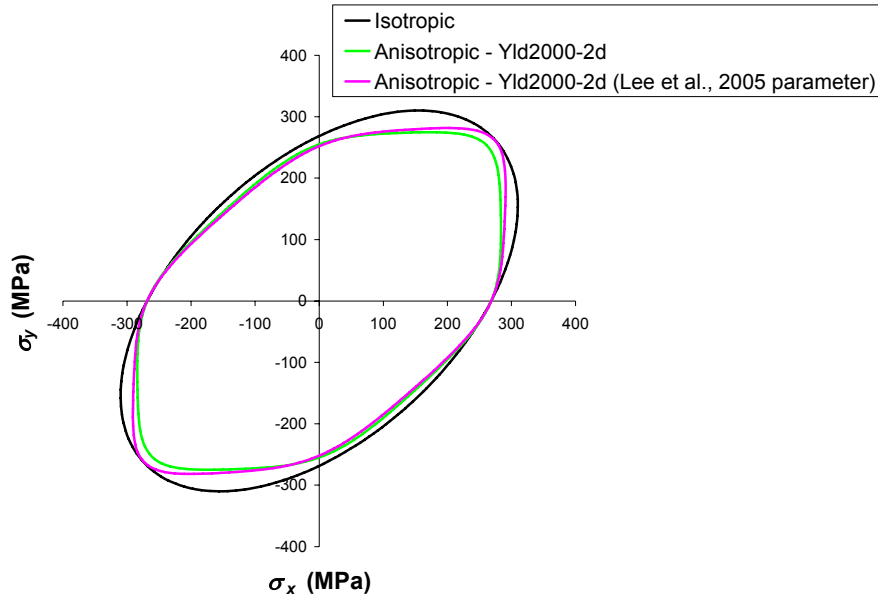
Figure 5.17: Isotropic and Yld2000-2d anisotropic plane stress yield surfaces for an AA5754 alloy at an effective plastic pre-strain of 0.19 ($\sigma_{xy} = 0$)
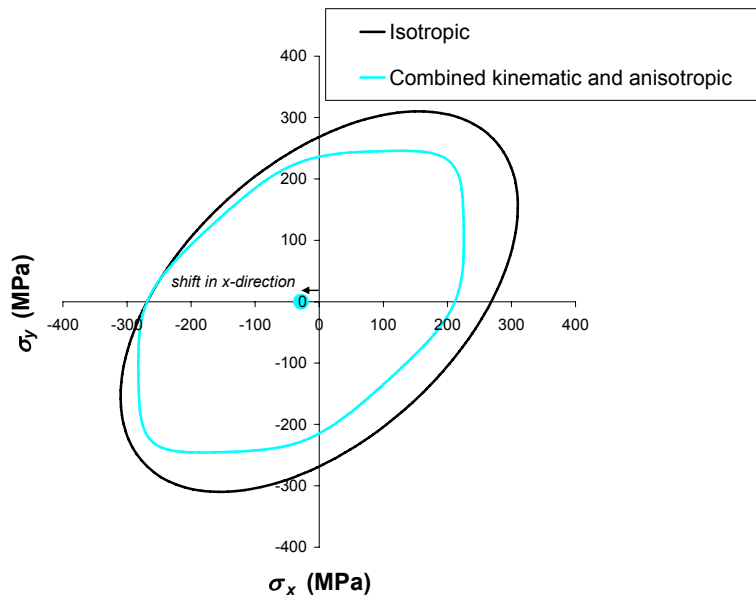
Figure 5.18: Isotropic and combined kinematic-anisotropic plane stress yield surfaces for an AA5754 alloy at an effective plastic pre-strain of 0.19 ($\sigma_{xy} = 0$)

Chapter 6 – Finite Element Predictions
Results and Discussion

This chapter presents the results of the hydroforming and impact simulations and compares the predicted response to the measured data. Hydroforming simulations were carried out corresponding to the experimental conditions presented in Table 2.2. The results of these simulations, mainly in the form of strain and thickness, were compared to the measured data to ensure the hydroforming simulations captured the hydroforming response. Mesh sensitivity studies were then performed for the axial crush operation to study the influence of element size and formulation. Once the element size and formulation were selected, several simulations were performed using the von Mises yield criterion with isotropic hardening for each of the experimental conditions outlined in Table 2.3. In addition, simulations were also performed to determine the influence of geometry, mass, work hardening, residual stress, and thickness changes associated with the hydroforming operation on the impact response. Simulations were also performed to study the influence of a number of potential sources of material non-linearity, such as damage, kinematic hardening (Bauschinger effect), yield surface anisotropy, and strain-rate effects.

6.1 Comparison of Simulation and Experiment – Hydroforming

All of the results presented in this section are based on simulations performed with a 4 mm mesh size using Belytschko-Tsay shell elements [94] to define the tube. Studies of mesh sensitivity and the influence of element formulation on the predicted axial crush response are presented in Section 6.2.

6.1.1 AA5754 Low Pressure Hydroforming

Figure 6.1 shows the predicted and measured engineering strains for the outer surface of AA5754 alloy tubes formed using the low pressure process with a die corner radius of 6 mm (results for corner radii of 12 and 18 mm are presented in Appendix A). The results show very good agreement between simulation and experiment, demonstrating that the simulations accurately captured the behaviour of the tube. There was a small difference in the flat sections of the tube where the measured strains were about –0.07 and the predicted strains were about –0.05, but it was not expected that this would significantly affect the crush response of the tube.
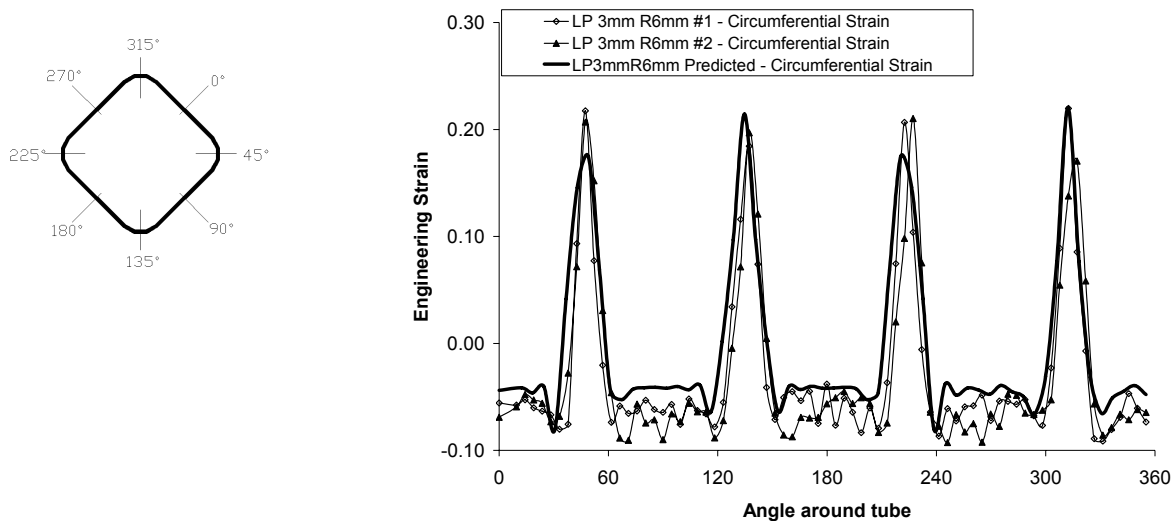
Figure 6.1: Predicted and measured strains for AA5754 tube formed using low pressure hydroforming process

6.1.2 AA5754 High Pressure Hydroforming

Figure 6.2 shows the predicted and measured engineering strains for AA5754 tubes formed using the high pressure process to a corner radius of 6 mm with 60 mm of end-feed. The results for all three corner radii cases with both the 60 and 40 mm end-feed levels are given in Appendix A. The results show that the predicted strains in the corners were greater than the actual strains. This may be attributed to the camera used to capture images of the circle grids etched onto the tube, which was designed for use on flat surfaces. As a result, the circumferential strains measured from an image captured on a sharp corner of a hydroformed tube would be affected. Figure 6.3 shows the strain results for tubes formed to an 18 mm corner radius with 60 mm of end-feed, showing much better agreement between predicted and measured data.

An ultrasonic measurement device was used to measure the as-hydroformed thicknesses of the tubes formed using the high pressure process [75]. Figure 6.4 shows the predicted and measured per cent change in thickness for tubes formed to a 6 mm corner radius with 60 mm of end-feed. The measured results show that there was almost no thickness reduction in the actual corner of the tube, as well as in the flats of the tube. The thickness reduction, of about 17 per cent, occurred in the area on either side of the corner of the tube where the tube was in contact with the die wall. This behaviour was not captured in the simulations, which were performed using shell elements. Also, there was an over-prediction of the thickness in the flat sections for tubes formed with 60 mm of end-feed. This could potentially be attributed to through-thickness stresses resulting from contact with the die wall which could be captured using solid elements in the simulations [75].

The thickness results for the AA5754 tubes with both 60 and 40 mm of end-feed with the 6, 12, and 18 mm corner radii are presented in Appendix A. Other than the thickness in the actual corner of the tube, the predicted behaviour was in reasonable agreement with the measured response, expect for tubes formed to an 18 mm corner radius with 60 mm of end-feed, as seen in Figure 6.5. For this configuration, the end-feed level was probably too high, which led to the creation of light wrinkles in the circular cross sections at the tube ends and ripples of the tube wall in the corner regions. These small wrinkles were still present after the hydroforming operation. It is likely that these wrinkles affected the longitudinal strains

127

generated at the half-length of the tube which led to the observed thickness reduction, whereas the simulations actually predicted a small increase in thickness.
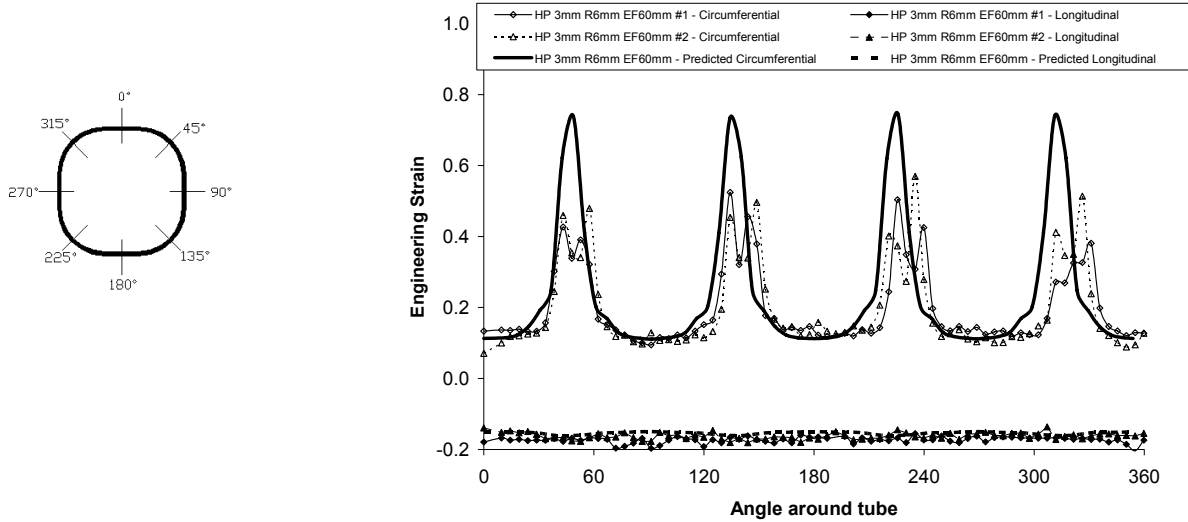
Figure 6.2: Predicted and measured strains for AA5754 tubes formed using high pressure hydroforming process with 60 mm of end-feed and a 6 mm corner radius
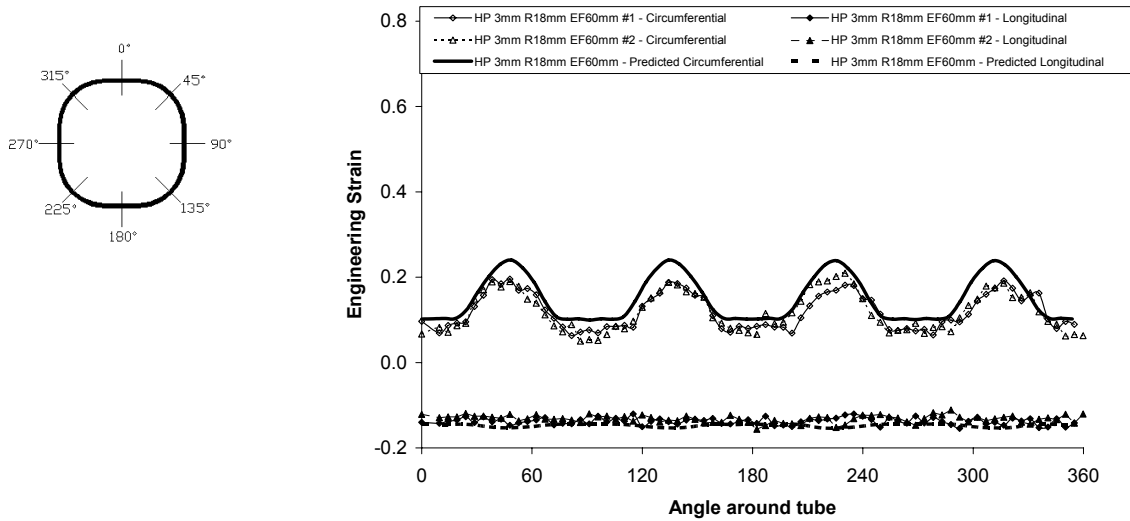
Figure 6.3: Predicted and measured strains for AA5754 tubes formed using high pressure hydroforming process with 60 mm of end-feed and an 18 mm corner radius
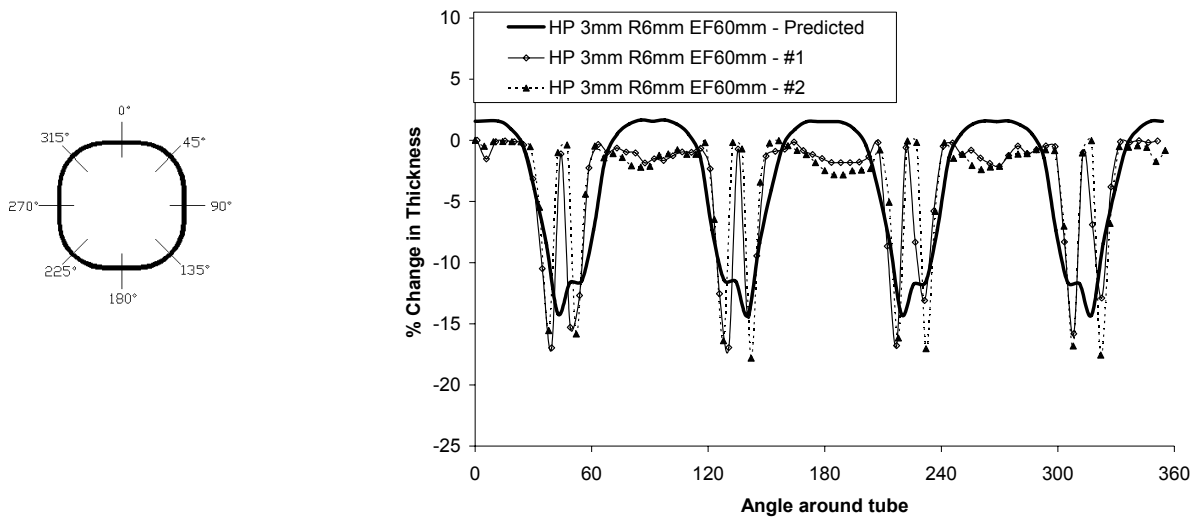
Figure 6.4: Per cent change in thickness for AA5754 tubes formed using high pressure hydroforming process with 60 mm of end-feed and a 6 mm corner radius
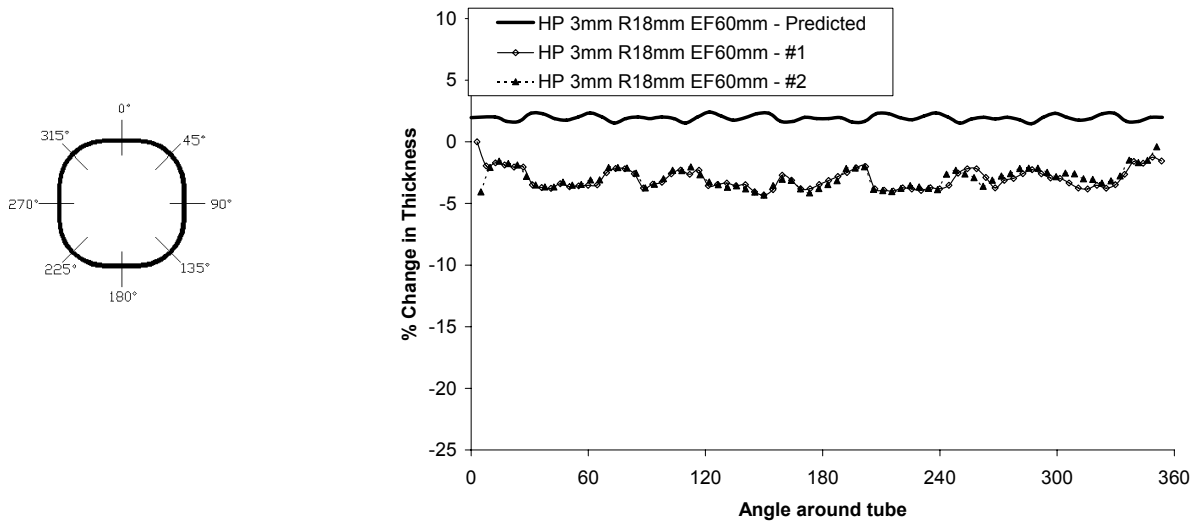
Figure 6.5: Per cent change in thickness for AA5754 tubes formed using high pressure hydroforming process with 60 mm of end-feed and an 18 mm corner radius

6.1.3 EN-AW 5018 Low Pressure Hydroforming

The predicted and measured strains from EN-AW 5018 tubes formed using the low pressure process with a corner radius of 6 mm are shown in Figure 6.6 (the results for all EN-AW5018 alloy tubes are presented in Appendix A). The results show that the peak strains are slightly higher at the 135° and 315° positions compared to the 45° and 225° locations. The higher peak strains occur in the two corners contained within the die during closure in the low pressure hydroforming operation. The lower peak strains occur where the tube is unsupported during the die closure stage due to the parting of the dies. In general, the predicted and measured results were in reasonable agreement, showing that the strains predicted from simulations are representative of the low pressure tube hydroforming process. As with the AA5754 low pressure tubes, thicknesses were not measured because there was little change resulting from the low pressure hydroforming process.
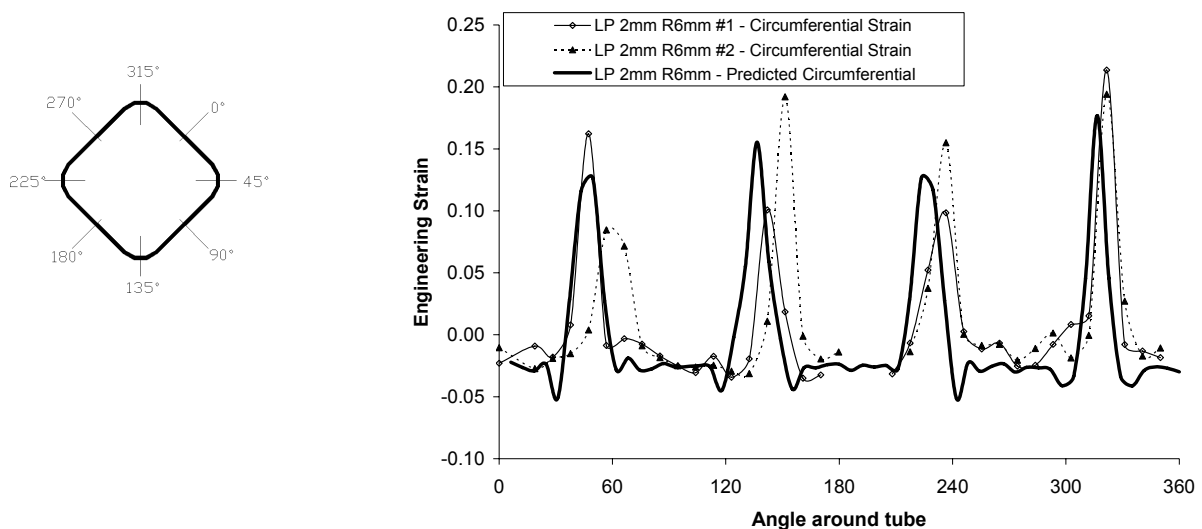
Figure 6.6: Predicted and measured strains for EN-AW 5018 tube formed using low pressure hydroforming process

6.1.4 EN-AW 5018 High Pressure Hydroforming

Figure 6.7 compares the predicted and measured strains for a 3.5 mm thickness tube formed to a corner radius of 27 mm. The 3.5 mm results show reasonable agreement between simulation and experiment. The results for all four corner radii are presented in

130

Appendix A and in all cases showed that the simulations reasonably predicted the strains resulting from the hydroforming process.
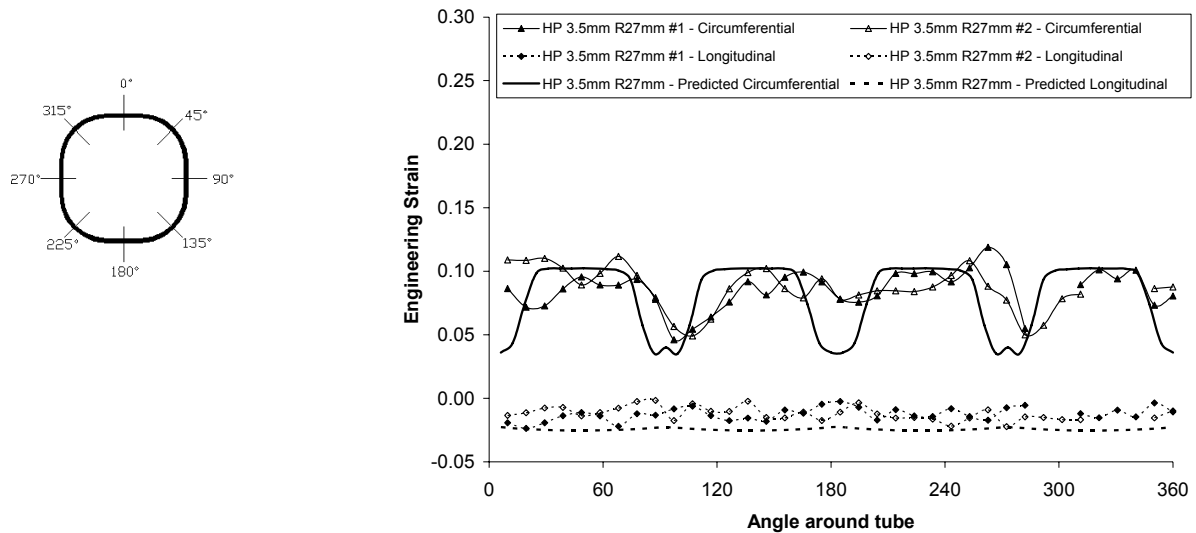
Figure 6.7: Predicted and measured strains for 3.5 mm thickness, EN-AW 5018 tube formed using high pressure hydroforming process

Figure 6.8 compares the predicted and measured engineering strains for the outer surface of a 2 mm thickness tube formed to a corner radius of 27 mm, showing that the predicted circumferential strains did not accurately match the measured data. The measured strains in the corner-fill regions were approximately 0.14, but the predicted strains were approximately 0.10. The results for the 33, 30, 27, and 24 mm corner radii cases for the 2 mm tubes are presented in Appendix A, and in all cases show an under prediction. The cause of this under prediction was not determined, but may be due to the influence of through-thickness stresses resulting from contact with the die which were not modelled in the simulations. Solid (brick) elements are required to further study the effects of through-thickness stresses, since shell elements in the models enforce the plane stress assumption. Future studies should be performed with brick elements to examine the effects of through-thickness stresses.

131
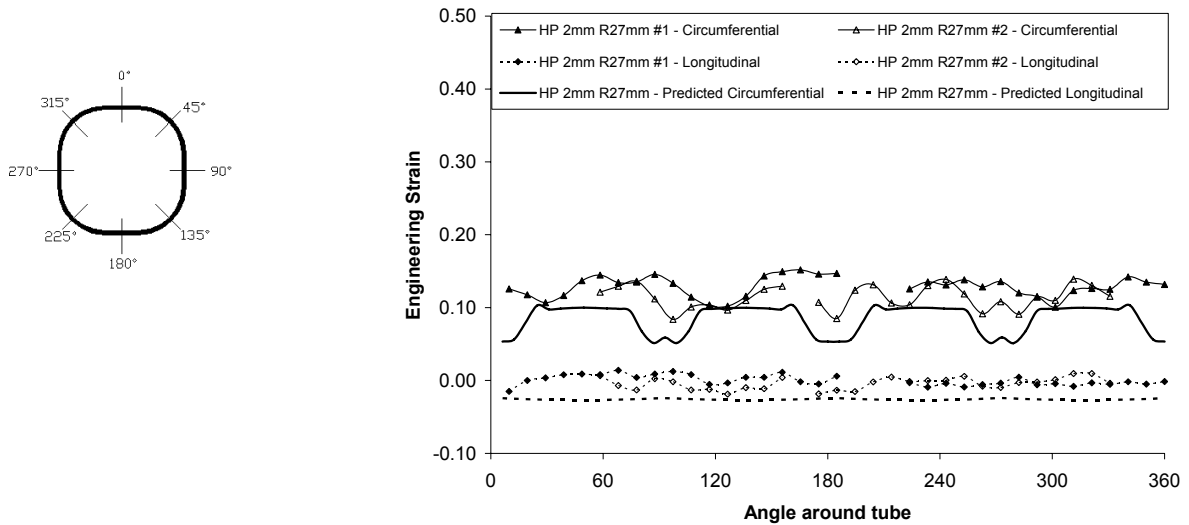
Figure 6.8: Predicted and measured strains for 2 mm thickness, EN-AW 5018 tube formed using high pressure hydroforming process

The predicted strain and thickness response obtained from all of the hydroforming simulations reasonably captured the measured response, except for the EN-AW5018 alloy tubes with 2 mm thickness formed using the high pressure process. After each hydroforming simulation, an implicit springback simulation was performed followed by a simulation of the fold initiator forming process (if necessary) and then another springback simulation. In each case, the predicted thicknesses, residual stresses, and work hardening (strain hardening) were carried forward to each subsequent simulation and finally to the axial crush simulations.

6.2 Effects of Element Formulation and Mesh Size

It has been shown that different energy absorption characteristics can be obtained when using different element sizes and types [80], such that mesh and element sensitivity studies were carried out in the current research for the axial crush structures. In the current study, two element sizes of 2 and 4 mm and two element types were utilized. Belytschko-Tsay shell elements (Type 2 in LS-DYNA) and fully integrated shell elements (Type 16 in LS-DYNA) [94] were utilized, with the difference being that stresses and strains are calculated at two by two points in-plane for the fully integrated element versus one location in-plane with the Belytschko-Tsay element, for each integration point through the thickness

of the elements. All simulations were performed using seven integration points through the thickness. The crush force versus displacement responses for all axial crush simulations performed in this mesh sensitivity study are presented in Appendix B. This section presents the results based on the mean crush loads taken at a crush distance of about 200 mm. The mean crush loads are presented versus the radius ratio of the tube, for which a radius ratio of unity represents the non-hydroformed, round tube. The mesh sensitivity studies were carried out using the von Mises yield criterion with isotropic hardening.

Figure 6.9 shows the predicted mean crush loads taken at a crush distance of 200 mm for simulations of tubes formed using both the high and low pressure processes with 6, 12, and 18 mm corner radii, in which the tubes were defined with a 4 mm mesh size using either Type 2 or 16 elements. The mean load plot shows that the Type 16 elements gave a higher prediction than the Type 2 elements, by an average of about 7%, indicating that the axial crush prediction is sensitive to element type. The Type 2 (single point in-plane integration) also resulted in predictions in closer agreement to the experimental data.
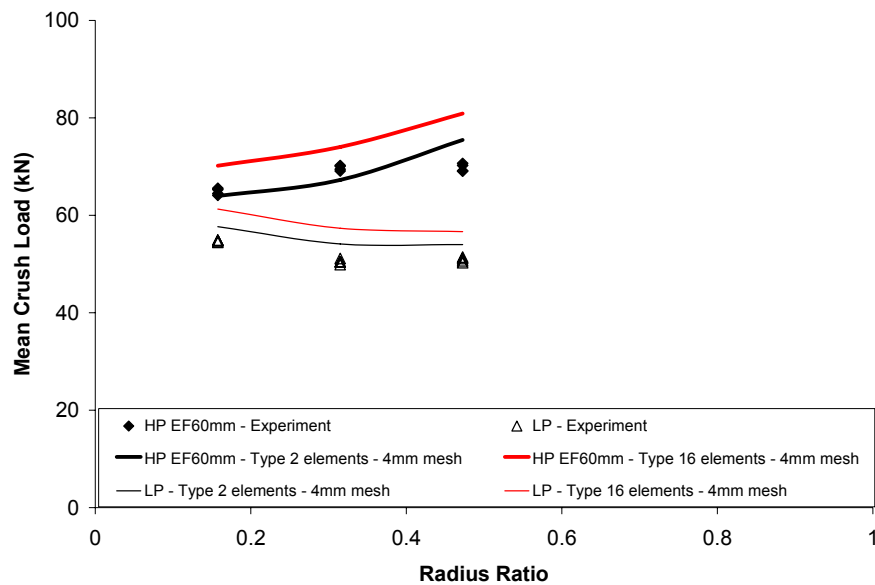
Figure 6.9: Predicted crush response with Type 2 and Type 16 elements with 4 mm mesh

Figure 6.10 shows the predicted crush pattern from a section of the tube with a 6 mm corner radius formed using the high pressure process, defined with either a 2 or 4 mm mesh size with Type 16 elements. The smaller element size can better capture the tight bends on

133

the fold of the axial crush structure. Figure 6.11 shows the predicted response based on simulations performed using Type 2 elements with either a 2 or 4 mm mesh size. The predictions of mean load with the 2 mm mesh size are less than the mean load predictions with the 4 mm mesh size by an average of about 4.7%. Figure 6.12 shows that the mean loads of the 2 mm mesh simulations were an average of 6.2% less than the 4 mm mesh results, when Type 16 elements were used.

a)   b)
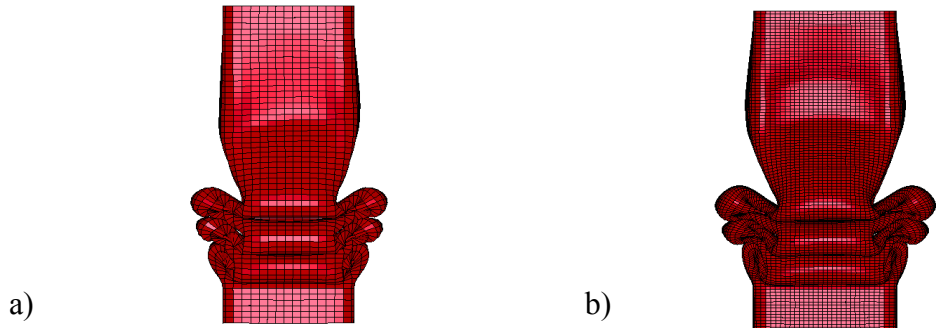
Figure 6.10: Predicted crush pattern a) 4 mm mesh and b) 2 mm mesh with Type 16 elements
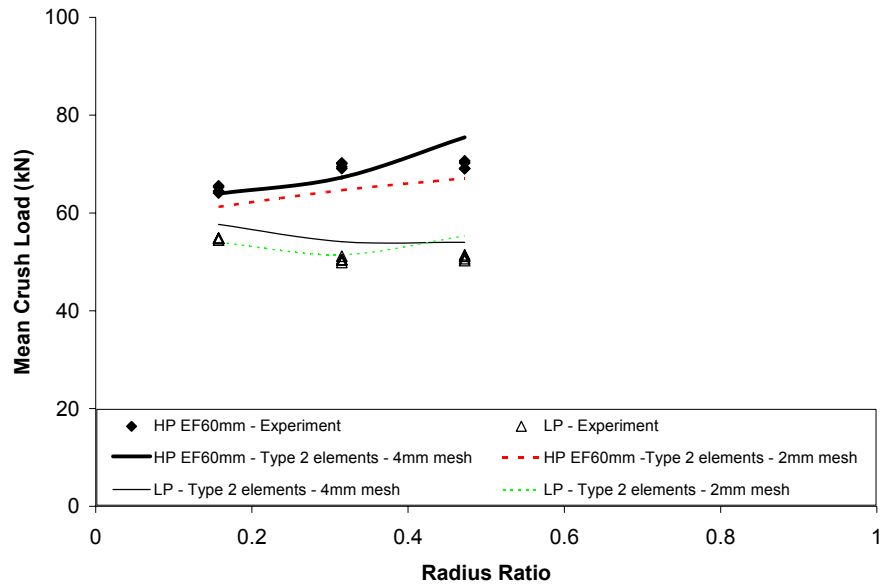
Figure 6.11: Predicted crush response between 2 mm and 4 mm mesh sizes with Type 2 elements

Figure 6.13 shows the crush response obtained based on simulations for which the impact was performed using Type 2 elements, but the hydroforming was performed with either Type 2 or 16 elements. In either case, the crush response was almost identical,

showing that the differences in predicted mean load between Type 2 and 16 elements resulted from the crush simulations and not the hydroforming simulations.
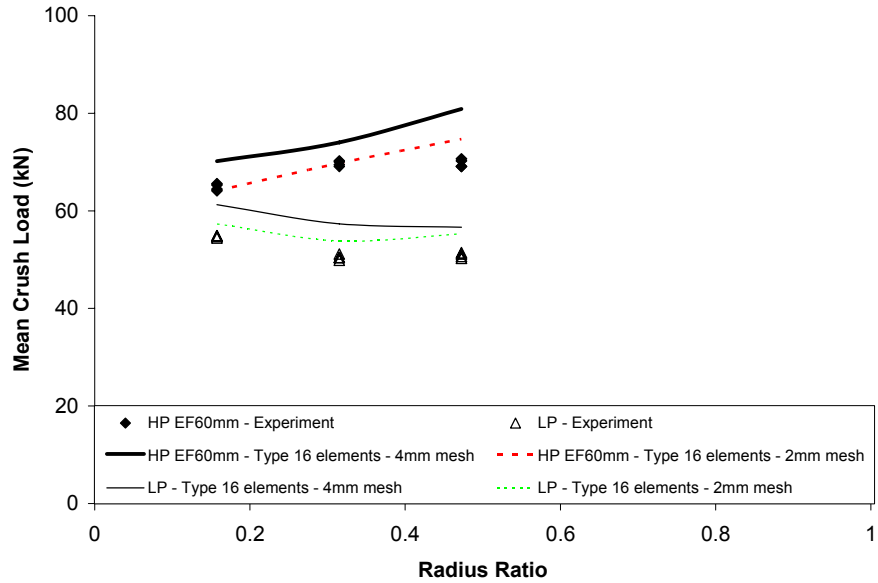
Figure 6.12: Predicted crush response between 2 mm and 4 mm mesh sizes with Type 16 elements
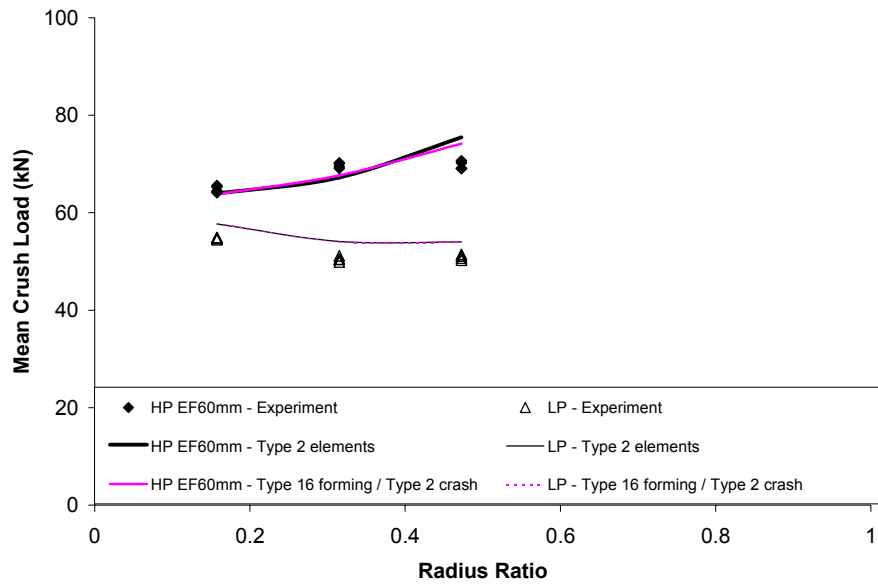
Figure 6.13: Predicted crush response using Type 2 elements for crash when using either Type 2 or 16 elements for forming with a 4 mm mesh size

The results presented in this section showed that predicted axial crush response can be sensitive to element size and type. Generally, mean load predictions from simulations with a 4 mm mesh size and Type 2 elements produced results that were in good accordance with measured mean loads. As a result, all subsequent simulations were performed using a 4 mm mesh size with Type 2 elements for both hydroforming and impact simulations.

6.3 Axial Crush Results – Comparison of Experiment and Simulation

This section provides a detailed comparison of the predicted and measured crush responses. All simulation results presented in this section were performed using the von Mises yield criterion with isotropic hardening. The crush response curves and the tabulated mean loads for all results presented in this section can be found in Appendix B.

6.3.1 AA5754 Axial Crush Results

The predicted and measured mean crush loads for the AA5754 tubes formed using the low pressure process are presented in Figure 6.14. The predicted results are about 6% greater than the experimental results for the tubes with crush initiators. When comparing the predicted and measured results for tubes without crush initiators it can be seen that the predicted loads were also greater than the measured loads, by about 13%. This discrepancy most likely resulted due to the lack of fold initiators. Without fold initiators the simulations over predicted the initial peak load because there was not a prescribed location for fold initiation. Also shown in Figure 6.14 is the predicted and measured response for the non-hydroformed, circular tubes (radius ratio equal to unity) showing reasonable agreement, with about a 7% over-prediction.

The predicted and measured mean crush loads for the AA5754 tubes formed using the high pressure hydroforming process are presented in Figure 6.15. The predicted values for cases with 60 mm of end-feed were slightly less than the experimental values, except for the 18 mm corner radius where there was an over-prediction. Also, the predicted and measured values were in good agreement for cases with 40 mm of end-feed, except for the 18 mm case in which there was again an over prediction. The predicted values are about 8.5% greater than the measured values for the tubes that were annealed after the hydroforming process.

Overall, the simulations appear to capture the forming history and produce accurate predictions for the crush response for cases in which the tubes incorporated fold initiators.
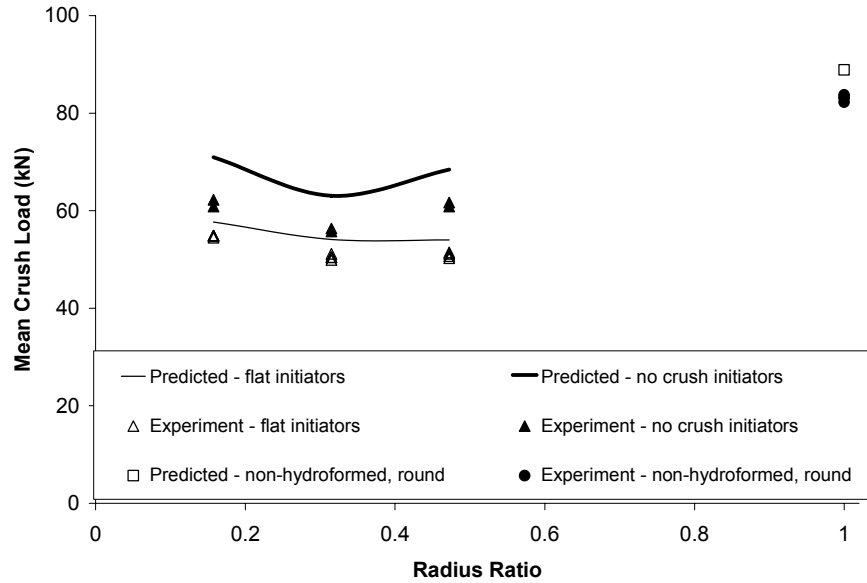
Figure 6.14: Mean crush loads for AA5754 tubes formed using low pressure hydroforming
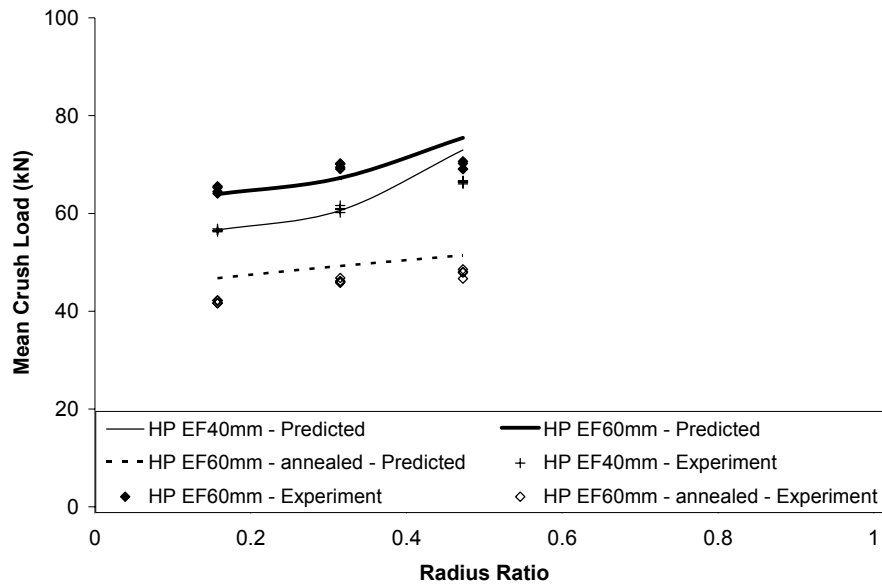
Figure 6.15: Mean crush loads for AA5754 tubes formed using high pressure hydroforming

6.3.2 EN-AW 5018 Axial Crush Results

Results of the axial crush testing of the EN-AW 5018 alloy tubes formed using the high pressure hydroforming process have been summarized by Williams et al. [81,82] and will briefly be discussed in this thesis. The predicted and measured mean crush loads at 200 mm of crush displacement for EN-AW 5018 tubes formed using both the low and high pressure hydroforming processes are shown in Figure 6.16. Tubes formed using the high pressure hydroforming process showed a significant decrease in energy absorption with decreasing radius ratio. This reduction was attributed to thinning due to circumferential expansion during hydroforming, which had a significant influence on the energy absorption characteristics during crash.
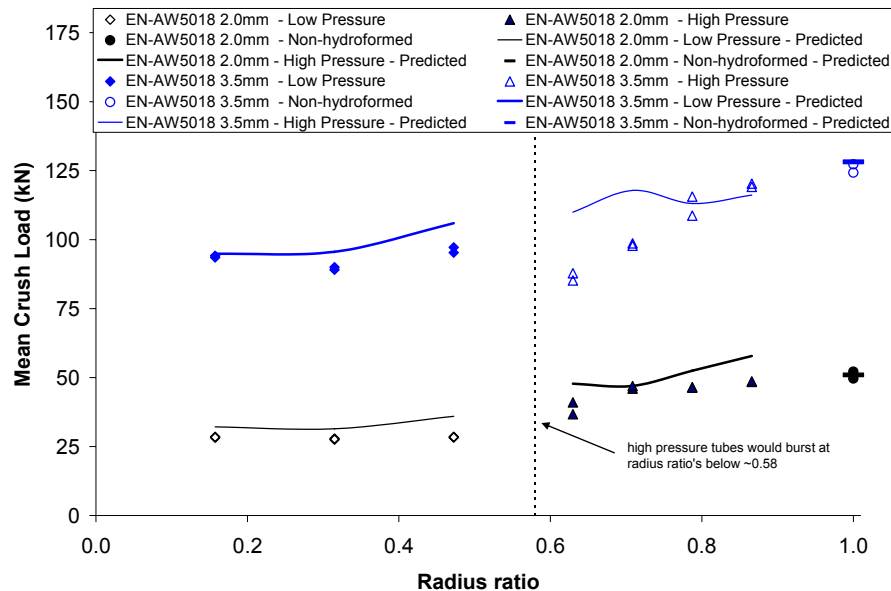
Figure 6.16: Predicted and measured mean crush loads for EN-AW 5018 axial crush structures

The results typically showed that the simulations over predicted the crush response. This over-prediction could have resulted because the initial peak load was not adequately captured in the simulations. In the experiments, the weld seam between the tube and the support plates could have acted as an initiation site for folding. This could have the effect of reducing the peak load, which could not be captured in the simulations, resulting in an over

prediction. The crush response for the 2 mm thickness tubes formed using the low pressure hydroforming process with a corner radius of 12 mm is shown in Figure 6.17. The mean crush load plot shows that the predicted peak load was much higher than that from the experiments, which helps to explain the over-prediction of mean load. The AA5754 axial crush tests were performed with crush initiators and were clamped, rather than welded to supports, to help better capture the initial peak load during an impact event.
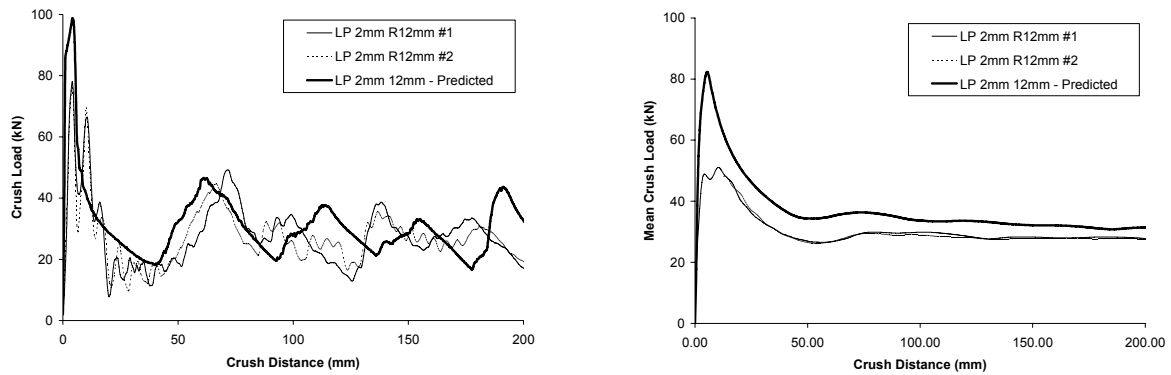
Figure 6.17: Crush response of EN-AW5018 tubes formed to 12 mm radius using low pressure hydroforming process

6.4 The Influence of Mass, Thickness, and Geometry on the Crush Response

As discussed in Chapter 2, one drawback of comparing specific energies (energy absorbed / mass) from the crush response is that the specific energy varies for tubes with different thickness and mass, which was partially explained using Equation 1.16, $P_m = 4\pi\sigma_0 w^{1/3} t^{5/3}$. In this research, the mass of the tubes formed using the high pressure hydroforming process was greater than the mass of the tubes formed using the low pressure process. It is a reasonable assumption that the mass of a tube is approximately proportional to its thickness for the tubes studied in this work. However, from Equation 1.16, it can be seen that, $P_m \propto t^{5/3}$, such that the specific energy increases with increasing thickness (or mass). Therefore, in order to compare the low and high pressure hydroforming operations, it is best to compare the crush response of tubes that are of the same mass. This would be expensive to accomplish experimentally because additional tubes with varying initial

diameter and thickness would be required to produce as-formed tubes with the same mass after hydroforming, as well as additional hydroforming equipment. As a result, this comparison of the crush response of tubes of the same mass was performed using finite element analysis.

Table 6.1 outlines five simulations developed to model the crush response of a tube with a 12 mm corner radius and an as-formed mass of approximately 920 grams after trimming to a length of 400 mm. In all cases, after the hydroforming simulation another simulation was performed to form the fold initiators, followed by the impact simulation. Conditions #1 and #3 correspond to the predicted crush response presented in Figure 6.15 for tubes hydroformed to a 12 mm corner radius with 60 mm of end-feed, with and without annealing.

The low pressure hydroforming experiments were conducted with a die of cross-section 65.5 mm and a corner radius of 12 mm. In order to produce a tube of 920 grams with this cross-section using the low pressure process, an initial tube thickness of about 3.70 mm was required in the model. A simulation was performed based on this initial thickness and the result is given in Table 6.1 as simulation #4.

The low pressure hydroforming operation could also be used to produce a tube with a 76.2 mm cross-section. A tube with an initial diameter of 87.3 mm requires a thickness of 3.11 mm to produce a 400 mm length tube weighing about 920 grams when using the low pressure operation without end-feeding. A new die geometry was modelled based on a cross-section of 76.2 mm, since the previous low pressure die geometry was based on a cross-section of 65.5 mm. The results from this condition are listed as simulation #2 in Table 6.1.

The final simulation, #5, was performed based on a tube with an initial diameter of 65.5 mm and thickness of 3.70 mm, formed using the high pressure process with end-feeding. The end-feeding profile given in Figure 2.15 was used in the simulation with 60 mm of end-feed at each end of the tube. This process was required in order to produce a tube with a mass of approximately 920 grams.

Table 6.1: Predicted axial crush results of tubes with mass of approximately 920 grams

Simulation	Hydroforming Process	End-Feed (mm)	Initial Tube Diameter (mm)	Initial Thickness (mm)	Cross-Sectional Width (mm)	Energy Absorption (J)	Distance at EA (mm)	Mean Load (kN)
#1	HP - annealed	60	76.2	3.07	76.2	9813.1	199.3	49.2
#2	LP	0	87.3	3.11	76.2	11575.3	199.2	58.1
#3	HP	60	76.2	3.07	76.2	13397.1	199.2	67.2
#4	LP	0	76.2	3.70	65.5	13658.4	175.8	77.7
#5	HP	60	65.5	3.70	65.5	13652.1	140.8	97.0

Figure 6.18 compares the mean loads obtained from the five simulations, showing that a 97% difference between the predicted loads can be obtained from the various conditions, even though the mass of the tubes was the same. The crush force versus crush distance curves can be found in Appendix D.
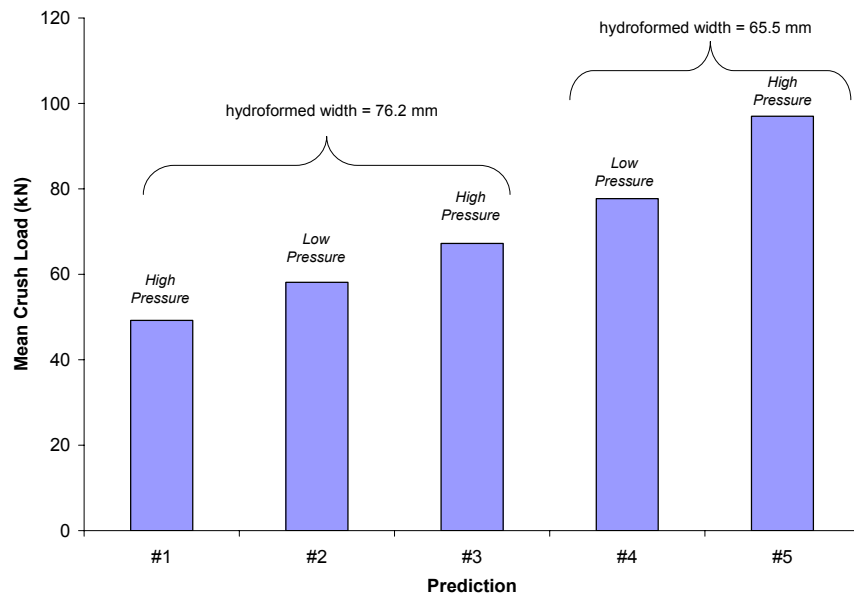
Figure 6.18: Comparison of predicted mean loads for AA5754 tube with approximate mass of 920 grams formed using different processes

From Equation 1.16, $P_m = 4\pi\sigma_0 w^{1/3} t^{5/3}$, it can be seen that in order to increase the mean load during axial crush, the cross-sectional width, w, should be reduced to increase the thickness, t. Also, the high pressure hydroforming process should be used to obtain greater work hardening (increased σ_0) compared to the low pressure process. This is confirmed with the results presented in Table 6.1 and Figure 6.18 where Simulation #5, corresponding to a high pressure process with the lower width, resulted in the highest mean crush load. Of all the simulations in Table 6.1, Simulation #5 had the smallest cross-section, largest thickness, and the greatest amount of work hardening.

Because of the variation in energy absorption that can be obtained for tubes of the same mass, caution should be used when trying to compare the energy absorption from axial crush between tubes of different material and density. It would be best to compare tubes formed using the same hydroforming process with the same cross-sectional geometry and mass. If a comparison were made between the AA5754 and EN-AW 5018 alloy tubes, it would be found that the EN-AW 5018 would have better energy absorption characteristics (if all other parameters were the same) since it has a higher strength. As shown in Chapter 2, the ultimate tensile strength of the EN-AW 5018 alloy is about 300 MPa versus 225 MPa for the AA5754 alloy.

For materials of different density, the following approach based on the theoretical equations is suggested to compare the energy absorption capabilities. For a square tube with no corner radius, the mass, m, can be approximated by,

$$m = 4wlt\rho \tag{6.1}$$

where, l is the length of the tube, w is the width of the tube, t is the thickness of the tube, and ρ is the density of the material. For two tube materials with different density, but equal mass, length, and width, Equation 6.1 can be used to show that,

$$t_2 = t_1 \frac{\rho_1}{\rho_2} \tag{6.2}$$

The energy absorption, EA, of the tube can be calculated as, $EA = P_m l$, where the mean load for a square tube is given by Equation 1.16. The predicted energy absorption for two

materials with different density can be compared using Equations 1.16 and 6.2, resulting in the following expression,

$$EA_2 = \left(\frac{\sigma_{02}}{\rho_2^{5/3}} \right) \left(\frac{\rho_1^{5/3}}{\sigma_{01}} \right) EA_1 \qquad (6.3)$$

This relationship shows that the material with the highest energy absorption capabilities can be determined by selecting the material with the highest value for the parameter, $\sigma_0 / \rho^{5/3}$. This relationship should be validated in future work by comparing the axial crush response from testing of materials such as high-strength steel to that of aluminum.

6.5 Influence of Forming History on the Crush Response

The forming history data transferred forward from the hydroforming simulation was comprised of the predicted thickness changes, work hardening (current flow stress), and residual stresses. In order to isolate the effect of each of these history variables on the energy absorption during impact, additional simulations were performed. The crush response curves for these simulations can be found in Appendix D.

For tubes formed using the low pressure hydroforming operation, three additional simulation conditions were performed: i) no thickness change but with work hardening and residual stress from the forming operation, ii) including thickness changes from hydroforming but without work hardening and residual stresses, and iii) only residual stresses were not included. The results of these simulations are compared in Figure 6.19 for a tube formed to a 6 mm corner radius using the low pressure process. The results show that there is no significant difference in the predicted mean load from simulations with the initial thickness of 3.07 mm and simulations in which the thickness changes from hydroforming were included. This close correspondence was expected since during the low pressure hydroforming operation the thickness of the tube did not change. The results also show that the residual stresses did not affect the energy absorption characteristics during impact. The most significant changes resulted when the work hardening was included indicating that strengthening effects due to forming must be included in the crash models.

143
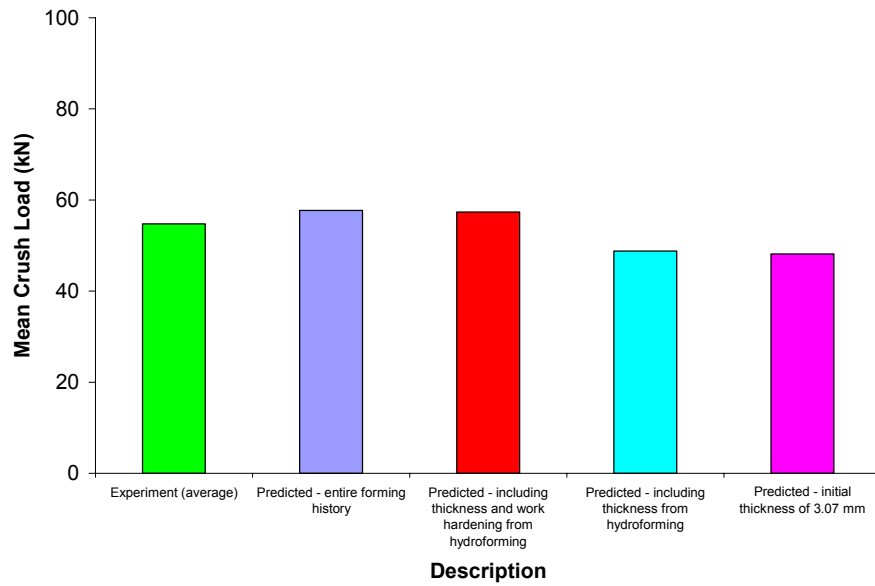
Figure 6.19: Influence of thickness, work hardening, and residual stresses on the predicted crush response of an AA5754 tube formed to a 6 mm radius using the low pressure process

Figure 6.20 shows the results from simulations of AA5754 alloy tubes with 6, 12, and 18 mm corner radii formed using the low pressure process, comparing the predicted mean loads to the measured data. The predicted mean loads from simulations with the entire forming history were greater by about 16%, compared to the cases in which work hardening was not included (which would be similar to annealed tubes), demonstrating the importance of accounting for the work hardening from the hydroforming operation.

Similar impact simulations were performed based on tubes formed using the high pressure hydroforming operation with 60 mm of end-feed. However, an additional condition was analysed, in which the initial tube thickness of 3.07 mm was used with the work hardening due to hydroforming. The results of these simulations are presented in Figure 6.21 for an AA5754 alloy tube formed to a 6 mm corner radius using the high pressure process. The results again showed that residual stresses had little influence on the energy absorption characteristics. However, in the high pressure case, thickness changes, mainly due to thinning in the corner regions, did affect the crush response of the tube compared to the case in which a nominal thickness of 3.07 mm was used. The simulation performed with an initial thickness of 3.07 mm in which work hardening was included had a mean load which was

144

11% higher compared to the simulation in which the predicted thickness changes were included. This indicates that thinning during hydroforming can reduce the energy absorption capabilities of the axial crush structure.
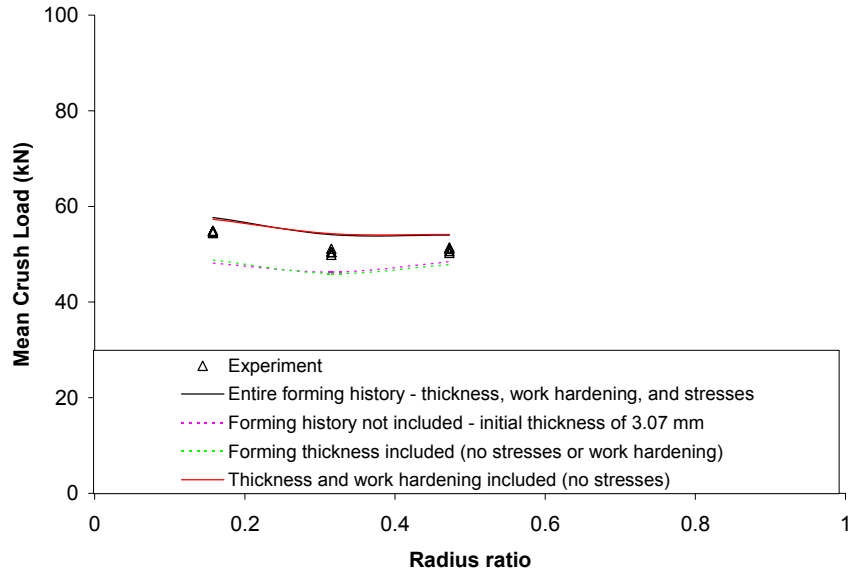
Figure 6.20: Effect of forming history on crush response for tubes formed using low pressure hydroforming process
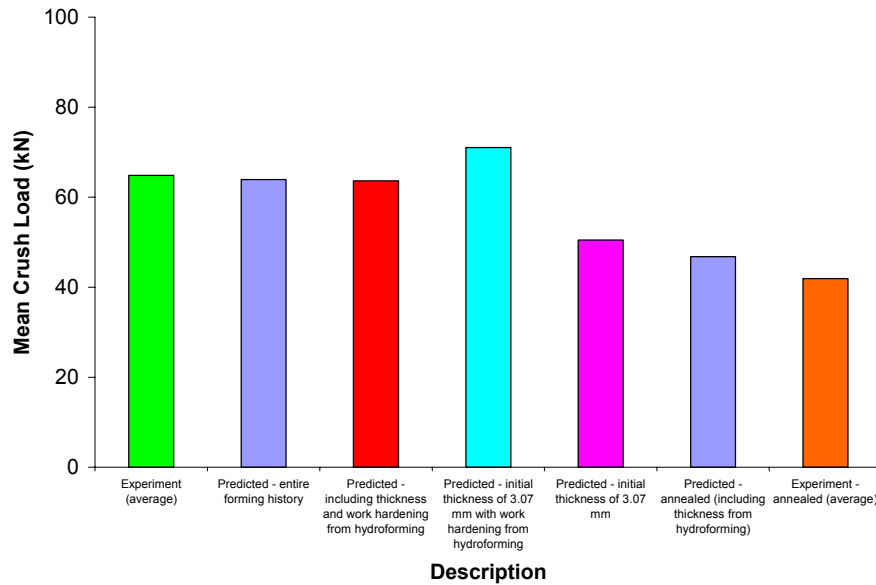
Figure 6.21: Influence of thickness, work hardening, and residual stresses on the predicted crush response of an AA5754 tube formed to a 6 mm radius using the high pressure process

The axial crush loads from simulations performed with AA5754 alloy tubes hydroformed to 6, 12, and 18 mm corner radii using the high pressure process with 60 mm of end-feed are presented in Figure 6.22 and compared with experimental data. As with the low pressure results, the most significant increases in energy absorption were predicted when work hardening was included. The mean crush loads increased by about 40% compared to the cases in which work hardening was not included, which would correspond to annealed tubes. The increase in mean load due to work hardening (resulting mainly from the material being formed in the corner regions) was much higher than the decrease due to thinning in the corner regions. This shows that work hardening is the most important forming effect from the hydroforming operations to consider in the axial crush simulations.
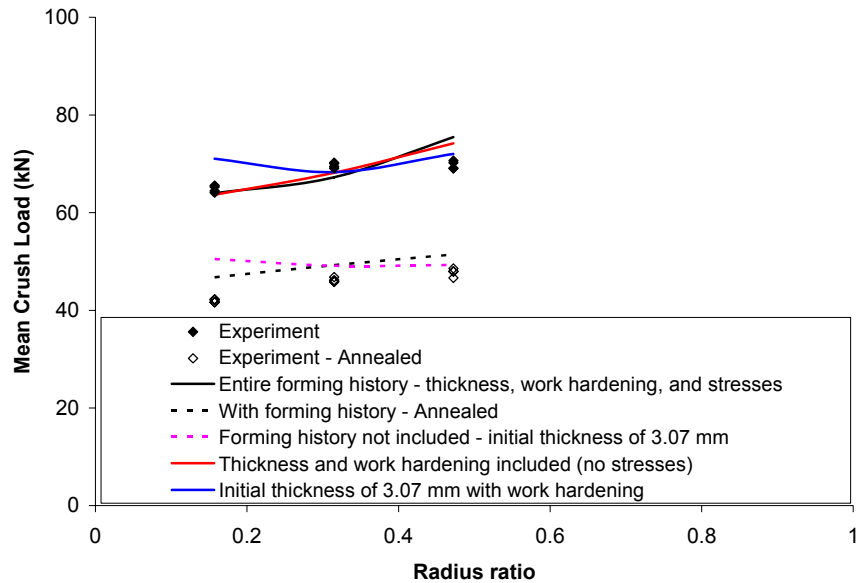
Figure 6.22: Effect of forming history on crush response for tubes formed using high pressure hydroforming process

The results demonstrate that it is important to consider thickness changes and work hardening from the hydroforming operation for subsequent deformation events, such as crash. Residual stresses from the hydroforming operation did not significantly affect the predicted crush response of the tube. These observations are similar to the conclusions of Kellicut et al. [32] who studied the crash response of a hydroformed S-shaped structure through simulation.

146

6.6 Axial Crush Predictions using GTN Damage Model

An investigation was performed to compare the measured crush response of hydroformed EN-AW 5018 alloy tube to the results of simulations incorporating the Gurson-Tvergaard-Needleman damage model. The details of this investigation are summarized by Williams et al. [81] and the predicted crush response from the GTN models of the EN-AW 5018 tubes are not presented in this thesis. However, an important result from this initial study was that a stress-based nucleation criterion (Equation 1.47) should be used instead of a strain-based nucleation criterion (Equation 1.46). The strain-based criterion, which calculates void nucleation as a function of the effective plastic strain, allowed void nucleation on the compressive side of the bend since the effective plastic strain was positive. However, the stress-based criterion treats the void nucleation rate as a function of the stress triaxiality. In compression, the hydrostatic stress would be negative, thereby preventing void nucleation.

GTN based numerical simulations of the crush response of the AA5754 alloy tubes are presented in this section. Results for tubes formed using the high pressure process with 60 mm of end-feed are presented in Figure 6.23 and compared to experimental data. The crush force versus displacement responses are presented in Appendix E. The von Mises simulations, also shown in the figure, were performed by setting the initial porosity and second phase particle fraction to zero and setting the nucleation stress to a very large value. The results show that the predictions between the two conditions are almost identical, indicating that in cases where the porosity is small (low levels of damage), there is no significant effect on the energy absorption capabilities of the material during axial crush. This shows that the GTN constitutive model need only be considered if fracture is likely to occur.

In order to investigate the level of damage predicted using the GTN model, two hydroforming experiments were considered. One case considered high pressure hydroforming of an AA5754 tube with an end-feed of 60 mm while the second considered an end-feel level of 30 mm, at each end of the tube. The end-feed displacement versus internal tube pressure profile for this second case is shown in Figure 6.24. The lower end-feed level was used to promote burst since burst did not occur for end-feed levels of 40 mm or greater. In this case, the tube burst at about 44 MPa.
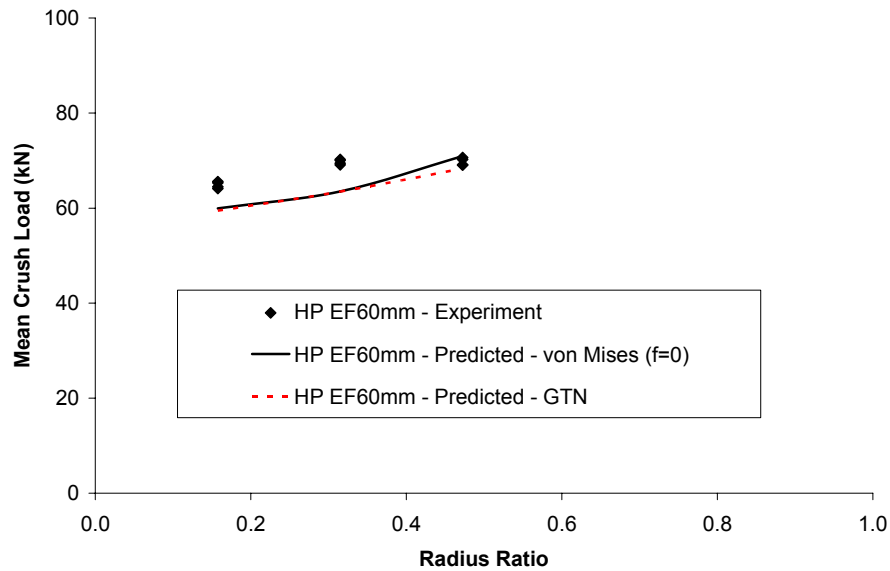
Figure 6.23: Predicted crush response of impacted tubes based on GTN and isotropic yielding criteria
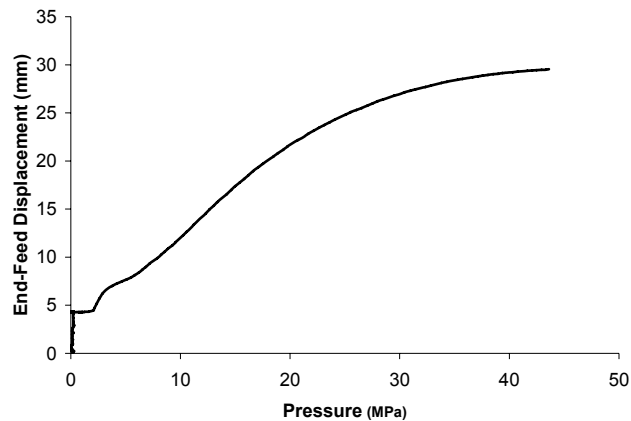
Figure 6.24: End-feed vs. pressure profile used for burst testing of AA5754 tubes

A simulation of the 30 mm end-feed experiment was performed using a nucleation stress of 550 MPa. A contour plot of the porosity for the outer surface of the tube is shown in Figure 6.25a, showing that the highest level of predicted porosity is 0.0031 on the outer surface of the tube with an average of 0.0027 for all points through the thickness at this location. This value was then compared to the porosity obtained from the simulation of the case with 60 mm of end-feed, for which the experimentally formed tube did not burst. A

contour plot of the porosity obtained on the outer surface of the tube is shown in Figure 6.25b that indicates the highest porosity at the end of the simulation was 0.0062 with an average porosity of 0.0036 considering all points through the thickness. This value is much higher than the value obtained from the burst simulation indicating that the simulation would have predicted failure in the 60 mm case which did not occur experimentally. This comparison shows that the current finite element models cannot be used to accurately predict failure of the tube. The primary reason for this is the adoption of shell elements which are not able to capture necking.
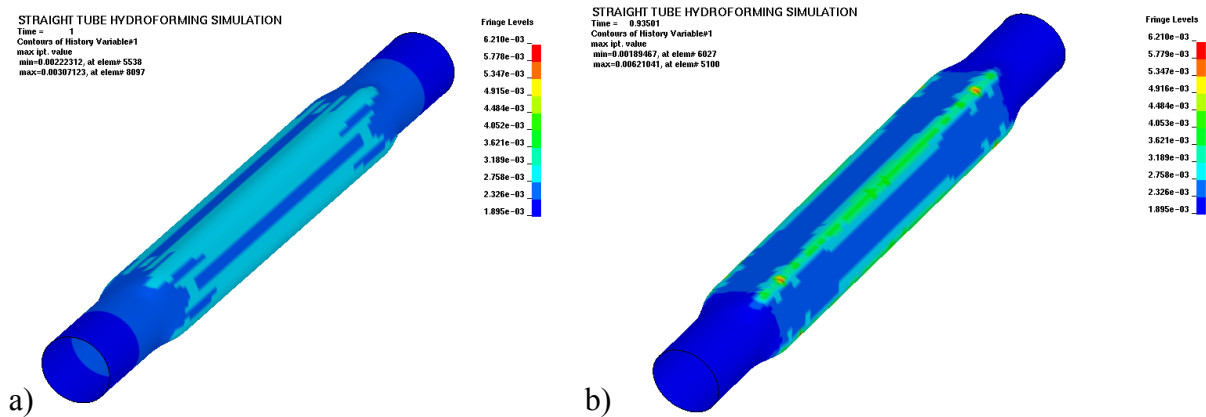
Figure 6.25: Contour plot of porosity for a) burst simulation and b) tube formed to a corner radius of 12 mm with 60 mm of end-feed

A cross-section of the burst tube is shown in Figure 6.26, showing significant thinning in the immediate vicinity of the fracture, indicating necking. During the neck, the strain localized such that it would have been high enough to cause damage to nucleate, perhaps within shear bands, leading to fracture. In order to account for damage in the neck, the finite element simulations must be capable of predicting necking. This could not be achieved when considering the current shell element formulation, but may be possible using brick elements that can capture necking modes of deformation. Future research could consider trying to capture the strain state during necking in hydroforming.

necking
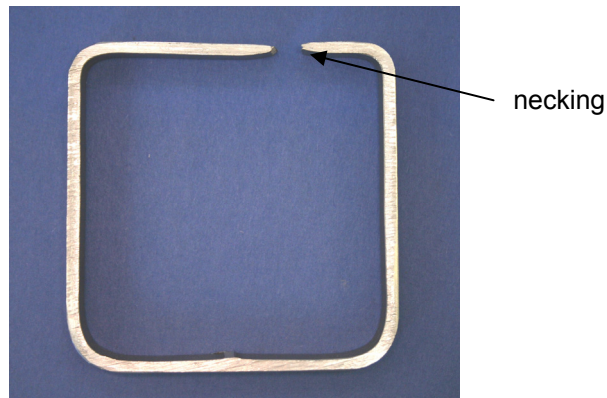
Figure 6.26: Section of AA5754 tube formed to burst with high pressure forming process

6.7 Influence of Strain-Rate, Kinematic Hardening, and Anisotropy

This section presents the predicted axial crush response that was obtained from the five different material models that were outlined in Chapter 4. In each case, the hydroforming, fold initiator, and impact simulations were all modelled using the same constitutive model. The predicted crush force versus distance response for each model presented in this section can be found in Appendix E, as well as the tabulated mean crush loads which were taken at a crush distance of about 200 mm. All predicted axial crush results in this section were based on AA5754 tubes formed using the high pressure process using 60 mm of end-feed in either the as-formed condition or when annealed.

Figure 6.27 shows the predicted mean loads under isotropic yielding and hardening behaviour for each of the five models studied. The isotropic predictions using the Johnson-Cook model were performed by setting C_{JC} and m to zero and C_{kin} and γ were set to zero for the isotropic prediction with the kinematic hardening model. In the Yld2000-2d anisotropic model, the α parameters were set to one with a=2. The objective in performing these calculations was to confirm that all of these advanced constitutive model implementations produced the same results under an isotropic yield and hardening assumption.
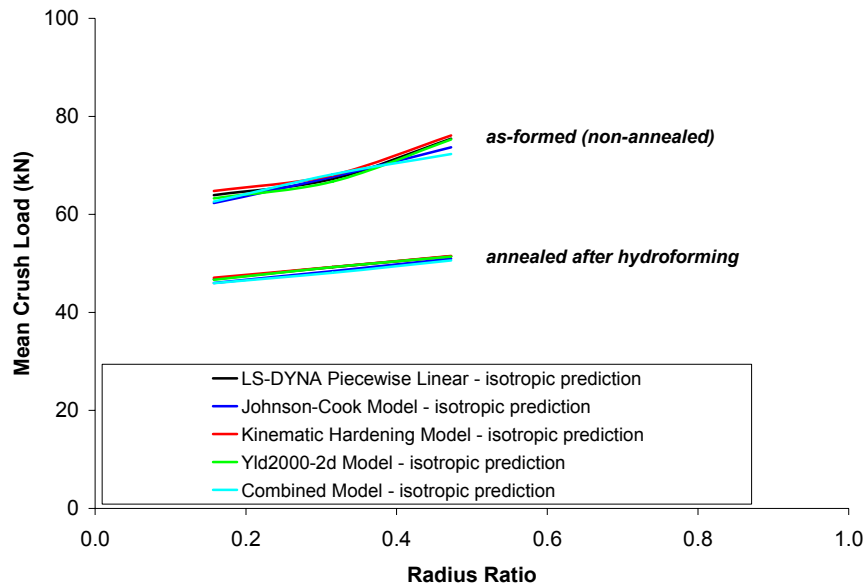
Figure 6.27: Comparison of isotropic crush response obtained from implementation of five different constitutive models

The average difference in the mean loads for a given condition (as-formed versus annealed) relative to the prediction performed using the von Mises and piecewise linear isotropic hardening model was 0.7%. The minor differences obtained for the isotropic solutions were attributed to slightly different convergence tolerances used in the various models. In all subsequent results presented below, the predicted mean loads from simulations incorporating the effects of strain-rate, kinematic hardening, and anisotropy are compared to isotropic predictions. The isotropic predictions were obtained by setting the constitutive parameters to values required to obtain an isotropic response, corresponding to the same constitutive model being considered.

Strain-rate and thermal softening effects were assessed by comparing the measured mean crush loads with predictions from isotropic simulations and simulations carried out with C_{JC} and m values of 0.006 and 2.4, respectively, as shown in Figure 6.28. The predicted increase of about 6% between the Johnson-Cook and isotropic simulations was expected since the C_{JC} value was calibrated to match the difference between dynamic and quasi-static results from the experiments which was also 6%. In general, the predicted responses including strain-rate effects were greater than the measured responses.

151
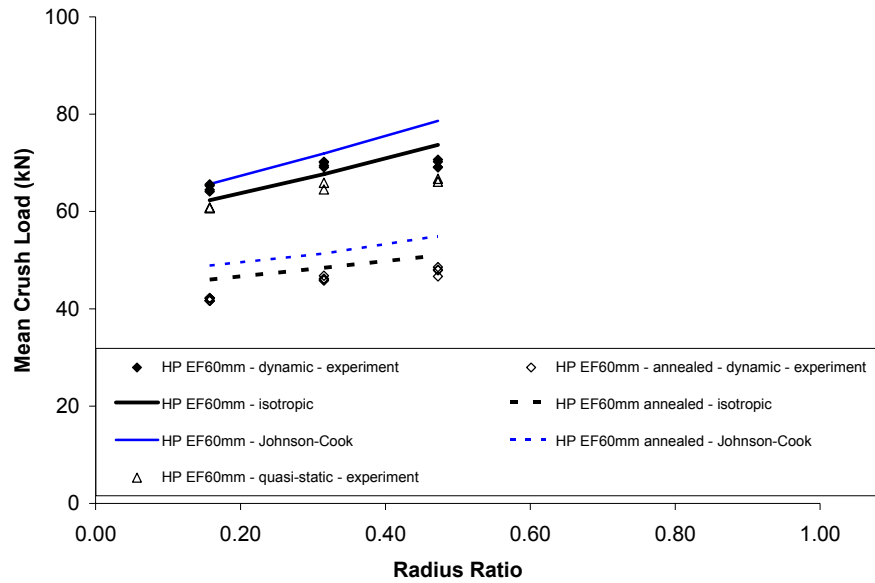
Figure 6.28: Comparison of predictions from the Johnson-Cook strain-rate model with isotropic predictions and measured data

Figure 6.29 compares the measured crush response with the predicted response from isotropic and kinematic simulations. There was approximately a 5% decrease between the isotropic and kinematic predictions for the non-annealed (as-formed) tubes. This shows that the compressive strains resulting from the end-feeding operation influenced the energy absorption during crash. However, there was about a 2% reduction between the isotropic and kinematic simulations for the tubes that were annealed. This shows that annealing removed most of the effects of the compressive pre-strains such that the Bauschinger effect was minimal.

As discussed in Section 5.4, the kinematic hardening behaviour of the material was not entirely captured based on the calibrated coefficients that were required in the model. The results presented in Figure 5.13, showed that in some cases the predicted hardening behaviour upon reverse loading did not match the measured data. If this transient response after yielding upon reverse loading could be better captured, which might require defining multiple yield surfaces [109], a greater than 5% difference might be predicted.
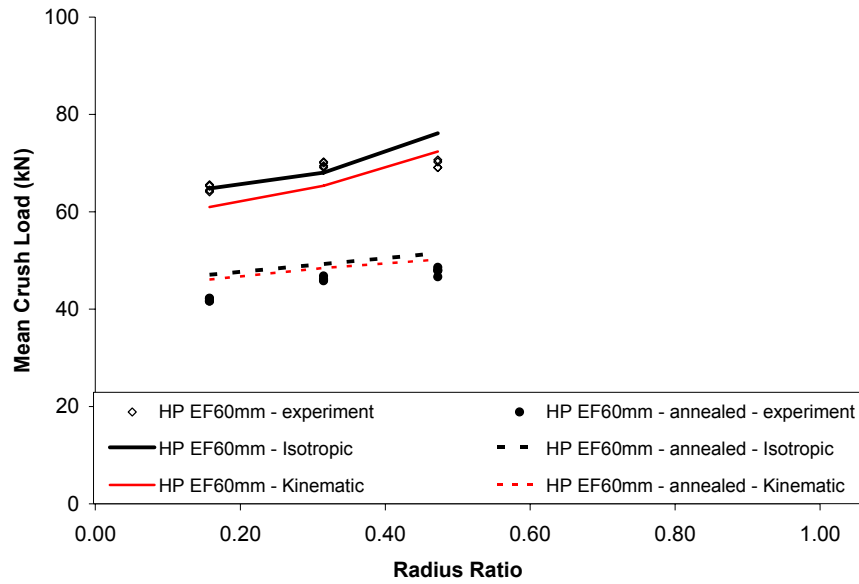
Figure 6.29: Comparison of predictions from the Chaboche-type isotropic-kinematic hardening model with isotropic predictions and measured data

Simulations were performed to isolate the effect of anisotropy using both sets of parameters in Table 5.2. The predicted mean loads from axial crush are compared to measured data in Figure 6.30. The results from both sets of anisotropy parameters show that the Yld2000-2d response under predicted the isotropic predictions by about 10%. Generally, the figure shows that the anisotropic mean crush load predictions were less than the measured mean loads, particularly for the tubes that were not annealed after hydroforming.

In the Yld2000-2d model, the shape of the yield surface (Figure 5.17) remains constant for all levels of effective plastic strain which was based on the results of experimental testing of specimens for which the effective strains were not much greater than about 15%. In the folds of the axial crush structure, the strain levels are much higher. Therefore, the shape of the yield surface should be studied at higher levels of deformation, perhaps approaching an effective strain level of 100%. It is suggested that a study of this nature be performed using crystal plasticity formulations, since it would be very difficult to obtain experimental data at effective strain levels of 100% with sheet material. The results of such an investigation could be used to verify the accuracy of the predicted 10% reduction in

153

energy absorption characteristics of the AA5754 structure obtained using the Yld2000-2d anisotropic constitutive model.
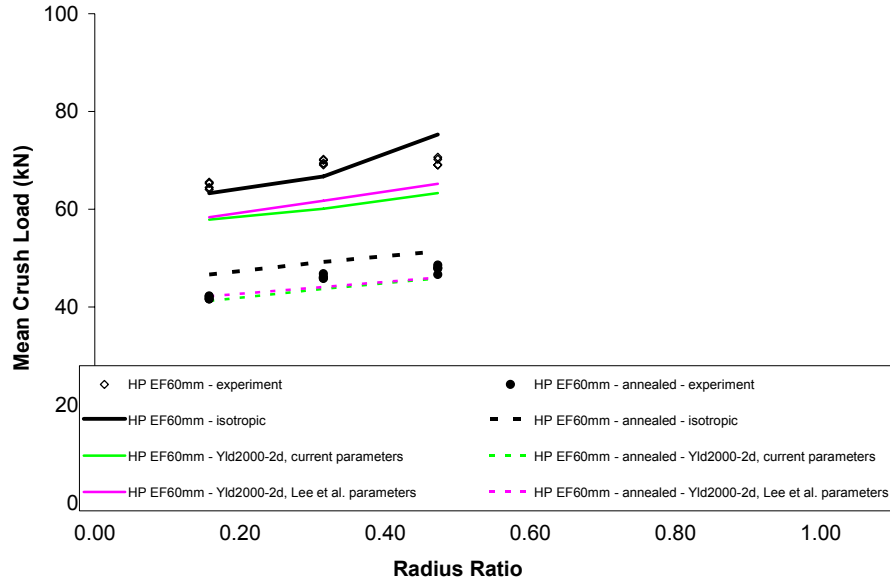
Figure 6.30: Comparison of predictions from the Yld2000-2d anisotropic model with isotropic predictions and measured data

The results of simulations performed using the constitutive model combining the effects of strain-rate, kinematic hardening, and anisotropy are presented in Figure 6.31. The isotropic predictions were also performed using the combined model. The anisotropic parameters were based only on the current parameter set given in Table 5.2. The mean crush loads from the simulations including the effects of strain-rate are about 4% greater than the isotropic predictions and the predictions including kinematic hardening effects are about 4% less than the isotropic predictions. These values are slightly different than the average increase of 6% due to strain-rate (Figure 6.28) and 5% decrease due to kinematic hardening (Figure 6.29) that were presented above which could be attributed to slightly different implementations of the constitutive models in the finite element code. The anisotropic predictions were an average of 9% less than the isotropic predictions which is similar to the 10% reduction observed in Figure 6.30. The predictions, when including all three effects are about 8% less than the isotropic predictions. In Figure 6.31d, the mean load predictions for the tubes with 12 and 18 mm corner radii that were not annealed are less than the measured

data. However, the other predictions are in reasonable agreement with the measured data. Generally, the results suggest that increases in energy absorption due to strain-rate effects are counteracted by decreases in the energy absorption due to kinematic hardening and anisotropy. However, the reduction in the predicted mean load due to kinematic hardening and anisotropy is greater than the increase in mean load due to strain rate effects, resulting in an overall decrease in the predicted mean load relative to the isotropic prediction.
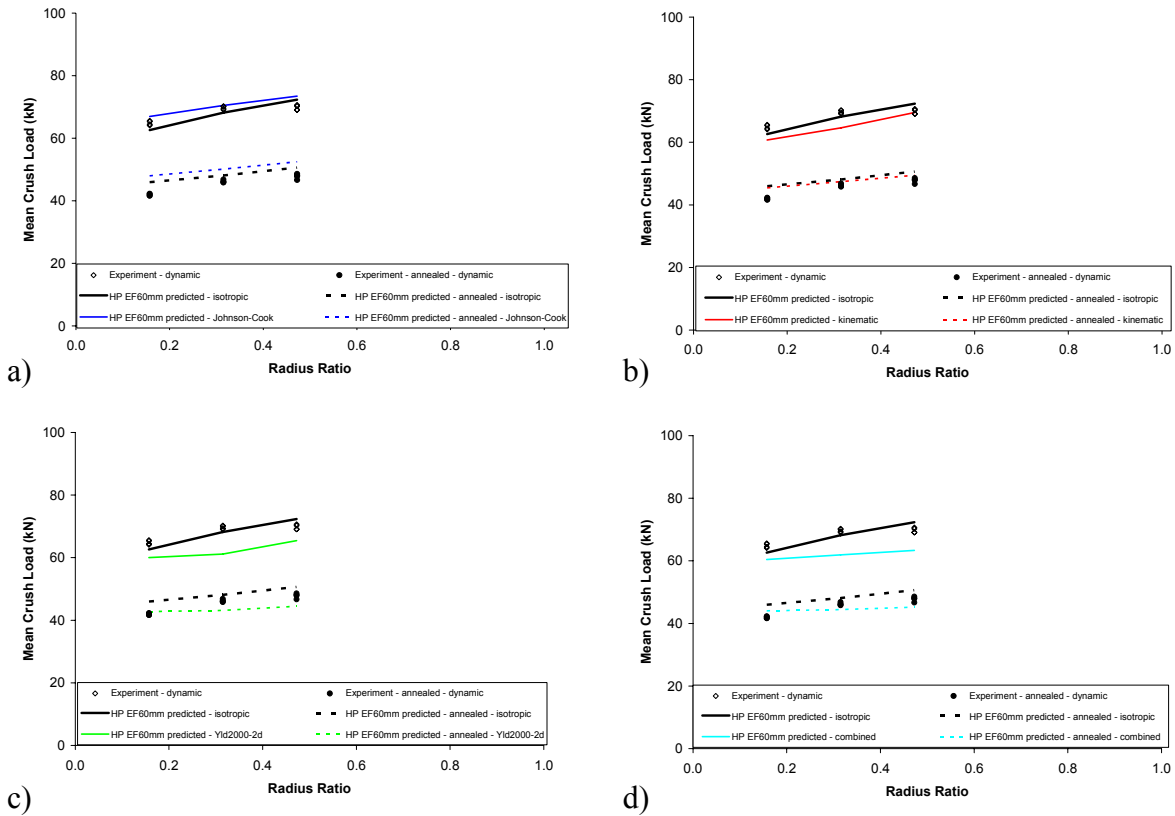
Figure 6.31: Comparison of predictions from the combined model with isotropic predictions and measured data a) Johnson-Cook response isolated, b) kinematic hardening response isolated, c) anisotropic response isolated, and d) response of all three effects combined

The current research has shown that it is important to account for kinematic hardening during axial crush of a hydroformed tube when end-feeding was used to form the tube. As a result, it is recommended to use a model combining the effects of strain-rate, kinematic hardening, and anisotropy to study impact problems where forming effects from previous operations are considered. Figure 6.32 presents the measured compression-tension

155

and tension-compression behaviour of a dual-phase steel obtained by Lee et al. [41], showing a significant Bauschinger effect. This effect would be important to capture if experiments similar to those performed in this research were carried out using dual-phase steels.
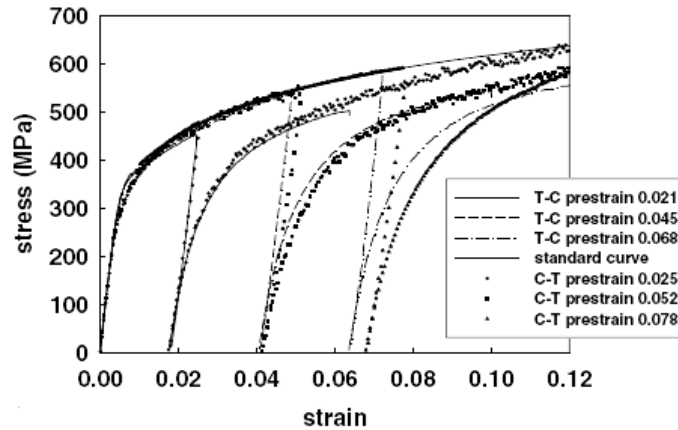
Figure 6.32: Stress-strain response from compression-tension and tension-compression tests of a dual-phase steel [41]

6.8 Discussion of the Combined Constitutive Model

There are several issues that arise when trying to develop a constitutive model incorporating strain-rate effects, kinematic hardening, and anisotropy that were not addressed in the combined model described above. Although the following issues are relevant, it would be difficult to speculate as to how they might affect the predicted results presented above for the AA5754 alloy considered in the current research.

The two parameters required for the kinematic hardening model and the eight coefficients determined to describe the materials anisotropic response were based on data from quasi-static testing. Therefore, further research should be performed to determine whether or not the parameters used in the anisotropic and kinematic hardening models vary with strain-rate.

When developing anisotropic constitutive models to describe the shape of the yield surface, most models describe the experimental behaviour based on data for which the effective strains are generally less than 30%. However, in the tight folds of the axial crush structure, the effective strains can reach much higher values than obtained from uniaxial

156

tests. The shape of the yield surface for a given shear stress will remain constant for all levels of effective strain with the Yld2000-2d model. Therefore, it is recommended that crystal plasticity be used to study the shape of the yield surface at high levels of deformation to determine whether or not the shape of the yield surface is affected.

Perhaps one of the most important effects that the combined model above does not account for is rotational hardening caused by plastic spin, as discussed by Dafalias [113,114]. Bunge and Nielson [115] measured texture development in pure aluminum sheet and observed a rotation rate of the reference system of 5° per 20% strain relative to the initial rolling direction. Similar rates were measured by Troung Qui and Lippmann [116] for aluminum sheet using macroscopic testing. As discussed by Han et al. [117], the plastic spin may be of minor importance for aluminum alloys in operations where deformation strains are less than 20%, but would be important in cases where the material deforms to high levels of strain. This is the case with the axial crush structure were the strain can reach very high values in the folds. Experiments by researchers such as Kim and Yin [118] show that the plastic spin is important to consider for steel sheet alloys even at lower deformation strains.

In order to determine the extent to which plastic spin affects the deformation behaviour of the AA5754 aluminum alloy used in the current research, it is again recommended to use crystal plasticity. This method is recommended to study deformation levels that reach levels of up to about 100%, which cannot be achieved experimentally for sheet material under all loading conditions.

Chapter 7 – Conclusions and Recommendations

7.1 Conclusions

The EN-AW 5018 alloy tubes did not incorporate crush initiators and were welded to support plates prior to the impact event. As a result, the weld seam between the tube and the support plates could have acted as an initiator reducing the peak load, which was not always captured in the simulations. The AA5754 axial crush tests were clamped to supports and did incorporate crush initiators for impact. It was then found that the measured peak load was better captured in the simulation results compared to the EN-AW 5018 crush results. In general, there was reasonable agreement between the experimental and simulation results when considering the von Mises yield criterion with isotropic material behaviour in the finite element models.

The measured results were also compared to predictions from theoretical equations. However, several assumptions were required in the analytical equations of the hydroforming operation that would limit their use to certain geometry and loading conditions. Also, the theoretical equations do not account for material non-linearity effects such as kinematic hardening and anisotropy. As a result, it is suggested that the analytical predictions only be used to gain insight into the deformation behaviour during hydroforming and axial crush.

Finite element simulations were carried out with particular attention to the transfer of the forming history, comprising the thickness changes, work hardening (strain hardening), and residual stresses, from the hydroforming to impact simulation. The results from axial crush testing and simulations of both materials showed that the increasing thickness

reduction in the corners of the tube caused by circumferential expansion during hydroforming decreased the energy absorption capability of the tube during axial crush. However, it was shown that work hardening, mainly due to material forming into the corner regions during hydroforming, significantly increased the energy absorption capabilities during axial crush, more than counter-acting the effects of thinning. The experiments showed that annealing the tube after the hydroforming operation significantly reduced the energy absorption of the material, by about 33%, compared to cases in which tubes were not annealed. This reduction was accurately predicted in the finite element models. Residual stresses were shown to have little effect on the energy absorption during crash

The mean crush loads of tubes formed using the high pressure hydroforming process were greater than the mean crush loads of tubes formed using the low pressure process. However, end-feeding during the high pressure process increased the mass of the tube such that it was important to make a comparison of the crush response between tubes of the same mass. This was accomplished through simulation. It was found that the tube with the highest predicted mean load and energy absorption was one for which the width of the tube was the smallest such that the thickness of the tube was the greatest. Also, the high pressure hydroforming process induces higher levels of work hardening compared to a tube formed using the low pressure hydroforming process, which further increases energy absorption. Overall, it was found that a large range in energy absorption could be obtained for tubes with the same mass by varying the geometry, thickness, and amount of work hardening. As a result, caution should be exercised when trying to compare the axial crush energy absorption characteristics of different materials.

Although it was found that the predictions using an isotropic material behaviour with the von Mises yield criterion gave good agreement with the experimental data, this might have resulted because of counteracting effects of kinematic hardening, anisotropy, and strain-rate sensitivity. Constitutive models for the effects of strain-rate, kinematic hardening, and anisotropy were studied through finite element simulations, including a model combining all three effects. The combined model did not account for the effect of rotational hardening due to plastic spin.

Compression-tension tests in the current research showed that the AA5754 alloy was susceptible to the Bauschinger effect. Simulations performed using a non-linear isotropic-kinematic hardening model showed that a 5% decrease in the predicted mean load was obtained compared to the isotropic case. Simulations isolating the anisotropic response of the material showed that about 10% reductions in the mean load were predicted relative to the isotropic cases. Further investigation should be performed, perhaps involving crystal plasticity, to study the evolution of the anisotropic yield surface of the AA5754 alloy to help determine whether or not the predicted 10% reduction in the energy absorption capabilities was realistic. Comparison of quasi-static and dynamic crush tests showed that there was approximately a 6% increase in the dynamic results. The results from simulations incorporating all three effects showed that the predicted mean crush loads were about 8% less than the isotropic predictions.

The Gurson-Tvergaard-Needleman constitutive damage model was also used to predict the axial crush response, but it was found that damage had little influence on the predicted energy absorption response for the EN-AW 5018 and AA5754 alloys, in the absence of fracture. In order to account for fracture, it was deemed necessary to capture necking which was not plausible within the shell elements used in the simulations.

In summary, it was found that the most important factors to be considered in the finite element models of the axial crush operation for the AA5754 aluminum alloy were as follows:

1) work hardening resulting from the hydroforming operation - energy absorption increased

2) the anisotropic behaviour of the aluminum alloy - energy absorption decreased

3) thinning in the corners of the tube during hydroforming - energy absorption decreased

4) the strain-rate sensitivity of the aluminum alloy - energy absorption increased

5) the kinematic hardening behaviour - energy absorption decreased

6) residual stresses from the hydroforming operation - little effect on the energy absorption

7) damage due to void growth, nucleation, and coalescence - little effect on the energy absorption in the absence of failure

7.2 Recommendations

The current research has shown that, in addition to capturing the forming history in the crash models, it is also important to account for effects of material non-linearity such as kinematic hardening, anisotropy, and strain-rate effects in the finite element models. Therefore, it is recommended that a model combining these three effects be utilized when studying the crash behaviour of components that have undergone prior forming operations.

In the current investigation, two constant parameters were required for use with the non-linear isotropic-kinematic hardening model that were calibrated based on quasi-static testing. It is possible that these parameters can vary with strain-rate, such that high rate testing of pre-strained specimens could be performed using split-Hopkinson bar apparatus. Also, the kinematic hardening model used in the current research did not entirely capture the transient response of the material upon reverse loading. In order to better capture this response it is suggested that an alternate kinematic hardening model be utilized, perhaps one that involves defining multiple yield surfaces.

It is recommended to use crystal plasticity to study the yield surface response of the AA5754 alloy at high levels of deformation. Crystal plasticity could also be used to assess the effect of rotational hardening due to plastic spin from which the results could be used to incorporate plastic spin in the combined model.

It was found that the Gurson-Tvergaard-Needleman constitutive damage model did not adequately account for fracture during hydroforming. It is suggested that most of the damage occurs after a neck forms in the material which was not predicted in the simulations. As an alternative to damage based failure criteria, forming limit criteria could be employed which are based on the state of strain or stress required to cause necking. Simulations involving solid elements would allow a study to be performed involving stressed-based FLDs. To this date, stress-based FLDs have not been used to study the axial crush response of the tubes. It is suggested that a study should be performed using the results from quasi-static axial crush tests. One difficulty in applying forming limit criteria for dynamic cases is that the extent to which strain-rate (inertia) effects influence the necking behaviour of the material must be studied.

References

[1]   H. Singh, *Fundamentals of Hydroforming*, Society of Manufacturing Engineers, 2003.

[2]   N. Asnafi, "Analytical modelling of tube hydroforming", *Thin-walled Structures*, Vol. 34, pp. 295-330, 1999.

[3]   A. Cherouat, K. Saanouni, and Y. Hammi, "Numerical improvement of thin tube hydroforming with respect to ductile damage", *International Journal of Mechanical Sciences*, Vol. 44, pp. 2427-2446, 2002.

[4]   W.J. Sauer, A. Goteras, F. Roff, and P. Huang, "Free forming of tubes under internal pressure and axial compression", Trans. NAMRC-VI, Michigan, pp. 228-235, 1978.

[5]   S. Thiruvarudchelvan, G.L. Seet, and H.E. Ang, "Computer-monitored hydraulic bulging of tubes", *Journal of Materials Processing Technology*, Vol. 57, pp 182-188, 1996.

[6]   K. Trana, "Finite element simulation of the tube hydroforming process – bending, preforming, and hydroforming", *Journal of Materials Processing Technology*, Vol. 127, pp. 401-408, 2002.

[7]   N. Abedrabbo, N. Zafar, R. Averill, F. Pourboghrat, and R. Sidu, "Optimization of a Tube Hydroforming Process", Materials Processing and Design: Modeling Simulation and Applications, pp. 1172-1177, Numiform 2004 Proceedings, 2004.

[8]   S. Jirathearanat and T. Altan, "Optimization of Loading Paths for Tube Hydroforming", Materials Processing and Design: Modeling Simulation and Applications, pp. 1148-1153, Numiform 2004 Proceedings, 2004.

[9]   Z. Marciniak, J.L. Duncan, and S.J. Hu, *Mechanics of Sheet Metal Forming*, 2nd Edition, Butterworth-Heinemann, 2002.

[10]   K.I. Johnson, B.N. Nguyen, R.W. Davies, G.J. Grant, and M.A. Khaleel, "A numerical process control method for circular-tube hydroforming prediction", *International Journal of Plasticity*, Vol. 20, pp. 1111-1137, 2004.

[11]   A.L. Browne and N.L. Johnson, "Conducting Dynamics Impact Tests using a 'Free-Flight' Drop Tower Facility – Part I: Theory", Proceedings of 2001 ASME International Mechanical Engineering Congress and Exposition, New York, November 2001.

[12] N.L. Johnson and A.L. Browne, "Conducting Dynamics Impact Tests using a 'Free-Flight' Drop Tower Facility – Part II: Practical Aspects", Proceedings of 2001 ASME International Mechanical Engineering Congress and Exposition, New York, November 2001.

[13] R. Mayer, W. Chen, and A. Sachdev, "Crashworthiness Performance of Mass-Efficient Extruded Structures", Transportation: Making Tracks for Tomorrow's Transportation, pp. 183-205, 2002 ASME International Mechanical Engineering Congress and Exposition, November, 2002.

[14] N. Jones, *Structural Impact*, Cambridge University Press, 1989.

[15] J.M. Alexander, "An approximate analysis of the collapse of thin cylindrical shells under axial loading", *Quarterly Journal of Mechanics and Applied Mathematics*, Vol. 13, pp. 10-15, 1960.

[16] F.C. Bardi, H.D. Yun, and S. Kyriakides, "On the axisymmetric progressive crushing of circular tubes under axial compression", *International Journal of Solids and Structures*, Vol. 40, pp. 3137-3155, 2003.

[17] W. Abramowicz and N. Jones, "Dynamic axial crushing of circular tubes", *International Journal of Impact Engineering*, Vol. 2, pp 263-281, 1984.

[18] A.A. Singace, H. Elsobky, and T.Y. Reddy, "On the eccentricity factor in the progressive crushing of tube", *International Journal of Solids and Structures*, Vol. 32, pp. 3589-3602, 1995.

[19] T. Wierzbicki, S.U. Bhat, W. Abramowicz, and D. Brodkin, "Alexander revisited – A two folding element model of progressive crushing of tubes", *International Journal of Solids and Structures*, Vol. 29, pp. 3269-3288, 1992.

[20] T. Wierzbicki, "Optimum design of integrated front panel against crash", Report to Ford Motor Company, Vehicle Component Dept., 1983.

[21] A. Pugsley and M. Macaulay, "The large scale crumpling of thin cylindrical columns", *Quarterly Journal of Mechanics and Applied Mathematics*, Vol. 13, pp. 1-9, 1960.

[22] W. Abramowicz and N. Jones, "Dynamic axial crushing of square tubes", *International Journal of Impact Engineering*, Vol. 2, pp 179-208, 1984.

[23]   N.K. Gupta, "Some aspects of axial collapse of cylindrical thin-walled tubes", *Thin-Walled Structures*, Vol. 32, pp. 111-126, 1998.

[24]   M. Langseth and O.S. Hopperstad, "Static and dynamic axial crushing of square thin-walled aluminium extrusions", *International Journal of Impact Engineering*, Vol. 18. pp. 949-968, 1996.

[25]   K.C. Shin, J.J. Lee, K.H. Kim, M.C. Song, and J.S. Huh, "Axial crush and bending collapse of an aluminum/GFRP hybrid square tube and its energy absorption capability", *Composite Structures*, Vol. 57, pp. 279-287, 2002.

[26]   A.G. Mamalis, D.E. Manolakos, M.B. Ioannidis, and D.P. Papapostolou, "On the response of thin-walled CFRP composite tubular components subjected to static and dynamic axial compressive loading: experimental", *Composite Structures*, Vol. 69, pp. 407-420, 2005.

[27]   M. Langseth, O.S. Hopperstad, and A.G. Hanssen, "Crash behaviour of thin-walled aluminium members", *Thin-Walled Structures*, Vol. 32, pp. 127-150, 1998.

[28]   M. Langseth, O.S. Hopperstad, and T. Berstad, "Crashworthiness of aluminium extrusions: validation of numerical simulations, effect of mass ratio and impact velocity", *International Journal of Impact Engineering*, Vol. 22, pp. 829-854, 1999.

[29]   A. Otubushin, "Detailed validation of a non-linear finite element code using dynamic axial crushing of a square tube", *International Journal of Impact Engineering*, Vol. 21, pp. 349-368, 1998.

[30]   V. Tarigopula, M. Langseth, O.S. Hopperstad, and A.H. Clausen, "Axial crushing of thin-walled high-strength steel sections", *International Journal of Impact Engineering*, Vol. 32, pp. 847-882, 2006.

[31]   C.A. Krauss and D.H. Laananen, "A parametric study of crush initiators for a thin-walled tube", *International Journal of Vehicle Design*, Vol. 15, pp. 385-401, 1994.

[32]   A. Kellicut, B. Cowell, K. Kavikondala, T. Dutton, S. Iregbu, and R. Sturt, "Application of the results of forming simulation in crash models", Numiform 1999 Proceedings, pp. 509-514, 1999.

[33]   W.F. Hosford, "A generalized isotropic yield criterion", *Journal of Applied Mechanics*, Vol. 39, p. 607, 1972.

[34]   A.P. Karafillis and M.C. Boyce, "A general anisotropic yield criterion using bounds and a transformation weighting tensor", *Journal of the Mechanics and Physics of Solids*, Vol. 41, pp. 1859-1886, 1993.

[35]   R. Hill, "A theory of the yielding and plastic flow of anisotropic materials", *Proc. Roy. Soc. London* A193, pp. 281-297, 1948.

[36]   F. Barlat and J. Lian, "Plastic behaviour and stretchability of sheet materials. Part I: a yield function for orthotropic sheets under plane stress conditions", *International Journal of Plasticity*, Vol. 5, pp. 51-66, 1989.

[37]   F. Barlat, D.J. Lege, and J.C. Brem, "A six-component yield function for anisotropic materials", *International Journal of Plasticity*, Vol. 7, pp. 693-712, 1991.

[38]   F. Barlat, Y. Maeda, K. Chung, M. Yanagawa, J.C. Brem, Y. Hayashida, D.J. Lege, K. Matsui, S.J. Murtha, S. Hattori, R.C. Becker, and S. Makosey, "Yield function development for aluminum alloy sheets", *Journal of the Mechanics and Physics of Solids*, Vol. 45, pp. 1727-1763, 1997.

[39]   F. Barlat, J.C. Brem, J.W. Yoon, K. Chung, R.E. Dick, D.J. Lege, F. Pourboghrat, S.H. Choi, and E. Chu, "Plane stress yield function for aluminum alloy sheets – part 1: theory", *International Journal of Plasticity*, Vol. 19, pp. 1297-1319, 2003.

[40]   J. Yoon, F. Barlat, R.E. Dick, K. Chung, and T.J. Kang, "Plane stress yield function for aluminum alloy sheets – part II: FE formulation and its implementation", *International Journal of Plasticity*, Vol. 20, pp. 495-522, 2004.

[41]   M. Lee, D. Kim, C. Kim, M.L. Wenner, R.H. Wagoner, and K. Chung, "Spring-back evaluation of automotive sheets based on isotropic-kinematic hardening laws and non-quadratic anisotropic yield functions Part II: characterization of material properties", *International Journal of Plasticity*, Vol. 21, pp. 883-914, 2005.

[42]   F. Barlat, H. Aretz, J.W. Yoon, M.E. Karabin, J.C. Brem, and R.E. Dick, "Linear transformation based anisotropic yield functions", *International Journal of Plasticity*, Vol. 21, pp. 1009-1039, 2005.

[43]   J. Lemaitre and J.L. Chaboche, *Mechanics of solid materials*, Cambridge University Press, 1990.

[44]   W. Prager, "A new method of analyzing stresses and strains in work-hardening", Plastic solids, *Journal of Applied Mechanics,* ASME 23, pp. 493-496, 1956.

[45] P.J. Armstrong and C.O. Frederick, "A Mathematical Representation of the Multiaxial Bauschinger Effect", G.E.G.B. Report RD/B/N, p. 731, 1966.

[46] B.K. Chun, J.T. Jinn, and J.K. Lee, "Modeling the Bauschinger effect for sheet metals, part I: theory", *International Journal of Plasticity*, Vol. 18, pp. 571-595, 2002.

[47] J.L. Chaboche, "On some modifications of kinematic hardening to improve the description of ratchetting effects", *International Journal of Plasticity*, Vol. 7, pp. 661-678, 1991.

[48] U.S. Lindholm, R.L. Bessey, and G.V. Smith, "Effect of Strain Rate on Yield Strength, and Elongation of Three Aluminum Alloy", *Journal of Materials*, JMLSA, Vol. 6, pp. 119-133, 1971.

[49] R. Smerd, S. Winkler, C. Salisbury, M. Worswick, D. Lloyd, and M. Finn, "High strain rate tensile testing of automotive aluminum alloy sheet", *International Journal of Impact Engineering*, Vol. 32, pp. 541-560, 2005.

[50] C.P. Salisbury, M.J. Worswick, and R. Mayer, "High rate constitutive modeling of aluminium alloy tube", Proceedings – 8th International Conference on Mechanical and Physical Behaviour of Materials under Dynamic Loading, *Journal De Physique IV*, Vol. 134, pp. 43-48, 2006.

[51] G.R. Johnson and W.H. Cook, Proc. 7th Intern. Symp. Ballistics, Am. Def. Prep. Org. (ADPA), Netherlands, 1983.

[52] F.J. Zerilli and R.W. Armstrong, "The effect of dislocation drag on the stress-strain behaviour of F.C.C metals", *Acta Metallurgia et Materialia*, Vol. 40, pp. 1803-1808, 1992.

[53] G.R. Johnson and W.H. Cook, "Fracture characteristics of three metals subjected to various strains, strain rates, temperatures and pressures", *Engineering Fracture Mechanics*, Vol. 21, pp. 31-48, 1985.

[54] J.E. Bird and J.M. Carlson, "Shear band formation during sheet-forming", *Journal of Metals*, Vol. 38, pp. 47-54, 1986.

[55] A.R. Rosenfield, "Criteria for Ductile Fracture of Two-Phase Alloys", *Metallurgical Reviews*, Vol. 13, pp. 29-40, 1968.

[56]   R.H. Van Stone, T.B. Cox, J.R. Jr. Low and J.A. Psioda, "Microstructural Aspects of fracture by dimpled rupture", *International Metals Reviews*, Vol. 30, pp. 157-179, 1985.

[57]   C.I.A. Thomson, Modeling the Effect of Particle Clustering on Ductile Failure, *Ph.D. Thesis*, Carleton Institute for Mechanical and Aerospace Engineering, Ottawa, 2001.

[58]   M.F. Ashby, J.D. Embury, S.H. Cooksley, and D. Teirlinck, "Fracture Maps With Pressure as a Variable", *Scripta Metallurgica*, Vol. 19, pp. 385-390, 1985.

[59]   S.P. Keeler and W.A. Backhofen, "Plastic instability and fracture in sheet stretched over rigid punches", *ASM Trans. Q.*, Vol. 56, pp. 25-48, 1964.

[60]   G.M. Goodwin, "Application of strain analysis to sheet metal forming in the press shop", SAE paper No. 680093, 1968.

[61]   A.K. Ghosh and J.V. Laukonis, "The influence of strain path changes on the formability of sheet steel", 9th Biennial Congress of the IDDRG, *Sheet Metal Forming and Energy Conservation*, ASM Publication, 1976.

[62]   A.F. Graf and W.F. Hosford, "Calculations of forming limit diagrams for changing strain paths", *Metall. Trans. A.*, Vol. 24, pp. 2497-2501, 1993.

[63]   T.B. Stoughton, "Stress-Based Forming Limits in Sheet-Metal Forming", *Journal of Engineering Materials and Technology*, Vol. 123, pp. 417-422, 2001.

[64]   T.B. Stoughton, "A general forming limit criterion for sheet metal forming", *International Journal of Mechanical Sciences*, Vol. 42, pp. 1-27, 2000.

[65]   A.L. Gurson, "Continuum Theory of Ductile Rupture by Void Nucleation and Growth: Part I-Yield Criteria and Flow Rules for Porous Ductile Media", *Journal of Engineering Materials and Technology*, Vol. 99, pp. 2-15, 1977.

[66]   V. Tvergaard, "Influence of Voids on Sheer Band Instabilities Under Plane Strain Condition", *International Journal of Fracture*, Vol. 17, pp. 389-407, 1981.

[67]   V. Tvergaard, "On Localization in Ductile Materials Containing Spherical Voids", *International Journal of Fracture*, Vol. 18, pp. 237-252, 1982.

[68]   V. Tvergaard and A. Needleman, "Analysis of the Cup-Cone Fracture in A Round Tensile Bar", *Acta Metallurgica*, Vol. 32, pp. 157-169, 1984.

[69] J. Gholipour, M.J. Worswick, D.A. Oliveira, and G. Khodayari, "Severity of the bend and its effect on subsequent hydroforming process for aluminum alloy tube", Numiform 2004 Proceedings, 2004.

[70] J. Gholipour, Damage in Hydroforming of Pre-Bent Aluminum Alloy Tubes, *Ph.D. Thesis*, University of Waterloo, 2005.

[71] M.J. Worswick and R.J. Pick, "Void growth and constitutive softening in a periodically voided solid", *Journal of the Mechanics and Physics of Solids,* Vol. 38, pp. 601-625, 1990.

[72] C. Chu and A. Needleman, "Effect of yield surface curvature on necking and failure in porous plastic solids", *Journal of Applied Mechanics*, Vol. 53, pp. 491-499, 1980.

[73] H. Shakeri, Personal communication, Aluminum Technology Center, 2006.

[74] W.F. Smith, *Structure and Properties of Engineering Alloys*, McGraw-Hill Inc., 1993.

[75] G. D'Amours and A. Rahem, "High-Pressure Hydroforming of Straight Aluminum Tubes – Experimental and Numerical Results", Report to General Motors of Canada, December 2005.

[76] E. Voce, "The relationship between stress and strain for homogeneous deformation", *Journal of the Institute for Metals*, Vol. 74, p. 537, 1948.

[77] D. Nélias, C. Jacq, G. Lormand, G. Dudragne, and A. Vincent, "New Methodology to Evaluate the Rolling Contact Fatigue Performance of Bearing Steels With Surface Dents: Application to 32CrMoV12 (Nitrided) and M50 Steels", *Journal of Tribology*, Vol. 127, pp. 611-622, 2005.

[78] M. Koç, Y. Aue-u-lan, and T. Altan, "On the characteristics of tubular materials for hydroforming – experiments and analysis", *International Journal of Machine Tools & Manufacture*, Vol. 41. pp. 761-772, 2001.

[79] F. Barlat, J.M.F. Duarte, J.J. Gracio, A.B. Lopes, and E.F. Rauch, "Plastic flow for non-monotonic loading conditions of an aluminum alloy sheet sample", *International Journal of Plasticity*, Vol. 19, pp. 1215-1244, 2003.

[80] D.A. Oliveira, M.J. Worswick, R. Grantab, B.W. Williams, and R. Mayer, "Effect of forming process variables on the crashworthiness of aluminum alloy tubes", *International Journal of Impact Engineering*, Vol. 32, pp. 826-846, 2006.

[81] B.W. Williams, D.A. Oliveria, C.H.M. Simha, M.J. Worswick, and R. Mayer, "Crashworthiness of straight section hydroformed aluminum tubes", *International Journal of Impact Engineering*, Vol. 34, pp. 1451-1464, 2007.

[82] B.W. Williams, D.A. Oliveira, M.J. Worswick, and R. Mayer, "Crashworthiness of High and Low Pressure Hydroformed Straight Section Aluminum Tubes", SAE paper no. 2005-01-0095, 2005.

[83] Y. Hwang and Y. Lin, "Analysis and finite element simulation of the tube bulge hydroforming process", *Journal of Materials Process Technology*, Vol. 125-126, pp. 821-825, 2002.

[84] Y. Hwang and W. Chen, "Analysis of tube hydroforming in a square cross-sectional die", *International Journal of Plasticity*, Vol. 21, pp. 1815-1833, 2005.

[85] J. Kim, S. Kim, W. Song, and B. Kang, "Analytical approach to bursting in tube hydroforming using diffuse plastic instability", *International Journal of Mechanical Sciences*, Vol. 46, pp. 1535-1547, 2004.

[86] S.C. Rama, K. Ma, L.M. Smith, and J.M. Zhang, "A two-dimensional approach for simulation of hydroforming expansion of tubular cross-sections without axial feed", *Journal of Materials Processing Technology*, Vol. 141, pp. 420-430, 2003.

[87] L.M. Smith, J.J. Caveney, and T. Sun, "Fundamental Concepts for "Corner" Forming Limit Diagrams and Closed-Form Formulas for Planar Tube Hydroforming Analysis", *Journal of Manufacturing Science and Engineering*, Vol. 128, pp. 874-883, 2006.

[88] R. Mayer, "Theoretical effects of hydroforming on crashworthiness of straight sections", Proceedings of the ASME Applied Mechanics Division - 2004, Vol. 255, pp. 591-603, 2004.

[89] T. Wierzbicki and W. Abramowicz, The Mechanics of Deep Collapse of Thin-Walled Structures, *Structure Failure*, Wiley, 1989.

[90] M. Langseth and O.S. Hopperstad, "Static and Dynamic Axial Crushing of Square Thin-Walled Aluminum Extrusions", *International Journal of Impact Engineering*, Vol. 18, pp. 949-968, 1996.

[91] S.P. Santosa, T. Wierzbicki, A.G. Hanssen, M. Langseth, "Experimental and numerical studies of foam-filled sections", *International Journal of Impact Engineering*, Vol. 24, pp. 509-534, 2000.

[92] W. Abramowicz, "The macro element approach in crash calculations", In: J.A.C. Ambrosio, M.F.O.S Pereira, F.P. Silva, editors, Crashworthiness of transportation systems: structural impact and occupant protection, NATO ASI Series E, *Applied Sciences*, Vol. 332, Dordrecht: Kluwer, 1997.

[93] T. Belytschko, W.K. Liu, and B. Moran, *Nonlinear Finite Elements for Continua and Structures*, John Wiley & Sons Ltd., 2000.

[94] LS-DYNA, *LS-DYNA Theory Manual*, LSTC, 1996.

[95] C.H.M. Simha, Personal communication, University of Waterloo, 2006.

[96] P. Rosakis, A.J. Rosakis, G. Ravichandran, and J. Hodowany, "A thermodynamic internal variable model for the partition of plastic work into heat and stored energy in metals", *Journal of the Mechanics and Physics of Solids*, Vol. 48, pp. 581-607, 2000.

[97] J.C. Simo and T.J.R. Hughes, *Mechanics & Materials: Computational Inelasticity (Interdisciplinary Applied Mathematics)*, Springer-Verlag, New York, 1998.

[98] N. Abedrabbo, F. Pourboghrat, and J. Carsley, "Forming of aluminum alloys at elevated temperatures – Part 2: Numerical modeling and experimental verification", *International Journal of Plasticity*, Vol. 22, pp. 342-373, 2006.

[99] N. Abedrabbo, F. Pourboghrat, and J. Carsley, "Forming of AA5182-O and AA5754-O at elevated temperatures using coupled thermo-mechanical finite element models", *International Journal of Plasticity*, doi:10.1016/j.ijplas.2006.10.005 (available online), 2006.

[100] M. Ortiz and J.C. Simo, "An analysis of a new class of integration algorithms for elastoplastic constitutive relations", *International Journal for Numerical Methods in Engineering*, Vol. 23, pp. 353-366, 1986.

[101] M.J. Worswick and P. Pelletier, "Numerical Simulation of Ductile Fracture During High Strain Rate Deformation", *The European Physical Journal - Applied Physics*, Vol. 4, pp. 257-267, 1998.

[102] J.A. Schey and P.C. Nautiyal, "Effects of surface roughness on friction and metal transfer in lubricated sliding aluminum alloys against steel surface", *Wear*, Vol. 146, pp. 37-51, 1991.

[103] A. Bardelcik, Personal communication, University of Waterloo, 2005.

[104] S. Winkler, Personal communication, University of Waterloo, 2006.

[105] R.K. Boger, R.H. Wagoner, F. Barlat, M.G. Lee, and K. Chung, "Continuous, large strain, tension/compression testing of sheet material", *International Journal of Plasticity*, Vol. 21, pp. 2319-2343, 2005.

[106] V. Tvergaard, "Effect of yield surface curvature and void nucleation on plastic flow localization", *Journal of the Mechanics and Physics of Solids*, Vol. 35, pp. 43-60, 1987.

[107] M.E. Mear and J.W. Hutchinson, "Influence of yield surface curvature on flow localization in dilatant plasticity", *Mechanics of Materials*, Vol. 4, pp. 395-407, 1985.

[108] W.B. Lievers, A.K. Pilkey, and M.J. Worswick, "The co-operative role of voids and shear bands in strain localization during bending", *Mechanics of Materials*, Vol. 35, pp. 661-674, 2003.

[109] M.G. Lee, D. Kim, C. Kim, M.L. Wenner, R.H. Wagoner, and K. Chung, "A practical two-surface plasticity model and its application to spring-back prediction", *International Journal of Plasticity*, doi:10.1016/j.ijplas.2006.10.011 (available online), 2006.

[110] A.M. Puzrin and G.T. Houlsby, "Fundamentals of kinematic hardening hyperplasticity, "*International Journal of Solids and Structures*", Vol. 38, pp. 3771-3794, 2001.

[111] D.A. Oliveira, Personal communication, University of Waterloo, 2006.

[112] N. Abedrabbo, Personal communication, University of Waterloo, 2006.

[113] Y.F. Dafalias, "Plastic spin: Necessity or redundancy?", *International Journal of Plasticity*, Vol. 14, pp. 909-931, 1998.

[114] H.W. Cho and Y.F. Dafalias, "Distortional and orientational hardening at large viscoplastic deformations", *International Journal of Plasticity*, Vol. 12, pp. 903-925, 1996.

[115] H.J. Bunge and I. Nielsen, "Experimental determination of plastic spin in polycrystalline materials", *International Journal of Plasticity*, Vol. 13, pp. 435-446, 1997.

[116] H.P. Truong Qui and H. Lippmann, "On the impact of local rotation on the evolution of an anisotropic plastic yield criterion", *Journal of the Mechanics and Physics of Solids*, Vol. 49, pp. 2577-2591, 2001.

[117] C.S. Han, Y. Choi, J.K. Lee, and R.H. Wagoner, "A FE formulation for elasto-plastic materials with planar anisotropic yield functions and plastic spin", *International Journal of Solids and Structures*, Vol. 39, pp. 5123-5141, 2002.

[118] K.H. Kim and J.J. Yin, "Evolution of anisotropy under plane stress", *Journal of the Mechanics and Physics of Solids*, Vol. 45, pp. 841-851, 1997.

Appendix A

Comparison of Engineering Strain after Hydroforming

Predicted versus Measured

The figures in this appendix compare the predicted and measured strain and thickness values after hydroforming for the EN-AW5018 and AA5754 alloy tubes.
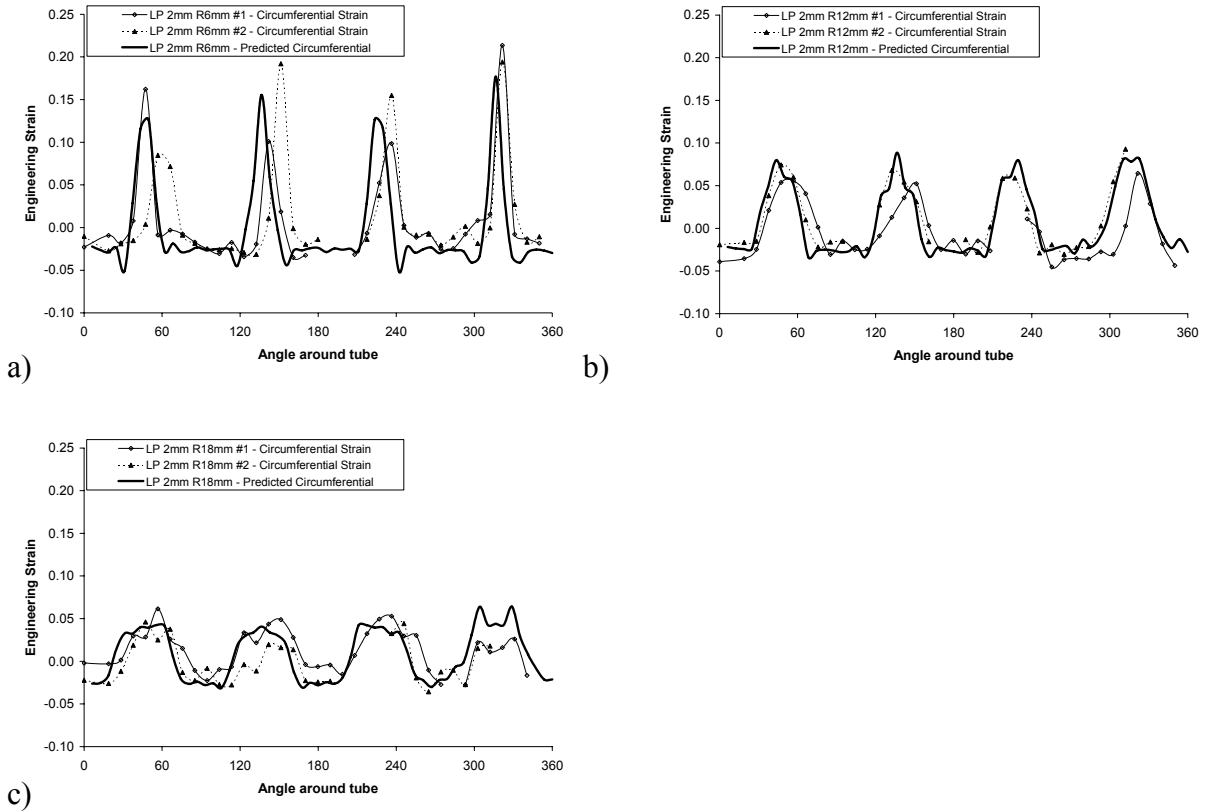
Figure A.1: Engineering strain for 2.0 mm thickness, EN-AW 5018 alloy tubes formed using low pressure hydroforming process

a) LP R6mm   b) LP R12mm   c) LP R18mm

a)

b)

c)
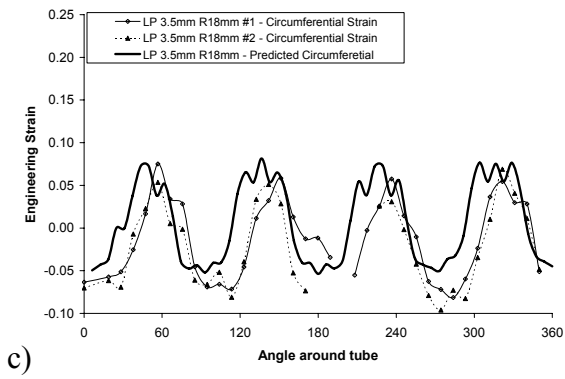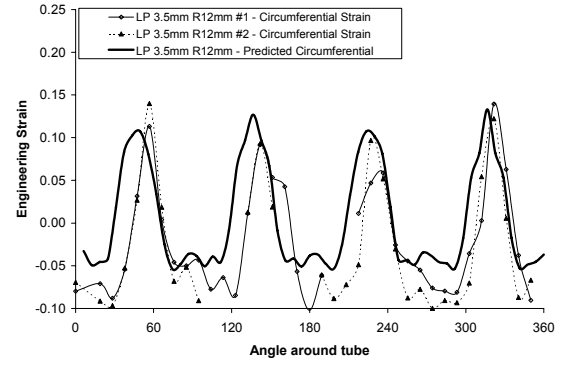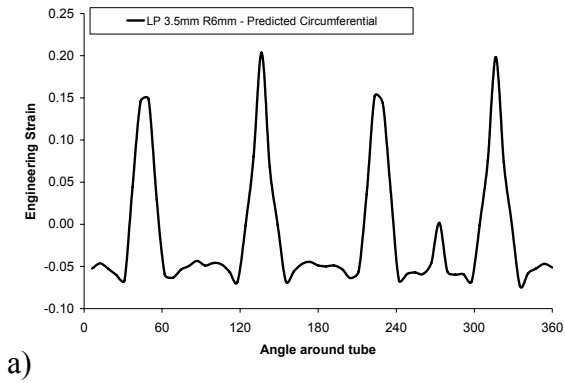
Figure A.2: Engineering strain for 3.5 mm thickness, EN-AW 5018 alloy tubes formed using low pressure hydroforming process

a) LP R6mm (no experimental data)   b) LP R12mm   c) LP R18mm
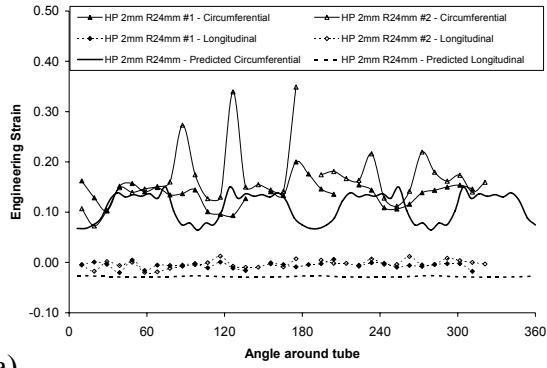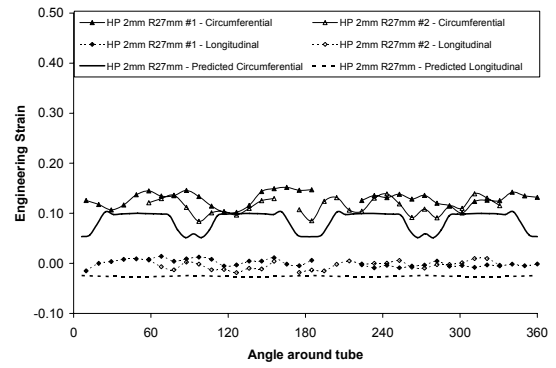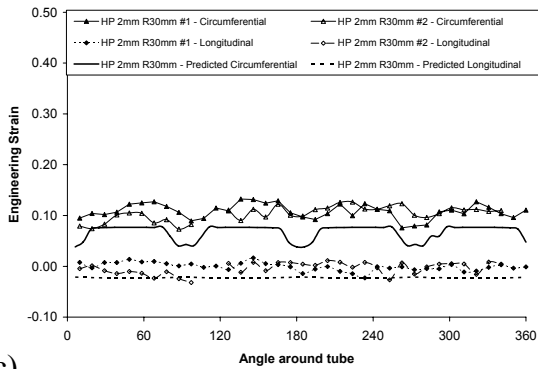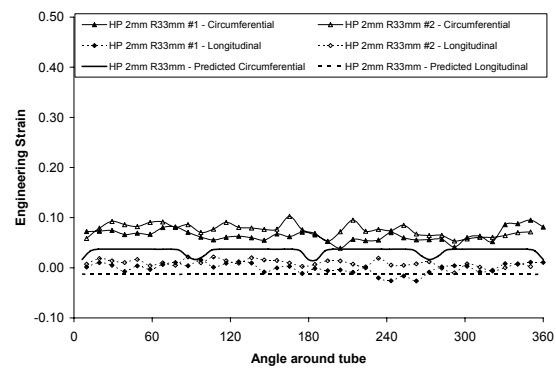
Figure A.3: Engineering strain for 2.0 mm thickness, EN-AW 5018 alloy tubes formed using high pressure hydroforming process

a) HP R24mm   b) HP R27mm   c) HP R30mm   d) HP R33mm
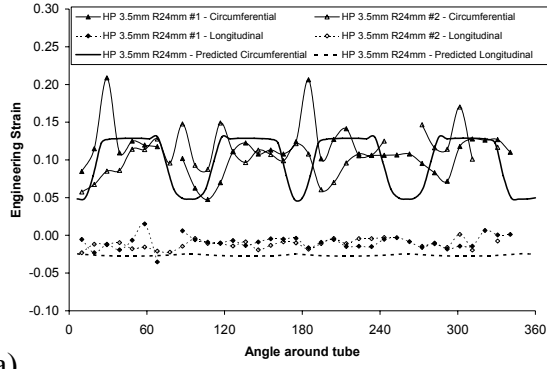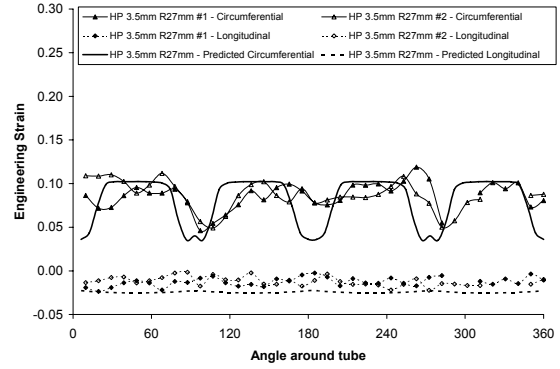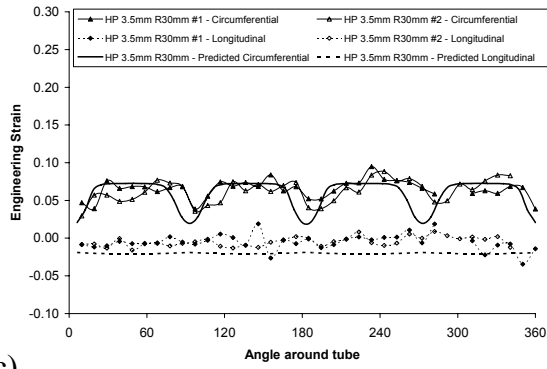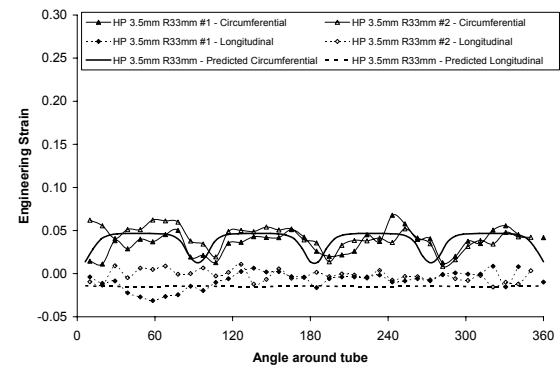
Figure A.4: Engineering strain for 3.5 mm thickness, EN-AW 5018 alloy tubes formed using high pressure hydroforming process

a) HP R24mm   b) HP R27mm   c) HP R30mm   d) HP R33mm
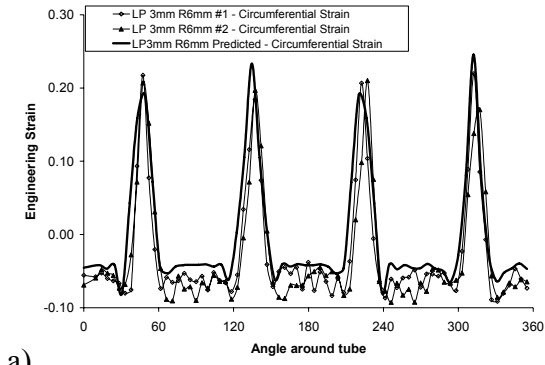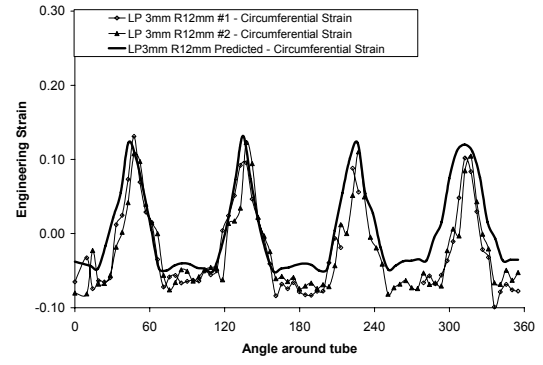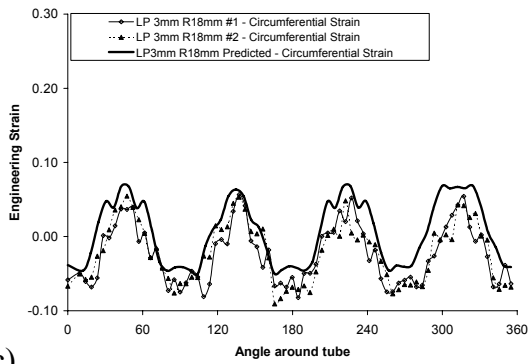
Figure A.5: Engineering strain for AA5754 alloy tubes formed using low pressure hydroforming process

a) LP R6mm   b) LP R12mm   c) LP R18mm

177
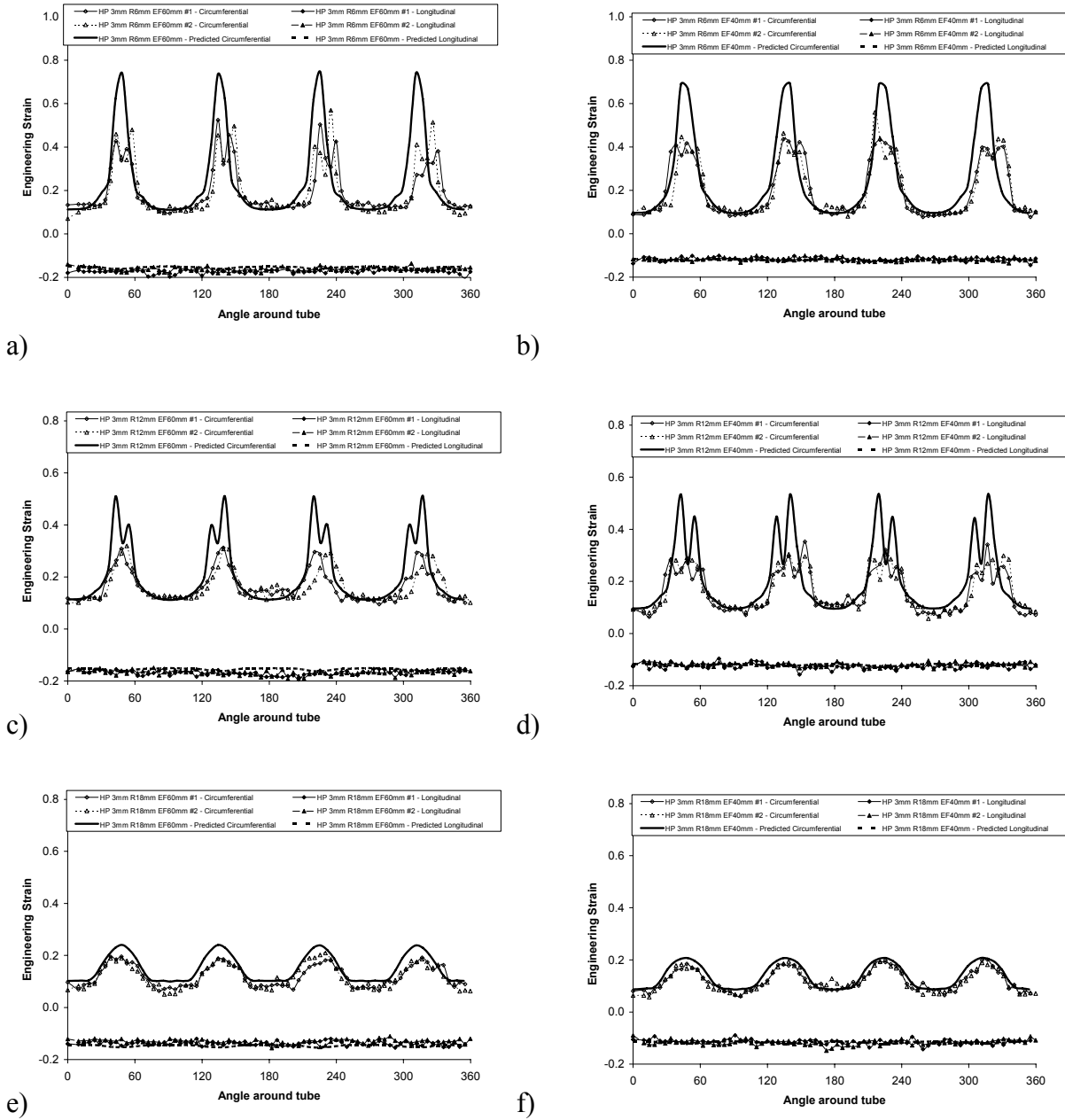
Figure A.6: Engineering strain for AA5754 alloy tubes formed using high pressure hydroforming process with end-feeding

a) HP R6mm EF60mm   b) HP R6mm EF40mm   c) HP R12mm EF60mm

d) HP R12mm EF40mm   e) HP R18mm EF60mm   f) HP R18mm EF40mm
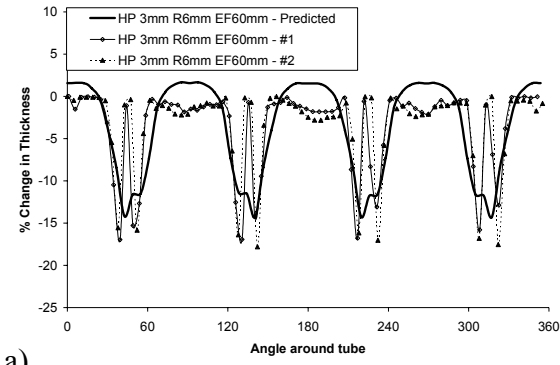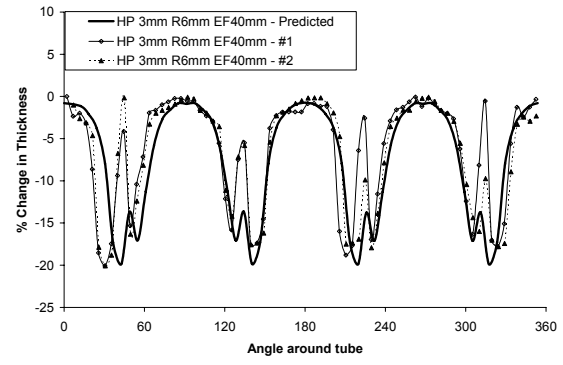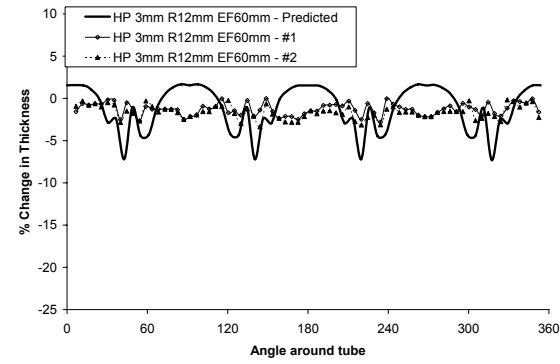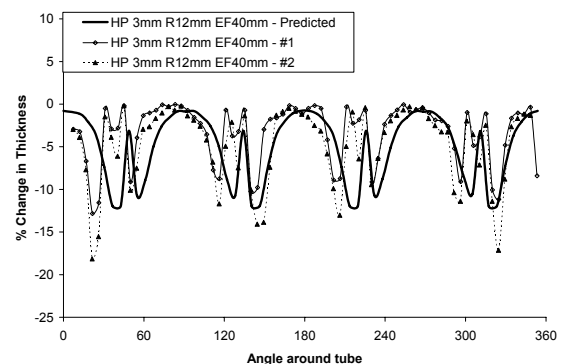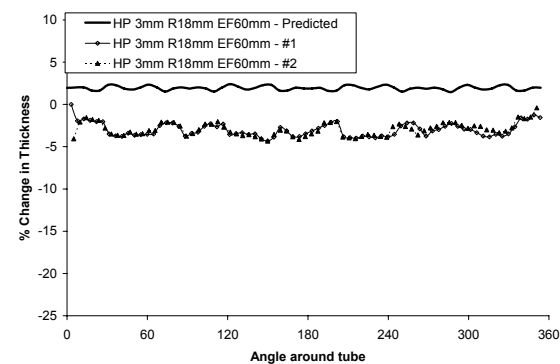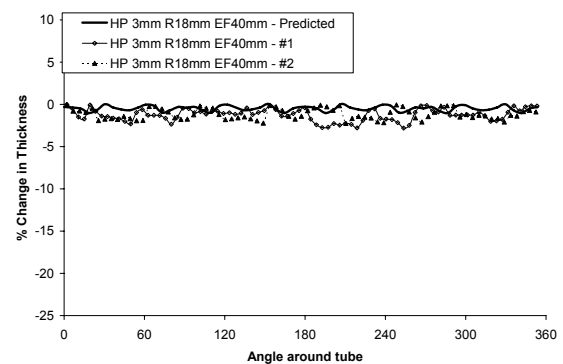
Figure A.7: Per cent change in thickness for AA5754 alloy tubes formed using high pressure hydroforming process with end-feeding

a) HP R6mm EF60mm　　　b) HP R6mm EF40mm　　　c) HP R12mm EF60mm

d) HP R12mm EF40mm　　　e) HP R18mm EF60mm　　　f) HP R18mm EF40mm

Appendix B

Crush Load Versus Crush Distance Results

EN-AW 5018 and AA5754 – Experiment versus Simulation

The tables and figures in this appendix provide the predicted and measured crush response of the EN-AW5018 and AA5754 aluminum alloy tubes. Comparisons are also given based on simulations performed with different element size and formulation. All simulation results presented were based on simulations performed using the von Mises yield criterion.

Table B.1: Predicted and experimental crush data for EN-AW 5018 alloy tubes with 2.0 mm thickness

Description	Test Apparatus	Impact Velocity (m/s)	Radius (mm)	Radius Ratio	Energy Absorption (J)	Distance at EA (mm)	Mean Load (kN)
Type 2 Elements - 4mm mesh							
round, non-hydroformed			38.1	1.00	10108.1	198.5	50.9
HP 2mm R33mm - Predicted			33	0.87	11482.6	198.4	57.9
HP 2mm R30mm - Predicted			30	0.79	10439.0	198.7	52.5
HP 2mm R27mm - Predicted			27	0.71	9312.2	198.3	47.0
HP 2mm R24mm - Predicted			24	0.63	9481.4	198.6	47.7
LP 2mm R18mm - Predicted			18	0.47	7165.2	199.2	36.0
LP 2mm R12mm - Predicted			12	0.31	6266.6	199.4	31.4
LP 2mm R6mm - Predicted			6	0.16	6409.6	199.3	32.2
Experiment							
round, non-hydroformed #1	drop tower	12	38.1	1.00	9881.6	199.3	49.6
round, non-hydroformed #2	drop tower	12	38.1	1.00	10409.6	199.4	52.2
HP 2mm R33mm #1	drop tower	12	33	0.87	9649.9	199.2	48.4
HP 2mm R33mm #2	drop tower	12	33	0.87	9677.9	199.3	48.6
HP 2mm R30mm #1	drop tower	12	30	0.79	9268.2	199.4	46.5
HP 2mm R30mm #2	drop tower	12	30	0.79	9217.3	199.1	46.3
HP 2mm R27mm #1	drop tower	12	27	0.71	9147.2	199.0	46.0
HP 2mm R27mm #2	drop tower	12	27	0.71	9357.7	199.4	46.9
HP 2mm R24mm #1	drop tower	12	24	0.63	8163.0	199.2	41.0
HP 2mm R24mm #2	drop tower	12	24	0.63	7311.5	199.2	36.7
LP 2mm R12mm #1	sled-track	5.2	12	0.31	5568.3	199.4	27.9
LP 2mm R12mm #2	sled-track	5.2	12	0.31	5480.3	199.3	27.5
LP 2mm R18mm #1	sled-track	5.2	18	0.47	5627.4	199.3	28.2
LP 2mm R18mm #2	sled-track	5.2	18	0.47	5687.3	199.3	28.5
LP 2mm R6mm #1	sled-track	5.2	6	0.16	5693.4	199.4	28.6
LP 2mm R6mm #2	sled-track	5.2	6	0.16	5617.4	199.3	28.2

Table B.2: Predicted and experimental crush data for EN-AW 5018 alloy tubes with 3.5 mm thickness

Description	Test Apparatus	Impact Velocity (m/s)	Radius (mm)	Radius Ratio	Energy Absorption (J)	Distance at EA (mm)	Mean Load (kN)
Type 2 Elements - 4mm mesh							
round, non-hydroformed			38.1	1.00	25480.0	198.8	128.2
HP 3.5mm R33mm - Predicted			33	0.87	23092.0	198.8	116.2
HP 3.5mm R30mm - Predicted			30	0.79	22418.0	198.2	113.1
HP 3.5mm R27mm - Predicted			27	0.71	23402.6	198.5	117.9
HP 3.5mm R24mm - Predicted			24	0.63	21850.6	198.7	110.0
LP 3.5mm R18mm - Predicted			18	0.47	21034.9	198.5	106.0
LP 3.5mm R12mm - Predicted			12	0.31	18979.7	198.5	95.6
LP 3.5mm R6mm - Predicted			6	0.16	15694.8	165.5	94.8
Experiment							
round, non-hydroformed #1	drop tower	12	38.1	1.00	24866.3	200.0	124.3
round, non-hydroformed #2	drop tower	12	38.1	1.00	25368.8	199.3	127.3
HP 3.5mm R33mm #1	drop tower	12	33	0.87	23977.5	199.4	120.3
HP 3.5mm R33mm #2	drop tower	12	33	0.87	23753.7	199.4	119.1
HP 3.5mm R30mm #1	drop tower	12	30	0.79	23028.8	199.1	115.6
HP 3.5mm R30mm #2	drop tower	12	30	0.79	21661.8	199.3	108.7
HP 3.5mm R27mm #1	drop tower	12	27	0.71	19460.2	199.0	97.8
HP 3.5mm R27mm #2	drop tower	12	27	0.71	19669.1	199.2	98.7
HP 3.5mm R24mm #1	drop tower	12	24	0.63	16958.8	199.0	85.2
HP 3.5mm R24mm #2	drop tower	12	24	0.63	17501.0	199.2	87.8
LP 3.5mm R18mm #1	sled-track	8.0	18	0.47	19345.0	199.0	97.2
LP 3.5mm R18mm #2	sled-track	8.0	18	0.47	18960.2	199.1	95.3
LP 3.5mm R12mm #1	sled-track	8.1	12	0.31	17903.0	199.0	90.0
LP 3.5mm R12mm #2	sled-track	8.1	12	0.31	17726.5	199.0	89.1
LP 3.5mm R6mm #1	sled-track	7.5	6	0.16	17198.9	183.9	93.5
LP 3.5mm R6mm #2	sled-track	7.5	6	0.16	17249.9	183.2	94.2

Table B.3: Predicted crush data from AA5754 impact simulations

Description	Radius (mm)	Radius Ratio	Energy Absorption (J)	Distance at EA (mm)	Mean Load (kN)	Energy Absorption (J)	Distance at EA (mm)	Mean Load (kN)
Type 2 Elements			*2mm mesh*			*4mm mesh*		
round, non-hydroformed	38.1	1.00	---	---	---	15842.5	178.3	88.9
LP R6mm Predicted - with initiators	6	0.16	10759.0	199.3	54.0	11073.3	191.9	57.7
LP R12mm Predicted - with initiators	12	0.31	10258.6	199.3	51.5	10783.7	199.3	54.1
LP R18mm Predicted - with initiators	18	0.47	11020.6	199.3	55.3	10760.6	199.3	54.0
LP R6mm Predicted - without initiators	6	0.16	---	---	---	13664.4	192.7	70.9
LP R12mm Predicted - without initiators	12	0.31	---	---	---	11069.7	175.6	63.0
LP R18mm Predicted - without initiators	18	0.47	---	---	---	13633.2	199.3	68.4
HP R6mm EF40 - Predicted	6	0.16	---	---	---	11278.5	199.1	56.6
HP R6mm EF60 - Predicted	6	0.16	12198.9	199.1	61.3	12746.0	199.3	64.0
HP R6mm EF60 - Predicted - annealed	6	0.16	---	---	---	9317.3	199.2	46.8
HP R12mm EF40 - Predicted	12	0.31	---	---	---	12072.0	199.2	60.6
HP R12mm EF60 - Predicted	12	0.31	12881.3	199.2	64.7	13397.1	199.2	67.2
HP R12mm EF60 - Predicted - annealed	12	0.31	---	---	---	9813.1	199.3	49.2
HP R18mm EF40 - Predicted	18	0.47	---	---	---	13636.6	186.9	73.0
HP R18mm EF60 - Predicted	18	0.47	13369.3	199.2	67.1	13631.4	180.6	75.5
HP R18mm EF60 - Predicted - annealed	18	0.47	---	---	---	10253.5	199.3	51.4
Type 16 Elements			*2mm mesh*			*4mm mesh*		
LP R6mm Predicted - with initiators	6	0.16	11073.7	193.2	57.3	11050.6	180.4	61.3
LP R12mm Predicted - with initiators	12	0.31	10721.6	199.3	53.8	11069.9	193.0	57.3
LP R18mm Predicted - with initiators	18	0.47	11021.3	199.3	55.3	11070.7	195.5	56.6
HP R6mm EF60 - Predicted	6	0.16	12777.0	199.2	64.1	13633.4	194.3	70.2
HP R12mm EF60 - Predicted	12	0.31	13635.9	195.4	69.8	13634.2	184.2	74.0
HP R18mm EF60 - Predicted	18	0.47	13631.4	182.5	74.7	13633.4	168.5	80.9
Type 16 forming, Type 2 crash			*2mm mesh*			*4mm mesh*		
LP R6mm Predicted - with initiators	6	0.16	---	---	---	11075.3	191.7	57.8
LP R12mm Predicted - with initiators	12	0.31	---	---	---	10763.1	199.3	54.0
LP R18mm Predicted - with initiators	18	0.47	---	---	---	10748.1	199.3	53.9
HP R6mm EF60 - Predicted	6	0.16	---	---	---	12702.2	199.1	63.8
HP R12mm EF60 - Predicted	12	0.31	---	---	---	13481.6	199.2	67.7
HP R18mm EF60 - Predicted	18	0.47	---	---	---	13630.3	183.8	74.1

Note: All simulations performed using von Mises yield criterion

Table B.4: Experimental crush data for AA5754 alloy tubes for non-hydroformed, circular tubes and tubes formed using the low pressure hydroforming process

Description	Impact Velocity (m/s)	Radius (mm)	Radius Ratio	Energy Absorption (J)	Distance at EA (mm)	Mean Load (kN)	Mass of Tube at Disp. at EA (g)	Specific Energy (kJ/kg)
round, non-hydroformed #1	7.54	38.1	1.00	16595.7	199.1	83.4	373.7	44.4
round, non-hydroformed #2	7.54	38.1	1.00	16375.8	199.2	82.2	373.9	43.8
round, non-hydroformed #3	7.54	38.1	1.00	16538.3	199.2	83.0	374.0	44.2
round, non-hydroformed #4	7.54	38.1	1.00	16674.3	199.1	83.8	373.8	44.6
LP R6mm #1 - with initiators	6.40	6	0.16	10939.0	199.3	54.9	374.2	29.2
LP R6mm #2 - with initiators	6.40	6	0.16	10911.8	199.2	54.8	374.1	29.2
LP R6mm #3 - with initiators	6.30	6	0.16	10939.5	199.4	54.9	374.3	29.2
LP R6mm #4 - with initiators	6.30	6	0.16	10851.4	199.3	54.4	374.2	29.0
LP R12mm #1 - with initiators	6.29	12	0.31	10059.4	199.4	50.5	375.5	26.8
LP R12mm #2 - with initiators	6.29	12	0.31	10198.0	199.3	51.2	375.4	27.2
LP R12mm #3 - with initiators	6.30	12	0.31	9942.9	199.3	49.9	375.4	26.5
LP R12mm #4 - with initiators	6.30	12	0.31	10044.5	199.2	50.4	375.1	26.8
LP R18mm #1 - with initiators	6.30	18	0.47	10094.1	199.3	50.7	373.9	27.0
LP R18mm #2 - with initiators	6.30	18	0.47	10015.3	199.3	50.3	373.9	26.8
LP R18mm #3 - with initiators	6.19	18	0.47	10255.8	199.4	51.4	374.1	27.4
LP R18mm #4 - with initiators	6.19	18	0.47	10196.6	199.4	51.1	374.1	27.3
LP R6mm #1 - without initiators	6.30	6	0.16	11474.8	184.4	62.2	346.2	33.1
LP R6mm #2 - without initiators	6.30	6	0.16	11185.7	183.8	60.9	345.0	32.4
LP R12mm #1 - without initiators	6.33	12	0.31	11230.8	199.3	56.3	375.4	29.9
LP R12mm #2 - without initiators	6.33	12	0.31	11112.5	199.4	55.7	375.5	29.6
LP R18mm #1 - without initiators	6.32	18	0.47	11466.4	188.4	60.9	353.5	32.4
LP R18mm #2 - without initiators	6.32	18	0.47	11540.1	187.2	61.7	351.2	32.9

Note: all tests were conducted on sled-track

Table B.5: Experimental crush data for AA5754 alloy tubes for tubes formed using the high pressure hydroforming process

Description	Impact Velocity (m/s)	Radius (mm)	Radius Ratio	Energy Absorption (J)	Distance at EA (mm)	Mean Load (kN)	Mass of Tube at Disp. at EA (g)	Specific Energy (kJ/kg)
HP R6mm EF40 #1	7.03	6	0.16	11255.4	199.0	56.6	435.1	25.9
HP R6mm EF40 #2	7.03	6	0.16	11252.7	199.2	56.5	435.6	25.8
HP R6mm EF40 #3	7.07	6	0.16	11205.6	199.2	56.3	435.5	25.7
HP R6mm EF40 #4	7.07	6	0.16	11320.3	199.1	56.9	435.2	26.0
HP R6mm EF60 #1	7.05	6	0.16	13002.7	199.1	65.3	455.8	28.5
HP R6mm EF60 #2	7.05	6	0.16	12836.8	199.1	64.5	455.8	28.2
HP R6mm EF60 #3	7.03	6	0.16	12765.9	199.2	64.1	455.9	28.0
HP R6mm EF60 #4	7.03	6	0.16	13064.9	199.3	65.6	456.1	28.6
HP R6mm EF60 #1 - annealed	6.33	6	0.16	8301.9	199.3	41.7	456.2	18.2
HP R6mm EF60 #2 - annealed	6.33	6	0.16	8422.8	199.3	42.3	456.2	18.5
HP R6mm EF60 #3 - annealed	6.29	6	0.16	8393.5	199.3	42.1	456.2	18.4
HP R6mm EF60 #4 - annealed	6.29	6	0.16	8301.1	199.3	41.6	456.3	18.2
HP R12mm EF40 #1	7.07	12	0.31	12122.7	199.3	60.8	437.6	27.7
HP R12mm EF40 #2	7.07	12	0.31	12280.6	199.2	61.6	437.5	28.1
HP R12mm EF40 #3	7.00	12	0.31	11989.0	199.1	60.2	437.3	27.4
HP R12mm EF40 #4	7.00	12	0.31	12152.8	199.2	61.0	437.4	27.8
HP R12mm EF60 #1	7.03	12	0.31	13769.2	199.3	69.1	458.9	30.0
HP R12mm EF60 #2	7.03	12	0.31	13957.7	199.3	70.1	458.8	30.4
HP R12mm EF60 #3	7.05	12	0.31	13840.1	199.3	69.5	458.9	30.2
HP R12mm EF60 #4	7.05	12	0.31	13993.7	199.3	70.2	458.9	30.5
HP R12mm EF60 #1 - annealed	7.03	12	0.31	9151.4	199.1	46.0	458.4	20.0
HP R12mm EF60 #2 - annealed	7.03	12	0.31	9327.8	199.3	46.8	458.9	20.3
HP R12mm EF60 #3 - annealed	6.33	12	0.31	9206.7	199.3	46.2	459.0	20.1
HP R12mm EF60 #4 - annealed	6.33	12	0.31	9136.0	199.4	45.8	459.1	19.9
HP R18mm EF40 #1	7.07	18	0.47	13213.7	199.1	66.4	431.7	30.6
HP R18mm EF40 #2	7.07	18	0.47	13265.7	199.2	66.6	431.9	30.7
HP R18mm EF40 #3	7.09	18	0.47	13159.4	199.2	66.1	431.8	30.5
HP R18mm EF40 #4	7.09	18	0.47	13289.0	199.2	66.7	431.9	30.8
HP R18mm EF60 #1	7.05	18	0.47	13768.2	199.3	69.1	441.8	31.2
HP R18mm EF60 #2	7.05	18	0.47	14076.5	199.2	70.7	441.8	31.9
HP R18mm EF60 #3	7.05	18	0.47	13760.7	199.2	69.1	441.7	31.2
HP R18mm EF60 #4	7.05	18	0.47	13996.5	199.3	70.2	441.9	31.7
HP R18mm EF60 #1 - annealed	6.32	18	0.47	9574.2	199.4	48.0	442.0	21.7
HP R18mm EF60 #2 - annealed	6.32	18	0.47	9543.3	199.2	47.9	441.7	21.6
HP R18mm EF60 #3 - annealed	6.32	18	0.47	9296.5	199.3	46.7	441.8	21.0
HP R18mm EF60 #4 - annealed	6.32	18	0.47	9673.0	199.1	48.6	441.6	21.9

Note: all tests were conducted on sled-track

Table B.6: Experimental crush data of hydroformed AA5754 alloy tubes tested under quasi-static loading conditions

Description	Radius (mm)	Radius Ratio	Energy Absorption (J)	Distance at EA (mm)	Mean Load (kN)
HP R6mm EF60 mm #1 - quasi-static	6	0.16	12097.0	199.4	60.7
HP R6mm EF60 mm #2 - quasi-static	6	0.16	12203.1	200.6	60.8
HP R12mm EF60 mm #1 - quasi-static	12	0.31	12988.4	201.3	64.5
HP R12mm EF60 mm #2 - quasi-static	12	0.31	13252.8	201.1	65.9
HP R18mm EF60 mm #1 - quasi-static	18	0.47	13345.2	200.1	66.7
HP R18mm EF60 mm #2 - quasi-static	18	0.47	13253.2	200.4	66.1

Figure B.1: Crush response for low pressure EN-AW 5018 alloy tubes with 2.0 mm thickness

a) LP R6mm   b) LP R6mm – mean load

c) LP R12mm   d) LP R12mm – mean load

e) LP R18mm   f) LP R18mm – mean load
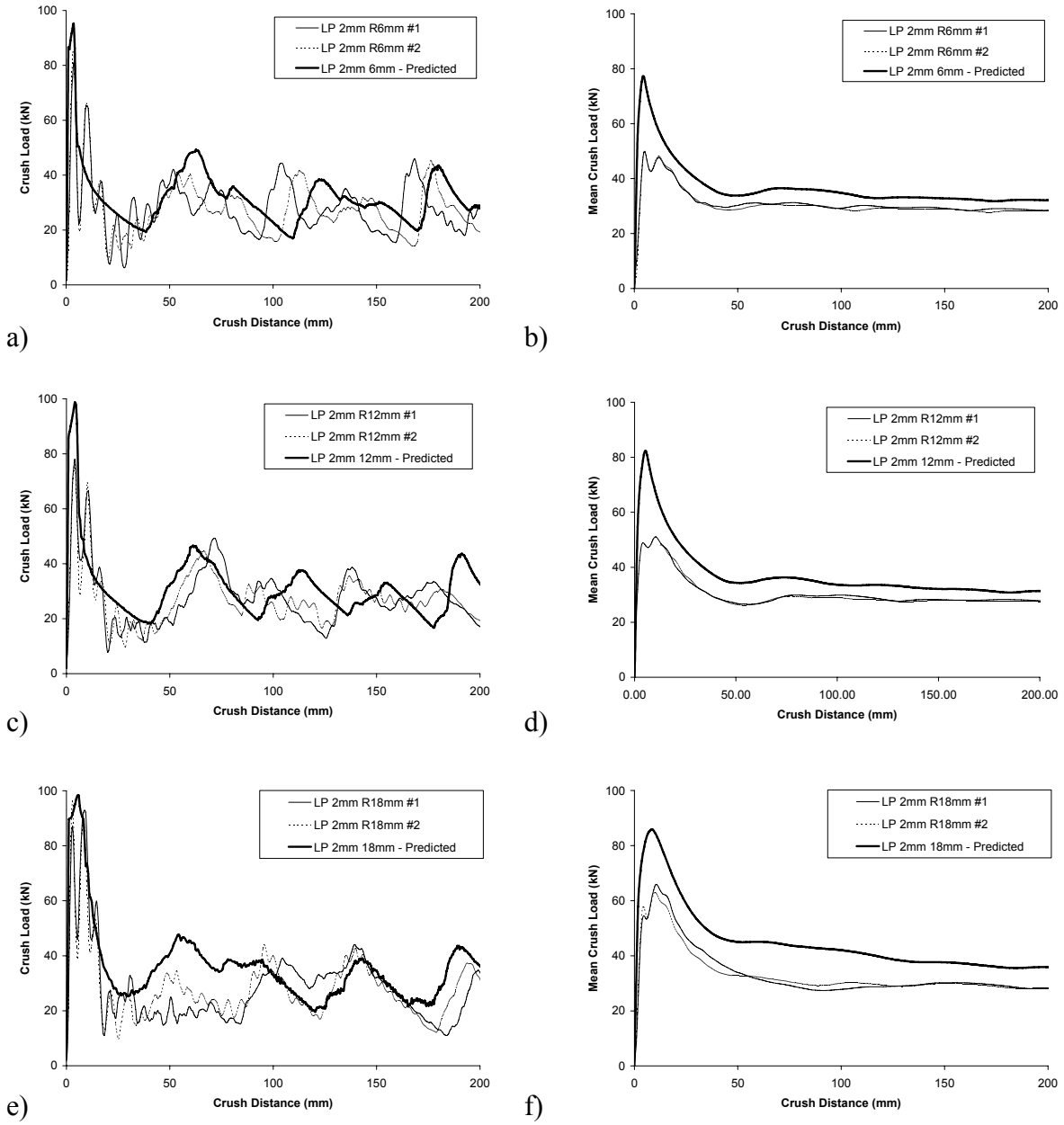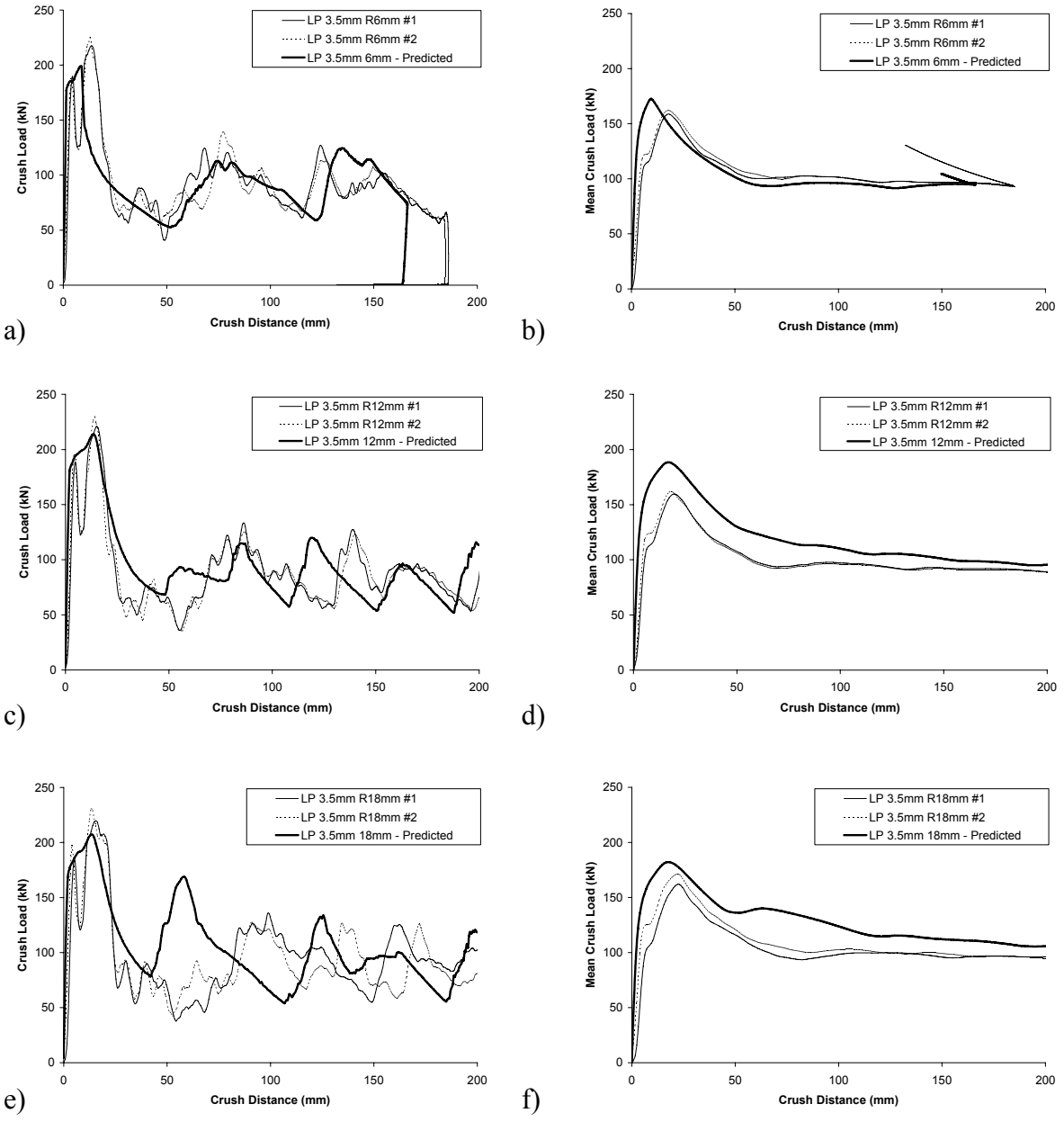
Figure B.2: Crush response for low pressure EN-AW 5018 alloy tubes with 3.5 mm thickness

a) LP R6mm   b) LP R6mm – mean load

c) LP R12mm   d) LP R12mm – mean load

e) LP R18mm   f) LP R18mm – mean load
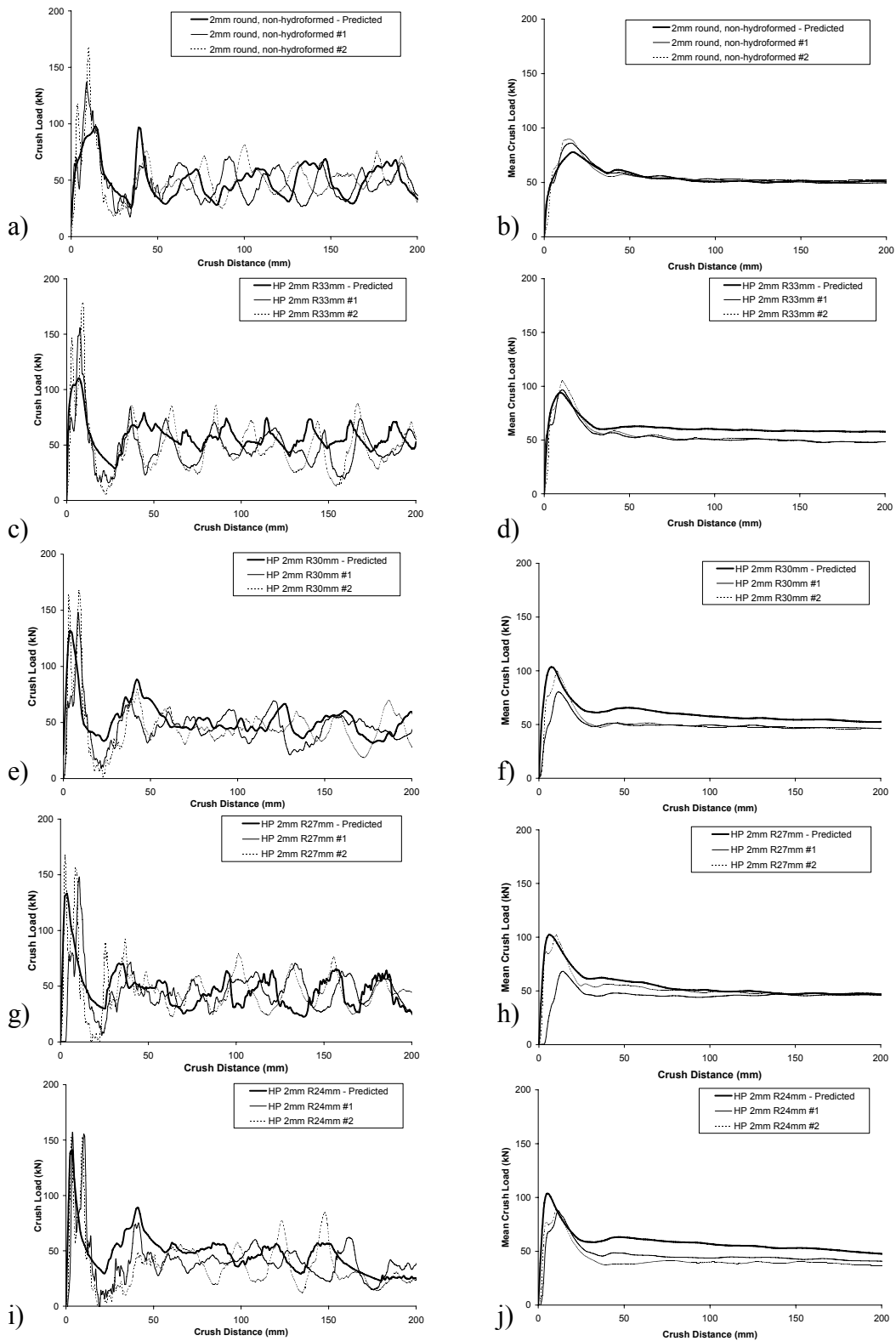
Figure B.3: Crush response for round, non-hydroformed EN-AW 5018 alloy tubes and high pressure hydroformed tubes, with 2.0 mm thickness

189
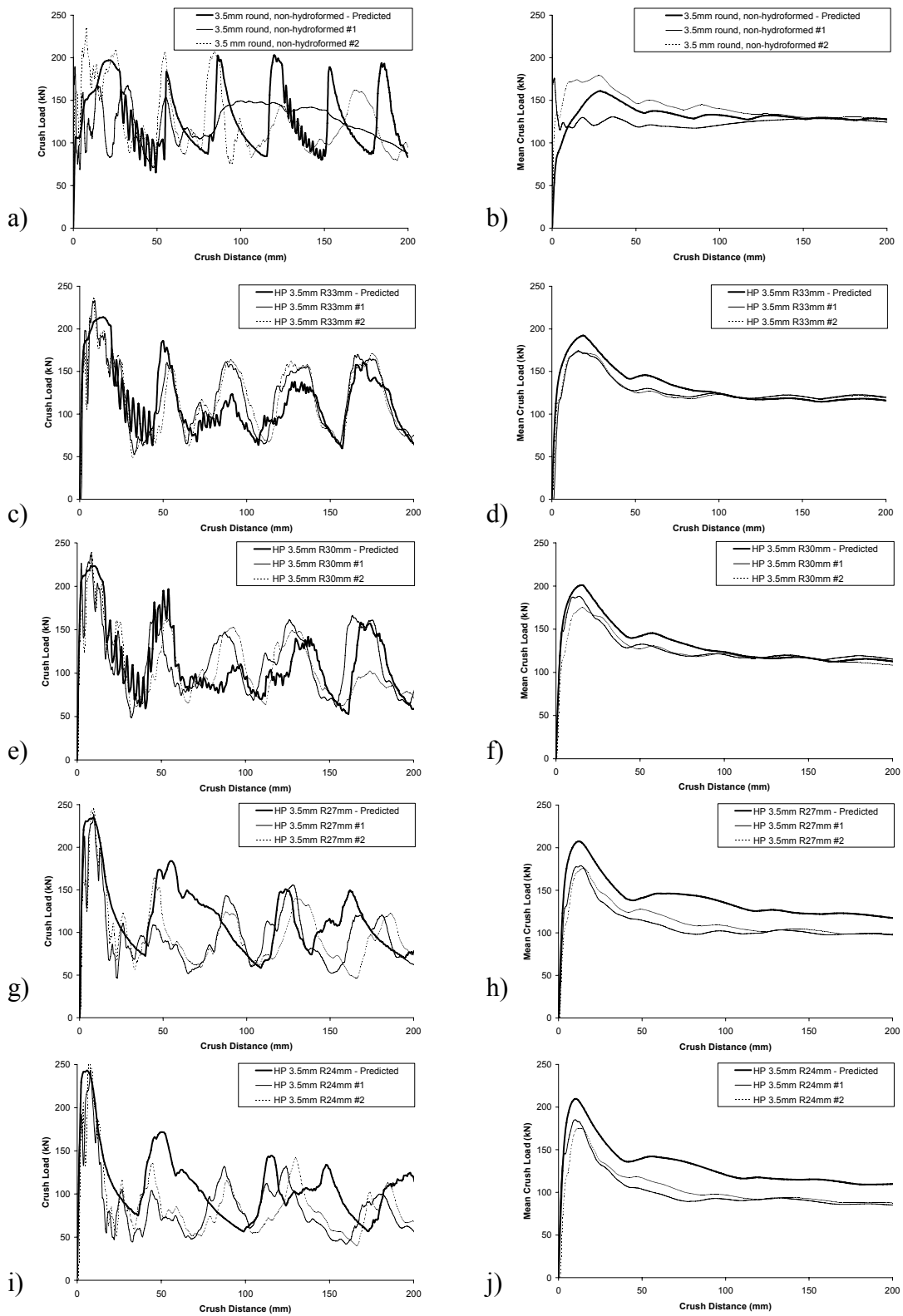
Figure B.4: Crush response for round, non-hydroformed EN-AW 5018 alloy tubes and high pressure hydroformed tubes, with 3.5 mm thickness

190

a)   b)
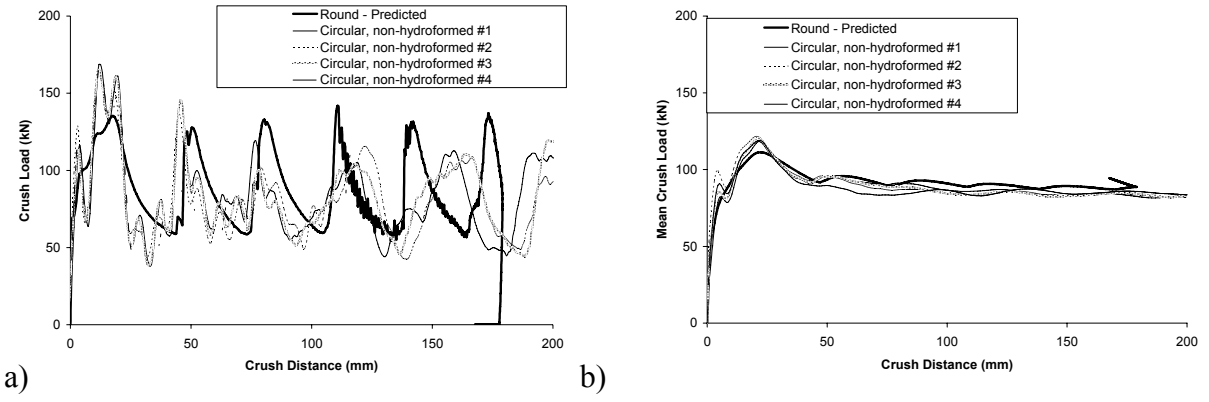
Figure B.5: Crush response for non-hydroformed, round AA5754 alloy tubes
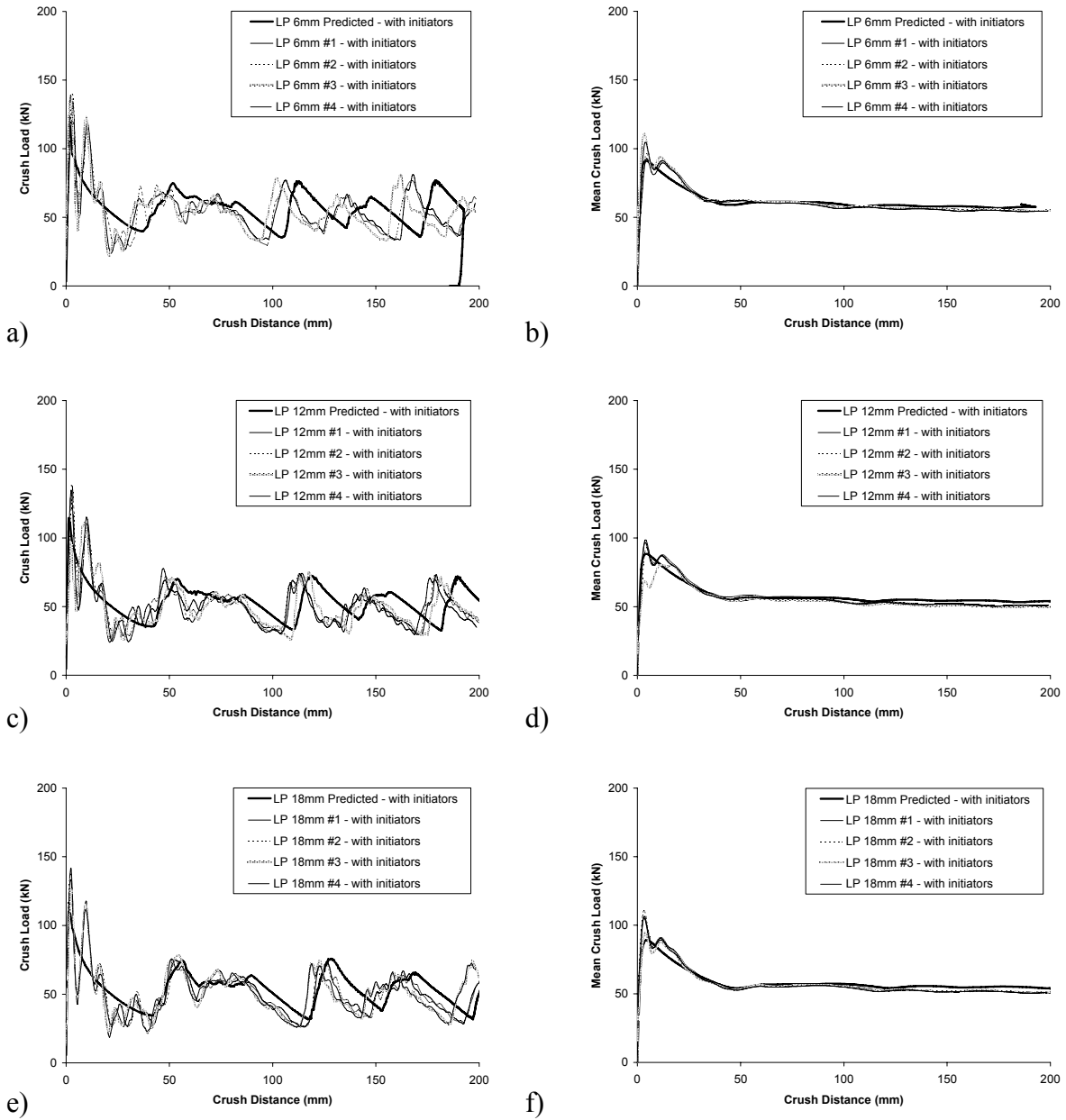
Figure B.6: Crush response for AA5754 alloy tubes formed using low pressure hydroforming process, with initiators

a) LP R6mm   b) LP R6mm – mean load

c) LP R12mm   d) LP R12mm – mean load

e) LP R18mm   f) LP R18mm – mean load
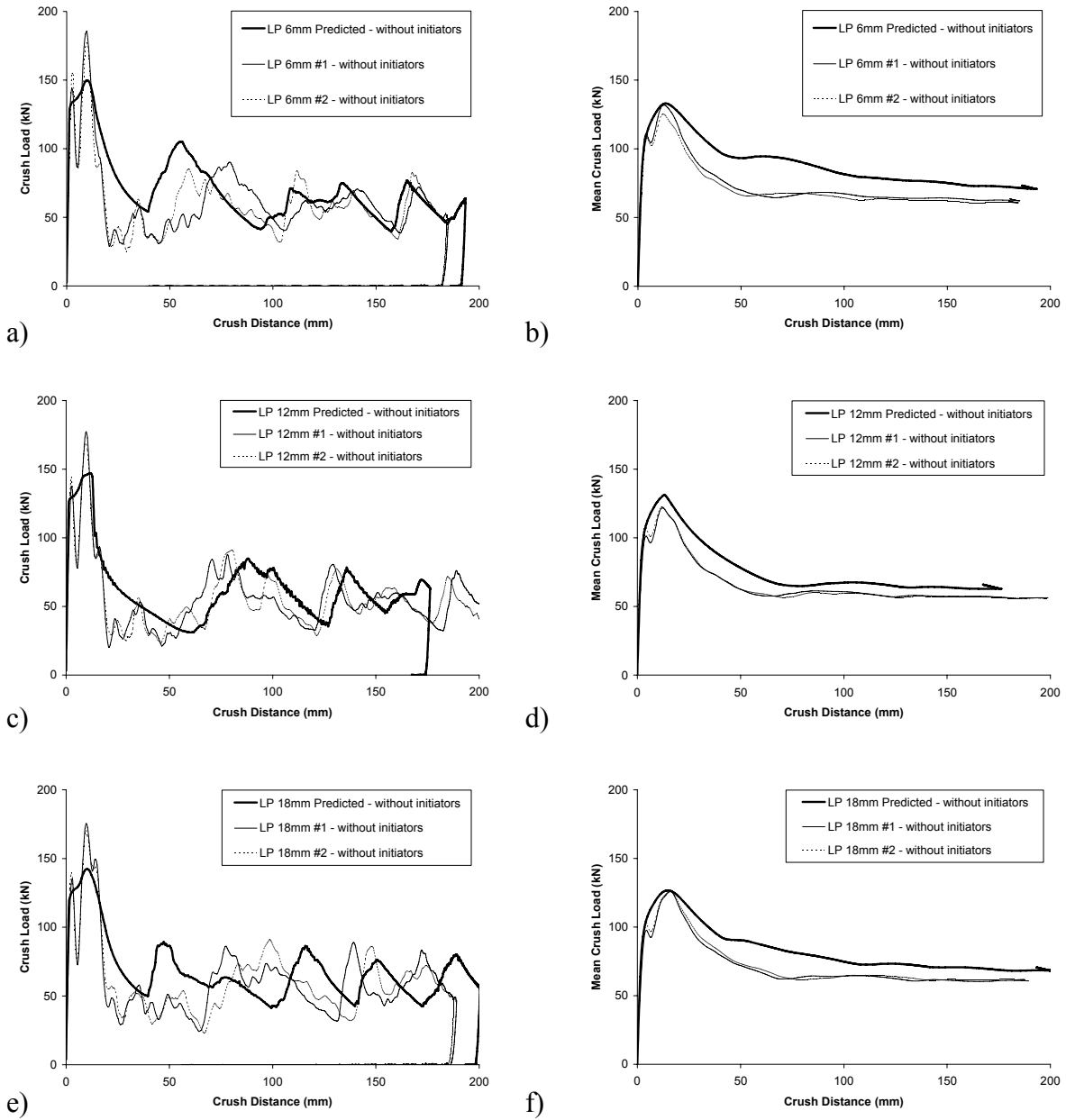
Figure B.7: Crush response for AA5754 alloy tubes formed using low pressure hydroforming process, without initiators

a) LP R6mm   b) LP R6mm – mean load

c) LP R12mm   d) LP R12mm – mean load

e) LP R18mm   f) LP R18mm – mean load

193

Figure B.8: Crush response for AA5754 alloy tubes formed using high pressure hydroforming process, with 6 mm corner radius

a) HP 6mm EF40mm   b) HP 6mm EF40mm – mean load

c) HP 6mm EF60mm   d) HP 6mm EF60mm – mean load

e) HP 6mm EF60mm - annealed   f) HP 6mm EF60mm - annealed – mean load

194

Figure B.9: Crush response for AA5754 alloy tubes formed using high pressure hydroforming process, with 12 mm corner radius

a) HP 12mm EF40mm   b) HP 12mm EF40mm – mean load

c) HP 12mm EF60mm   d) HP 12mm EF60mm – mean load

e) HP 12mm EF60mm - annealed   f) HP 12mm EF60mm - annealed – mean load

195
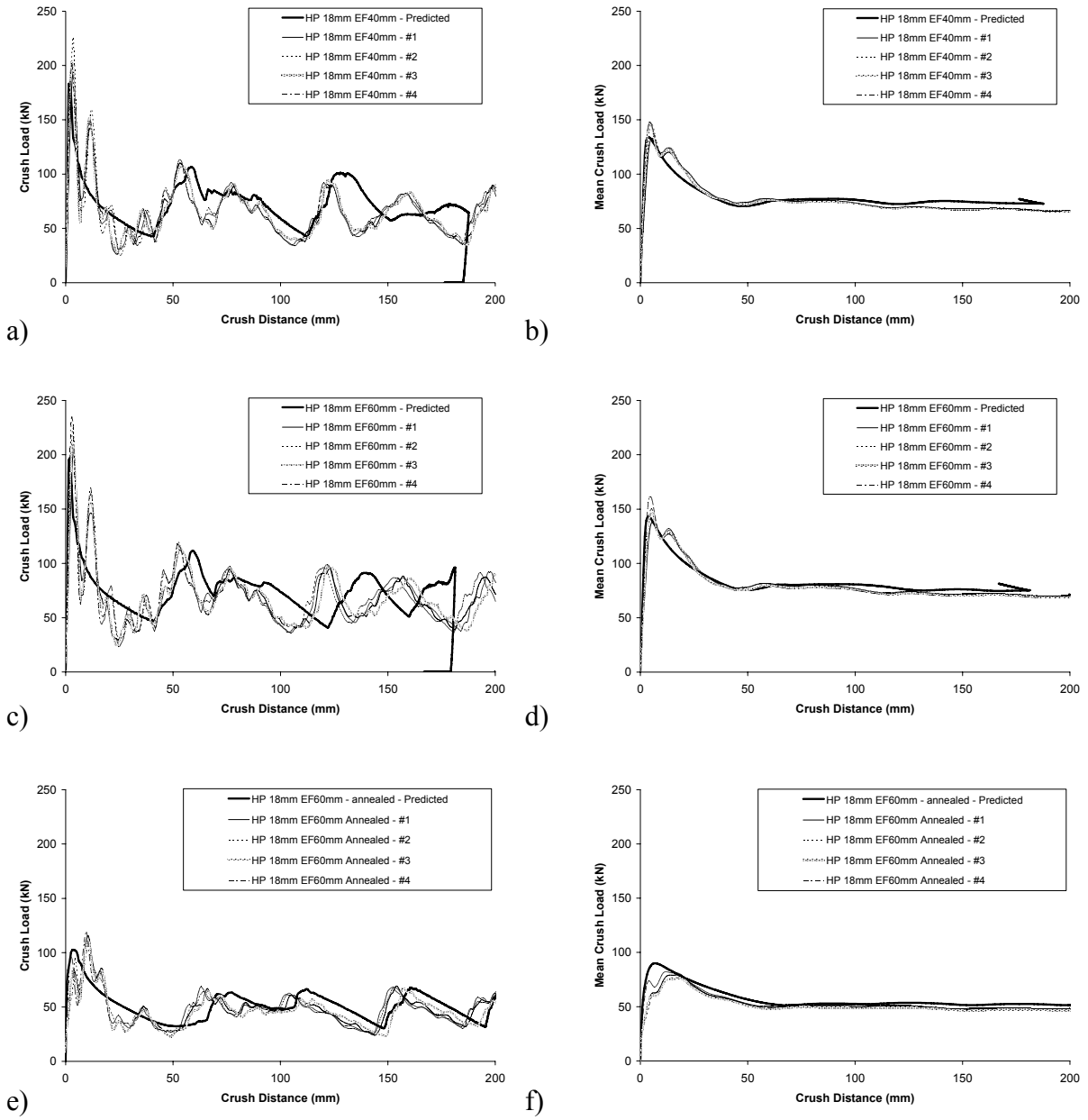
Figure B.10: Crush response for AA5754 alloy tubes formed using high pressure hydroforming process, with 18 mm corner radius

a) HP 18mm EF40mm   b) HP 18mm EF40mm – mean load

c) HP 18mm EF60mm   d) HP 18mm EF60mm – mean load

e) HP 18mm EF60mm - annealed   f) HP 18mm EF60mm - annealed – mean load

196
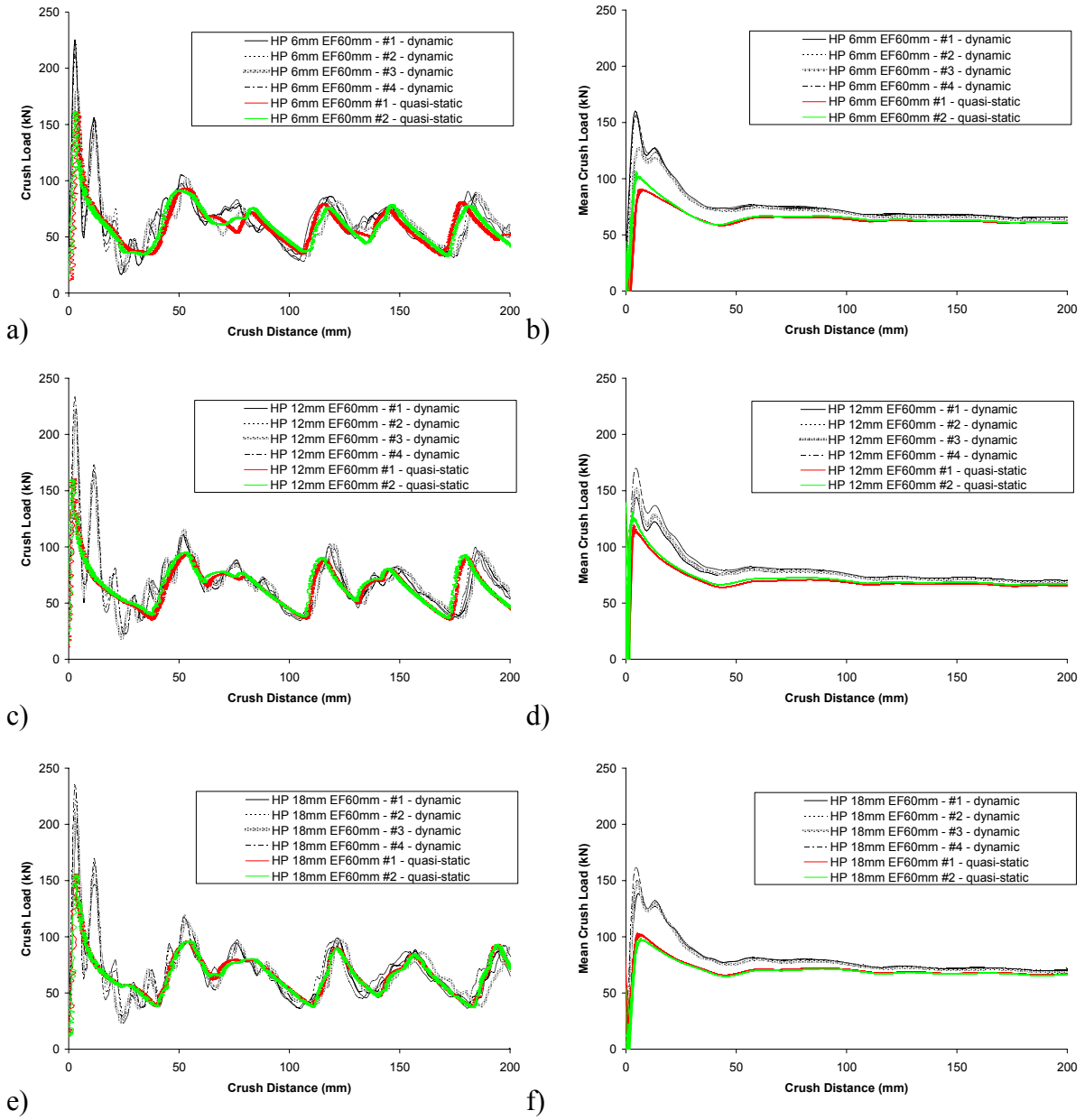
Figure B.11: Measured quasi-static and dynamic axial crush response of AA5754 alloy tubes

a) HP 6mm EF60mm   b) HP 6mm EF60mm – mean load

c) HP 12mm EF60mm   d) HP 12mm EF60mm – mean load

e) HP 18mm EF60mm   f) HP 18mm EF60mm – mean load
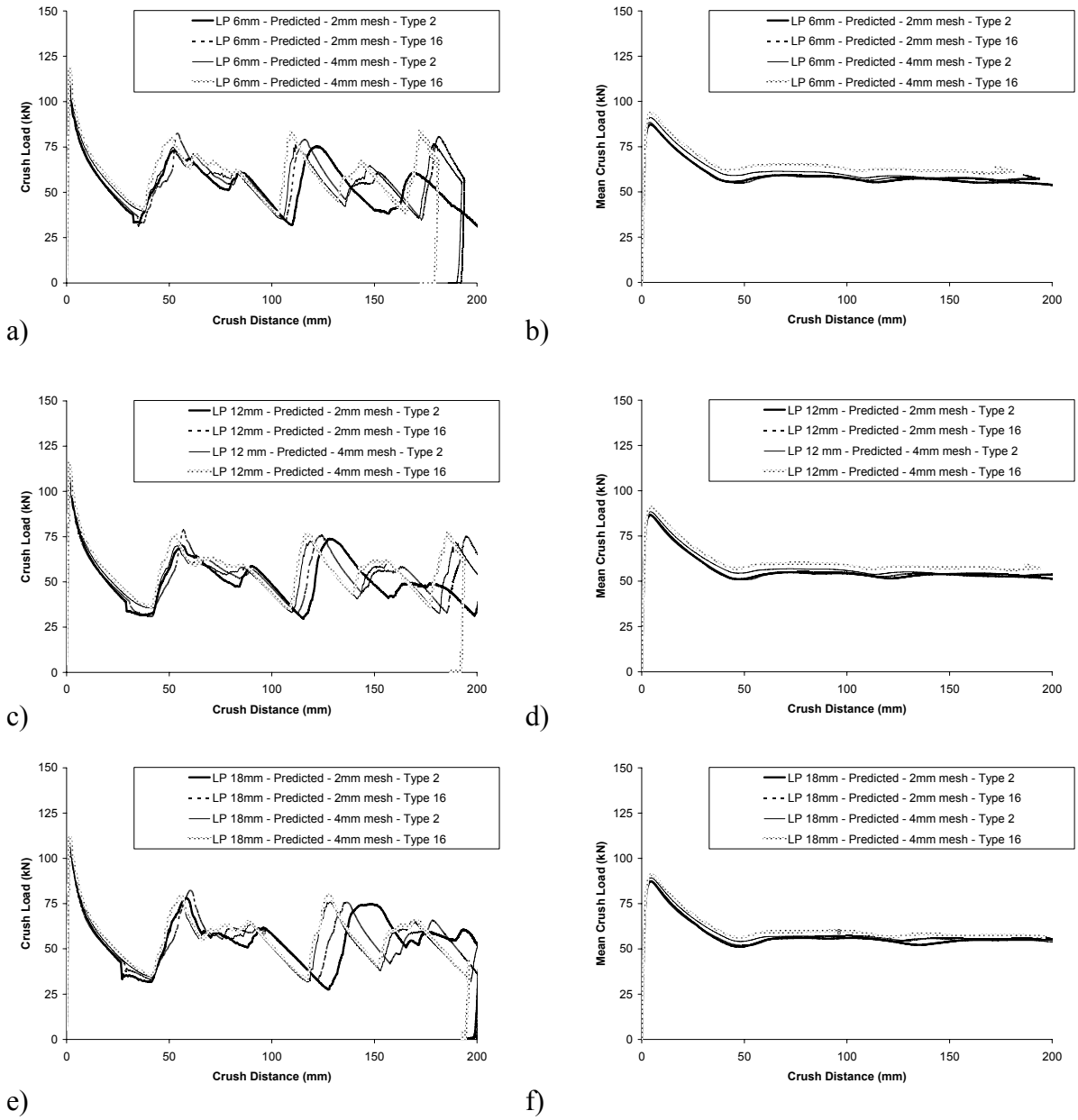
Figure B.12: Mesh sensitivity for AA5754 alloy tubes formed using low pressure hydroforming process

a) LP 6mm   b) LP 6mm – mean load

c) LP 12mm   d) LP 12mm – mean load
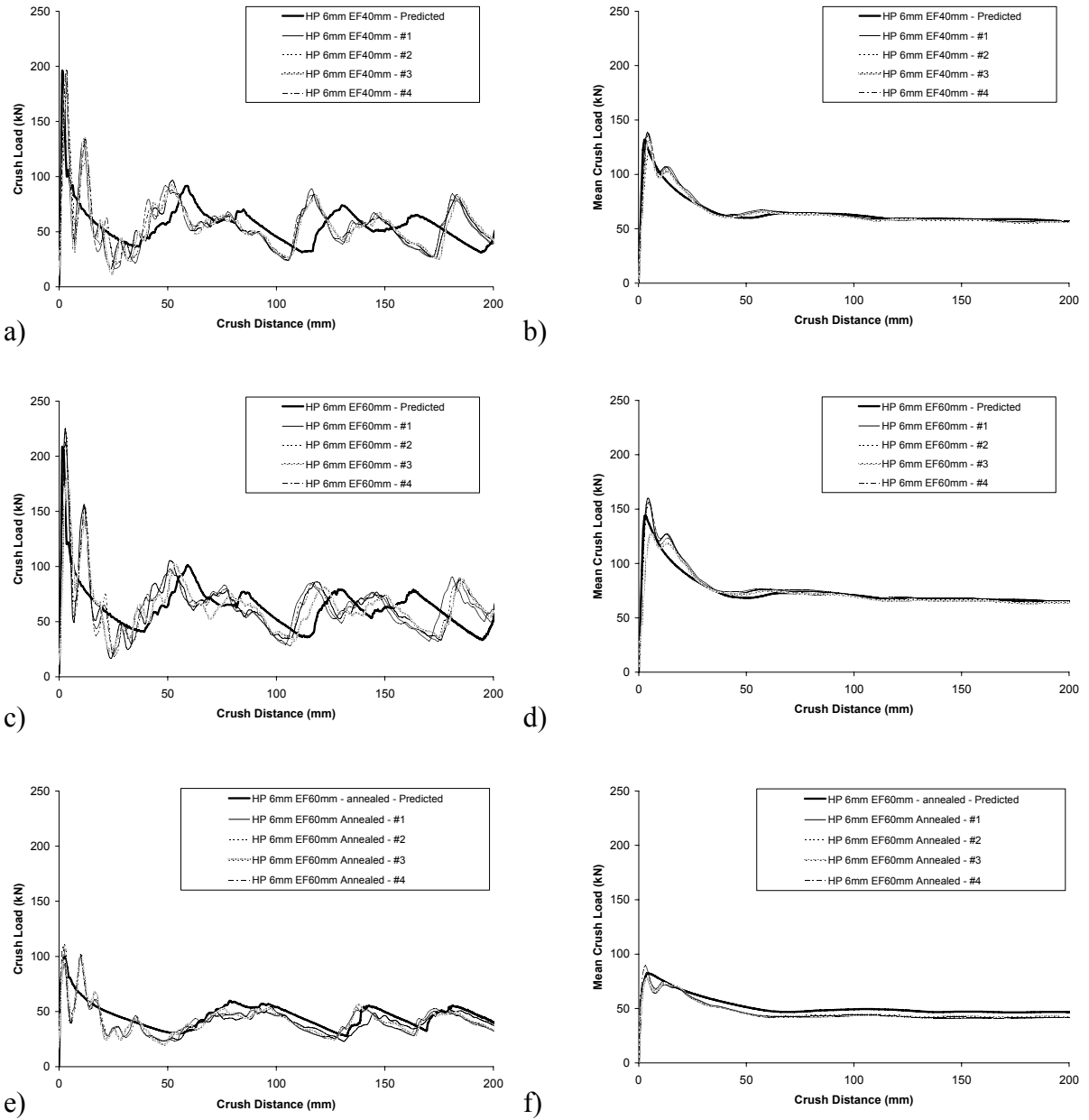
e) LP 18mm   f) LP 18mm – mean load
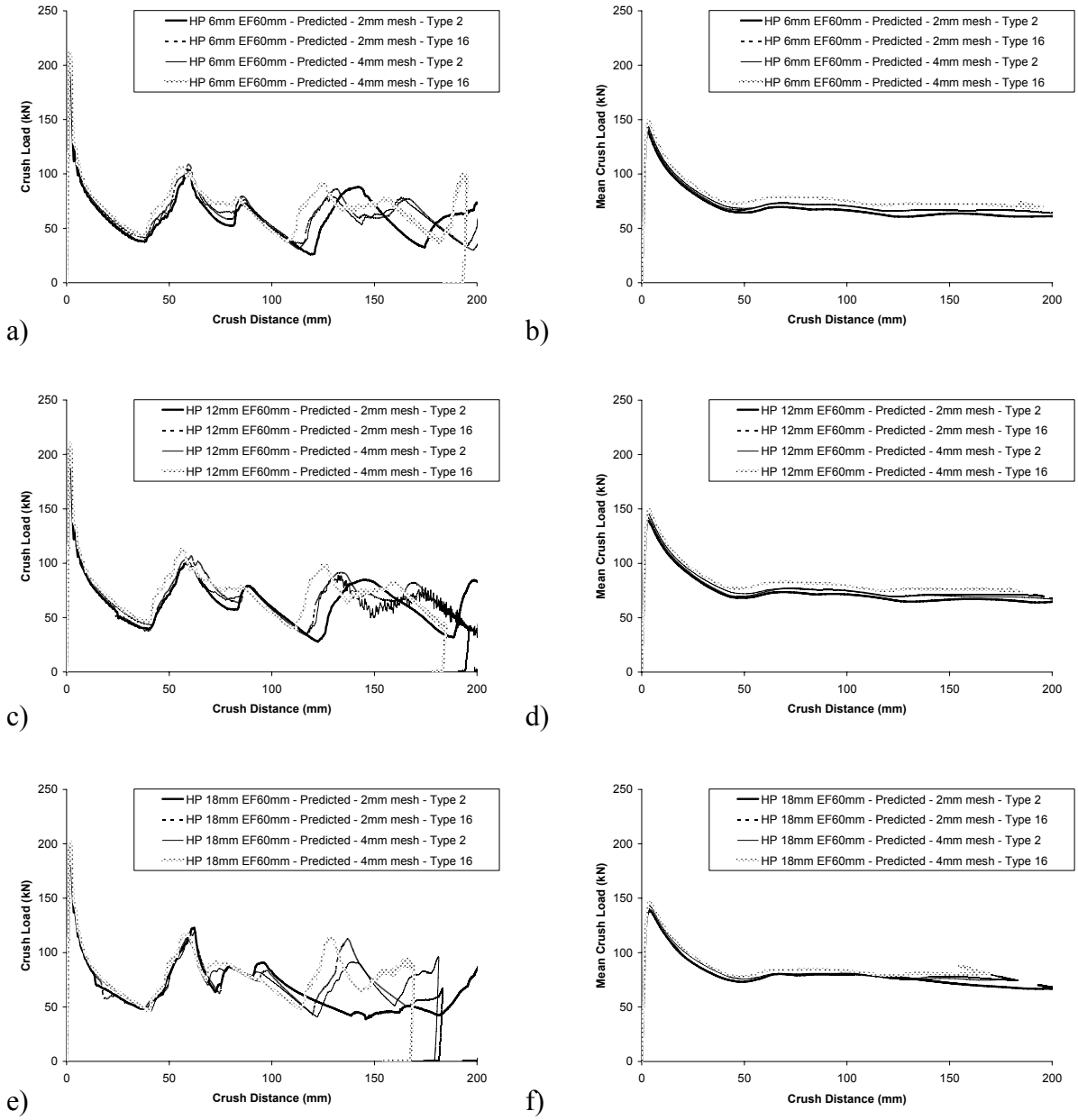
Figure B.13: Mesh sensitivity for AA5754 alloy tubes formed using high pressure hydroforming process

a) HP 6mm EF60mm   b) HP 6mm EF60mm – mean load

c) HP 12mm EF60mm   d) HP 12mm EF60mm – mean load

e) HP 18mm EF60mm   f) HP 18mm EF60mm – mean load
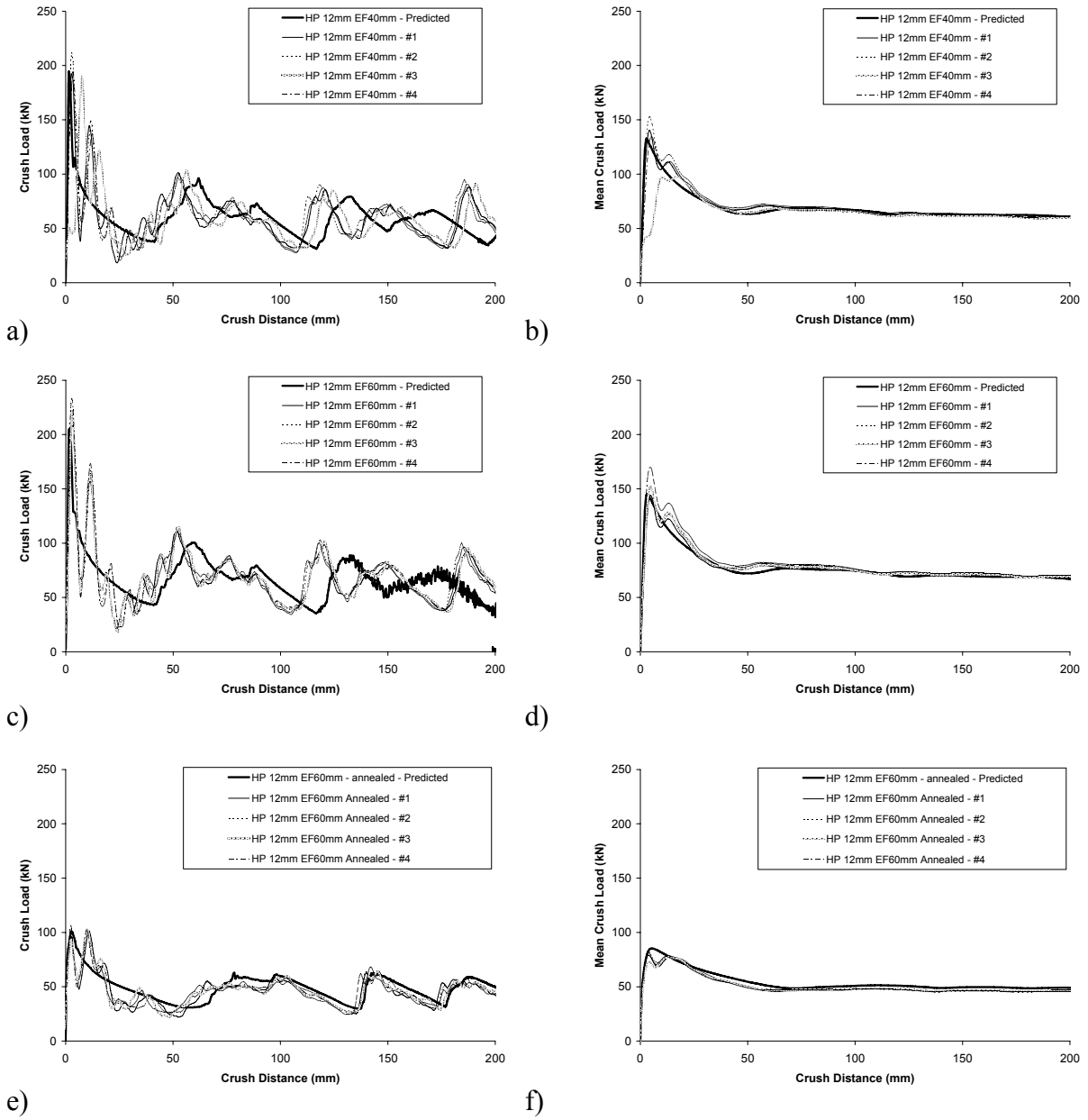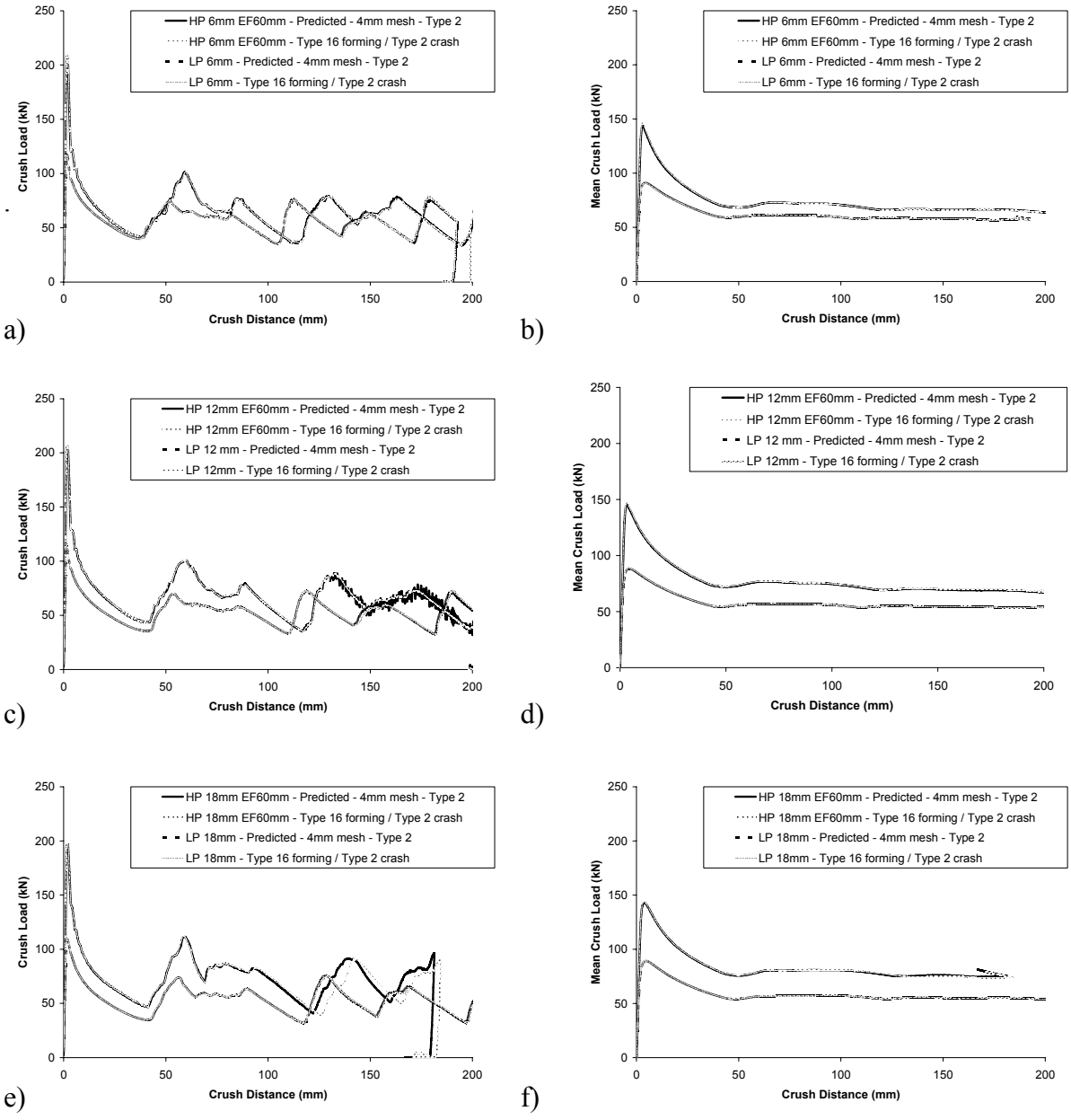
Figure B.14: Predicted crush response for AA5754 alloy tubes comparing element formulation between hydroforming and crash

a) 6mm   b) 6mm – mean load

c) 12mm   d) 12mm – mean load

e) 18mm   f) 18mm – mean load

Appendix C

Theoretical Calculations and Predictions

The following equations provide details about how the thickness of the tube during hydroforming was calculated for a given corner radius of the tube, R, under the assumption of sticking friction (Figure C.1).
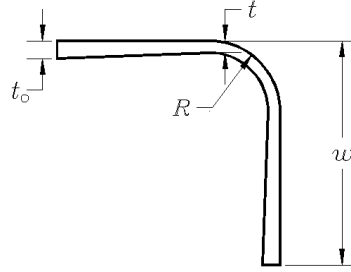
Figure C.1: ¼ profile of tube cross-section assuming sticking friction

The original ¼ area, A_0, of the circular tube is described by,

$$A_0 = \frac{\pi[R_0^2 - (R_0 - t_0)^2]}{4}$$

(C.1)

where, R_0 is the original outer radius of the tube. The increase in area, ΔA, due to an end-feed increment, Δl, can be described by,

$$\Delta A = \frac{\Delta l A_0}{l_0 - \Delta l}$$

(C.2)

where, l_0 is the original length of the tube. This equation was based on the assumption that the increment in area is constant over the entire length of the tube.

The current area of the tube can be described by,

$$A^i = A^{i-1} + \Delta A^i$$

(C.3)

where, the subscript i represents the current increment of the end-feed. This is also equal to the cross-section area shown in Figure C.1, given by,

$$A^i = 2\left[(w - R)t + \frac{1}{2}(w - R)(t_0 - t)\right] + \frac{\pi\left[R^2 - (R - t)^2\right]}{4}$$

(C.4)

where, t_0 is the initial tube thickness, t is the thickness in the corner region, and w is the original outer radius of the tube. The thickness was determined by equating Equations C.3

202

and C.4 and then rearranging to solve for the thickness using the positive root of the quadratic equation,

$$t = \frac{-b + \sqrt{b^2 - 4ac}}{2a}$$ (C.5)

where,

$$a = -\frac{\pi}{4} \qquad b = R_0 + R\left(\frac{\pi}{2} - 1\right) \qquad c = t_0 R_0 - R t_0 - A^i$$ (C.6)

 are the coefficients in the quadratic equation.

Once the thickness was determined, the procedure described in Chapter 3 was followed to determine the nominal thickness and effective strain resulting from the high pressure hydroforming operation. The theoretical strain predictions are shown in Figure C.2 and are compared to measured data for the AA5754 tubes formed using the high pressure process. The thickness predictions are compared to measured data in Figure C.3.
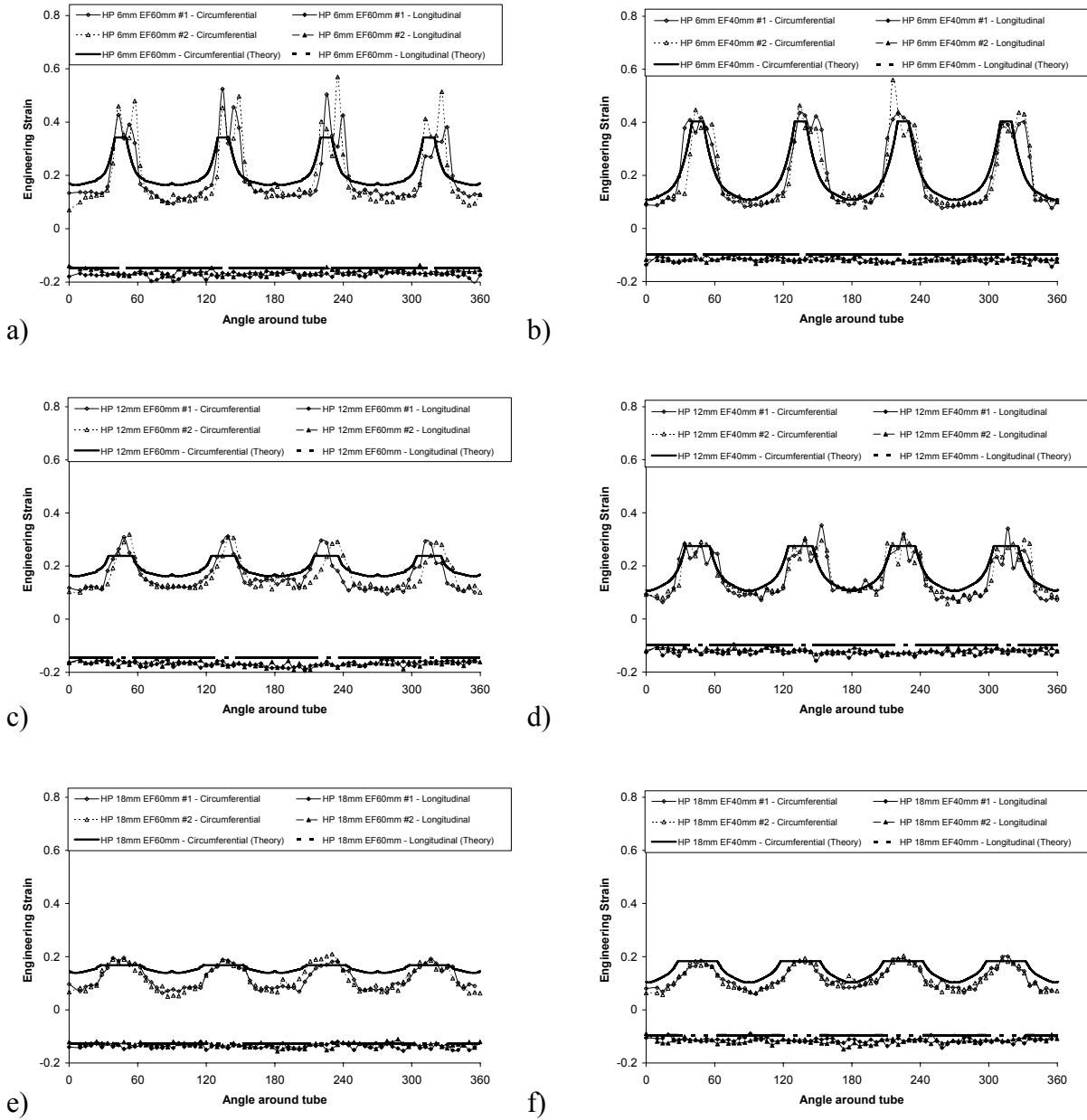
Figure C.2: Comparison of theoretical and measured circumferential and longitudinal strains for AA5754 tubes formed using the high pressure hydroforming process

a) HP 6mm EF60mm   b) HP 6mm EF40mm   c) HP 12mm EF60mm

d) HP 12mm EF40mm   e) HP 18mm EF60mm   f) HP 18mm EF40mm
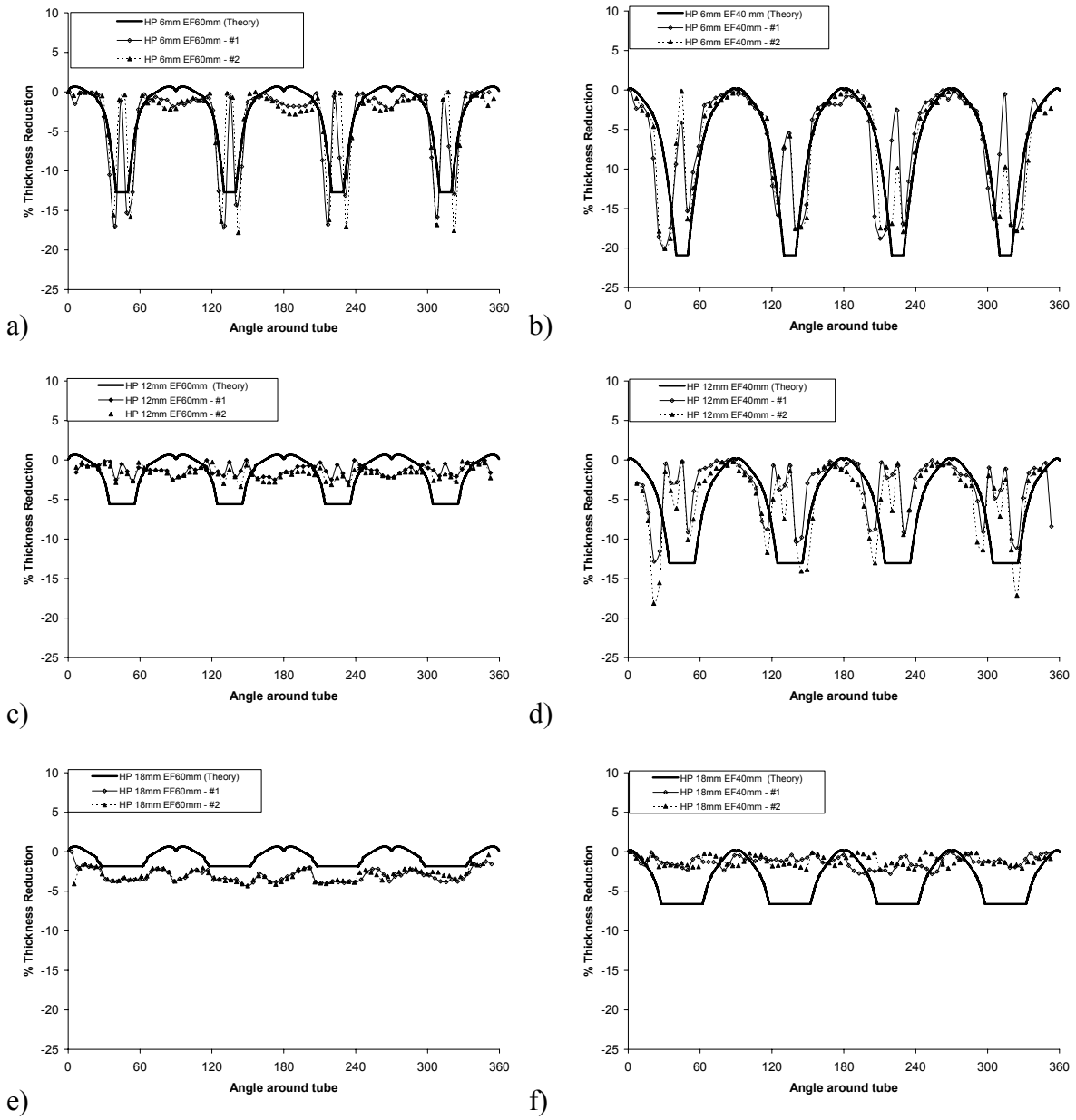
Figure C.3:   Comparison of theoretical and measured thicknesses for AA5754 tubes formed using the high pressure hydroforming process

a) HP 6mm EF60mm   b) HP 6mm EF40mm   c) HP 12mm EF60mm

d) HP 12mm EF40mm   e) HP 18mm EF60mm   f) HP 18mm EF40mm

The strain on the tensile and compressive sides of a bend can be determined based on the equations given below assuming that the original circular profile had no previous strain. A section of the bend is shown in Figure C.4, where l_{t0} and l_{c0} represent the original arc lengths on the outer and inner surface of the tube, respectively, and N.A. represents the neutral axis.
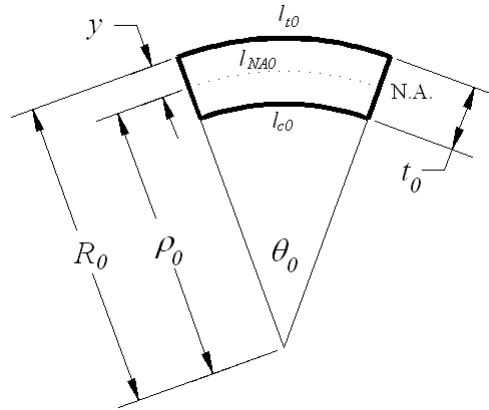
Figure C.4: Section of bend in sheet material

The true strain on the tensile side of the bend is given by,

$$\varepsilon_{tensile} = \ln\left(\frac{l_t}{l_{t0}}\right) = \ln\left[\frac{l_{NA}\left(1+\dfrac{y}{\rho}\right)}{l_{NA0}\left(1+\dfrac{y}{\rho_0}\right)}\right] = \ln\left(\frac{l_{NA}}{l_{NA0}}\right) + \ln\left(\frac{1+\dfrac{y}{\rho}}{1+\dfrac{y}{\rho_0}}\right) \tag{C.7}$$

where, $y = t_0/2$, $\rho_0 = R_0 - t_0/2$, and $\rho = R - t/2$, with R_0 and t_0 being the initial radius and thickness of the bend, and R being the current radius of the bend. The length of the outer surface of the tube after the bend is given by l_t. If the strain of the neutral axis is ignored, then Equation C.7 can be simplified to give,

$$\varepsilon_{tensile} = \ln\left[\frac{1+\dfrac{t_0/2}{R-t_0/2}}{1+\dfrac{t_0/2}{R_0-t_0/2}}\right] \tag{C.8}$$

206

which is the equation provided in Chapter 3. The true strain on the compressive side of the bend can be expressed by,

$$\varepsilon_{compresive} = \ln\left(\frac{l_c}{l_{c0}}\right) = \ln\left[\frac{l_{NA}\left(1-\frac{y}{\rho}\right)}{l_{NA0}\left(1-\frac{y}{\rho_0}\right)}\right] = \ln\left(\frac{l_{NA}}{l_{NA0}}\right) + \ln\left(\frac{1-\frac{y}{\rho}}{1-\frac{y}{\rho_0}}\right) \qquad (C.9)$$

where, l_c is the length of the surface on the compressive side of the bend. This equation can be simplified to give,

$$\varepsilon_{compressive} = \ln\left[\frac{1-\frac{t_0/2}{R-t_0/2}}{1-\frac{t_0/2}{R_0-t_0/2}}\right] \qquad (C.10)$$

Equations C.8 and C.10 were used to determine the maximum strains on the tensile and compressive sides in the corner of a tube formed using the low pressure hydroforming process. It was then assumed that the strain decreased to a value of zero at the beginning of the flat section in the cross-section of the tube. The length of the outer surface, l_{of}, of the corner of the hydroformed tube shown in Figure C.5, is equal to,

$$l_{of} = \frac{2\pi R}{4} \qquad (C.11)$$

which can then be used to determine the original outer length in the non-hydroformed circular tube, l_{o0}, given by,

$$l_{o0} = \frac{l_{of}}{\exp(\varepsilon_{t_{nominal}})} \qquad (C.12)$$

It was reasonable to assume that the outer circumference of the tube does not change, such that if the outer surfaces of the corners are in tension, then the outer surface of the flat regions must be in compression. The original length of this section in the non-hydroformed tube is described by,

$$l_{0_{flat}} = \frac{(2\pi R - 4l_{o0})}{4} \qquad (C.13)$$

207

which can then be used to determine the compressive strain, $\varepsilon_{flat_{outer}}$, acting in the flat sections on the outer surface of the hydroformed tube, expressed by,

$$\varepsilon_{flat_{outer}} = \ln\left[\frac{R_0 - 2R}{l_{0_{flat}}}\right] \tag{C.14}$$

A similar procedure was then used to determine the tensile strain on the inner surface of the flat regions of the hydroformed tube. In all cases, the strain at the neutral axis was assumed to be zero. Once a profile for the circumferential strain was predicted, Equations 3.3 and 3.4 were used to determine the effective strain acting in the cross-section. The results of the theoretical predictions of the low pressure hydroforming operation of AA5754 tubes are compared to experimental strain data in Figure C.6.
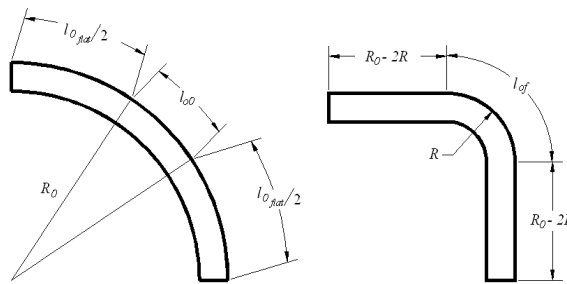
Figure C.5: ¼ profile of non-hydroformed and hydroformed section

It should be noted that with this simple procedure, there is a strain discontinuity at the end of the flat regions in the tube, where the strain goes from zero to the value determined from Equation C.14 (for the outer surface), which does not occur experimentally. However, since this method was only meant as an approximation of the strain hardening in the tube, there was no attempt to address this issue in this research. As suggested in Chapter 3, it is best to use finite element models to predict thickness and strain hardening during the hydroforming operation.
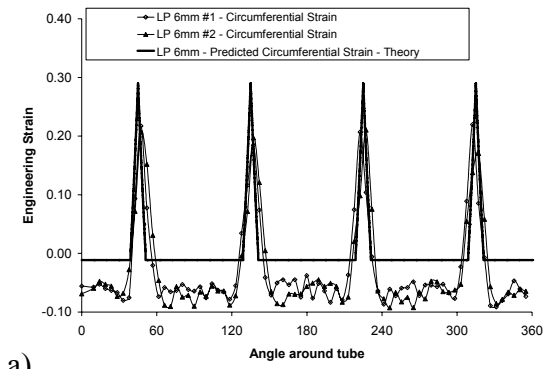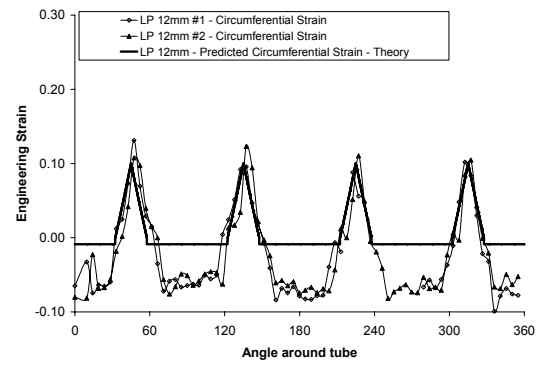
a)   b)
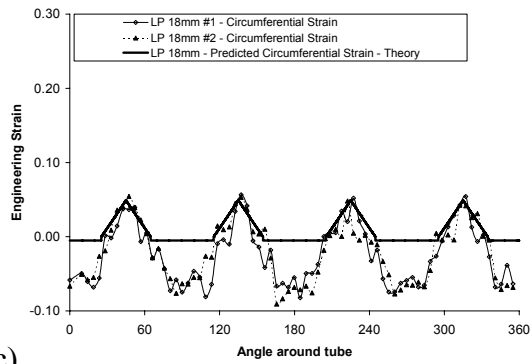
c)

Figure C.6:   Comparison of theoretical and measured circumferential strain for AA5754 tubes formed using the low pressure hydroforming process

a) LP 6mm   b) LP 12mm   c) LP 18mm

209

Once the nominal values for thickness and effective strain in the tubes were determined based on the equations discussed above, the theoretical mean loads from axial crush were calculated using the equations discussed in Chapter 3. The values are given in Table C.1.

Table C.1: Theoretical mean loads based on several methods to calculate the energy equivalent flow stress, σ_0

Hydroforming Process	Description	Method to Determine σ_0	Theoretical Mean Load (kN)		
			R6mm	R12mm	R18mm
high pressure	sticking friction	#1	71.2	73.0	75.1
		#2	73.8	75.4	77.0
		#3	74.1	75.6	76.6
		#4	68.5	69.9	70.8
	sticking friction - annealed	#1	62.1	63.4	64.6
		#2	63.4	64.7	65.9
		#3	53.3	54.4	55.5
		#4	45.5	46.5	47.3
	non-sticking friction	#4	62.8	67.1	71.2
	non-sticking friction - annealed	#4	41.8	44.6	47.4
low pressure	---	#1	68.5	66.0	65.5
		#2	68.4	66.3	66.1
		#3	64.5	59.4	58.0
		#4	59.1	53.2	51.3

The following table provides several theoretical calculations for the non-hydroformed AA5754 alloy tubes based on either an axisymmetric or non-axisymmetric crush mode. The theoretical equations were presented in Chapter 1. In all cases, Method 4 was used to determine the energy equivalent flow stress. The radius and thickness used in the calculations was 36.6 mm and 3.07 mm, respectively. The yield strength and tensile strength, which were also required for the predictions, were 100 MPa and 225 MPa, respectively.

Table C.2: Theoretical predictions for non-hydroformed, circular tubes

Crush Mode	Prediction Model	Theoretical Mean Load (kN)
Axisymmetric (concertina)	Alexander, 1960	40.6
	Singace et al., 1995	37.4
	Wierzbicki, 1992	50.6
	Abramowicz and Jones, 1984	42.8
Non-axisymmetric (diamond)	Abramowicz and Jones, 1984	93.5
	Wierzbicki, 1983	68.3
	Pugsley and Macaulay, 1960	85.1

Appendix D

Influence of Thickness Changes, Work Hardening, Residual Stresses, Geometry, and Mass

This appendix provides the crush response curves based on simulations that studied the influence of geometry, mass, thickness, work hardening, and residual stresses, resulting from the hydroforming operation, on the axial crush response of the tubes.

Table D.1: Predicted crush data from simulations studying the influence of forming history

Description	Radius (mm)	Radius Ratio	Energy Absorption (J)	Distance at EA (mm)	Mean Load (kN)
Low Pressure Hydroforming Process					
With entire forming history - thickness, work hardening, and residual stresses	6	0.16	11073.3	191.9	57.7
With entire forming history - thickness, work hardening, and residual stresses	12	0.31	10783.7	199.3	54.1
With entire forming history - thickness, work hardening, and residual stresses	18	0.47	10760.6	199.3	54.0
Initial thickness of 3.07 mm	6	0.16	9592.7	199.2	48.1
Initial thickness of 3.07 mm	12	0.31	9214.0	199.2	46.3
Initial thickness of 3.07 mm	18	0.47	9629.0	199.0	48.4
Predicted thickness, without work hardening and residual stresses	6	0.16	9717.5	199.2	48.8
Predicted thickness, without work hardening and residual stresses	12	0.31	9151.8	199.1	46.0
Predicted thickness, without work hardening and residual stresses	18	0.47	9514.2	198.9	47.8
Removed residual stresses	6	0.16	11414.8	199.1	57.3
Removed residual stresses	12	0.31	10809.9	199.1	54.3
Removed residual stresses	18	0.47	10787.2	199.3	54.1
High Pressure Hydroforming Process					
With entire forming history - thickness, work hardening, and residual stresses	6	0.16	12746.0	199.3	64.0
With entire forming history - thickness, work hardening, and residual stresses	12	0.31	13397.1	199.2	67.2
With entire forming history - thickness, work hardening, and residual stresses	18	0.47	13631.4	180.6	75.5
With forming history - annealed	6	0.16	9317.3	199.2	46.8
With forming history - annealed	12	0.31	9813.1	199.3	49.2
With forming history - annealed	18	0.47	10253.5	199.3	51.4
Initial thickness of 3.07 mm	6	0.16	10047.0	199.0	50.5
Initial thickness of 3.07 mm	12	0.31	9789.4	199.2	49.1
Initial thickness of 3.07 mm	18	0.47	9815.3	199.2	49.3
Removed residual stresses	6	0.16	12688.4	199.3	63.7
Removed residual stresses	12	0.31	13585.5	199.3	68.2
Removed residual stresses	18	0.47	13629.3	183.7	74.2
Initial thickness of 3.07 mm with work hardening	6	0.16	13639.4	192.0	71.0
Initial thickness of 3.07 mm with work hardening	12	0.31	13606.9	199.3	68.3
Initial thickness of 3.07 mm with work hardening	18	0.47	13635.5	189.4	72.0

Note: All simulations performed using von Mises yield criterion, type 2 elements, and 4 mm mesh
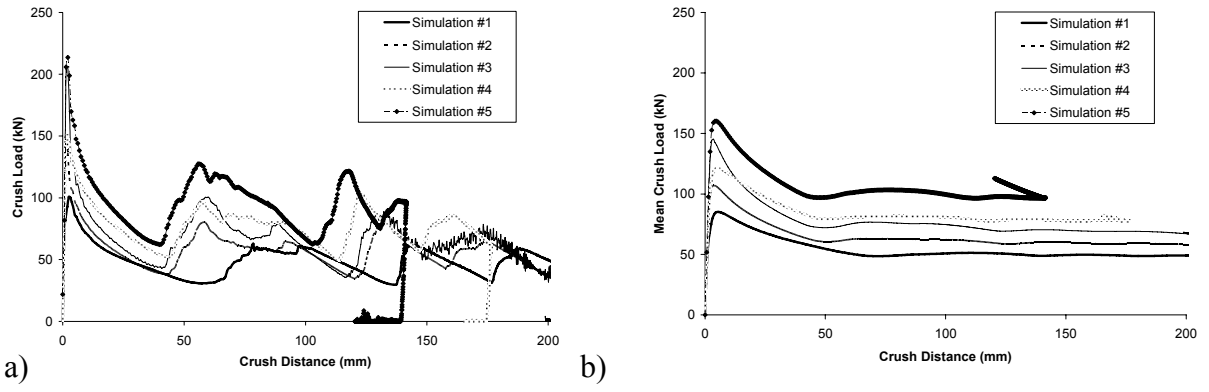
a) b)

Figure D.1: Crush response of tubes with a mass of approximately 920 grams with varying geometry and thickness
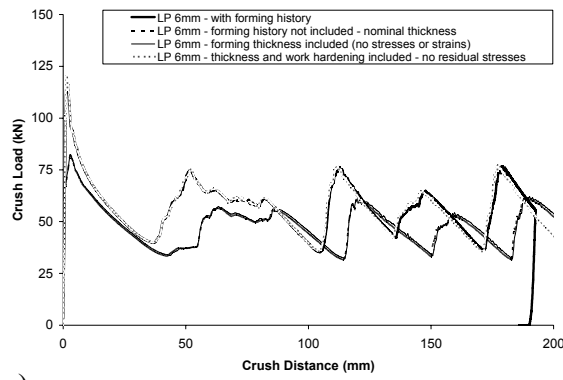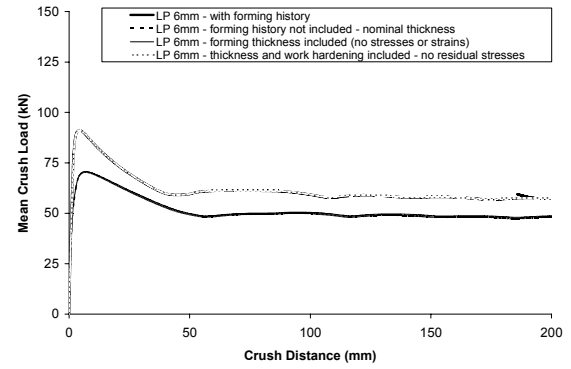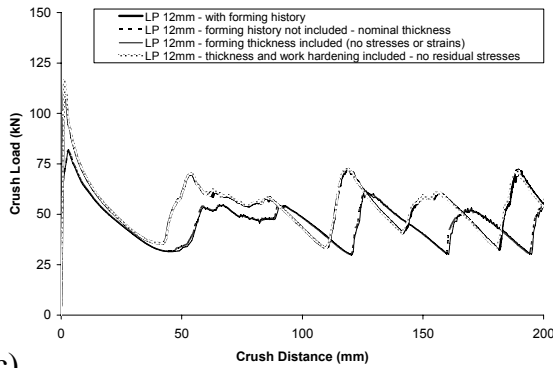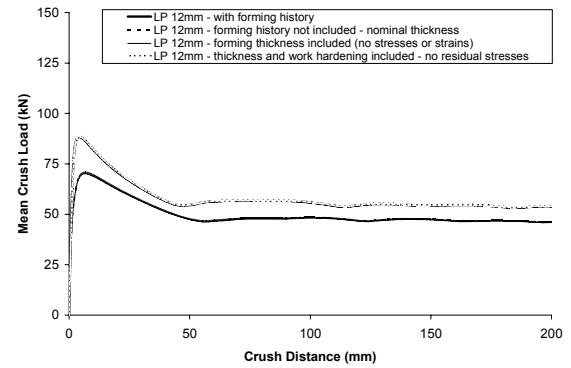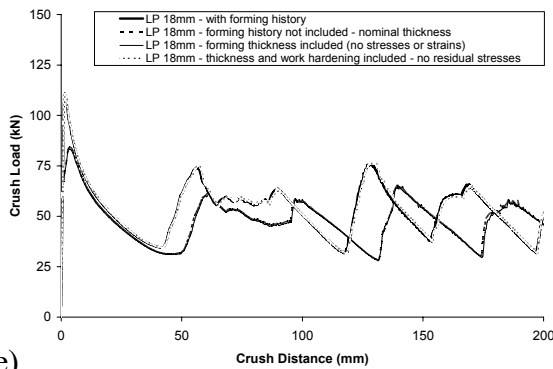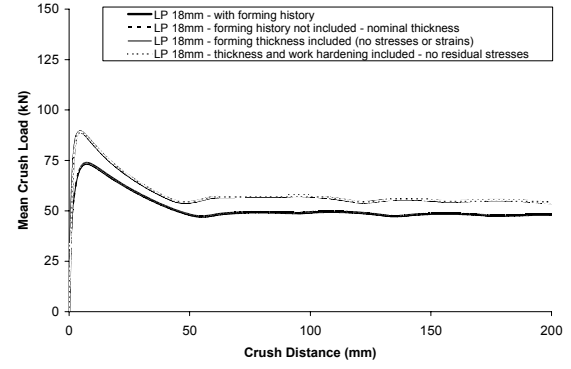
Figure D.2: Influence of thickness, residual stress, and work hardening for AA5754 alloy tubes formed using low pressure hydroforming process

a) LP 6mm   b) LP 6mm – mean load

c) LP 12mm   d) LP 12mm – mean load

e) LP 18mm   f) LP 18mm – mean load
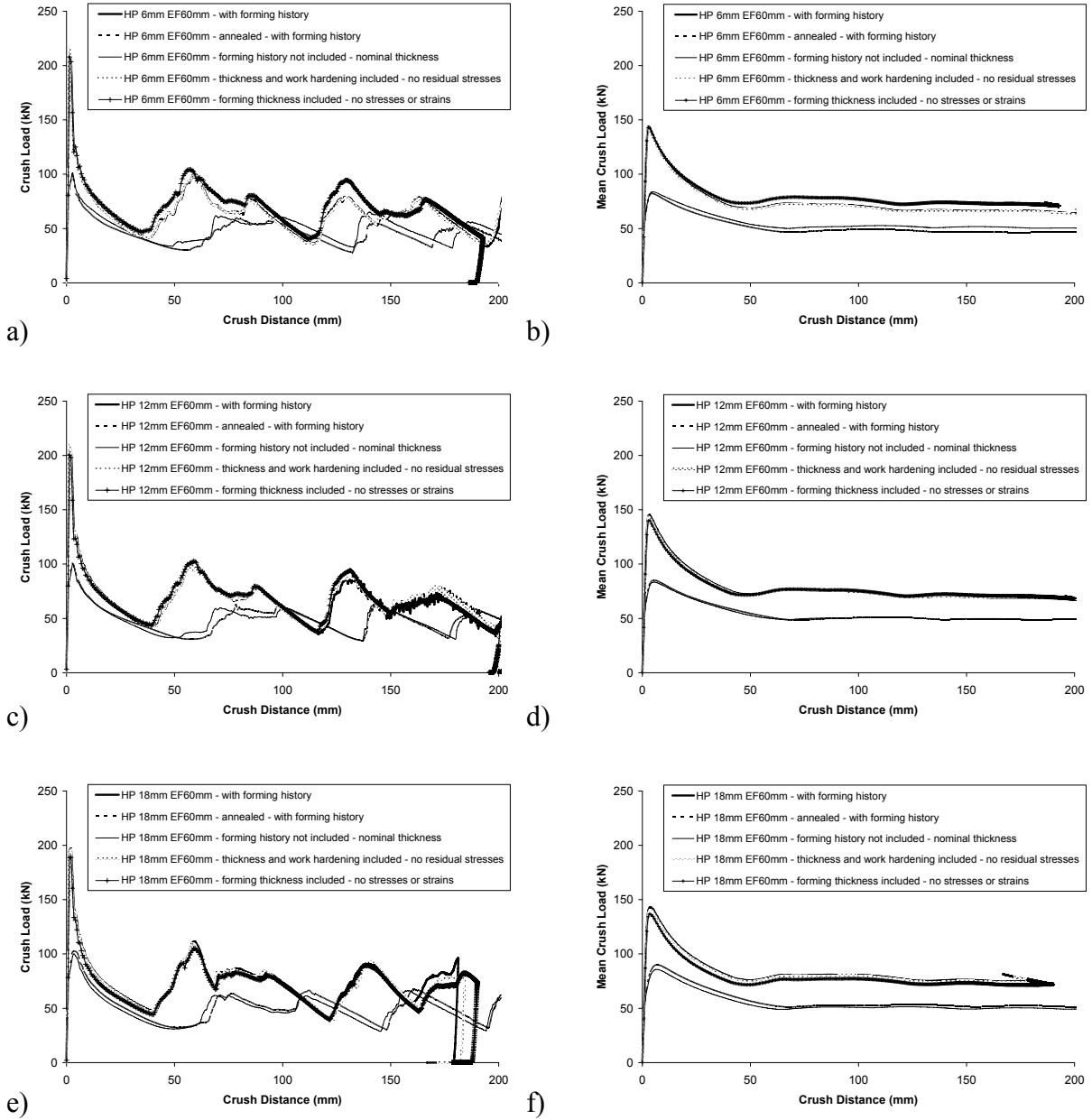
Figure D.3: Mesh sensitivity for AA5754 alloy tubes formed using high pressure hydroforming process

a) HP 6mm EF60mm　　　　　　　　b) HP 6mm EF60mm – mean load

c) HP 12mm EF60mm　　　　　　　　d) HP 12mm EF60mm – mean load

e) HP 18mm EF60mm　　　　　　　　f) HP 18mm EF60mm – mean load

216

Appendix E

Influence of Damage, Strain-Rate, Kinematic Hardening, and Anisotropy

The following appendix provides the predicted crush response of the hydroformed AA5754 alloy tubes based on constitutive models incorporating damage, kinematic hardening, anisotropy, and strain-rate effects. The results are compared to isotopic predictions.

Table E.1: Predicted crush response using Gurson-Tvergaard-Needleman damage model

| Description	Radius (mm)	Radius Ratio	Energy Absorption (J)	Distance at EA (mm)	Mean Load (kN)
HP R6mm EF60mm - isotropic	6.0	0.16	11948.3	199.3	60.0
HP R12mm EF60mm - isotropic	12.0	0.31	12655.3	199.2	63.5
HP R18mm EF60mm - isotropic	18.0	0.47	13632.9	192.2	70.9
HP R6mm EF60mm - GTN	6.0	0.16	11853.5	199.2	59.5
HP R12mm EF60mm - GTN	12.0	0.31	12641.5	199.2	63.5
HP R18mm EF60mm - GTN	18.0	0.47	13620.4	199.3	68.3

Table E.2: Predicted crush response from the Johnson-Cook strain-rate model

Description	Radius (mm)	Radius Ratio	Energy Absorption (J)	Distance at EA (mm)	Mean Load (kN)
HP R6mm EF60mm - isotropic	6.0	0.16	12414.1	199.3	62.3
HP R12mm EF60mm - isotropic	12.0	0.31	13483.6	199.2	67.7
HP R18mm EF60mm - isotropic	18.0	0.47	13632.2	185.0	73.7
HP R6mm EF60mm annealed - isotropic	6.0	0.16	9166.0	199.2	46.0
HP R12mm EF60mm annealed- isotropic	12.0	0.31	9646.1	199.2	48.4
HP R18mm EF60mm annealed - isotropic	18.0	0.47	10157.9	199.3	51.0
HP R6mm EF60mm - Johnson-Cook	6.0	0.16	13072.9	199.2	65.6
HP R12mm EF60mm - Johnson-Cook	12.0	0.31	13635.7	189.6	71.9
HP R18mm EF60mm - Johnson-Cook	18.0	0.47	13629.8	173.3	78.6
HP R6mm EF60mm annealed - Johnson-Cook	6.0	0.16	9738.9	199.2	48.9
HP R12mm EF60mm annealed - Johnson-Cook	12.0	0.31	10231.2	199.2	51.4
HP R18mm EF60mm annealed - Johnson-Cook	18.0	0.47	10949.0	199.3	54.9

Table E.3: Predicted crush response from the non-linear isotropic-kinematic hardening model

Description	Radius (mm)	Radius Ratio	Energy Absorption (J)	Distance at EA (mm)	Mean Load (kN)
HP R6mm EF60mm - isotropic	6.0	0.16	12904.2	199.1	64.8
HP R12mm EF60mm - isotropic	12.0	0.31	13554.7	199.3	68.0
HP R18mm EF60mm - isotropic	18.0	0.47	13633.6	179.1	76.1
HP R6mm EF60mm annealed - isotropic	6.0	0.16	9386.3	199.3	47.1
HP R12mm EF60mm annealed- isotropic	12.0	0.31	9820.4	199.4	49.3
HP R18mm EF60mm annealed - isotropic	18.0	0.47	10267.6	199.3	51.5
HP R6mm EF60mm - kinematic	6.0	0.16	12142.0	199.2	61.0
HP R12mm EF60mm - kinematic	12.0	0.31	13022.5	199.2	65.4
HP R18mm EF60mm - kinematic	18.0	0.47	13631.3	188.3	72.4
HP R6mm EF60mm annealed - kinematic	6.0	0.16	9186.3	199.4	46.1
HP R12mm EF60mm annealed - kinematic	12.0	0.31	9657.1	199.3	48.4
HP R18mm EF60mm annealed - kinematic	18.0	0.47	9997.0	199.2	50.2

Table E.4: Predicted crush response from the Yld2000-2d anisotropic model

Description	Radius (mm)	Radius Ratio	Energy Absorption (J)	Distance at EA (mm)	Mean Load (kN)
HP R6mm EF60mm - isotropic	6.0	0.16	12611.2	199.2	63.3
HP R12mm EF60mm - isotropic	12.0	0.31	13292.6	199.2	66.7
HP R18mm EF60mm - isotropic	18.0	0.47	13632.8	181.0	75.3
HP R6mm EF60mm annealed - isotropic	6.0	0.16	9288.0	199.1	46.7
HP R12mm EF60mm annealed- isotropic	12.0	0.31	9794.2	199.0	49.2
HP R18mm EF60mm annealed - isotropic	18.0	0.47	10240.4	199.2	51.4
HP R6mm EF60mm - Yld2000-2d, current parameters	6.0	0.16	11523.3	199.2	57.9
HP R12mm EF60mm - Yld2000-2d, current parameters	12.0	0.31	11963.5	199.1	60.1
HP R18mm EF60mm - Yld2000-2d, current parameters	18.0	0.47	12614.3	199.2	63.3
HP R6mm EF60mm annealed - Yld2000-2d, current parameters	6.0	0.16	8217.5	199.2	41.3
HP R12mm EF60mm annealed - Yld2000-2d, current parameters	12.0	0.31	8694.2	199.0	43.7
HP R18mm EF60mm annealed - Yld2000-2d, current parameters	18.0	0.47	9132.0	199.2	45.9
HP R6mm EF60mm - Yld2000-2d, Lee et al. parameters	6.0	0.16	11631.5	199.3	58.4
HP R12mm EF60mm - Yld2000-2d, Lee et al. parameters	12.0	0.31	12293.0	199.1	61.7
HP R18mm EF60mm - Yld2000-2d, Lee et al. parameters	18.0	0.47	13002.4	199.3	65.2
HP R6mm EF60mm annealed - Yld2000-2d, Lee et al. parameters	6.0	0.16	8403.8	199.2	42.2
HP R12mm EF60mm annealed - Yld2000-2d, Lee et al. parameters	12.0	0.31	8787.2	199.2	44.1
HP R18mm EF60mm annealed - Yld2000-2d, Lee et al. parameters	18.0	0.47	9152.6	198.9	46.0

Table E.5: Predicted crush response from the combined constitutive model studying the effects of strain-rate, kinematic hardening, and anisotropy

Description	Annealed (yes/no)	Radius (mm)	Radius Ratio	Energy Absorption (J)	Distance at EA (mm)	Mean Load (kN)
Isotropic	no	6	0.16	12474.7	199.3	62.6
	no	12	0.31	13588.7	199.3	68.2
	no	18	0.47	13633.7	188.5	72.3
	yes	6	0.16	9154.2	199.2	46.0
	yes	12	0.31	9585.9	199.3	48.1
	yes	18	0.47	10087.8	199.3	50.6
Johnson - Cook strain rate model	no	6	0.16	13338.3	199.2	67.0
	no	12	0.31	13632.9	193.5	70.5
	no	18	0.47	13629.5	185.5	73.5
	yes	6	0.16	9559.2	199.2	48.0
	yes	12	0.31	9990.0	199.4	50.1
	yes	18	0.47	10456.4	199.3	52.5
Non-linear isotropic-kinematic hardening	no	6	0.16	12100.3	199.3	60.7
	no	12	0.31	12876.6	199.2	64.6
	no	18	0.47	13634.3	196.2	69.5
	yes	6	0.16	9052.1	199.3	45.4
	yes	12	0.31	9449.1	199.3	47.4
	yes	18	0.47	9845.5	199.2	49.4
Yld2000-2d anisotropic (current parameters)	no	6	0.16	11959.3	199.2	60.0
	no	12	0.31	12180.0	199.3	61.1
	no	18	0.47	13032.3	199.3	65.4
	yes	6	0.16	8519.3	199.3	42.8
	yes	12	0.31	8589.0	199.1	43.1
	yes	18	0.47	8855.1	199.2	44.5
Combined model	no	6	0.16	12033.0	199.1	60.4
	no	12	0.31	12330.2	199.1	61.9
	no	18	0.47	12616.0	199.2	63.3
	yes	6	0.16	8774.6	199.3	44.0
	yes	12	0.31	8848.7	199.3	44.4
	yes	18	0.47	9006.4	199.3	45.2

Note: all predictions are based on tubes formed using the high pressure process with 60 mm of end-feed
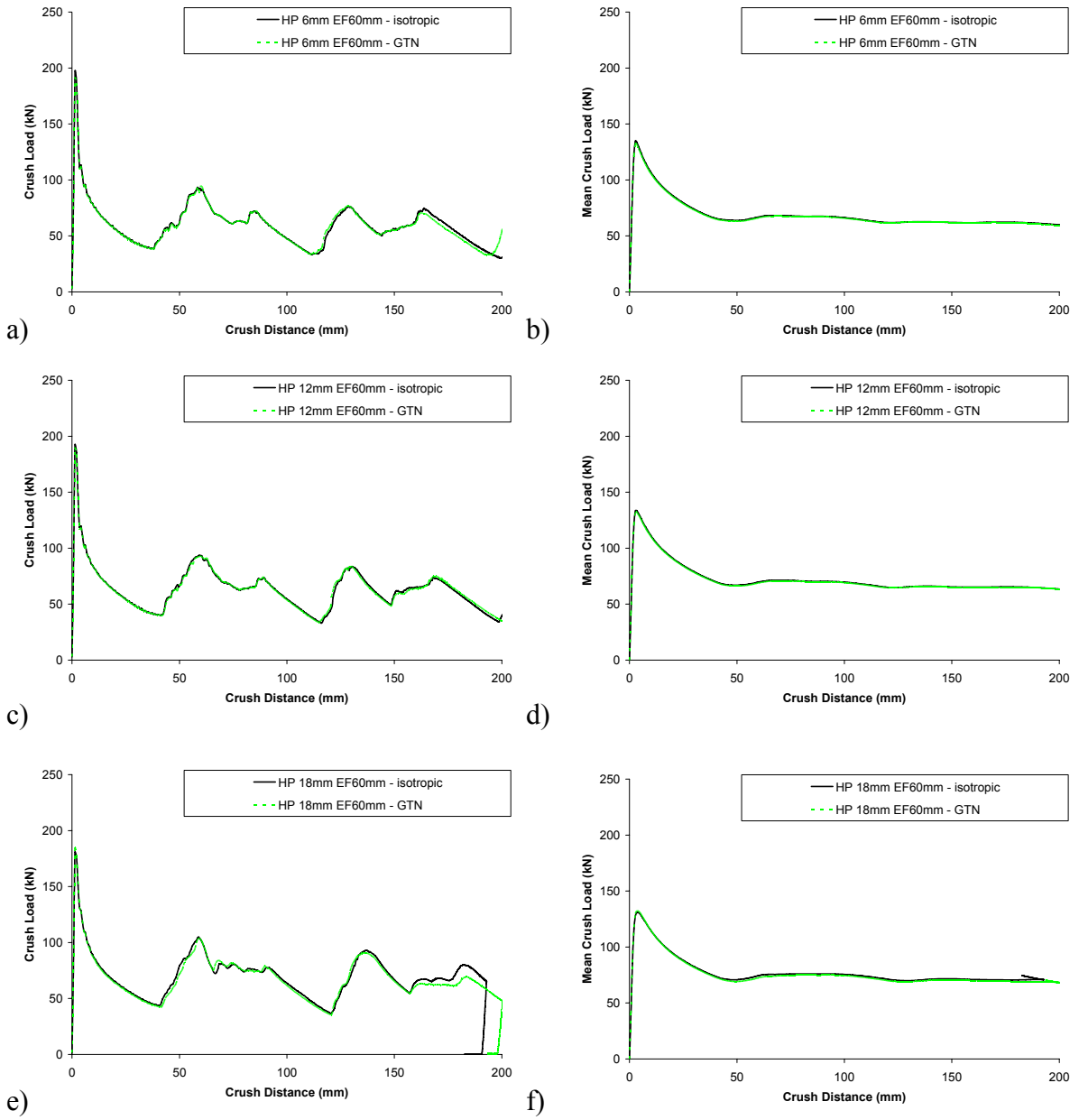
Figure E.1: Comparison of predicted crush response between isotropic and GTN models

a) HP 6mm EF60mm   b) HP 6mm EF60mm – mean load

c) HP 12mm EF60mm   d) HP 12mm EF60mm – mean load

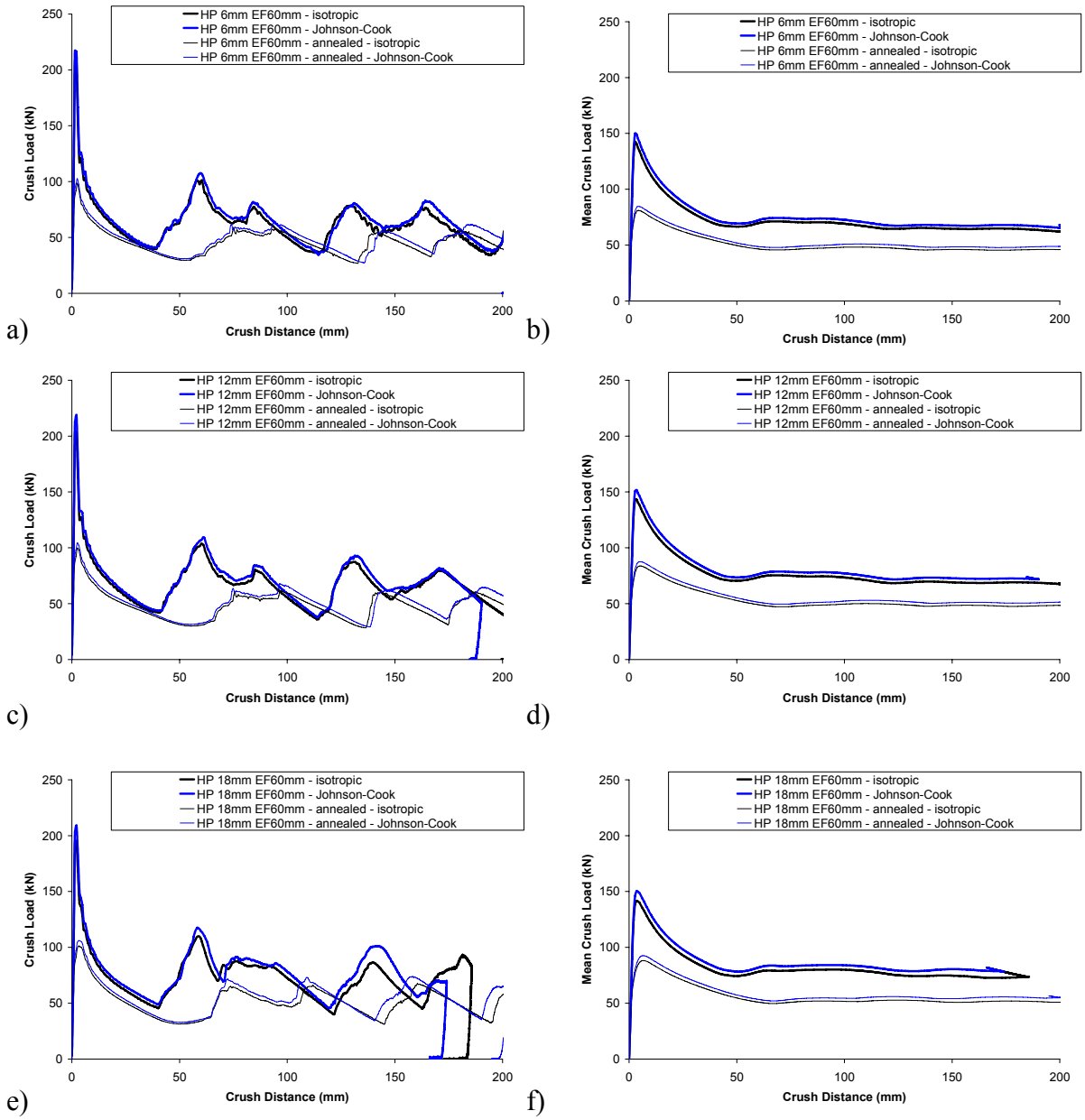e) HP 18mm EF60mm   f) HP 18mm EF60mm – mean load

Figure E.2: Comparison of crush response between isotropic and Johnson-Cook predictions

a) HP 6mm EF60mm

b) HP 6mm EF60mm – mean load

c) HP 12mm EF60mm

d) HP 12mm EF60mm – mean load

e) HP 18mm EF60mm

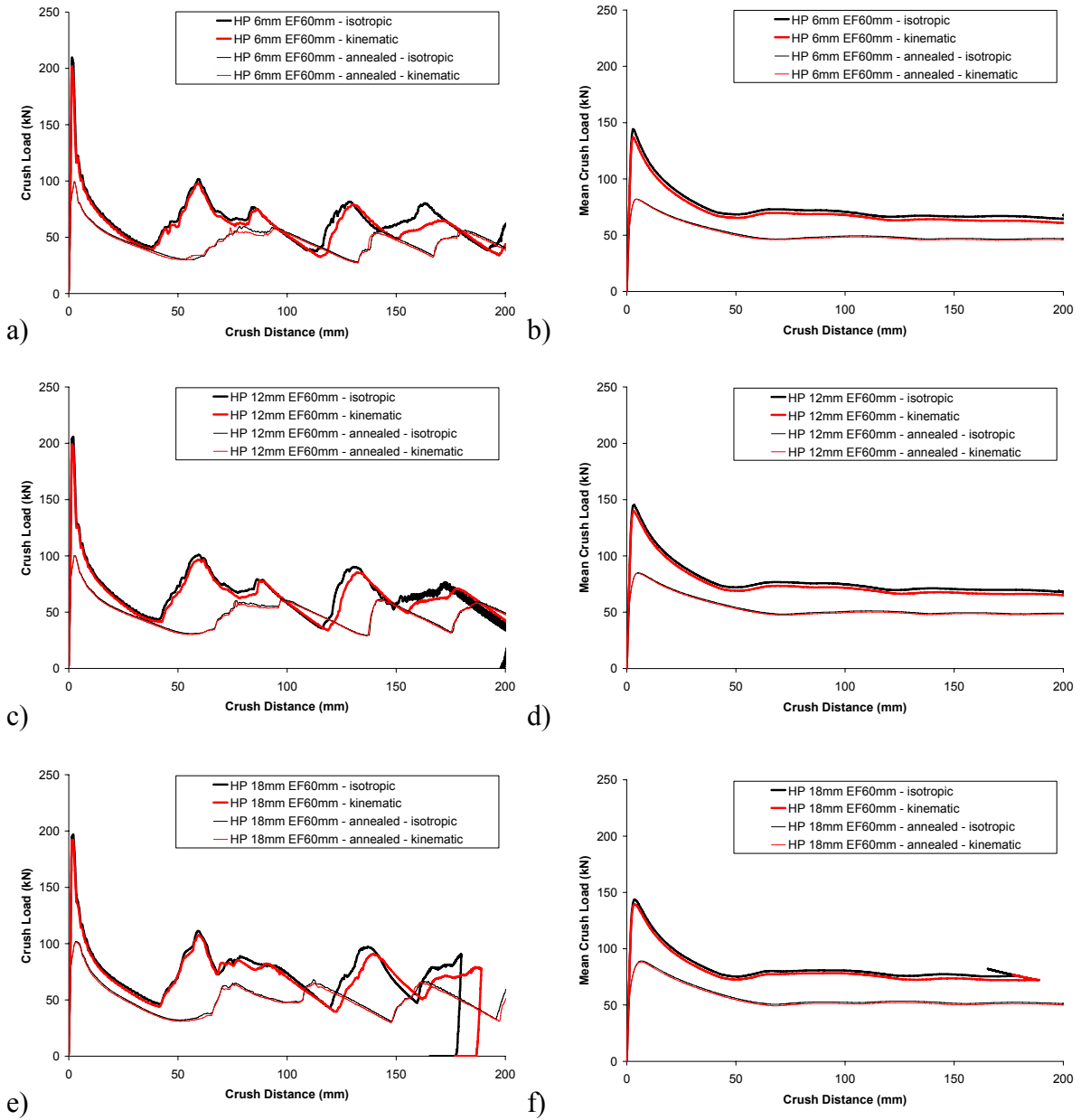f) HP 18mm EF60mm – mean load

Figure E.3: Comparison of crush response between isotropic and kinematic hardening predictions

a) HP 6mm EF60mm   b) HP 6mm EF60mm – mean load

c) HP 12mm EF60mm   d) HP 12mm EF60mm – mean load

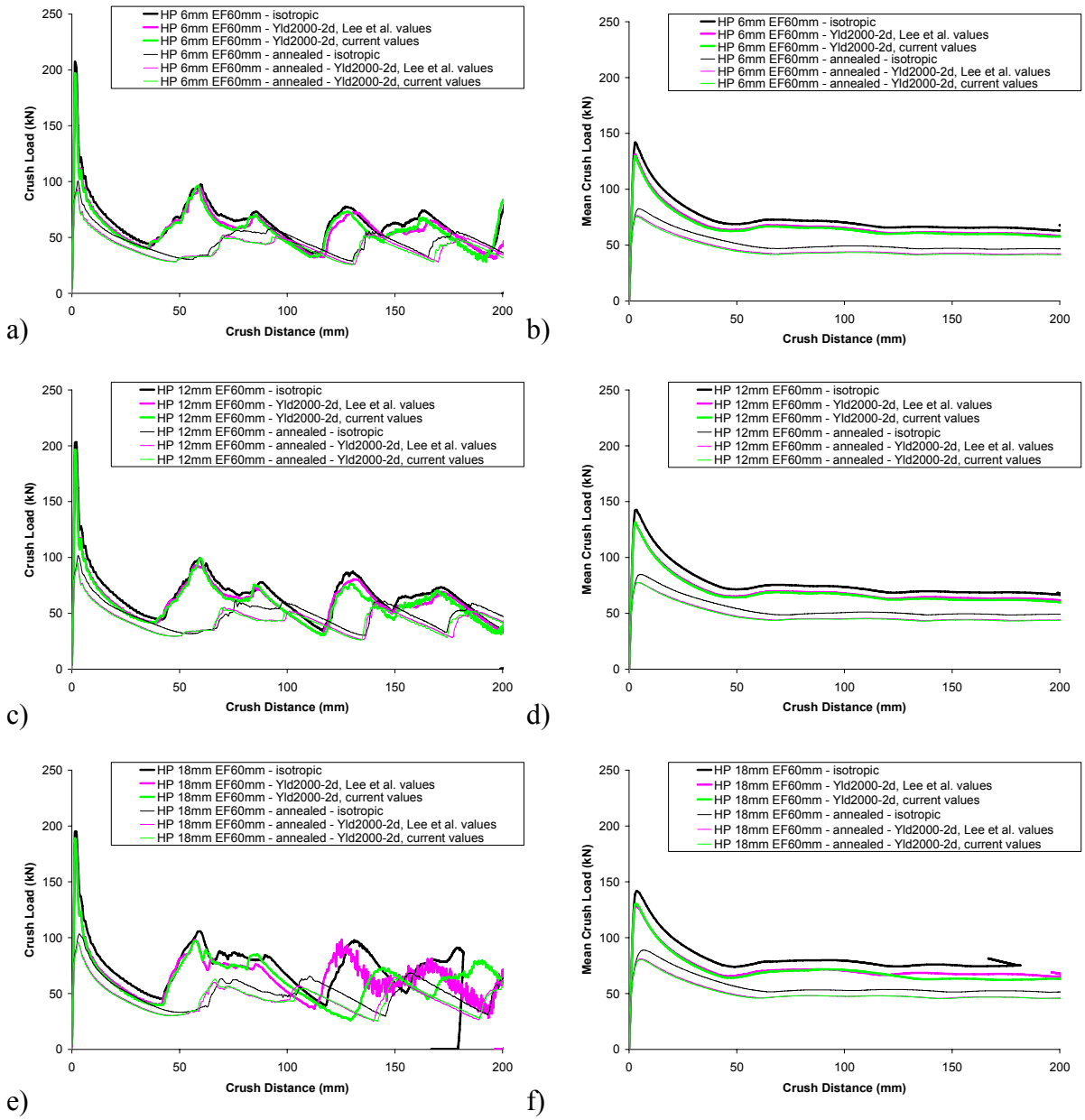e) HP 18mm EF60mm   f) HP 18mm EF60mm – mean load

Figure E.4: Comparison of crush response between isotropic and anisotropic predictions

a) HP 6mm EF60mm   b) HP 6mm EF60mm – mean load

c) HP 12mm EF60mm   d) HP 12mm EF60mm – mean load

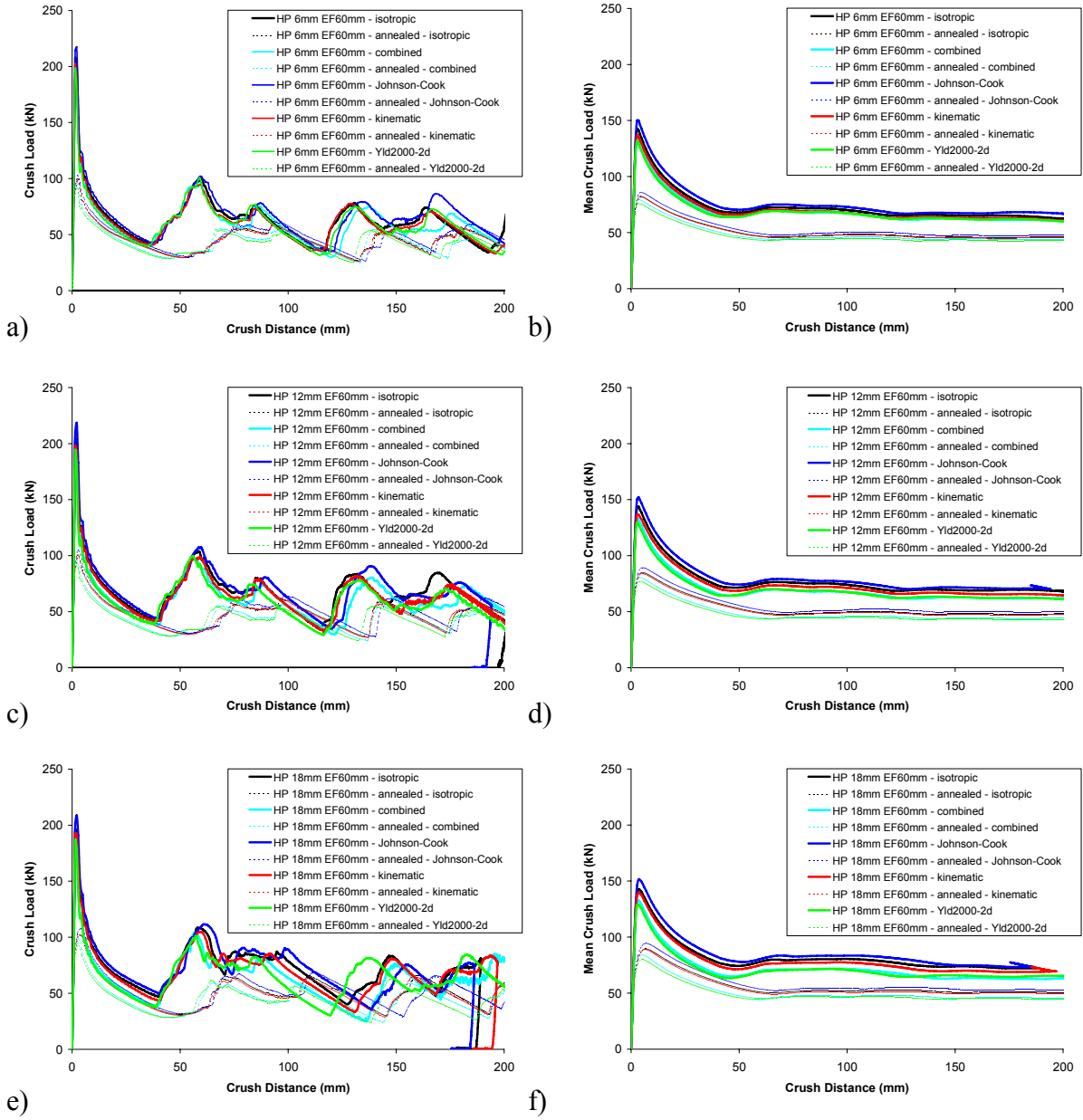e) HP 18mm EF60mm   f) HP 18mm EF60mm – mean load

Figure E.5: Comparison of crush response between isotropic, strain-rate, kinematic hardening, anisotropic, and combined predictions (obtained from combined material model)

a) HP 6mm EF60mm   b) HP 6mm EF60mm – mean load

c) HP 12mm EF60mm   d) HP 12mm EF60mm – mean load

e) HP 18mm EF60mm   f) HP 18mm EF60mm – mean load